UNIVERSITY OF HYDERABAD

Effects of Gamma and Swift Heavy Ion irradiation on the performance of HfO_2 based Resistive Random Access Memory (RRAM) Devices

A thesis submitted by

NIMMALA ARUN

in the partial fulfillment of the requirements

for the degree of

DOCTOR OF PHILOSOPHY

In

Electronics Science

Centre for Advanced Studies in Electronics Science and Technology (CASEST)

School of Physics

University of Hyderbabd

Telangana-500046

February, 2021

Dedicated to my Sisters

Haru and *Archu*

iii

Declaration

I, **Nimmala Arun**, declare that this thesis titled, "**Effects of Gamma and Swift Heavy Ion irradiation on the performance of HfO_2 based Resistive Random Access Memory (RRAM) Devices**" submitted to the University of Hyderabad in partial fulfillment for the award of **Doctor of Philosophy (Ph.D)** in **Electronics Science** is an original research work carried out by me under the supervision of Prof. S V S Nageswara Rao in **Centre for Advanced Studies in Electronics Science and Technology (CASEST)**, School of Physics, University of Hyderabad, Telangana, India. I also declare that this work has not been submitted previously in part or in full to this Univeristy or any other University or institution for the award of any degree or diploma. **A report on plagiarism statistics from the University librarian is enclosed**.

Signed: _____

(NIMMALA ARUN, 14PHPE03)

Date: 10-02-2021

Certificate

This is to certify that the work embodied in this thesis entitled "Effects of Gamma and Swift Heavy Ion irradiation on the performance of HfO_2 based Resistive Random Access Memory (RRAM) Devices" has been carried out by Mr. NIMMALA ARUN (Reg. No. 14PHPE03), in partial fulfilment of the requirements for the award of Doctor of Philosophy (Ph.D) in Electronics Science, is a bonafide work carried out by him under my supervision and guidance.

This thesis is free from plagiarism and has not been submitted previously, in part or in full to this or any other University or Institution, for an award of any degree or diploma. Further, the student has the following publications before the submission of the thesis for adjudication.

[1]. **N. Arun**, K. Vinod Kumar, A. P. Pathak, D. K. Avasthi S. V. S. Nageswara Rao, "Hafnia based resistive switching devices for non-volatile memory applications and Effects of gamma irradiation on device performance", Rad. Eff. Def. In Sol., 173 (3-4) **(2018)**, 239-249 (part of Chapter 4).

[2]. **N. Arun**, K. Vinod Kumar, A. Mangababu, S. V. S. Nageswara Rao A. P. Pathak, "Influence of the bottom metal electrode and gamma irradiation effects on the performance of HfO_2-based RRAM devices", Rad. Eff. and Def. in Sol., 174 (1-2), **(2019)**, 66-75 (part of Chapter 4).

[3]. **N. Arun**, L.D. Varma Sangani, K. Vinod Kumar, A. Mangababu, M. Ghanashyam Krishna, A. P. Pathak, and S.V.S. Nageswara Rao, "Effects of swift heavy ion irradiation on the performance of HfO_2 thin films based resistive random access memory devices",Journal of Materials Science: Materials in Electronics, DOI: 10.1007/s10854-020-05049-0,**(2021)** (part of Chapter 5).

[4]. **N. Arun**, S. V. S. Nageswara Rao, A. P. Pathak, "Effects of Swift Heavy Ion irradiation on RRAM devices of Au/HfO_x/Au/Si cross-bar structures" (part of chapter 6). (to be submitted)

[5]. **N. Arun**, S. V. S. Nageswara Rao, A. P. Pathak, "Effects of Interfacial/metal-insulator layer on switching parameters of RRAM devices of (Al, Cr, Au)/HfO_x/Au/Si cross-bar structures"(part of chapter 6). (to be submitted)

Conference Proceedings

[1]. **N. Arun**, J. Prabana, K. Vinod Kumar, A. P. Pathak, and S. V. S. Nageswara Rao, "Fabrication of HfO_2 based MOS and RRAM devices: A study of Thermal Annealing Effects on these Devices", AIP Conf. Proc. 2115, **(2019)**, 030216-1–030216-4 (part of chapter 4).

Further, the student has passed the following courses towards fulfilment of coursework requirement for Ph.D.:

Course code	Name of the course	Credits	Pass/Fail
IC801	Semiconductor Device Physics and Modeling	4	Pass
IC802	Integrated Circuits and nano fabrication Technology	4	Pass
IC803	VLSI Design Technology	4	Pass
IC804	RF and Microwave IC's Theory	4	Pass
PY821	Research Methodology	4	Pass

S. V. S. Nageswara Rao
10/02/2021

Prof. S V S Nageswara Rao (Supervisor)

Head, CASEST (Centre for Advanced Studies in Electronics Science & Technology) School of Physics University of Hyderabad.

Prof. S.V.S. NAGESWARA RAO
School of Physics
University of Hyderabad
Hyderabad-500 046, INDIA.

Head CASEST

Dean (School of Physics)

DEAN
School of Physics
University of Hyderabad
Hyderabad-500 046, INDIA

Acknowledgements

First, I would like to express my sincere thanks and gratitude to my thesis supervisor Prof. S. V. S. Nageswara Rao, Centre for Advanced Studies in Electronics Science and Technology (CASEST), School of Physics, University of Hyderabad for his esteemed supervision, inspiration, constant encouragement, support and help throughout my research carrier. I personally and individually thank both of my supervisor. I thank Prof. Ashok Chatterjee, Dean, School of Physics and former Deans Prof. Seshubai, Prof. Bindu A Bambha, Prof. Rajendra Sing, Prof. S. Chaturvedi, Prof. S. P. Tewari for their co-operation in providing facilities and infrastructure in School of Physics. I also would like to thank Prof. K. C. James raju, Head, CASEST and former Heads Prof. S. L.Sabat, Prof. G. Rajaram for their co-operation in providing facilities and infrastructure in CASEST. I am very privileged to have Prof. M. Ghanashyam Krishna and Prof. S. L.Sabat as my Doctoral committee members whose suggestions, encouragement and insights have improved the understanding of our results. I express my sincere gratitude to Prof. A. P. Pathak for his valuable suggestions during my research work

I thank Dr. D. Kanjilal, Director, IUAC for his useful suggestions during discussions. I express my sincere thanks to Dr. S. A. Khan for technical discussions and help during beam time experiments at Inter University Accelerator Center (IUAC), New Delhi and during his visits to of University of Hyderabad. I thank Dr. D. Kabiraj and Mr. Abhilash for allowing us to utilize the facilities in target lab. I would like to thank Mr. Sunil Ojha for his help during RBS measurements. I am also thankful to the members of Pelletron Accelerator group and other scientists at IUAC for necessary support during experiments. I also thank the CeNSE (Indian Nanoelectronics Users Program (INUP) for providing necessary facilities for the XPS experiments and Mask fabrication at IISc, Bengaluru. I would like to thank UGC, New Delhi for providing fellowship as JRF and SRF. I also thank personally the technical staff Mr. Rajeev, Mr. Tajgaraj, Mr. Prashanth, Mr. Rajendra Prasad, Mr. Pankaj, Ms. Sunitha, Mr. Naresh, for their help during the experiments. I would like to thank all non-teaching staff in school of physics and nano center for their help during my Ph.D., time.

I personally thank my close and childwood (JNV-C) friends Mr. Nakka Ajay, Mr. K. Sathish, Mr. T. Sampath, Mr B. Srinivas, Mr. J Thiru, Mr. R. Sammi, for financial and moral support during the Ph.D time. I also thank my graduation (B. Tech) friends Mr. Hemanth.

S, Mr. Rakesh. V, Mr. Amar. B, Mr. Krishana Prasad.K, Mr.Ramakoteswaraju. R, Inilhas .G, Ms. Nagasri.K for their moral support and encouragement during my Ph.D. time.

I thank all my friends who have helped me when I was in struggle. I would like to thank my seniors Dr. S. L. D Varma, Dr. Manikanthababu, and Dr. Vendamani and Dr. Dhanujaya for sharing their knowledge and lab experiences. I would like to thank to Mr. Vinod, Mr. Mangababu, Ravi, Sai prasad and Rena Rakesh for their help in various aspects.

It wouldn't be enough to say simply thanks to my parents Mr. Lachaiah Nimmala, Ms. Prameela Nimmala and grand parents Anjaiah Nimmala , Yashoda Nimmala, who brought me where I am now. I would like to express my sincere thanks to my sisters, Ms. Haritha, Ms. Archana and my wife Manisha Rao Also, I specially thank all other family members for their timely support. I would like to thank all of them who are involved either directly or indirectly for the completion of my Ph.D. successfully.

Contents

List of Figures

List of Tables

List of Abbreviations

ALD	Atomic layer Deposition
BE	Bottom electrode
BRIT	Board of Radiation Isotope Technology
BLC	Bulk Limited Conduction
CAD	Computer-Aided Design
CBRAM	Conductive BridgeRandom Access Memory
CDF	cumulative distribution function
CVD	Chemical Vapor Deposition
CFN	Centre for Nanotechnology
CERN	European Organization for Nuclear Research
CD	Compact disc
CMOS	Complementary Metal Oxide Semiconductor
CF	Conductive filaments
DRAM	Dynamic random access memory
DC	Dirct cuurent
DVDs	Digital Versatile Discs
DT	Dirct Tunneling
DUV	Deep Ultra violet
DI	De-ionized
EPROM	Erasable Programmable Read Only Memory
ECM	Electrohemical Mechanism
ELC	Electrode-Limited Conduction
EDS	Enegry x-ray Dispersive Spectroscopy
EBL	e-beam lithography
EHT	Extra High Tension
FeRAM	Ferroelectric Random Access Memory

FN	Fowler-Nordheim
FE	Fieled Emission
FESEM	Field Emission Scanning Electron Microscopy
FC	Faraday Cup
GI-XRD	Glancing incident X−ray diffraction
GB	Grain Boundaries
HF	Hydrofluoric
HCL	Hydrochloric acid
H_2O_2	Hydrogen peroxide
HRS	High Resistance State
I-V	Current voltage
IC	Integrated circuits
IISC	Indian Institute of Sciences
INUP	Inter University User program
IUAC	Inter University accelerator centre
Icc	Current compliance
JDPDS	Joint Committee on Powder Diffraction Standards
LRS	Low resistance state
MRAM	Magnetoresistive Random-Access Memory
MOS	Metal Oxide semiconductor
MIM	Metal insulator metal
MOSCAPs	Metal oxide semiconductor capacitors
MPSMU	Medium Power Source/Measure Unit
NIR	Near infra red
NH_4OH	Ammonium Hydroxide
NEC	National Electrostatic Cooperation
NVM	Non Volatile Memory
OD	oxide deposition
PCRAM	Phase-Change Random Access Memory
PL	Photoluminscence
PF	Pool Frenkel

PR	Photo Resist
PVD	Physcial vapor deposition
PnA	Particle nanoAmpere
PLD	Pulsed laser deposition
ROM	Read only memory
RRAM	Random Resistance Access Memory
R_{on}	Resistance ON
R_{off}	Resistance OFF
R_{off}/R_{on}	Resistance OFF/Resistance ON
RF	Radio Frequency
RBS	Rutherford-Backscattering Spectrometry
RMBE	Reactive Molecular Beam Epitaxy
RS	Resistve switching
SRAM	Static Random-Access Memory
SE	Schottky emission
SCLC	Space-Charge-Limited Conduction
SHI	SWift Heavy Ion
SRIM	Stopping and Range of Ions in Matter
SNICS	Source of Negative Ions by Cesium Sputtering
SCCM	standard cubic centimeters per minute
SIMNRA	Simulation of Ions in Matter and Nuclear Reaction Analysis
SDA	Semiconductor Device Analyzer
1TIR	One-Transistor One-Resistor
1T1C	One-Transistor One-Capacitor
TMO's	Transitional Metal Oxides
TID	Total Ionizing Dose
TAT	Trap-Assisted Tunneling
TE	Top Electrode
UV	Ultra violet
UoH	University of Hyderabad
UD	Unit Double

Vis	Visible
VCM	Valence Change Memory
V_{Reset}	Reset Voltage
V_{set}	Set Voltage
V_{tr}	Threshold Voltage
V_{TFL}	Trap filled Limit Voltage
XRR	X−ray Reflectivity
XPS	$X-$ ray Photoelectron Spectroscopy

Abstract

HfO_2 based Resistive Random Access Memory (RRAM) devices have been fabricated by employing various physical vapor deposition and photolithography techniques. These devices have exhibited superior switching properties which include high resistance ratio (R_{Off}/R_{On} >10^5), endurance and retention time. These devices are found to be of forming free type with uni-polar switching behavior. HfO_2 films deposited by RF sputtering and HfO_x films deposited by e-beam evaporation have been employed as active layers. The influence of various metal electrodes on the performance of these RRAM devices has been investigated. Further, the effects of thermal annealing, gamma irradiation and swift heavy ion (SHI) irradiation on the switching properties of these devices have been studied in detail. As expected, thermal annealing has introduced monoclinic phase in otherwise amorphous films. SET and RESET voltages are found to increase with increase in annealing temperature for HfO_x films. Gamma irradiation deteriorated the performance of these devices whereas SHI irradiation has improved their performance below a critical fluence. It is shown that the spread in the switching voltages is reduced and switching voltages can be lowered by low fluence SHI irradiation. These results provide useful information to tailor as well as to study the reliability of these devices in radiation harsh environment. This thesis addresses some important aspects related to the fabrication, radiation response and reliability of emerging RRAM devices that are critical for the development of electronics science and technology.

Chapter 1

Introduction and Background

1.1 Introduction and Motivation

Resistive Random Access Memory (RRAM) devices have been identified as potential building blocks for future Non-volatile Memory (NVM) and reconfigurable hardware devices [1-3]. RRAMs have attracted significant attention because of their high-density memory architecture [4,5], low power consumption [6,7], faster switching [4] and longer retention time when compared to conventional NVM devices [8]. These emerging devices are expected to replace the currently used floating gate devices, in near future [9-11]. Applications of RRAMs are not limited to data storage devices alone but they may also be used for processing elements such as logic gates [12,13]. "In-memory computation" is envisaged with the advent of RRAM based digital logic circuits. Based on the nature of switching mechanisms involved, RRAMs also find applications in neuromorphic systems [14-16]. A natural consequence of the promise shown by RRAM devices is their deployment in space and nuclear electronics which operate in radiation harsh environments. It is, thus, important to study the effects of ion irradiation, radiation damage and reliability of these devices. However, such studies are very limited in literature [13]. The main objective of this thesis has been to fabricate micro-electronic compatible RRAM devices by employing various thin-film deposition and photolithography techniques and to study their radiation response.

1.2 Introduction to memory technologies

In the present digital world, information is stored in the modern electronic memory devices. Digital memory has become an integral part of our lives, by being a critical element in the smart and intelligent devices around us, in the current age of Internet of Things (IOT)[9].

These memory devices are mainly fabricated by using CMOS based technology. There has been significant progress in terms of memory capacity, speed, retention time and endurance as the memory technologies have evolved through punched cards, magnetic memories, optical memories to current solid state memory devices. Inview of their importance and applications in several areas, memory technology has been at the focus of attention of research for many years[17]. As a result, over the past few decades, the size and cost of the memory devices are decreasing as predicted by the Moore's law [13,18]. As a consequence of these efforts, different kinds of memory technologies have emerged.

Some major examples of modern memory devices are magnetic memories, optical memories and CMOS memories[19-21]. In comparison to other memory technologies CMOS memories are superior in many aspects including memory capacity and ease of access to data. In CMOS memories, there are different memory technologies based on factors such as speed, volatility , cost and density. The categories of currently available semiconductor storage devices are presented in *Figure* 1.1(a). The CMOS based semiconductor storage devices are mainly categorized based on two factors: (a) the maximum number of times that they are rewriteable and (b) their retention capacity to store the information over longer periods [10]. Based on the number of rewritable cycles and access speed, memories can be divided into RAM and ROM. Information can be read and written multiple times in a RAM very fast [22]. In contrast, in a ROM, the information can be written only once, but reading can be done for a multiple number of cycles[4]. Such devices are called EPROM if they are erasable and reprogrammable. On the other hand, the access speed of ROM is relatively less than that of RAM. The devices such as Optical, magnetic and flash memories come under the category of ROM. Based on the second factor, data retention, memory devices can also be divided into two categories: 1) volatile devices, which lose the data when the power is switched off and 2) non-volatile devices, which retain the data even after power is switched off.

Based on the application, the term "memory" in the semiconductor industry is defined at different levels in the computer memory hierarchy[23]. It consists of three main components; cache, main memory and storage memory [24]. The memory hierarchy is given in the *Figure* 1.1(b). These three categories were chosen based on the capability/performance of the available memory components. Among them, cache is an ultrafast memory that is on chip along with the processor. A specific characteristic low latency of SRAM makes it

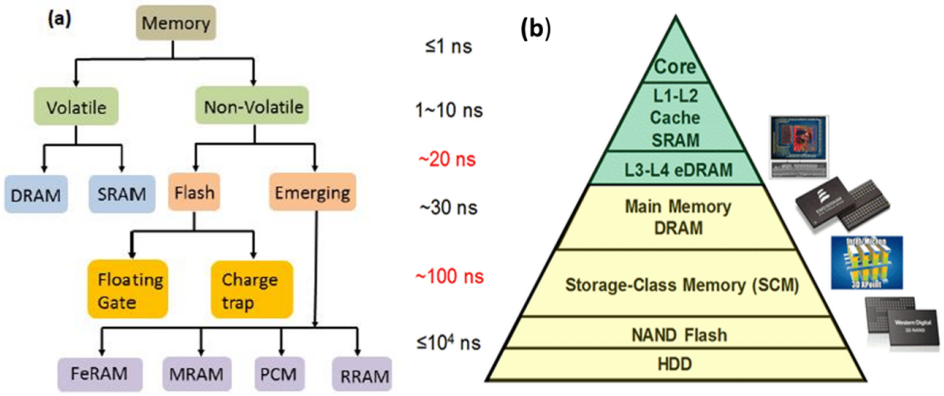

FIGURE 1.1: a) Categorical representation of different types of memory devices, and (b) representation of memory hierarchy.

ideal for cache[21]. However, its low density and volatile nature made the researchers look for alternative secondary levels in the memory hierarchy [23]. This level of memory is a low latency level with high density, where a concept of DRAM comes into picture for this purpose. When compared, the DRAM is not as fast as SRAM, but it provides much higher density and hence it is cost effective. Meanwhile, SRAM and DRAM are volatile, so one more level of memory is required to back up the data. Furthermore, here the storage for memory comes in the next level hierarchy.

As discussed above, to further comparison, the device structures of DRAM, SRAM and Flash memories are shown in *Figure* 1.2. DRAM simply consists of 1T1C structure whereas SRAM has six transistors. The DRAM is denser and slower in writing and erasing the data than SRAM and needs additional circuitry to refresh the stored data. Similarly, the Flash memories are also single transistor based memory devices (see in *Figure* 1.3). and are non-volatile in nature. However, the CMOS transistor based memory devices have difficulties for further miniaturization due to physical limits that lead to the excessive leakage current and short channel effects.

Considering the above-mentioned points, the demand for further improvements in memory technologies has continued to increase[23]. There is a need and possibility for the other evolving new memory device technologies to fulfill the current and future requirements[5,25].

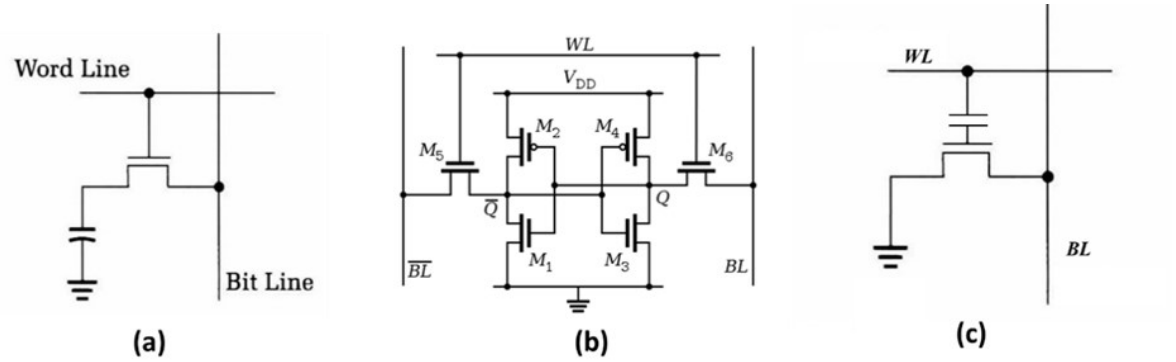

FIGURE 1.2: The device structure of a) DRAM, b) SRAM and c) Flash memory.

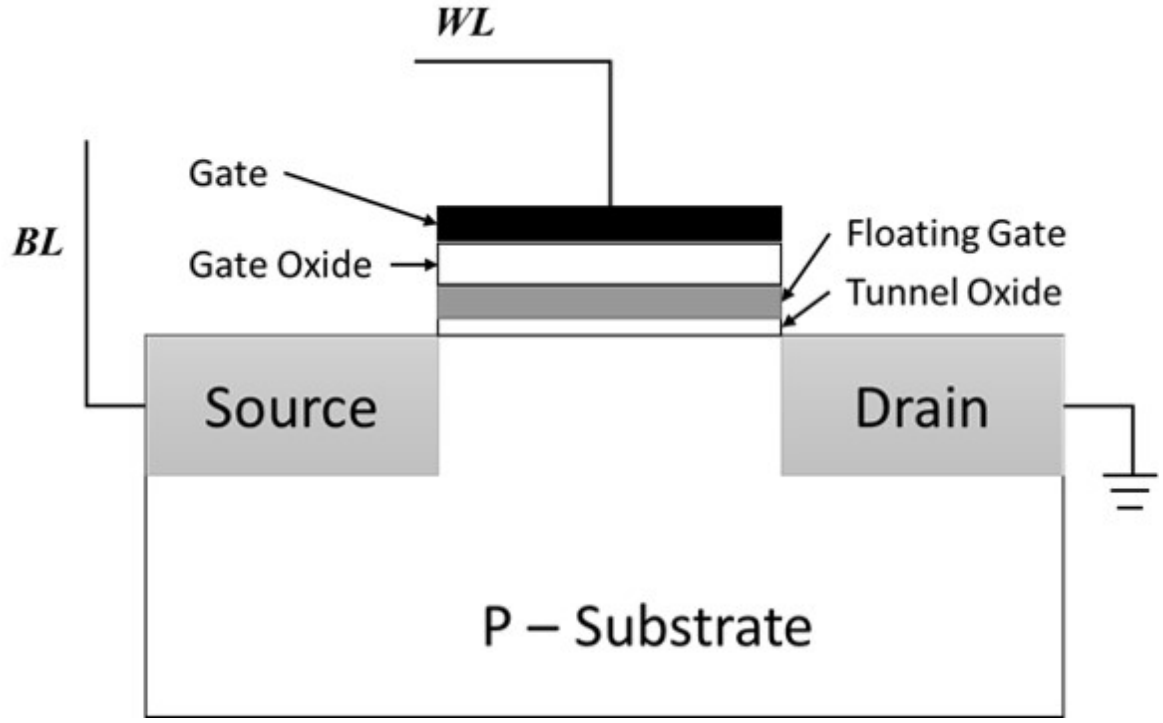

FIGURE 1.3: Schematic view of flash memory device structure.

1.3 Emerging candidates for alternate technologies

Next generation novel memory devices have been extensively researched in recent years. Some such devices are FeRAM, PCRAM, MRAM and RRAM devices[8]. The FeRAM device structure is similar to that of a DRAM, i.e. one transistor and one capacitor structure (see *Figure* 1.4(a)). The ferroelectric and a linear dielectric material are used for capacitor fabrication for FeRAM and DRAM, respectively. Switching can be achieved in FeRAM by means of a change in polarization of the ferroelectric by applying a DC bias[8]. The dipoles tend to align in the direction of the applied electric field. This effect will be observed after the removal of the applied field so that the reversal in polarization is hysteretic in nature. This phenomenon can be used in a non-volatile memory device[26]. FeRAM can be operated at low power and high writing speed compared to flash memories [8].

Similarly, in MRAM the main switching layer is a free magnetic layer and switching is due to relative magnetization. Basically it has a tri-layer structure, as a thin insulating tunnelling layer is sandwiched between two magnetic layers, as shown in *Figure* 1.4(b). One is with permanent magnet having a specific polarity and the other one is a free magnet. The magnetization can be varied by applying an external field for the free magnet. Based on the relative orientation between these two magnetic layers, results in resistance change as parallel and anti-parallel alignment. The device will be in low resistance state when the magnetic orientations of the two layers are parallel and in high resistance state when the orientation is anti-parallel [27].

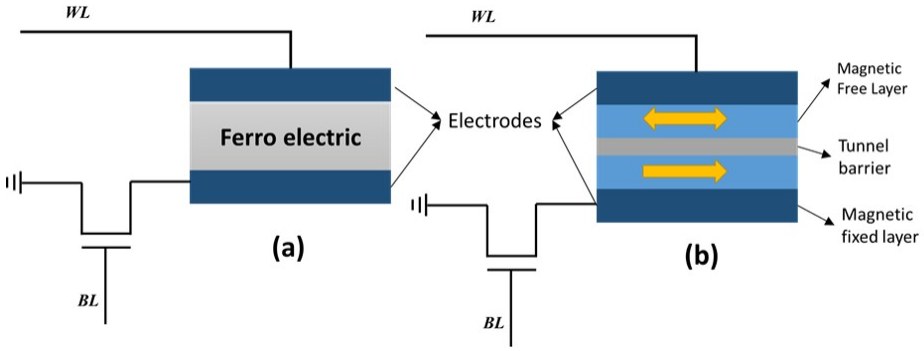

FIGURE 1.4: Schematic diagram of a) FeRAM and b) MRAM structures.

The MRAM and FeRAM devices are non-volatile in nature and operate at high speeds with good endurance. However, scaling down FeRAMs is non-trivial and it takes high current in the range of mA to program the cell[28]. Similarly, scaling down MRAM devices is

a challenge and they also require high writing current. Furthermore, PRAM has a phase changeable material as switching layer[29]. Typically, high chalcogenides are used since these can be reversible and show transitions between amorphous and crystalline phases under heating. Mostly in the present scenario, it can be seen/found in rewritable optical memory discs, e.g. CDs, DVDs and blue-ray DVDs[29]. This can be achieved by heating with a laser to induce the phase transitions in the material. PRAMs display high operation speed, good scalability and good endurance[10]. However, PRAMs are known to consume more power for operation in addition to being temperature sensitive [10]. It is, thus, evident that there is a strong need for replacing the present memory devices which are facing difficulties for further improvement. Flash Non-volatile memory devices played a crucial role and have currently dominated memory devices in the market of electronic products.

However, the read and write speeds are very low and operating voltages and/or currents are high as compared to that of the volatile memories such as SRAM and DRAM. Memory devices that couple the benefits of both RAM and ROM (high density, high-speed, low operating voltages/currents and non-volatile memories) have to be produced. In this prospective, RRAMs have the potential to provide the required benefits such as non-volatility, high density low cost and high speed. The switching principle for a RRAM is similar to that of the PRAM. 1T1R forms one memory cell where the transistor acts as a selector for the memory cell. In recent reports, the selector transistors have been replaced by diodes which increases the density and complexity of the structure. Attempts to avoid the selector by varying cross-bar architecture are also reported [28-30]. Resistive switching is shown in a wide variety of materials ranging from metal oxides,semiconductors, polymers, Chalcogenides, ceramics etc..,[31]. RRAM devices are more amenable to scaling down than other emerging memories with higher speed and lower current density to switch between the states. Owing to these advantages over other memories, RRAMs have a higher potential for future memory technologies. More details about RRAM devices are given in the following sections. *Figure* 1.5 shows the comparison of present and emerging memory devices and related parameters.

	Traditional Memory				Emerging Memory			
	DRAM	SRAM	Flash NOR	Flash NAND	FeRAM	MRAM	PCRAM	RRAM
Feature size (F) (nm)	36	45	45	16	180	65	45	<5
Read time	2 ns	0.2 ns	15 ns	0.1 ms	40 ns	35 ns	12 ns	1 ns
Write time	2 ns	0.2 ns	1 us	0.1 ms	65 ns	35 ns	100 ns	<1 ns
Retention time	4 ms	n/a	>10 yr	>10 yr	>10 yr	>10 yr	>10 yr	>10 yr
V_{write} (V)	2.5	1	8-10	15-20	1.3-3.3	1.8	3	<0.5
V_{read} (V)	1.7	1	4.5	4.5	1.3-3.3	1.8	1.2	<0.2
Write endurance	$> 10^{16}$	$> 10^{16}$	10^5	10^5	10^{14}	10^{12}	10^9	$> 10^{12}$
Write energy (J/bit)	$4x10^{-15}$	$5x10^{-16}$	10^{-10}	$4x10^{-16}$	$3x10^{-14}$	$2.5x10^{-12}$	$6x10^{-12}$	$< 10^{-12}$

FIGURE 1.5: Comparison of present and emerging memory parameters.

1.4 Memristor

Capacitors, resistors and inductors, discovered in1745, 1827 and 1831 respectively, are the only known fundamental passive elements for many decades although theory predicts a fourth element. In 1971, the memristor was proposed as the missing fourth fundamental circuit element, by Leon Chua [32]. According to Chua, as shown in *Figure* 1.6, the elements resistor, capacitor and inductor relate voltage-to-current, voltage-to-charge and current-to-flux respectively. The Voltage-flux and charge -current can be related without any circuit element but there was one missing element for relating charge and flux. Therefore, he proposed an element which realizes this and named it as memristor[33]. He derived the relationship given in the *equation 1.1*

$$d\phi = Mdq \tag{1.1}$$

Where ϕ is flux, q is charge and M is memristance.

As the name suggests the memristor (memory + resistor) may be treated as a storage element with the units of resistance. The concept of memristor, as a storage resistive element, is employed in MRAM, PRAM and RRAM technologies. The storage is obtained by switching between two stable states as high (off) and low (on) resistance states. However, the memristor mechanism is not yet fully adopted and RRAM is categorized as a family of memristors [33].

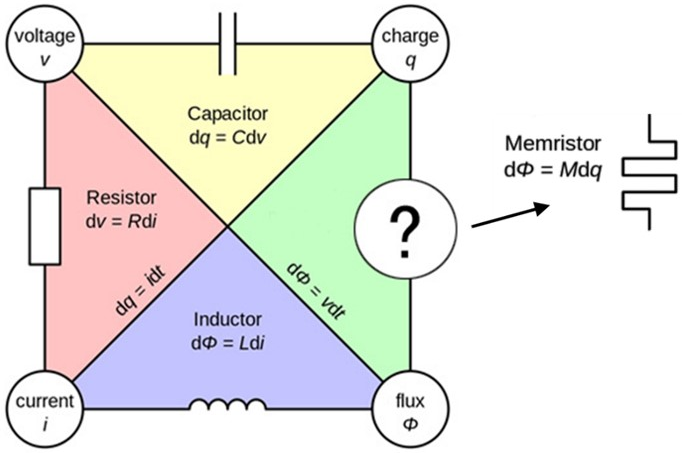

FIGURE 1.6: Relation between the four fundamental electronic variables.

1.5 Resistive Random Access Memory

As mentioned earlier, RRAM is one of the most popular emerging non-volatile memory devices in the current digital world scenario. It has a simple MIM structure. The resistance levels of the insulating (I) layers play an important role in the resistive switching and memory storage operation. The schematic of RRAM is shown in *Figure* 1.7. The resistive switching behavior of the I film is reversible and switches between two stable resistance states: these are high resistance state (HRS) and low resistance state (LRS) by application of either an external dc bias voltage or current. This device remains in the switched or particular resistance state after removing the supply. It is the key for the non-volatile nature of these devices. This kind of reversible switching phenomenon was first reported in the late 1960s [34]. After that in recent times the interest in resistive switching began in the late 1990s.

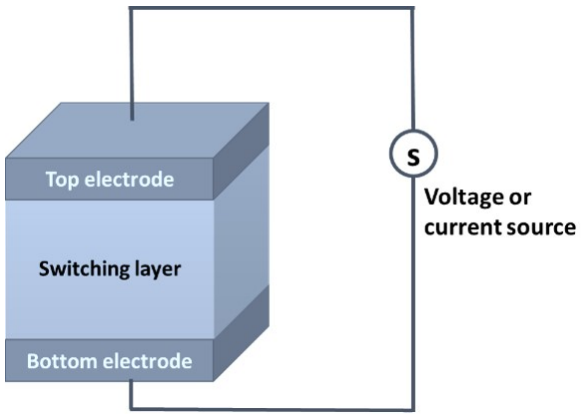

FIGURE 1.7: The schematic view of a RRAM device.

This switching behavior is observed in many of the materials such as perovskite oxides

of $SrTiO_3$, $SrZrO_3$, binary metal oxides such as NiO, Cu_xO, HfO_2 and TiO_2[35,36], organic materials, semiconductors, ferroelectric materials and ferromagnetic materials. Here, the mechanism of switching in different materials is entirely dependent on several factors. As mentioned above, not the only insulating layer but also the choice of metal electrode material and their interfacial effects can also influence the switching behavior of the memory devices. Hence, it is important to adopt an appropriate insulator and the metal electrodes for the fabrication of the RRAM devices. Furthermore, it is worth mentioning that the RRAM devices have many applications in logic gates, analog circuits, random number generators and in neutral networks [37-39].

In many situations, the RRAMs have attracted industrial attention, due to their simple structure, cost effectiveness for the processing and most importantly adaptability to the currently existing CMOS technology. Scaling is more advantageous for RRAM devices than the transistor based CMOS memories[40]. Each memory cell occupies only $4F^2$ area (where F is the minimum feature size) which is relatively smaller than that of the other emerging memories; the smallest cell size so far being 10 nm [41]. It also supports 3D architecture that enables much denser memory structures and further decrease in the effective cell size.

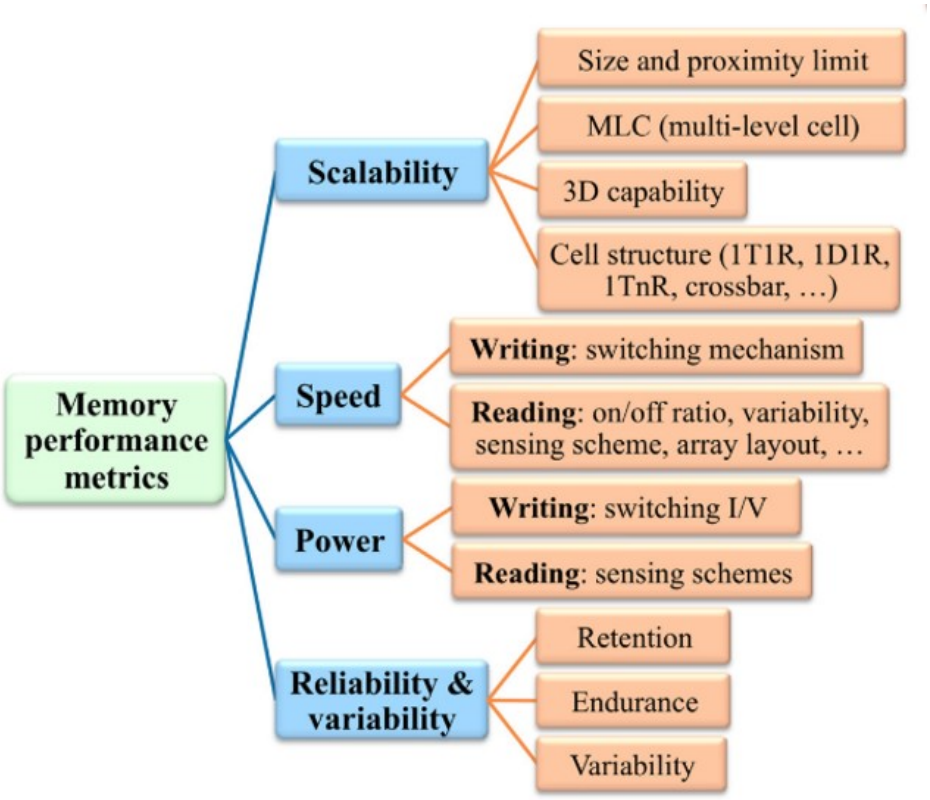

FIGURE 1.8: The RRAM device memory performance metrics.

RRAM also works at good operating speed and low power with good endurance and retention. Hermes et al.[42] demonstrated TiO_2 based ultrafast RRAM devices with 5 ns operating speed and Yang et al. [43] reported TaO_x based devices with endurance greater than 10^{10} cycles. In this connection, it is worth mentioning that the performance of the RRAM device is judged by the few key factors/parameters such as scalability, power consumption, speed and reliability studies. *Figure* 1.8 shows the memory devices performance metrics for the RRAM.

1.6 Operating principles of RRAM

Normally, the RRAM devices show a hysteresis curve in I-V characteristics. This clearly distinguishes a large variation between two different resistance states, namely HRS and LRS. The switching can be controlled either by a DC bias source of voltage or current. Usually, the device will exhibit the high resistance state. By applying a proper external DC bias, it comes to a low resistance state. The very first and initial switching from insulating (or HRS) to conducting (or LRS) is called formation process. Secondly, switching back to HRS from LRS is called reset operation. Thereafter, HRS to LRS switching takes place at voltages lower than formation voltage and this is named as set process. Hence, the formation is an initial step in device operation which prepares the device for memory operation by forming conducting paths in the as-prepared or pristine cell. Set and reset are the steps to switch the device into the desired state i.e. either LRS or HRS. Some devices are reported to be of forming free type [9,11,20,29] and the devices studied in this thesis are mostly of forming free type, may be because of the pre-existing defects in the as grown oxide films.

Basically, the operation of the RRAM devices based on the polarities are classified into two categories: unipolar and bipolar devices. If the switching characteristics of a device happen to be in the same direction (or if both the set and reset are triggered by a single directional/polarity bias voltage) then it is termed as an uni-polar device. In contrast, the set takes place in one polarity and the reset occurs at opposite polarity in the case of the bi-polar devices. Furthermore, set and reset operations are dependent only on the amplitude but not on the direction then they are called non-polar devices. However, in the bipolar case, the switching direction is dependent on both the amplitude and direction. All the possible

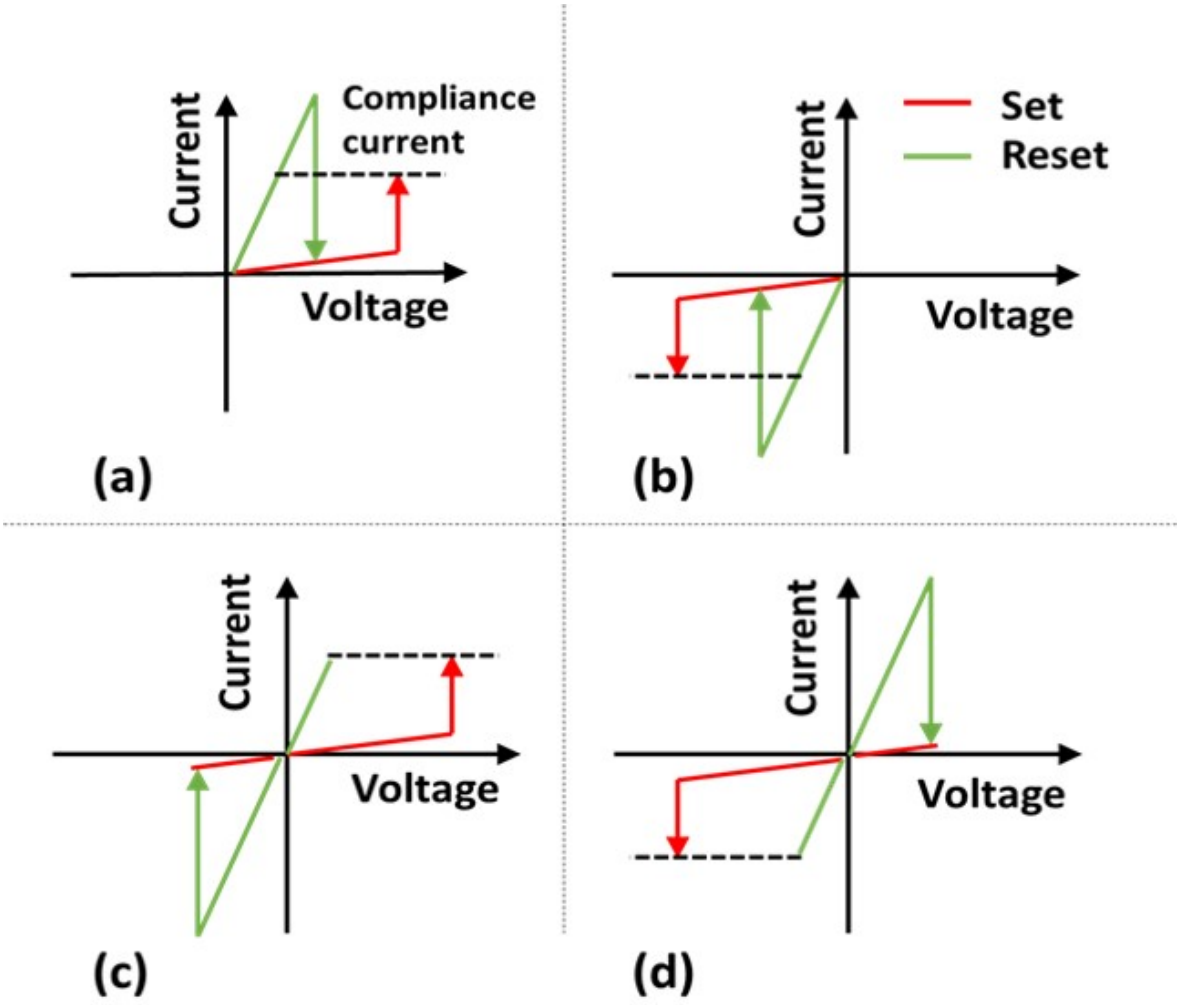

FIGURE 1.9: Basic resistive switching: a, b) Unipolar and c,d) bipolar modes.

switching characteristics of the resistive memory device are shown in *Figure* 1.9(a)-(d). Some resistive devices and their switching modes are mentioned in *Table* 1.1.

TABLE 1.1: List of memory devices and their switching modes

Unipolar	Bipolar
Pt/NiO/Pt [35]	Pt/NiO/$SrRuO_3$ [44]
Pt/TiO_2/Pt [36]	Pt/TiO_2/TiN [45]
Pt/ZnO/Pt [46]	TiN/ZnO/Pt [47]
Pt/ZrO_2/Pt [48]	Ti/ZrO_2/Pt [48]
Pt/HfO_2/Pt [49]	TiN/HfO_2/Pt [50]
Pt/Al_2O_3/Pt [51]	Ti/Al_2O_3/Pt [52]

1.6.1 Mechanisms of resistive switching

The switching behavior of a RRAM device from HRS to LRS and reversing back to HRS from LRS in dielectric or semiconducting materials is very complex. Knowledge of the typical switching mechanism of the RRAM is essential to tailor its performance. As mentioned above, one of the important factors is the interface contact of the metal and insulator of the cross bar structure in RRAM devices. Hence, it is important to investigate the contribution to the switching performance in the conduction mechanisms of these RRAM devices.

Interestingly, it is found that the switching mechanism is not the same for all types of the active layers used in these devices. Based on the investigation and availability of data, several models have been proposed to explain the switching mechanisms. Two of the most commonly observed mechanisms in the majority of the RRAM devices are: (i) ECM[53,54] and (ii) VCM[54-56]. Among these, ECM is mostly found to be more effective for the active metal electrode and is purely of Filamentary type conduction (due to metal ions diffusion). Whereas, the VCM can be either of Filamentary type or interfacial effects from the oxygen vacancies in the insulating material. Therefore, the choice of the metal and insulator can play a crucial role in the RRAM device performance. Further, it is observed that it can also influence the switching mechanism and switching modes (*Table* 1.1). Some of these mechanisms are discussed in the following sections.

1.6.1.A. Electrochemical metallization mechanism

Electrochemical metallization mechanism is mainly observed in most of the RRAMs for which either one of the electrochemically active electrodes (e.g. Ag, Ni, Cu and Ti etc..) and other of inert electrode (e.g. Au, Pt, W, etc..) are used in the cross-bar structures[20]. However, an insulating layer of a solid electrolyte is sandwiched between these metal electrodes. A schematic representation of ECM switching mechanism is shown in *Figure* 1.10. In ECM, the electrochemically active electrode gets deposited at an inert metal electrode and starts forming or growing nano–sized conductive filaments upon applying a voltage to the top and bottom electrodes. The formation of these conductive filaments, making a transformation to LRS from HRS, is called set operation, Thereafter, the breaking of those conductive filaments is called reset operation (i.e. to HRS from LRS). This can be reproduced for a multiple number of cycles and usually it happens to be in bipolar switching mode [53]

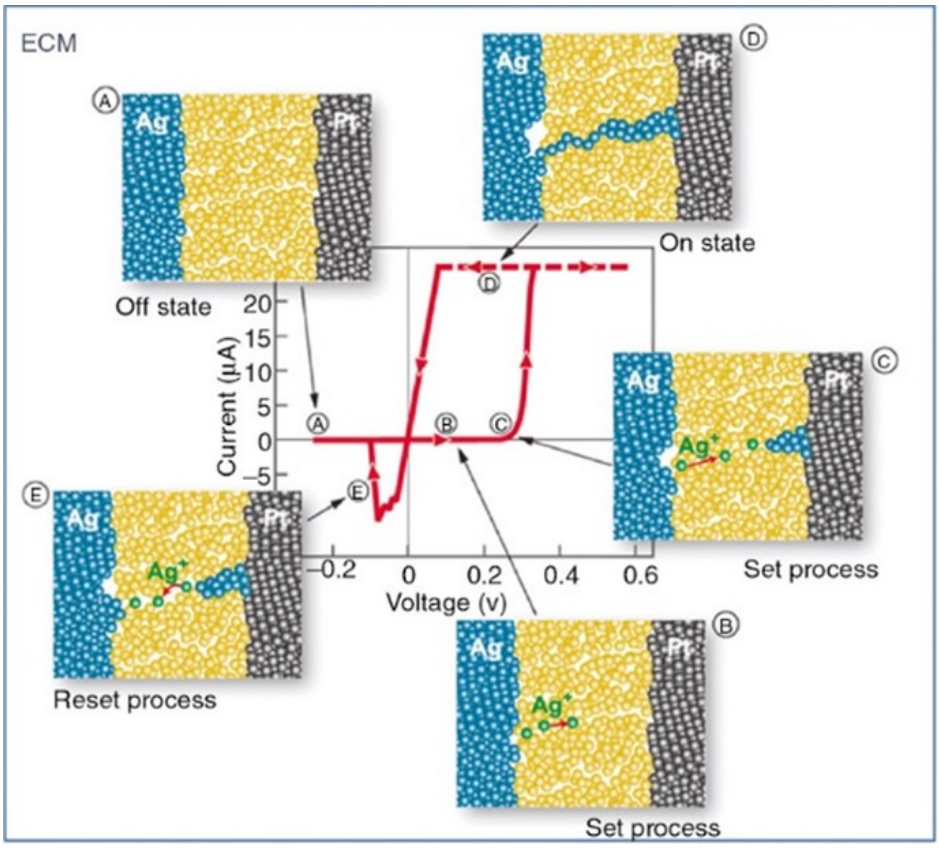

FIGURE 1.10: Schematic representation of ECM switching mechanism of RRAM device.

1.6.1.B. Filamentary mechanisms

In transition metal oxides, resistive switching is mostly observed to be of filamentary type and it can be of both, unipolar/non-polar and bipolar modes[53]. A schematic representation of the switching mechanism is shown *Figure* 1.11. Basically, in this case, the conductive filaments formation can be explained by migration of oxygen ions (O_2^-) towards the top or positively biased metal electrode, there by leaving an oxygen vacancy (V_O^{2+}) in the switching layer. Furthermore, it is found that the switching mode can be unipolar or bipolar, based on the oxygen ions (O_2^-) diffusion or drift in the insulating layer, respectively. The formation of the oxygen vacancies acts as CF in the switching layer. These conductive filaments can be ruptured by means of joule heating effects for reset operation in unipolar devices. It is to be noted that the local heating in the filaments causes the temperature to rise to several hundred Kelvins due to high current density. This enables the oxygen ion migration or diffusion into CFs[7]. Whereas, in bipolar devices the diffusion due to joule heating may not be sufficient to rupture the portion of the filament[57]. A voltage bias opposite in polarity to the set bias enables the oxygen ions to drift, enabling the oxygen ions to migrate into CFs causing a portion of filament to be ruptured.

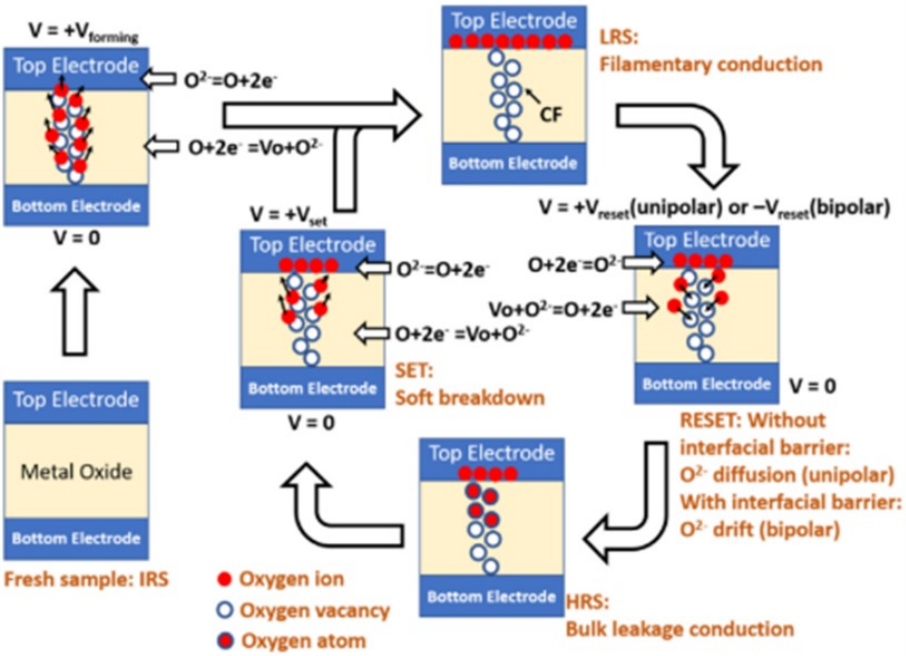

FIGURE 1.11: Schematic illustration of the switching process in the binary metal oxides based RRAM devices.

1.6.1.C. Interfacial mechanism

The interfacial mechanism usually applicable for the reactive metal electrodes (either of BE or TE). The interface contact of a metal electrode with an oxide or a switching layer will results in the reduction of resistance due to the external bias in the RRAM devices. Hence, the resistive switching between HRS and LRS is mainly due to valency change in the switching layer, as shown in *Figure* 1.12. Therefore, it depends on the active/switching layer cell area of the device. The effective resistance of both LRS and HRS increases with a decrease in cell size whereas in ECM and filamentary conduction they are independent of memory cell area [58].

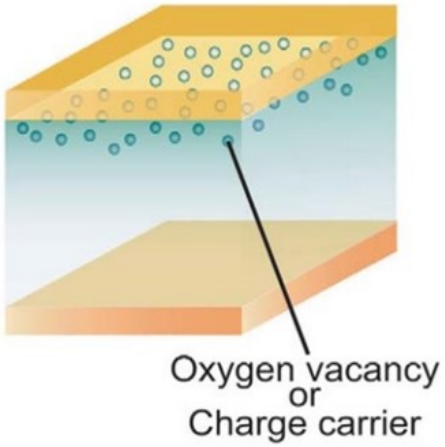

FIGURE 1.12: The simple interfacial based switching mechanism of RRAM device.

1.6.2 Important Terminologies

The Resistive switching nature is measured by few critical parameters to judge the performance of the RRAM device. Therefore, the key terminologies are given and explained below.

A. Forming Voltage

Forming is the phenomena of the formation of the conductive filaments in the electrolyte for the first time in a fresh/untested/pristine device. It is denoted by V_{Form} and the forming voltages are typically higher and are proportional to the thickness of the dielectric. As

explained above, it can be of conductive filaments as metal ion (diffusion) for electrolyte and/or oxygen vacancies (diffusion or drift) for the metal oxides in the switching layers.

B. Set Voltage

Set is the phenomena of building back the conductive filament bridge after it has been disintegrated at least once either by the Joule's heating or by electrochemical migration of ions (first reset operation). Set voltages V_{Set}, are logically lower than forming voltage, since this time, the bridge is being "re-formed" only partially. The set and forming both lead the device into LR state and this is called ON state. The resistance of the switch during this state is also called as R_{on}.The significant advantage of RRAMs over other types of memory devices is that they operate at a very low voltages. The set voltages below 1 voltage are preferable for the proper integration of memory devices with current CMOS technology.

C. Reset Voltage

Similarly, reset is a phenomenon of breaking or rupturing of the conductive filaments either by the ion migration (bipolar mode) or thermal dissolution caused by Joule's heating (unipolar mode) and it is denoted by V_{Reset}. This operation leads the device into the HR state or the OFF state. The resistance of the switch during the reset state is also called as R_{Off}.

D. Current compliance

During the forming or set operation, a limiting current is applied to the resistive switching circuit from the external circuit so as to prevent the permanent damage of the device by the flow of excess current and thereby excessive heat into the circuit. This is called as compliance current and denoted by I_{CC}. The compliance current is generally set at higher values for realizing the reset operation by means of joule heating.

E. Resistance ratio

The ratio of the R_{Off}/R_{On} is termed as the resistance ratio of the resistive switch. Typically, R_{Off}/R_{On} ratio > 10 are required for cost effective RRAM chips. The Higher is the R_{Off}/R_{On} ratio, the better is the performance of RRAMs.

F. Endurance

Endurance of a resistive switch denotes the maximum number of times the cell can be set and reset until the ON or OFF state falls out of the predefined acceptance window. This determines the life and reliability of RRAMs.

G. Retention

Retention is the ability of the resistive memory cell to keep the stored information if the cell is not powered. It tells how long the data stored in RRAM is reliable.

1.7 Conduction mechanisms

In the previous section, the mechanisms and modes of the resistive switching were discussed. However, it is also important to understand the origin of conductivity in materials that are intrinsically non-conducting (insulating nature of the TMO's). Basically, the conductivity of the switching/insulating layers are mainly categorized into two groups, ELC mechanism and BLC. Furthermore, the SE, F-NT, DT and thermionic field emission are the sub-categories under ELC. Similarly, P-F emission, TAT or Hopping conduction, Ohmic conduction, SCLC, ionic conduction and grain boundary limited conduction are the sub-categories under BLC. While, ELC depends on the electrical properties of the electrode-dielectric interface, the BLC depends on the dielectric properties of the switching layer itself. The simple flow chart is given in *Figure* 1.13. In this connection, some of these conduction mechanisms are explained below.

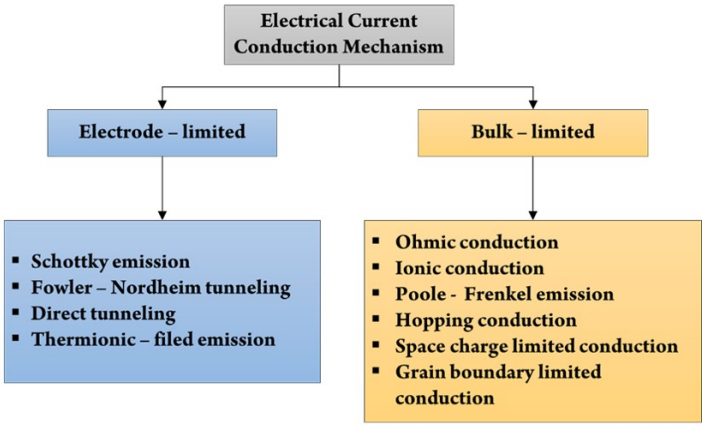

FIGURE 1.13: Classifications of the conduction mechanism for the RRAM device.

1.7.1 Conduction due to Schottky emission

Schottky emission is field-enhanced thermionic emission in which conduction is due to hot electron transport from the metal surface to the insulator. A schematic of Schottky emission energy band diagram under bias is shown in *Figure* 1.14.

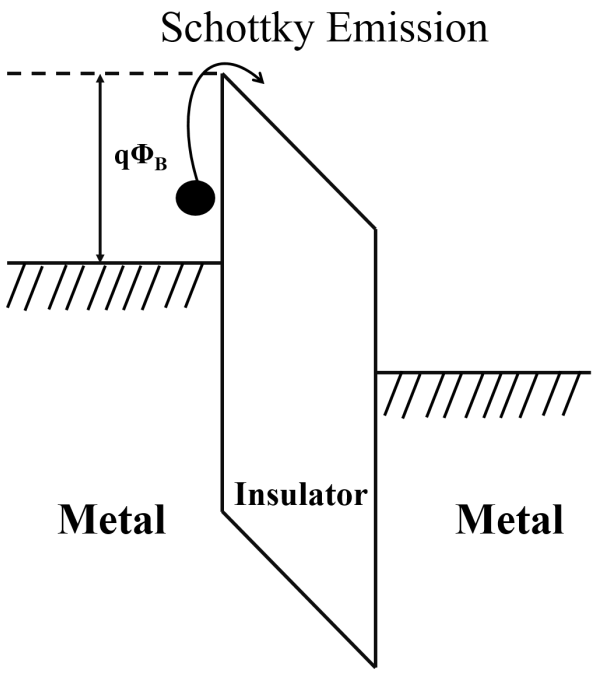

FIGURE 1.14: Schottky emission energy band diagram.

When a field is applied between the electrodes, electrons in the metal get sufficient energy to overcome the potential barrier at the metal insulator interface and conduction takes place. Schottky emission can be expressed by the *equation 1.2 and 1.3*

$$J = A^* T^2 exp[-q(\phi_T - \sqrt{qE/\pi\epsilon_r\epsilon_o})kT] \tag{1.2}$$

$$A^* = 4\pi k^2 m^* h^3 = 120 m^* m_o \tag{1.3}$$

where J is the current density, T is the absolute temperature, A^* is the effective Richardson constant, m^* is the effective electron mass in the dielectric, m_0 is the free electron mass, q is the electronic charge, $q\phi_B$ is the Schottky barrier height, E is the electric field across the dielectric, h is the Planck's constant, k is the Boltzmann's constant, ϵ_0 is the permittivity in vacuum, and ϵ_r is the optical dielectric constant.

1.7.2 Fowler – Nordheim (F-N) and Direct tunneling (DT) conduction

Direct tunnelling is attributed to the possible penetration of electrons through the potential barrier when the insulator film is less than 10 nm thick. Fowler-Nordheim tunnelling is electron tunnelling when the potential barrier at the interface is sheared under a high electric field. A schematic of Fowler-Nordheim tunnelling and direct tunneling are shown in *Figure* 1.15 and *Figure* 1.16 respectively. The expression of the these are given in the below *equation 1.4 and 1.5* for Fowler-Nordheim and direct tunneling respectively,

$$J_{F-N} = q8\pi h\phi_B E^2 exp[-8\pi\sqrt{2qm^*}3hE\phi_B^{3/2}] \tag{1.4}$$

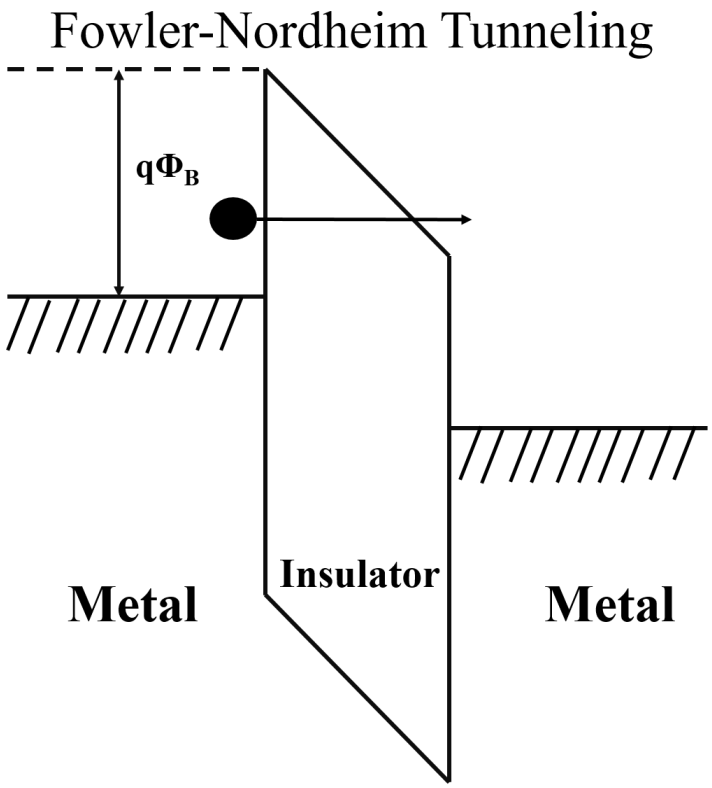

FIGURE 1.15: Energy band diagram of Fowler-Nordheim tunneling.

$$J_{DT} = exp[-8\pi\sqrt{2q}3h(m^*.\phi_B)^{1/2}k.t_{ox,eq}] \tag{1.5}$$

$t_{ox,eq}$ is the effective thickness of the film and the other parameters are the same as those defined in the *equation 1.2*.

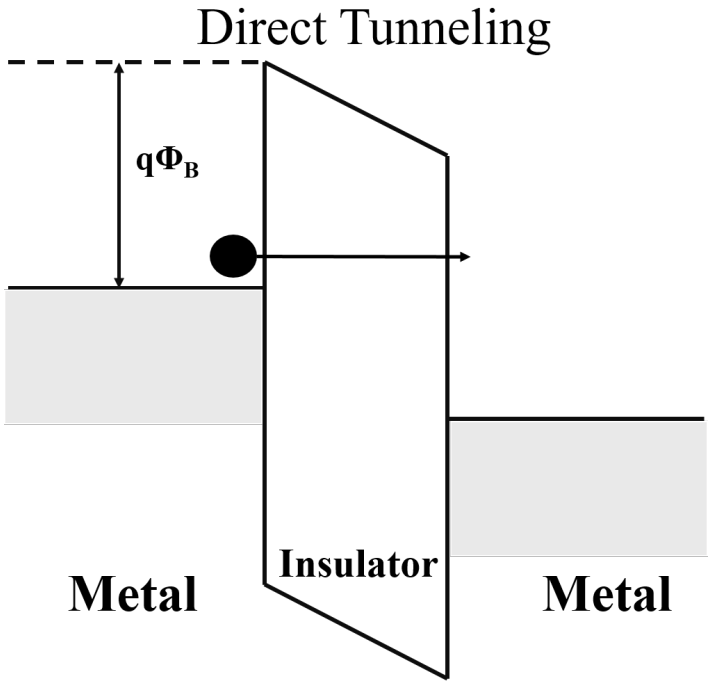

FIGURE 1.16: Energy band diagram of direct tunneling.

1.7.3 Poole – Frenkel conduction

PF emission is similar to the Schottky emission from traps states and the electron is emitted into the conduction band of the insulating layer through the intermediate traps[59,60].

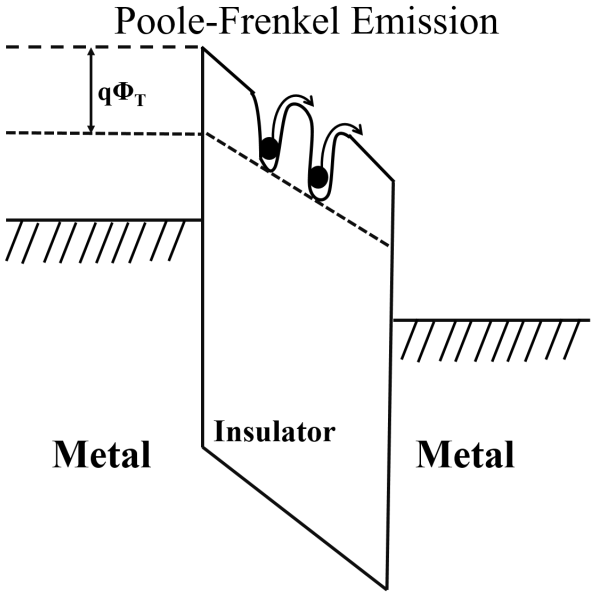

FIGURE 1.17: Energy band diagram of Pool-Frenkel emission.

This emission is also called internal Schottky emission. The traps due to defects create potential wells where the electrons can be trapped. An electron is emitted from the trap to

another due to thermionic effect i.e. it is a bulk conduction mechanism. The energy band diagram of Poole-Frenkel emission is shown schematically in *Figure* 1.17. The P-F current density can be expressed using the *equation 1.6*.

$$J = q\mu N_c E exp[-q(\phi_T - \sqrt{qE/\pi\epsilon_r\epsilon_o})kT] \tag{1.6}$$

where μ is the electronic drift mobility, N_c is the density of states in the conduction band, $q\phi_T$ is the trap energy level, and the other parameters are same as defined in the *equation 1.2*.

1.7.4 Trap assisted tunneling or hopping conduction

Trap assisted tunneling conduction is due to the presence of traps and it takes place when the distance between the traps is very small and the trapped electrons tunnel from one trap to another. The energy band diagram for hopping conduction is depicted in *Figure* 1.18. The expression is given in *equation 1.7*.

$$J_{TAT/HOPP} = exp{-8\pi\sqrt{2qm^*}3hE\phi_T^{3/2}} \tag{1.7}$$

the parameters are same as defined in the *equation1.2*

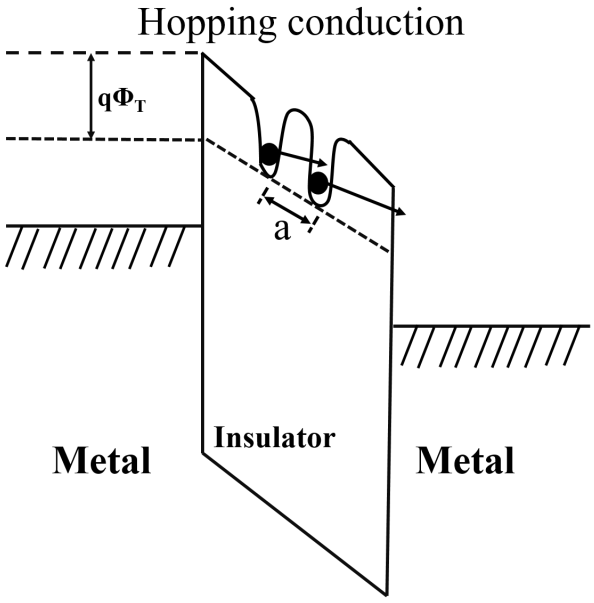

FIGURE 1.18: Hopping conduction energy band diagram.

1.7.5 Space charge limited conduction

SCLC is due to the formation of space charge and it occurs when the equilibrium carrier concentration value is dominated by injected free carriers. It is a defect controlled conduction mechanism. The typical I-V characteristics are shown in *Figure* 1.19 and the expression is given in *equation 1.8*.

$$J_{SCLC} = 98\epsilon\mu\theta v^2 d^3 \tag{1.8}$$

where θ is the ratio of free to shallow trapped charge and d is thickness of the oxide and the other parameters are same as defined in the *equation1.2*.

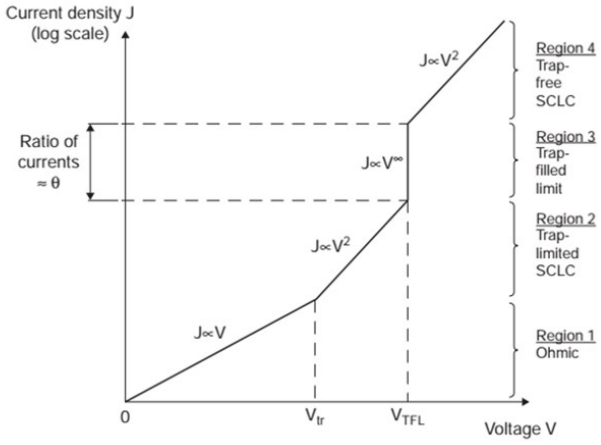

FIGURE 1.19: Space charge limited conduction typical I-V characteristics.

I-V characteristics in SLSC consist of four different slope regions. In the low voltage region, it shows Ohmic behaviour due to thermally activated charge carriers. Beyond a certain V_{tr} injected free carrier current dominates and shows non-Ohmic nature in the characteristics. When all traps are filled by injected carrier at the V_{TFL}, the Fermi energy level crosses the trap energy level. As a result, an abrupt rise in current is observed and then I-V characteristics follow Child's square law ($I \propto V^2$).

Although an RRAM device shows characteristics similar to SLSC conduction, the change in resistance once's takes place is permanent. In contrast, SLSC will not retain the resistance of the second region and comes to the resistance of the first region once the bias is removed. All these conduction mechanism expressions are summarized in the *Figure* 1.20. Notwithstanding the progress made in RRAM devices, some issues such as high reset and leakage current still need improvement.

Conduction Mechanism	Current Density Expression	Electric Field and Temperature Dependency [b]
Schottky Emission	$J_{SE} = \frac{4\pi q m^*(kT)^2}{h^3}\exp\left[\frac{-q(\phi_B - \sqrt{qE/4\pi\varepsilon})}{kT}\right]$	$J_{SE} \propto T^2\exp\left(A\frac{\sqrt{E}}{T} - B\right)$
Fowler-Nordheim (F-N) Tunneling	$J_{FN} = \frac{q^2}{8\pi h\phi_B}E^2\exp\left(\frac{-8\pi\sqrt{2qm^*}}{3hE}\phi_B{}^{3/2}\right)$	$J_{FN} \propto E^2\exp\left(\frac{-A}{E}\right)$
Direct Tunneling	$J_{DT} \approx \exp\left\{\frac{-8\pi\sqrt{2q}}{3h}(m^*\phi_B)^{1/2}\kappa \cdot t_{ox,eq}\right\}$	$J_{DT} \propto \exp(-A \cdot \kappa t_{ox,eq})$
Poole-Frenkel (P-F) Emission	$J_{PF} = q\mu N_C E\exp\left[\frac{-q(\phi_T - \sqrt{qE/\pi\varepsilon})}{kT}\right]$	$J_{PF} \propto E \cdot \exp\left(A\frac{\sqrt{E}}{T} - B\right)$
Space-charge-limited Conduction (SCLC) [a]	$J_{SCLC} = \frac{9}{8}\varepsilon_i\mu\theta\frac{V^2}{d^3}$	$J_{SCLC} \propto E^2$
Trap-assisted Tunneling (TAT)	$J_{TAT} = A\exp\left(\frac{-8\pi\sqrt{2qm^*}}{3hE}\phi_T^{3/2}\right)$	$J_{TAT} \propto \exp\left(\frac{-A}{E}\right)$

[a] High field only, low field follows Ohm's Law; [b] A & B are constants.

FIGURE 1.20: the summarized of all the conduction mechanism expressions.

The choice of switching material is very important to understand the fundamental aspects of switching. In the following section, the materials used in this study as switching layer are discussed.

1.8 Choice of the material

A wide variety of TMO's show resistive switching behavior[31,56]. One of the TMO's under active consideration is hafnium oxide or Hafnia. Hafnia is used as the gate dielectrics in the fabrication of CMOS technology as insulating material[61]. It has many applications in the Si based semiconductor industry. The transparency of hafnia in the near UV to far IR region has enabled various applications for HfO_2 such as astronomical Si-based CCDs [62], night vision and IR optical devices [63], UV-IR protective layers [64,65], solar cells anti-reflection coatings [66]. Hafnium oxide is intrinsically a p-type semiconductor [67]. The unit cells of HfO_2 is shown in *Figure* 1.21. HfO_2 has a high refractive index ($\sim$ 2), large band gap (5.7 eV) [61], wide transparent range from UV region to IR region. Material properties of the HfO_2 are shown in *Table* 1.2. More details about the importance of HfO_2 and HfO_x in RRAM technology are given in the following chapters.

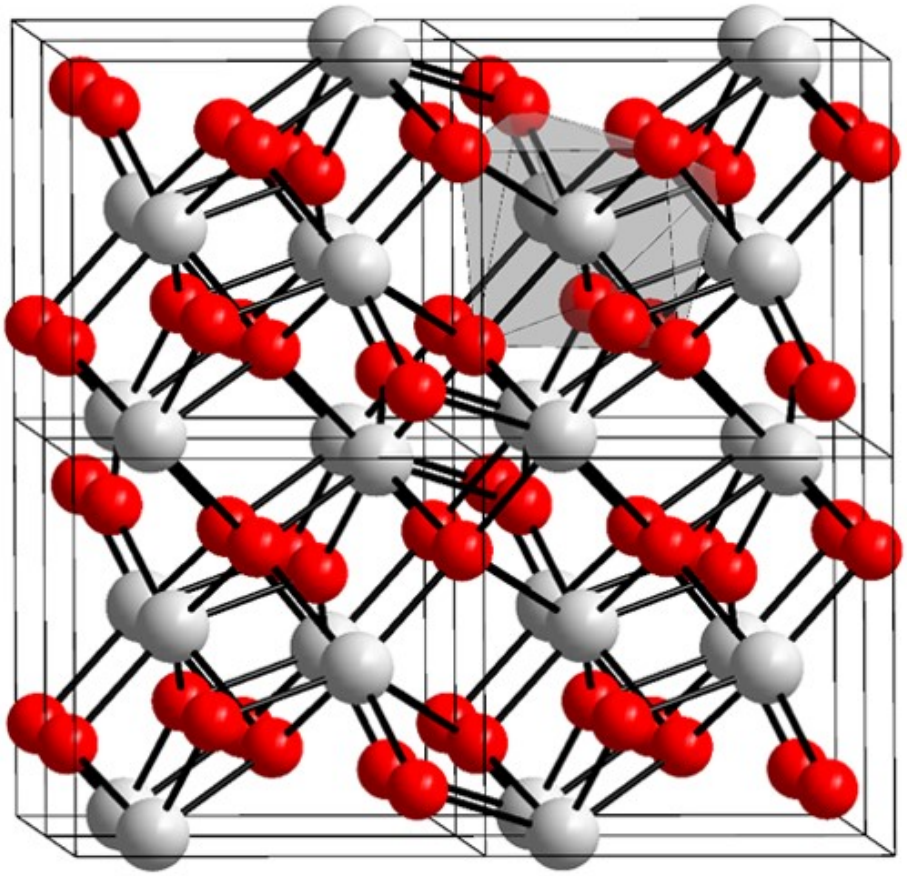

FIGURE 1.21: Unit cell structures of HfO_2.

TABLE 1.2: The properties of the HfO_2.

parameter	
Formulae	HfO_2
Dielectric constant	(25-30)
Band gap	5.7 eV
Refractive Index	~ 2
Melting point	3000 K
Boiling point	5500 K
Electron mean free path	9.2 nm
Thermal conductivity	1.1 W/m-K
Specific heat	272 j/Kg. K
Density	9.68 g/cm^3
Young's module	57 Gpa
Specific heat capacity	120 J/Kg-K
Thermal diffusivity	0.95 m^2/s
Thermal Expansion	6.0 μm/m-K
Linear expansion	5.8 X 10^{-6}/K

1.9 Basics of ion-solid interactions

The research on ion beams in physics dates back to more than hundred years ago. The journey be considering started in 1911 with Rutherford's famous gold foil experiment using alpha particles. Following Rutherford's gold foil experiment, many researchers started the understanding of ion beams and interaction of ion beams with matter. Later in 1932, John Cockcroft and Ernest Walton developed the Cockcroft–Walton–accelerator and studied the transmutation of Lithium into Helium after irradiation with energetic protons [23,67]. When an energetic (accelerated) ion beam interacts with the material atoms in a solid, this leads to the modification of the material and can lead to a number of interesting phenomena as discussed below: When an energetic ion is incident on a solid, it interacts with nuclei and electrons of that solid depending on its energy. Interaction of ions with electronic subsystems is more significant when its velocity is comparable or greater than the Bohr velocity of electrons [69,70]. The interaction of low velocity ions with material atoms is mostly by elastic collisions and energy lost by ions in this process is called nuclear energy loss ($(dE/dx)_{nuc}$ or S_n). Whereas the interactions of energetic ions with electrons of the target solid are inelastic in nature that lead to the excitation and ionization of atomic electrons of the solid. The energy lost by ions in this process is named as electronic energy loss ($(dE/dx)_{ele}$ or S_e). Depending on the strength of these interactions, ions can pass through a maximum depth

(called projected range, R_p) in a given material before they come to rest. S_e, S_n, and R_p critically depend on ion-solid combination. The charge (Z_1), mass and energy, of incident ion and the charge (Z_2) and density of target material are the crucial parameters as seen in following *equation 1.9*. The values of S_e, S_n, and R_p can be estimated for any ion-solid combination by a famous computer simulation program known as SRIM-2013[71].

$$(dE/dx) = (dE/dx)_{ele} + (dE/dX)_{nuc} = -N\epsilon(E) \tag{1.9}$$

The nuclear energy loss depends on the elastic collisions between the projectile and stable material atoms. In this case, the initial and final momenta & kinetic energy are conserved. The nuclear energy loss can be described by the *equation 1.10*.

$$(dE/dX)_{nuc} = (4\pi Z_1^2 Z_2^2 e^4 N v^2 M_2)(ln[b_{max}/b_{min}]) \tag{1.10}$$

where N is the number of atoms per unit volume Z_1 e, M_1 and v are the projectile charge, mass and velocity while Z_2 e, M_2 are the target atom charge and mass, b is impact parameter. Electronic energy loss is an inelastic process. Most of the projectile ion energy is shared by the electronic system of the target. The energy loss of incident ion per unit distance is calculated by multiplying the energy transfer per collision with the differential cross section and integrated over all the impact parameters (from b_{min} to b_{max}). The electronic energy loss per unit distance is given by the *equation 1.11*.

$$(-dE/dX)_{ele} = (4\pi Z_1^2 e^4 n v^2 m)(ln[b_{max}/b_{min}]) \tag{1.11}$$

- If the incident ion energy is of the order of few eV ($\sim$ 5 eV), the incident ion may be absorbed into the solid or bounce off from the solid surface. In this case, the momentum of the incident ion is not enough to influence the atomic bindings in the solid.

- If the incident ion energy is between the 5 eV to 5 keV, the resulting momentum transfer between the incident ion and solid causes the electron pickup, ionization, desorption and sputtering of the solid surface to occur. The surface atoms are ejected from the solid surface when the incident ion kinetic energy overcomes the surface binding energy. Generally, the average surface binding energy and covalent bonding energy

of solids are of the order of few eV ($\sim$ 5 eV). The elastic collisions between the projectile ion and solid atom cause the sputtering and similarly inelastic collisions cause the ionization and charge exchange.

- If the incoming ion energy is more than 5 keV to MeV, the projectile passes into the solid and loses its energy by either elastic scattering or inelastic scattering. In this case, phonons and secondary electrons are produced due to scattering. The average penetration depth of an ion in a particular material is known as ion range. The ion range may vary depending on the material and typically ion range varies from 1 nm to several µm. The resulting phenomena of Ion implantation is the most important technique for semiconductor and certain device fabrication.

- The swift ions lose their energy by two main processes 1) transferring to target electrons known as electronic energy loss (S_e), and 2) transferring the energy to target atoms known as nuclear energy loss (S_n). The stopping cross section describes the energy loss of swift ion in the material per unit length as given in below *equations*. In addition to that, ionization, sputtering of the target atoms, defect creation in the target and charge state modification takes place in the process of ion irradiation. The SHI irradiation and consequent effects will be discussed in the following sections.

1.9.1 Radiation damages

A. Displacement Damage:

At lower energies, atoms are moved from their lattice sites by incident radiation. This affects the crystal electronic characteristics. This depends on the energy and momentum that is transferred to the lattice atoms and is therefore dependent on the particle type (mass) and energy. This can lead to the formation of various kinds of point defects which can seriously affect the electronic properties of many materials. Displacement damage can be estimated by SRIM.

B. Ionization Damage:

Ionization radiation can be caused by photons, electrons, protons or atomic ions, as long as they have energy to liberate an electron from an atom, creating an ion or an electron-hole

pair in the material of interest. Incoming radiation ionizes the device and liberates charge carriers, depending on its energy. These carriers then travel around the device and become trapped, resulting in areas of concentrated charge and therefore parasitic fields. This is independent on the type of radiation but depends on the absorbed energy through which ionization is the dominant absorption mechanism. For example, if a photon were to create electron-hole pairs radiation in a piece of silicon, the photon energy must be greater than the band gap of silicon. Thus, the energy needed will differ for material type whereby Eγ > 1.1 eV for silicon and Eγ >9 eV for silicon dioxide. The type of ionizing damage that occurs in insulators is referred to as total Dose effects (TID)[30,72]. The total dose is the amount of energy deposited in any material by ionizing radiation and is given in units of Rad or Gray, (1 Gray = 100 Rad). The number of electron-hole pair generated is directly proportional to the total dose.

1.9.2 Swift Heavy Ion (SHI) irradiation

Irradiation of a material with high energy ions has imperative effects on the electrical and optical properties of materials. SHI irradiation is a versatile technique to modify various materials, nanoparticles and embedded nanostructures in the materials [73]. Along with that, the ion beams can be used as a tool to synthesize the materials as well as to characterize the materials [74]. Smaller systems of ion accelerators are used for basic studies in physics [75], chemistry [76], medicine [77] and nano-electronics [78] applications. The ion energies, ion flux, fluence, and temperatures affect their respective phenomenon like sputtering, preferential sputtering by surface modification and nanostructures. SHI irradiation is a unique method to modify the material in a controlled manner. With SHI irradiation, one can increase the critical current density, improve the magnetism in magnetic materials, create the nanostructured materials for sensor devices applications and modify the nanostructured materials that are embedded in dielectrics for memory applications[79,80]. SHI can attain energies in the order of MeV/amu and can travel with up to15 % of velocity of light. As energetic ions traverse through a material, they lose their energy via electronic energy loss (S_e) and nuclear energy loss (S_n) processes. (S_e) dominates at high ion energies (>0.5 MeV/μm), while S_n dominates at low energies ($\ll$ 0.5 MeV/μm). In *Figure* 1.22 we show the stopping power calculations of ions in the range of 10 keV to 10 GeV.

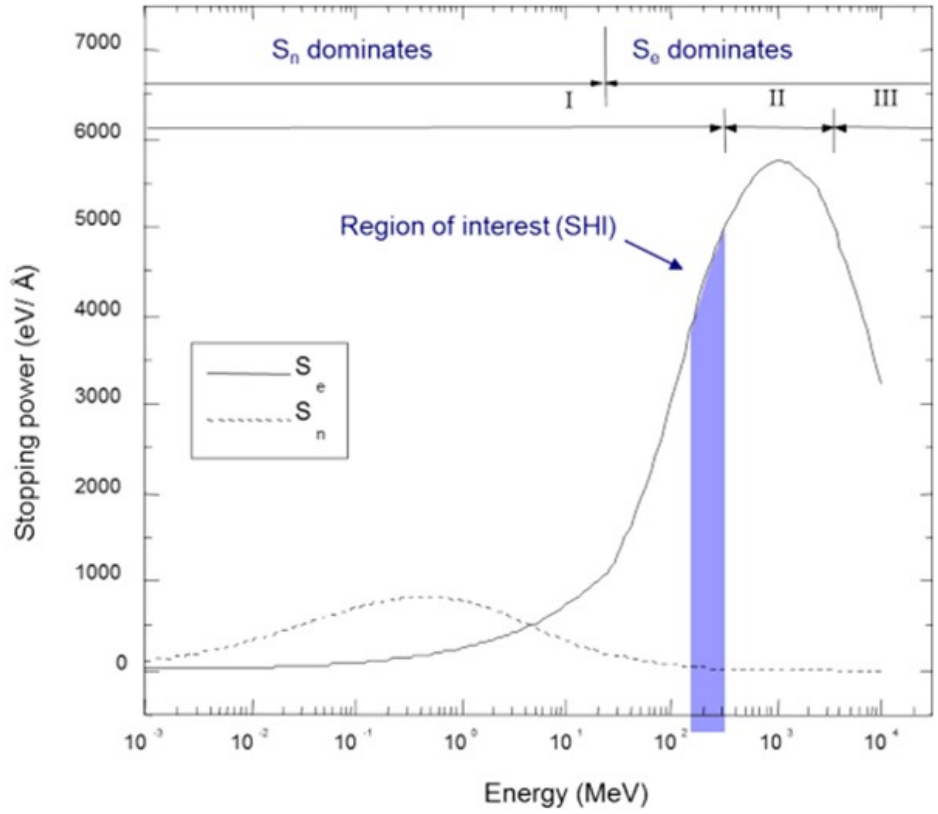

FIGURE 1.22: Stopping power calculations of ions in the range of 10 keV to 10 GeV, calculated using the Monte-Carlo software SRIM-2003.

The subsequent energy losses create damage in cylindrical zones throughout the ion path known as "ion track". The ion track diameter can range between 1 nm to several nm and purely depend on the type of material and ion energy. At these energies, ions deposit most of their energy to the electronic subsystem and will cause huge electronic excitations. This is then transferred to the lattice by means of electron-phonon coupling processes. There are two models to describe these coupling mechanisms. The "Thermal spike model"[81] explains the lattice heating that can lead to melting, vaporization and thermal quenching causing track formation. Similarly, the "Coulomb explosion model" mainly focuses on the formation of charged cylindrical zones along the ion tracks and leading to atomic displacements, which is mostly applicable in insulating materials. "Self-trapping exciton model" explains the highly concentrated excitons created resulting in consequent defects formation. The "Bond weakening model" explains the atomic bonding which excludes the physical parameters.

Among all these models the thermal-spike and Coulomb explosion models are prominent to explain the latent track formation and subsequent effects. A model of the formation

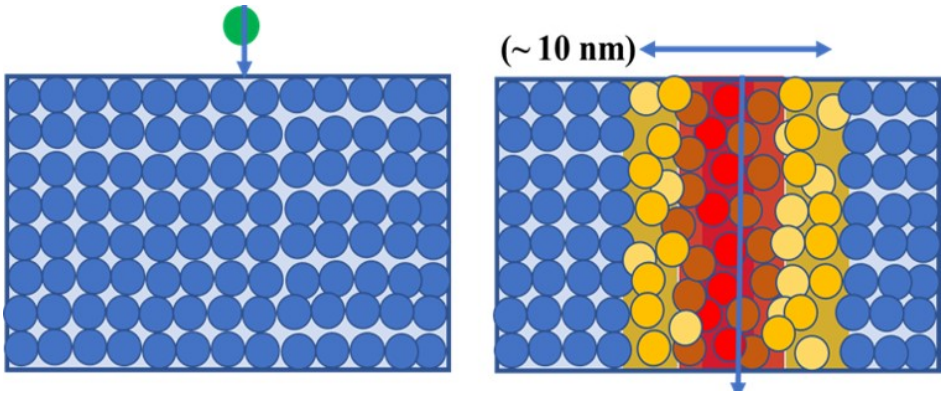

FIGURE 1.23: Sketch diagram of SHI irradiation.

of the latent track during SHI irradiation is shown in *Figure* 1.23.

1.9.3 Thermal spike model

This model is used to explain the structural modifications and track formation induced by SHI in materials. The thermal spike model can also account for defect creation or annihilation and phase transformations in the materials[82]. This model accounts for the atomic and electronic systems separately. Thermal spike model explains the transient energy converted to the thermal energy in the subatomic system. Initially, the energetic ions share their energy with the target electrons, known as ionization process. The excited electrons can enter conduction band leaving a hole in the valence band. This process happens on the time scale of 10^{-17} sec, just like a delta distribution. The excited incoherent electrons interact with the target electrons and lose their energy via quasi-thermal distribution. This process happens within 120 fs after the excitation. The electron-electron interaction increases the electronic temperatures. The quasi-thermal electrons in the conduction band further lose their energy via electron-phonon interaction. This process happens on the time scale of 1-10 ps after the excitation. In this situation, the sharp rise of temperature in the target material may attain the melting temperatures in some materials. The affected region is approximately 1-100 nm diameter around and all along the ion trajectory known as ion track. The track diameter depends on the irradiation parameters and irradiated material[83].

1.9.4 Coulomb explosion model

The "Coulomb explosion" is another model to explain the SHI interaction with the matter and track formation. The major difference between the thermal-spike model and Coulomb

explosion model is the difference in mechanism of SHI energy deposition into the subatomic lattice. The similar way in the above case, the SHI energy transferred to the material electrons in the time scale of 10^{-17} sec. The excited electron cloud produce charge separation in the SHI passage region. The transiently produced positive charge cores repel each other and cause track formation, which is called "Coulomb explosion" model [84]. The transiently generated electric field is enough to overcome the bond strength of the material and cause the displacements of atoms in the ionic core. Fleisher, Price, and Walker [85] established the Coulomb explosion model for causing of ion tracks in solids. Coulomb explosion model is more prominent in insulators and semiconductors than the metals where neutralization and screening is much faster than lattice relaxation. Plasmon frequencies are much higher than the phonon frequencies [86]. Therefore, electrons return to their vacant orbitals much faster than the lattice atoms can move. Both the thermal spike and Coulomb explosion processes are expected in the materials of interest (HfO_2) in this work. However, the thermal spike seems to be more significant in HfO_2.

1.9.5 Radiation Hardness of logic and memory

Events, such as the failure of the Telstar satellite in 1962, have shown that it is the semiconductor devices that are most prone to failure when irradiated [57]. The type of radiation with different environments caused by a range of activities including fission reactors, high energy particle experiments such as those in CERN, space and nuclear industry. When a semiconductor device is irradiated, two types of radiation damages can occur from a range of particles such as photons (in the form of X-rays, Gamma rays etc..) charged particles (such as electrons, protons), neutrons and atomic ions. In the nuclear and space environment, the main cause of displacement damage in semiconducting devices will be from the release of neutrons[30,68].

1.10 Objective and outline of the thesis

The literature review on RRAM (their structure, conduction mechanism and TMO's used) presented in the previous sections indicate that there are many issues that need to be addressed, before the technology can become viable. Some of the issues to be resolved are understanding the exact role of defects and metal–insulator interfaces in determining the

switching characteristics. Secondly, the role of stoichiometry in the oxides is also not well understood. An investigation on the processing methods and their impact on the quality of switching layer has not been carried out. Methods of reducing dielectric break down and formation voltage have not been reported extensively. This dissertation presents a detailed study on the fabrication, characterization and radiation response of three different types of HfO_2-based RRAM devices.

The main motivation of this thesis is to report on the fabrication and understanding of HfO_2 and HfO_x based RRAM devices and their response to thermal annealing, gamma irradiation and ion irradiation. RF and e-beam deposition techniques have been employed to fabricate the RRAMs. Thermal annealing and SHI irradiation studies showed phase transformations and consequent effects on the performance of the RRAM devices. In these studies, the as-deposited, annealed and irradiated (Gamma and SHI) samples were characterized by different techniques such as RBS, GI-XRD, FESEM, EDS, XPS and PL for their structural and optical properties to understand the growth and physics of ion beam interaction with thin films of HfO_2 layer. Switching characteristics have been studied by employing a semiconductor device analyzer.

Chapter 1: Introduction and Motivation

Chapter 1 describes the motivation for the present thesis work. Current technology needs for alternate memory devices have been presented. The choice of materials, the basics and relevant literature, current trends in the fabrication and characterization of memory devices have been discussed in detail.

Chapter 2: Experimental Methods

Chapter 2 gives full details of experimental facilities and analysis methods utilized in the study for the present thesis. Various physical deposition methods such as RF sputtering and e-beam evaporation techniques have been employed to deposit metal, HfO_2 and HfO_x thin-films. The patterned device structures were fabricated by lithography techniques available at CFN, University of Hyderabad. Few HfO_2 films were subjected to thermal annealing. Furthermore, the swift heavy ion and gamma irradiation of samples have been carried out using the 15 MV Pelletron accelerator and gamma irradiation facilities available at IUAC, New Delhi. The pristine and irradiated samples were characterized by GI-XRD, RBS, FESEM, EDS, UV-Vis-NIR and photo luminescence spectroscopy techniques. Similarly, the stoichiometry analysis of the thin films by XPS is performed at Cense IISc, Bangalore.

Basics of micro fabrication methods, experimental details and characterization techniques as employed for the thesis work have been given in this chapter. Electrical properties of RRAM devices such as set and reset cycles, endurance cycling, retention time tests have been performed by using Agilent B1500 A semiconductor device analyzer at CFN, University of Hyderabad.

Chapter 3: Synthesis, optimization and characterization of HfO_2 thin films

Chapter 3 presents the experimental results on the synthesis, optimization and characterization of HfO_2 thin films deposited by RF sputtering technique. The duration of the deposition varies for different films. The thickness of these thin films is characterized by profilometer and XRR techniques. Furthermore, RBS is employed to characterize the elemental composition. Similarly, EDS and XPS are also performed to estimate the stoichiometry of the thin films. XPS reveals that the films deposited by RF sputtering possess non-lattice oxygen (O-O bond at 532.90 peak/eV) in nature. The surface morphology of these films were characterized by FESEM. UV-Vis-NIR spectroscopy is performed to estimate and analyze the energy band-gap and refractive index of these films. Synthesis, post-synthesis process and optimization of these films will be discussed in this chapter.

Chapter 4: Effects of gamma irradiation on the performance of HfO_2 based RRAM devices

Chapter 4 explains the fabrication and characterization of simple MIM like structure HfO_2 based RRAM devices by RF sputtering. Effects of gamma irradiation on the switching properties of these devices have been studied and presented.

Tri-layered $Ag/HfO_2/(Au,Pt)$ thin films were fabricated on Si substrate at room temperature by RF magnetron sputtering. Ag/HfO_2(50 nm)/Au based devices (pristine samples) showed reasonably good switching and retention characteristics. The gamma irradiation (12 and 24 kGy dose) resulted in the deterioration of device performance by reducing the number of successful switching cycles (i.e endurance) and variation in retention time. Another set of Ag/HfO_2(30 nm)/(Au,Pt) structure devices have also been fabricated and and subjected to gamma irradiation with different (12, 24, 48 kGy) doses. The effects of gamma irradiation and the role of the bottom electrode on the performance of the RRAMs have been presented in this chapter[87,88].

Chapter 5: Effects of Swift Heavy Ion irradiation on the performance of RRAM devices

Chapter 5 presents a study of HfO_2 based RRAM devices as fabricated by photolithography techniques at CFN, University of Hyderabad. Four sets of devices with active area of 10

μm x 10 μm and 20 μm x 20 μm and thickness of 50 nm and 30 nm were fabricated. Further, the SHI irradiation using the 15 MV Pelletron accelerator at the IUAC, New Delhi has been performed on 30 nm thickness of 10 μm x 10 μm and 20 μm x 20 μm devices to investigate the effects of SHI on the performance of these RRAM devices. The devices were irradiated with 120 MeV Ag ions at various fluences ranging from 5 x 10^{10} to 5 x 10^{12} ions/cm^2.It is shown that the SHI irradiation can improve or deteriorate the performance of these devices based on the fluence. These details are discussed in this chapter[89].

Chapter 6: Non-stoichiometric HfO_x thin films and effects of Swift Heavy Ion irradiation on the performance of corresponding RRAM devices

Chapter 6 describes the deposition and optimization of HfO_x thin films prepared by e-beam evaporation technique at University of Hyderabad. Film thickness and surface morphology are measured by XRR and FESEM respectively. Furthermore, the film stoichiometry is investigated by EDS and XPS measurements. XPS reveals that the films deposited by e-beam evaporation possess non-lattice oxygen (O-O bond at 529.22 and 532.46 peak/eV) and Hf rich (16.08 peak/eV) oxide in nature. Initially, we have investigated the thermal annealing effects on the performance of RRAM devices with active area of 10 μm x 10 μm. The RRAM device characteristics, such as set and reset voltages, endurance and retention time showed improvement for the devices annealed at 500 ^{o}C. Further, we have investigated the effects of the SHI (120 MeV Ag ions) irradiation on the switching properties of RRAMs with an active area 10 μm x 10 μm. It is found that the SHI can cause annealing effects in the films at lower fluences. Finally, we have fabricated three sets of devices with different top metal electrodes (Au, Cr, and Al) to elucidate their role on the performance of the RRAM devices. All these devices showed better switching properties whereas the device with Cr as top electrode is found to be more favorable in endurance cycling. These results will be discussed in this chapter.

Chapter 7: Conclusions and Future Outlook

The results are summarized and the future scope of the work is discussed in this chapter.

Bibliography

[1] T. Chang and X. Miao, "Nonvolatile reconfigurable sequential logic in a HfO_2 resistive random access memory array", Nanoscale, vol. 9, no. 20, pp. 6649–6657, **(2017)**, doi: 10.1039/c7nr00934h.

[2] S. Petzold, S. U. Sharath, J. Lemke, E. Hildebrandt, C. Trautmann, and L. Alff, "Heavy Ion Radiation Effects on Hafnium Oxide-Based Resistive Random Access Memory", IEEE Trans. Nucl. Sci., vol. 66, no. 7, pp. 1715–1718, **(2019)**, doi: 10.1109/TNS.2019.2908637.

[3] D. S. Jeong et al., "Emerging memories: Resistive switching mechanisms and current status", Reports Prog. Phys., vol. 75, no. 7, **(2012)**, doi: 10.1088/0034-4885/75/7/076502.

[4] M. Yuan et al., "Enhancing the Electrical Uniformity and Reliability of the HfO_2-Based RRAM Using High-Permittivity Ta_2O_5 Side Wall," IEEE J. Electron Devices Soc., vol. 6, no. June, pp. 627–632, **(2018)**, doi: 10.1109/JEDS.2018.2833504.

[5] B. H. P. Wong et al., "Metal – Oxide RRAM", **(2012)**.

[6] L. Goux, J. G. Lisoni, X. P. Wang, M. Jurczak, and D. J. Wouters, "Optimized Ni oxidation in 80-nm contact holes for integration of forming-free and low-power Ni/NiO/Ni memory cells", IEEE Trans. Electron Devices, vol. 56, no. 10, pp. 2363–2368, **(2009)**, doi: 10.1109/TED.2009.2028378.

[7] Y. T. Li, S. B. Long, Q. Liu, H. B. Lü, S. Liu, and M. Liu, "An overview of resistive random access memory devices," Chinese Sci. Bull., vol. 56, no. 28–29, pp. 3072–3078, **(2011)**, doi: 10.1007/s11434-011-4671-0.

[8] J. S. Meena, S. M. Sze, U. Chand, and T. Y. Tseng, "Overview of emerging non-volatile memory technologies", Nanoscale Res. Lett., vol. 9, no. 1, pp. 1–33, **(2014)**, doi: 10.1186/1556-276X-9-526.

[9] D. Ielmini, "Resistive switching memories based on metal oxides: Mechanisms, reliability and scaling", Semicond. Sci. Technol., vol. 31, no. 6, pp. 1–25, **(2016)**, doi: 10.1088/0268-1242/31/6/063002.

[10] A. Prakash, D. Jana, and S. Maikap, "TaO_x-based resistive switching memories: Prospective and challenges", Nanoscale Res. Lett., vol. 8, no. 1, pp. 1–17, **(2013)**, doi: 10.1186/1556-276X-8-418.

[11] D. S. Jeong et al., "Emerging memories: Resistive switching mechanisms and current status", Reports Prog. Phys., vol. 75, no. 7, **(2012)**, doi: 10.1088/0034-4885/75/7/076502.

[12] S. Kvatinsky, N. Wald, G. Satat, A. Kolodny, U. C. Weiser, and E. G. Friedman, "MRL - Memristor Ratioed Logic", Int. Work. Cell. Nanoscale Networks their Appl., pp. 1–6, **(2012)**, doi: 10.1109/CNNA.2012.6331426.

[13] S. Kvatinsky, "Memristor-Based Circuits and Architectures", pp. 1–174, **(2014)**, [Online]. Available: http://www.ece.rochester.edu/users/friedman/Shahar Kvatinsky PhD.pdf.

[14] S. Park et al., "RRAM-based synapse for neuromorphic system with pattern recognition function", Tech. Dig. - Int. Electron Devices Meet. IEDM, pp. 231–234, **(2012)**, doi: 10.1109/IEDM.2012.6479016.

[15] Q. Liu et al., "Controllable growth of nanoscale conductive filaments in solid-electrolyte-based ReRAM by using a metal nanocrystal covered bottom electrode", ACS Nano, vol. 4, no. 10, pp. 6162–6168, **(2010)**, doi: 10.1021/nn1017582.

[16] G. Niu et al., "Electron holography on HfO_2/HfO_{2-x} bilayer structures with multilevel resistive switching properties", Nanotechnology, vol. 28, no. 21, **(2017)**, doi: 10.1088/1361-6528/aa6cd9.

[17] D. Lu, "Emerging Memory Device Technologies", **(2016)**, [Online]. Available: http://myweb.ncku.edu.tw/ darsenlu/papers/ micro16 emerging mem tutorial darsen.pdf.

[18] S. Mohsenifar and M. H. Shahrokhabadi, "Gate Stack High- Materials for Si-Based MOSFETs Past , Present , and Futures", Microelectron. Solid State Electron., vol. 4, no. 1, pp. 12–24, **(2015)**, doi: 10.5923/j.msse.20150401.03.

[19] H.-S. Philip Wong, "Beyond the conventional transistor", Solid. State. Electron., vol. 49, no. 5, pp. 755–762, **(2005)**, doi: 10.1016/j.sse.2004.10.014.

[20] H. Akinaga and H. Shima, "Resistive random access memory (ReRAM) based on metal oxides", Proc. IEEE, vol. 98, no. 12, pp. 2237–2251, **(2010)**, doi: 10.1109/JPROC.2010.2070830.

[21] N. Z. Haron, N. Arshad, and F. Salehuddin, "Performance analysis of memristor models for RRAM cell array design using SILVACO EDA", J. Teknol. (Sciences Eng., vol. 68, no. 3, pp. 1–6, **(2014)**, doi: 10.11113/jt.v68.2920.

[22] Y. Li, S. Long, Q. Liu, H. Lv, and M. Liu, "Resistive Switching Performance Improvement via Modulating Nanoscale Conductive Filament, Involving the Application of Two-Dimensional Layered Materials", Small, vol. 13, no. 35, pp. 1–35, **(2017)**, doi: 10.1002/smll.201604306.

[23] D. S. Korolev et al., "Influence of ion irradiation on the resistive switching parameters of SiO_x-based thin-film structures", J. Phys. Conf. Ser., vol. 643, no. 1, **(2015)**, doi: 10.1088/1742-6596/643/1/012094.

[24] M. A. Zidan, J. P. Strachan, and W. D. Lu, "The future of electronics based on memristive systems", Nat. Electron., vol. 1, no. 1, pp. 22–29, **(2018)**, doi: 10.1038/s41928-017-0006-8.

[25] A. Prakash and H. Hwang, "Multilevel cell storage and resistance variability in resistive random access memory", Phys. Sci. Rev., vol. 1, no. 6, pp. 1–16, **(2019)**, doi: 10.1515/psr-2016-0010.

[26] M. Lanza, "A review on resistive switching in high-k dielectrics: A nanoscale point of view using conductive atomic force microscope", Materials (Basel)., vol. 7, no. 3, pp. 2155–2182, **(2014)**, doi: 10.3390/ma7032155.

[27] D. S. Jeong et al., "Emerging memories: resistive switching mechanisms and current status.", Rep. Prog. Phys., vol. 75, no. 7, p. 76502, Jul. **(2012)**.

[28] A. Sawa, "Resistive switching in Rapid advances in information technology rely on high-speed", Mater. Today, vol. 11, no. 6, pp. 28–36, **(2008)**, doi: 10.1016/S1369-7021(08)70119-6.

[29] J. S. Meena, S. M. Sze, U. Chand, and T. Y. Tseng, "Overview of emerging non-volatile memory technologies", Nanoscale Res. Lett., vol. 9, no. 1, pp. 1–33, **(2014)**, doi: 10.1186/1556-276X-9-526.

[30] Z. Ye, R. Liu, J. L. Taggart, H. J. Barnaby, and S. Yu, "Evaluation of Radiation Effects in RRAM-Based Neuromorphic Computing System for Inference", IEEE Trans. Nucl. Sci., vol. 66, no. 1, pp. 97–103, **(2019)**, doi: 10.1109/TNS.2018.2886793.

[31] D. S. Jeong et al., "Emerging memories: Resistive switching mechanisms and current status", Reports Prog. Phys., vol. 75, no. 7, 2012, doi: 10.1088/0034-4885/75/7/076502.

[32] L. Chua, "Memristor-The missing circuit element", IEEE Trans. Circuit Theory, vol. 18, no. 5, pp. 507–519, **(1971)**.

[33] D. B. Strukov, G. S. Snider, D. R. Stewart, and R. S. Williams, "The missing memristor found.", Nature, vol. 453, no. 7191, pp. 80–3, May **(2008)**.

[34] I. Introduction et al., "Low-Frequency Negative Resistance in Thin Anodic Oxide Films", vol. 205, no. 1959, **(1962)**.

[35] S. Seo et al., "Reproducible resistance switching in polycrystalline NiO films", vol. 85, no. 23, pp. 5655–5657, **(2004)**.

[36] C. Rohde, B. J. Choi, D. S. Jeong, S. Choi, J. S. Zhao, and C. S. Hwang, "Identification of a determining parameter for resistive switching of TiO_2 thin films", Appl. Phys. Lett., vol. 86, pp. 1–3, **(2005)**.

[37] J. Kim et al., "Nano-Intrinsic True Random Number Generation", pp. 1–9, **(2017)**.

[38] E. Covi, S. Brivio, J. Frascaroli, M. Fanciulli, and S. Spiga, "(Invited) Analog HfO_2-RRAM Switches for Neural Networks", ECS Trans., vol. 75, no. 32, pp. 85–94, Jan. **(2017)**.

[39] D. S. Jeong, K. M. Kim, S. Kim, B. J. Choi, and C. S. Hwang, "Memristors for Energy-Efficient New Computing Paradigms", Adv. Electron. Mater., vol. 2, no. 9, p. 1600090, Sep.**(2016)**.

[40] N. Z. Haron, N. Arshad, F. Salehuddin, G. Gonzalez-Cordero, J. B. Roldan, and F. Jimenez-Molinos, "Performance analysis of memristor models for RRAM cell array design using SILVACO EDA", J. Teknol. (Sciences Eng., vol. 68, no. 3, pp. 0–3, **(2017)**, doi: 10.1109/CDE.2017.7905250.

[41] D. Jana, S. Samanta, S. Roy, Y. F. Lin, and S. Maikap, "Observation of Resistive Switching Memory by Reducing Device Size in a New $Cr/CrO_x/TiO_x/TiN$ Structure", Nano-Micro Lett., vol. 7, no. 4, pp. 392–399, **(2015)**, doi: 10.1007/s40820-015-0055-3.

[42] C. Hermes et al., "Analysis of Transient Currents During Ultrafast Switching of TiO_2 Nanocrossbar Devices", IEEE Electron Device Lett., vol. 32, no. 8, pp. 1116–1118, Aug. **(2011)**.

[43] J. J. Yang et al., "High switching endurance in TaO_x memristive devices", Appl. Phys. Lett., vol. 97, no. 23, p. 232102, **(2010)**.

[44] J. S. Choi et al., "Different resistance switching behaviors of NiO thin films deposited on Pt and $SrRuO_3$ electrodes", Appl. Phys. Lett., vol. 95, no. 2, p. 22109, **(2009)**.

[45] C. Yoshida, K. Tsunoda, H. Noshiro, and Y. Sugiyama, "High speed resistive switching in Pt / TiO_2 / TiN film for nonvolatile", pp. 14–16, **(2007)**.

[46] W.-Y. Chang, Y.-C. Lai, T.-B. Wu, S.-F. Wang, F. Chen, and M.-J. Tsai, "Unipolar resistive switching characteristics of ZnO thin films for nonvolatile memory applications", Appl. Phys. Lett., vol. 92, p. 22110, **(2008)**.

[47] N. Xu et al., "Bipolar switching behavior in TiN/ZnO/Pt resistive nonvolatile memory with fast switching and long retention", Semiconductor Science and Technology, vol. 23. p. 75019, **(2008)**.

[48] Chih-Yang Lin et al., "Effect of Top Electrode Material on Resistive Switching Properties of Film Memory Devices", IEEE Electron Device Lett., vol. 28, no. 5, pp. 366–368, May **(2007)**.

[49] Y.-M. Kim and J.-S. Lee, "Reproducible resistance switching characteristics of hafnium oxide-based nonvolatile memory devices", J. Appl. Phys., vol. 104, no. 11, p. 114115, Dec. **(2018)**.

[50] L. Goux et al., "On the Gradual Unipolar and Bipolar Resistive Switching of TiN_2Memory Systems", Electrochem. Solid-State Lett., vol. 13, no. 6, p. G54, **(2010)**.

[51] K. M. Kim, B. J. Choi, B. W. Koo, S. Choi, D. S. Jeong, and C. S. Hwang, "Resistive Switching in $Pt/Al_2O_3/TiO_2/Ru$ Stacked Structures", Electrochem. Solid-State Lett., vol. 9, no. 12, p. G343, **(2006)**.

[52] C.-Y. Lin, C.-Y. Wu, C.-Y. Wu, C. Hu, and T.-Y. Tseng, "Bistable Resistive Switching in Al_2O_3 Memory Thin Films", J. Electrochem. Soc., vol. 154, no. 9, p. G189, **(2007)**.

[53] R. Waser, R. Dittmann, C. Staikov, and K. Szot, "Redox-based resistive switching memories nanoionic mechanisms, prospects, and challenges", Adv. Mater., vol. 21, no. 25–26, pp. 2632–2663, **(2009)**, doi: 10.1002/adma.200900375.

[54] Z. Shen et al., "Advances of RRAM devices: Resistive switching mechanisms, materials and bionic synaptic application", Nanomaterials, vol. 10, no. 8, pp. 1–31, **(2020)**, doi: 10.3390/nano10081437.

[55] E. Lim and R. Ismail, "Conduction Mechanism of Valence Change Resistive Switching Memory: A Survey", Electronics, vol. 4, no. 3, pp. 586–613, **(2015)**, doi: 10.3390/electronics4030586.

[56] E. W. Lim and R. Ismail, "Conduction mechanism of valence change resistive switching memory: A survey", Electron., vol. 4, no. 3, pp. 586–613, **(2015)**, doi: 10.3390/electronics4030586.

[57] X. Zhang et al., "Effect of Joule Heating on Resistive Switching Characteristic in AlO_x Cells Made by Thermal Oxidation Formation", Nanoscale Res. Lett., vol. 15, no. 1, **(2020)**, doi: 10.1186/s11671-019-3229-y.

[58] A. Chen, "Area and thickness scaling of forming voltage of resistive switching memories", IEEE Electron Device Lett., vol. 35, no. 1, pp. 57–59, **(2014)**, doi: 10.1109/LED.2013.2288262.

[59] N. Manikanthababu, N. Arun, M. Dhanunjaya, S. V. S. Nageswara Rao, and A. P. Pathak, "Gamma irradiation-induced effects on the electrical properties of HfO_2-based MOS devices", Radiat. Eff. Defects Solids, vol. 171, no. 1–2, pp. 77–86, **(2016)**, doi: 10.1080/10420150.2015.1135152.

[60] V. A. Gritsenko, T. V Perevalov, and D. R. Islamov, "Electronic properties of hafnium oxide: A contribution from defects and traps," vol. 613, pp. 1–20, **(2016)**, doi: 10.1016/j.physrep.2015.11.002.

[61] M. Lesser, Opt. Eng., 26, 911-915 **(1987)**.

[62] M. Fadel, O.A. Azim, O.A. Omer, and R.R. Basily, Appl. Phys. A 66, 335-343 **(1998)**.

[63] A. Callegari, E. Cartier, M. Gribelyuk, J.F. Okorn-Schmidt, and T. Zabel, J. Appl. Phys., 90, 6466-6475 **(2001)**.

[64] M. Toledano-Luque, E. San Andrés, A. del Prado, I. Mártil, M. L. Lucía, and G. González-Díaz, F. L. Martínez, W. Bohne, J. Röhrich, and E. Strub, J. Appl. Phys., 102, 044106 **(2007)**.

[65] E. Hildebrandt et al., "Controlled oxygen vacancy induced p-type conductivity in HfO_{2-x}thin films Controlled oxygen vacancy induced p -type conductivity in HfO_{2-x} thin films", vol. 112902, no. 2011, **(2016)**, doi: 10.1063/1.3637603.

[66] B. Butcher et al., "Proton-based total-dose irradiation effects on Cu/HfO_2:Cu/Pt ReRAM devices", Nanotechnology, vol. 21, no. 47, **(2010)**, doi: 10.1088/0957-4484/21/47/475206.

[67] Anand P. Pathak, Phy. Rev. B, 13, 460-463 **(1976)**.

[68] Anand P. Pathak, Radiation Effects & Defects in Solids, 43, 55-59 **(1979)**.

[69] J. F. Ziegler, "SRIM-2003". Nucl. Instr. Meth. B, 1027, 219-220 **(2014)**.

[70] F. Yuan, Z. Zhang, J. Wang, L. Pan, J. Xu, and C. Lai, "Total ionizing dose (TID) effects of γ ray radiation on switching behaviors of Ag / AlO_x/Pt RRAM device", pp. 1–6, **(2014)**.

[71] Y. K. Mishra, F. Singh, and D. K. Avasthi, Appl. Phys. Lett. 91, 063103 **(2007)**.

[72] 66. S. Mohapatra, Y. K. Mishra, Jay Ghatak, and D. K. Avasthi, Adv. Mat. Lett., 4, 444 **(2013)**.

[73] A. A. V. Krasheninnikov and K. Nordlund, J. Appl. Phys., 107, 070301 **(2010)**.

[74] D.K. Avasthi, Def. Sci. J., 59, 401-412 **(2009)**.

[75] Anand P. Pathak, Radiation Effects & Defects in Solids, 166, 549–551 **(2011)**.

[76] L. C. Feldman, and J. W. Mayer "Fundamentals of surface and thin film analysis", Elsevier Science Publisher **(1986)**.

[77] P. J. King, "Hafnium oxide-based dielectrics by atomic layer deposition", no. January, **(2013)**.

[78] M. Dhanunjaya, K. Vinod Kumar, N. Manikanthababu, S. V. S. Nageswara Rao, and A. P. Pathak, "Swift heavy ion irradiation assisted Si nanoparticle formation in $HfSiO_x$ nano-composite thin films deposited by RF magnetron sputtering method", Nucl. Instruments Methods Phys. Res. Sect. B Beam Interact. with Mater. Atoms, vol. 446, no. March, pp. 37–42, **(2019)**, doi: 10.1016/j.nimb.2019.03.027.

[79] A. Benyagoub, Eur. Phys. J. B, 34, 395–398 **(2003)**.

[80] M. Dhanunjaya, D. K. Avasthi, A. P. Pathak, S. A. Khan, and S. V. S. Nageswara Rao, "Grain fragmentation and phase transformations in hafnium oxide induced by swift heavy ion irradiation", Appl. Phys. A Mater. Sci. Process., vol. 124, no. 9, p. 0, **(2018)**, doi: 10.1007/s00339-018-2000-z.

[81] M. Toulemonde, C. Dufour, A. Meftah, E. Paumier, Nucl. Instr. Meth. B Beam. Interact. Atoms., 166, 903–912 **(2000)**.

[82] G. Szenes, Nucl. Instr. Meth. B Beam. Interact. Atoms., 2, 1–4 **(1996)**.

[83] N. Manikanthababu et al., "Electronic excitation induced defect dynamics in HfO_2 based MOS devices investigated by in-situ electrical measurements", Appl. Phys. Lett., vol. 112, no. 13, **(2018)**, doi: 10.1063/1.5012269.

[84] M. Toulemonde, J.M. Costantini, C. Dufour, A. Meftah, E. Paumier, F. Studer, Nucl. Instr. Meth. B Beam. Interact. Atoms., 116, 37–42 **(1996)**.

[85] A. Benyagoub, Phys. Rev. B, 72, 094114 **(2005)**.

[86] N. Itoh, D.M. Duffy, S. Khakshouri, and M. Stoneham, J. Phys. Condens. Matter., 21, 474205 **(2009)**.

[87] N. Arun, K. Vinod Kumar, A. Mangababu, S. V. S. Nageswara Rao & A. P. Pathak, "Influence of the bottom metal electrode and gamma irradiation effects on the performance of HfO_2-based RRAM devices", Rad. Eff. and Def. in Sol., 174 (1-2) **(2019)**, 66-75.

[88] N. Arun, K. Vinod Kumar, A. P. Pathak, D. K. Avasthi & S. V. S. Nageswara Rao, "Hafnia based resistive switching devices for non-volatile memory applications and Effects of gamma irradiation on device performance", Rad. Eff. Def. In Sol., 173 (3-4) **(2018)**, 239-249.

[89] N. Arun, L.D. Varma Sangani, K. Vinod Kumar, A. Mangababu, M. Ghanashyam Krishna, A. P. Pathak, and S.V.S. Nageswara Rao, "Effects of swift heavy ion irradiation on the performance of HfO_2 thin films based resistive random access memory devices",Journal of Materials Science: Materials in Electronics, **(2021)** (part of Chapter 5).

Chapter 2

Experimental Details

2.1 Introduction

In this chapter, different thin film deposition systems and their usage for thin film deposition, material characterization techniques, device fabrication and their irradiation by SHI and gamma rays, which are mainly used in thesis work, are presented. The experimental setup is explained in detail in subsequent sections. PVD techniques such as RF/DC magnetron sputtering, e-beam, and thermal evaporation were used in depositing thin films. The Fabrication details of cross-bar structure-based RRAM devices by using an in-house optical lithography instrument are explained. The thin-films' surface morphological properties were investigated by using FESEM, stoichiometry by EDS, thickness measurements by RBS and Profilometer. Further, crystal structure is investigated by GI-XRD, and stoichiometry by XPS for the same films. Similarly, defects in the films were analyzed by PL technique and UV-Vis-NIR Spectroscopy. The irradiation facilities such as SHI and Gamma are also discussed.

The electrical properties of the devices were measured by using a semiconductor device analyzer. There are different varieties of deposition techniques such as CVD and PVD [1-3], electrochemical deposition or electroplating, chemical solution deposition or sol-gel technique and spray coating which are used for depositing thin films. As mentioned earlier, PVD is the most routine and popular technique to deposit good quality thin films. It has more advantages compared to the rest of the techniques such as better control over growth kinematics, uniformity of thin films and so on.

FIGURE 2.1: Physical vapor deposition process steps for the preparation of thin films.

The PVD systems usually require a source material (target to be sputtered or evaporated), transport medium (Plasma, Vapor) and substrate (on which the film should get deposited). Here, the solid material is sputtered, then evaporated as gaseous material, and deposited as a solid material on the substrate.

Figure 2.1 shows the various stages of the PVD process. The Current thesis-work employed the most popular techniques such as RF sputtering and e-beam evaporation. These popular techniques are used for the deposition of thin films of the switching layer metal electrodes.

2.2 Physical vapor deposition systems

2.2.1 Thermal evaporation

It is one of the most commonly used techniques for depositing thin films and preferably for the metal contacts deposition in electronics device manufacturing industry [4]. It includes the principle of evaporating the solid source material by a resistive heating method in a high vacuum environment (typically in the order of 10^{-5} to 10^{-6} mbar). To carry this out, a high vacuum chamber is required to improve the mean free path of the molecules. This is done mainly for the source material to evaporate and get deposited uniformly on the substrate to form a thin film.

In the minimal optimized conditions, thermal evaporation gives good uniformity, high deposition rate, and good quality films [5]. Despite such advantages, the probability of contamination is high in depositing source materials with a boiling point nearly equal to the melting point of the evaporation boat. It is used for depositing Al , Au and other metal electrode contacts. *Figure* 2.2 represents the schematic of the thermal evaporation setup.

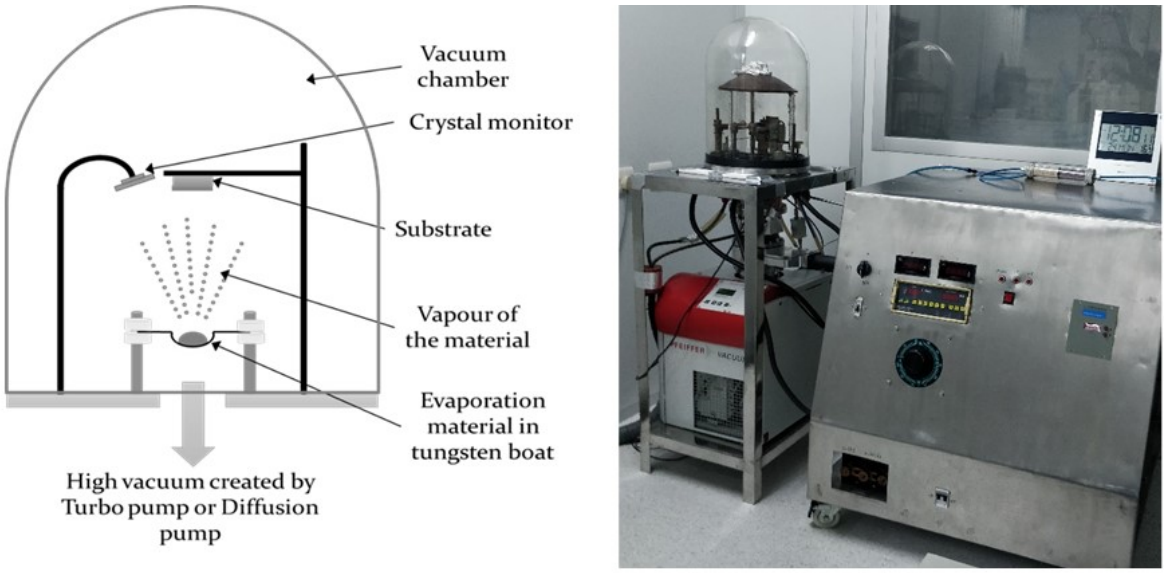

FIGURE 2.2: (a) Schematic diagrams and (b) facility setup of the thermal evaporation system at UoH.

2.2.2 e-beam evaporation

Another technique similar to thermal evaporation is electron beam evaporation. In this, a beam of focused electrons ejecting from a tungsten filament, is directed towards the source material using a strong magnetic field. The evaporation takes place when a large amount of energy (typically in the order of several million watts per square inch) is transferred on to the source material. The process takes place in a high vacuum chamber (typically in the order of 10^{-5} to 10^{-6} mbar).

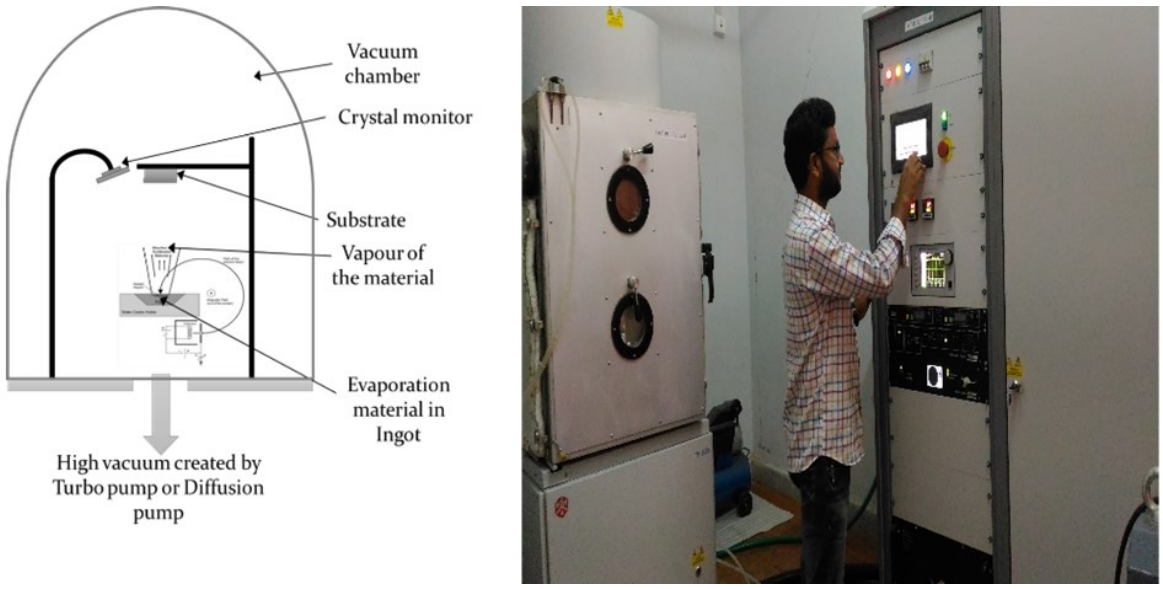

FIGURE 2.3: Schematic and image of e-beam evaporation setup.

TABLE 2.1: The comparison of thermal and e-beam PVD systems.

Evaporation type		Thermal	e-beam
Power	:	240 V and 106 A	5-10 kV(12-15 mA)
Vacuum levels	:	10^{-5} to 10^{-6} mbar	10^{-5} to 10^{-6} mbar
Principle method	:	Joule effect	electron beam
Choice of the materials	:	low melting point	high melting point
Deposition rate	:	50 Å/s	<100 Å/s
Uniformity	:	Moderate	Good
Type of materials for loading the source materials	:	Spirals/boats (Molybedenum and Tungsten)	Crucibles (copper)

The e-beam evaporation is normally suitable for the high melting point materials. In the present work, it is used for the deposition of Cr as a metal contact layer, and HfO_2 as a resistive switching layer. The detailed deposition conditions for the materials are discussed in the respective chapters.

In this present thesis work, Tungsten (W) boat is used for Au and Spiral for the Al for loading the source materials. *Figure* 2.3 represents the schematic of the e-beam evaporation setup. The film deposition conditions are given in respective chapters. The comparison of thermal and e-beam evaporations PVD system is given in *Table* 2.1.

2.2.3 RF/DC Magnetron sputtering

Radio Frequency (RF) magnetron sputtering is the most popular PVD system used for depositing thin films of dielectric materials [6]. In this technique, the principle of variation of an alternating electrical potential of the current at frequencies (typically 13.56 MHz) is involved. At this radio frequency, the AC prevents the charge building up on the target materials during alternate cycles. The sputtering process takes place in a high vacuum chamber (typically in the order of 10^{-5} to 10^{-6}mbar). Here, a cathode is negatively biased, by pumping Ar gas into the chamber, thereby ionized Ar^+ ion (Positive charge) are directed towards the cathode.Therefore, energized charged particles knock out the atoms of the target materials which then traverse in the vacuum chamber and get deposited on to substrate (positively biased).

Similarly, in DC sputtering, a negative potential is applied to the target with respect to the substrate. Here, the positively charged ions (Ar^+) bombarding the target material eject

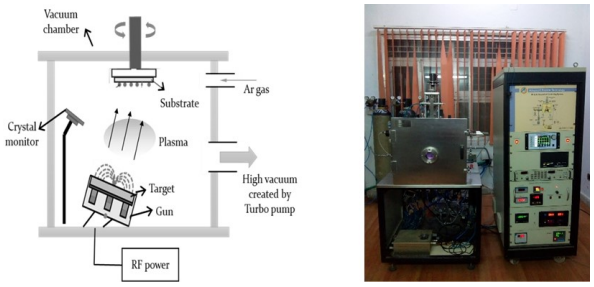

FIGURE 2.4: (a) Schematic view and (b) image of RF magnetron sputtering installed at Sop, UoH.

TABLE 2.2: The comparison of RF and DC sputtering PVD systems.

Sputtering type		RF	DC
Power	:	6 kW	1 kW
Vacuum levels	:	10^{-5} to 10^{-6} mbar	10^{-5} to 10^{-6} mbar
Principle method for heating	:	Ionized inert gas particle to sputter atoms from atoms target materials	Ionized inert gas particle to sputter from target materials
Choice of the materials	:	Dielectric	Metals
Deposition rate	:	50 Å/s	<100 Å/s
Uniformity	:	Moderate	Moderate
Type of materials for loading the source materials	:	Standard target dimens ions (2″ in diameter)	Standard target dimensions (2″ in diameter)

the atoms from it. The atoms then get condensed on a substrate and form thin films. The main limitation of the DC sputtering over RF is that the target should be conducting in nature. Hence, the DC sputtering is used for depositing metal films. Also, RF sputtering can be used to deposit both conductors and insulators whereas DC sputtering can only work for conducting materials. In both sputtering techniques, the magnetron is used such that the magnets are placed behind the cathode, so that the ionized particles are confined near to the target surface. Hence, there is an increase in the collision of particles. The direction of the magnet field is perpendicular to the target cathode electric field [5,6]. The schematic of the RF magnetron sputtering is shown in *Figure* 2.4. The comparison of RF and DC sputtering PVD systems is given in *Table* 2.2. Present thesis work uses an RF sputtering technique for HfO_2 film deposition.

2.3 Device fabrication

In electronics, device fabrication consists of several process steps. In this thesis work all the seven different stages of the processes, right from scribing and cleaving to lift-off and stripping have been used as shown in *Figure* 2.5.

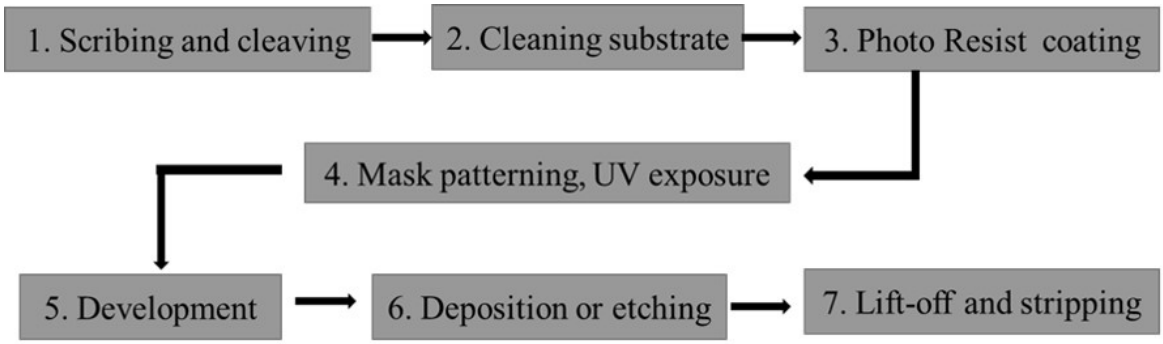

FIGURE 2.5: the process flow steps of the sample cleaning and fabrication of the RRAM devices.

As mentioned above, all the seven steps are employed for fabricating the micron/nano dimension devices. These process steps have to be performed in a controlled humidity and pressure under a clean environment in clean rooms. Based on the number and size of dust particles. As per the size of the dust particles (greater than or equal to 0.5 μm per cubic feet), cleanrooms are classified into different classes (e.g., class 10, class100 and class 1000). The present thesis work is performed in class 1000 for all the stages as mentioned above. Each processing stage is described in a detailed way in the following.

2.3.1 Wafer cutting (scribing and Cleaving)

A single crystal Silicon (Si) substrate is used for this device fabrication in the current thesis work. The detailed specifications of the substrate are given in *Table* 2.3. In all these device fabrication processes, we primarily started with wafer cutting and cleaning as per the requirements and applications.

In semiconductor device industries, usually, wafer cutting (wafer dicing) is employed either by focused laser or by a mechanical saw. It includes a two-step process, scribing and cleaving. The schematic picture (*Figure* 2.6(a)), shows the process of scribing and cleaving the wafer. For scribing, a diamond tip scriber (Suss Microtech HR 100 shown in *Figure* 2.6(b) is used inscribing the lines on the wafer at most with a precision of 0.5 mm as per the

TABLE 2.3: Si wafer specifications.

Silicon wafer specifications	
type	p-Type
Grade	Prime CZ
Surface	Single ploished
Dopant	Boron
Diameter	3 inch
Orientation	<100>
Resistivity	1-10 ohm-cm
Thickness	$380 \pm 25\mu$m

required dimensions up to 4-inch wafer. These lines are perpendicular (90 ^{o}) to the crystallographic orientation (i.e. <100>) for the cleaving. By applying tension on the opposite side of the scribed lines then it cleaves the portion.

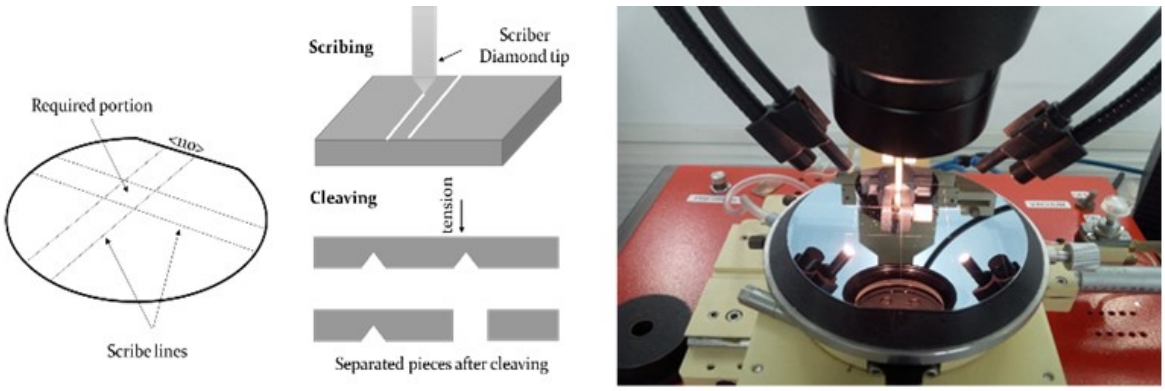

FIGURE 2.6: (a) Pictorial illustrations of scribing and cleaving of Si wafer and (b) set up at CFN, UoH .

2.3.2 Wafer cleaning process

The cleaning of wafer plays a pivotal role in device fabrication and influences device performance. Basically, cleaning removes the impurities and dust particles from surfaces of the substrate without damaging the actual surface. For this process, a standard RCA [7] cleaning procedure is followed, which was developed in 1965 by Werner Kern. This RCA process of cleaning includes the removal of organic and ionic contaminants. The details are explained below in the following three-step process.

Step 1: Initially, a solution of DI water, NH_4OH and H_2O_2 are prepared in the ratio of 5:1:1 respectively. The Si substrates are kept in a beaker with this solution for 15 min at 70 ^{o}C in an Utrasonicator, then the substrate is rinsed with DI water. The dust particles and

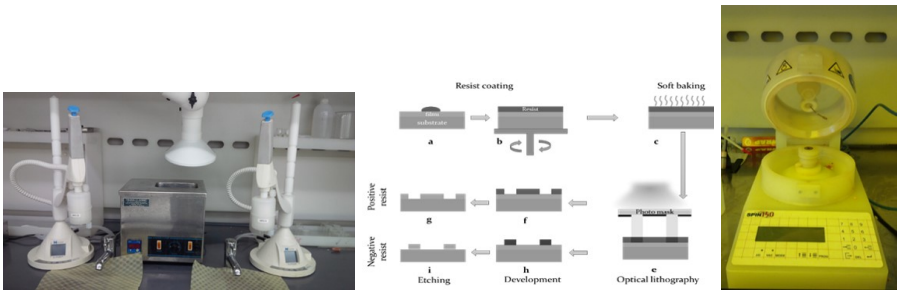

FIGURE 2.7: a) The wet bench set up for sample cleaning b) fabrication process steps using optical lithography and c) the spin coater facility at CFN, UoH

organic impurities are removed, but it forms a very thin layer of oxide grown on Si substrate typically around 10 Å.

Step 2: Further, at room temperature, Si substrates are placed in solutions which are prepared with DI water and HF in the ratio 1:20 respectively for 15 s in an Utrasonicator. With this, a thin layer of the oxide layer is stripped or removed. This step is crucial for those devices, where interface studies directly influence or limit their performance. For the present studies it is an optional step.

Step 3: Finally, a solution of the mixture in the ratio 6:1:1 of DI water, HCl acid and H_2O_2 respectively is used for the cleaning. The substrates are kept for 10 min at 70 ^oC in Utrasonicator than rinsed with the DI water for about a minute. The metallic contaminations are removed from the surface by performing this step.

In order to remove the remaining water droplets, the substrates are dried by blowing a nitrogen gas, followed by placing them on a hotplate at 105 ^oC for a few minutes. All the crucial RCA cleaning steps are done for making good quality devices. *Figure* 2.7 shows the wet bench set up for sample cleaning at CFN, UoH.

2.3.3 Pattern Transfer

Lithography is a technique to define the structures of patterns that are to be transferred on to the substrates. There are wide varieties of Lithography techniques. Among them, photo or optical (UV and Laser) lithography is a universal technique used for the micron size, typically less than 0.5 μm, device structures. In general, lithography consists of a coating of resist followed by soft baking, exposure; development; oxide deposition or etching; lift-off and stripping. These are performed at each stage of the specified patterns or masks. *Figure* 2.7(b) illustrates the process steps for optical lithography.

TABLE 2.4: Spin coating conditions and nominal thickness.

	Spin coating conditions			
Photoresist type	1^{st} Step	2^{nd} Step	Soft baking	Thickness of the film
Positive	500 rpm for 5 s	4500 rpm for 30 s	80 ^{o} for 20 Minutes	$\approx 1.2\ \mu$m

A. Photoresist

Photoresist (PR) is a photosensitive material by its property and is used in many processes of lithography techniques. When exposed to light, PR changes its properties. If its exposed part is removed by dipping in a developer, it becomes positive resist (*Figure* 2.7(b)-f &g. Alternately, if the unexposed part is removed it becomes negative resist (*Figure* 2.7(b)-f &g [8]. For the present thesis work, Fujifilm OIR 620-10M photoresist is used for optical lithography. PR is coated using a spin coater. Resist thickness can be varied by the spin speed and substrate. The spin coater is shown in *Figure* 2.7(c). The spin coating conditions are specified in *Table* 2.4.

B. Optical lithography

Optical lithography is used to pattern micron size devices using a beam of light. In this work, the SUSS MICROTEC MJB4 mask aligner is used in the range of UV wavelengths. This can be achieved by using different kinds of light sources such as Uv and DUV light. In the mercury lamp, the spectra show strong intensity near to UV at 436 nm, 405 nm, and 365 nm and they are also known as g-line, h-line, and i-line, respectively [8]. *Figure* 2.8(a) shows the mask aligner. The mask aligner is operated in contact mode at a constant power of 25 mW/cm^2 (for positive PR). For exposure, the intense peak of 365 nm (i-line) wavelength of light is used. The exposure time of 5 s is used for PR thickness 1000 nm over Si substrates. The exposed samples are developed using Tetramethylammonium hydroxide (TMAH) for 30 seconds.

2.3.4 Etching and lift-off

For selective removal of the material, two kinds of processes can be adopted, etching and lift-off. In the etching process, the developed area is etched using appropriate etchants whereas,

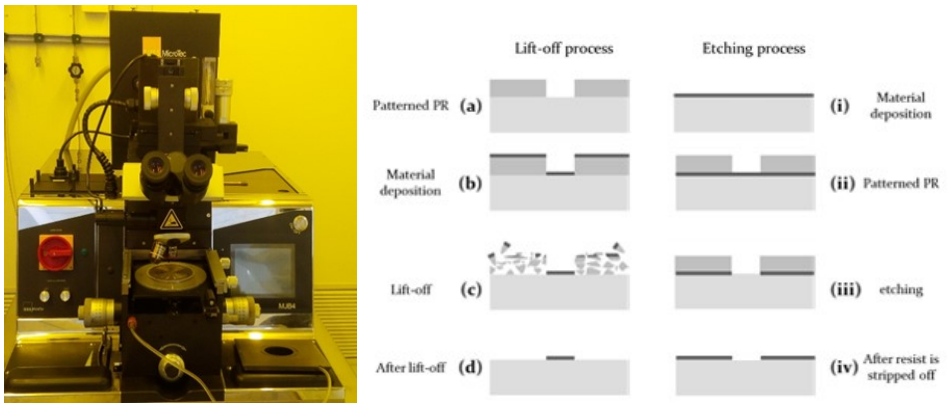

FIGURE 2.8: MJB lithography facilities at CFN, UoH and Illustration of a-d) lift-off, i-iv) etching process steps.

in lift-off, the undeveloped area is stripped away along with the deposited material using solvents like Acetone. *Figure* 2.8(b) illustrates steps in lift-off and etching processes.

2.3.5 Mask details

For present work, 5″x5″ Chrome-coated quartz plate based mask prepared by using EBL technique is employed. RRAM mask used in this work consists of a crossbar array with 25 devices of each cell. These cells vary with different sizes of 10 μm x 10 μm, 20 μm x 20 μm, 40 μm x 40 μm and 80 μm x 80 μm.

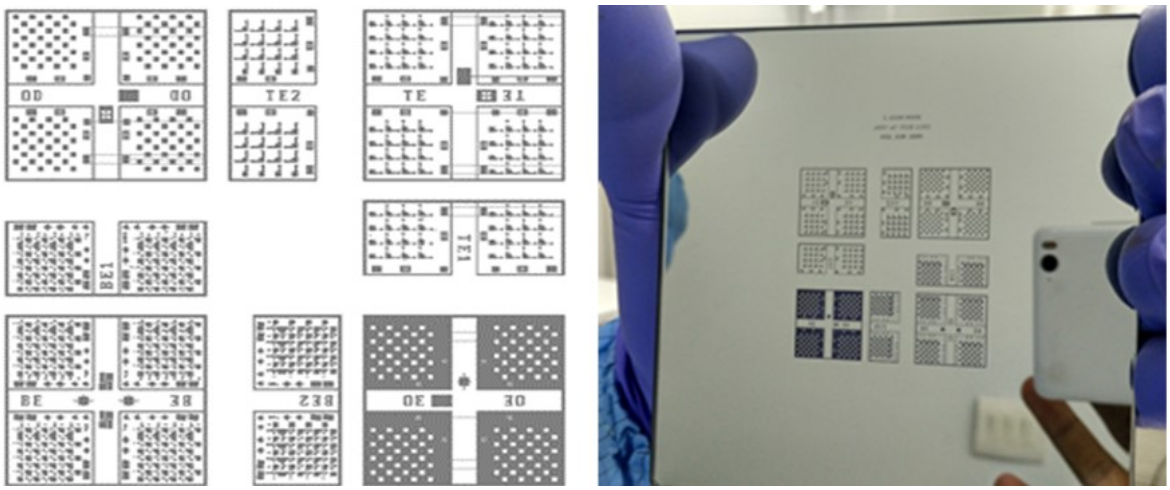

FIGURE 2.9: a) CAD layout for RRAM mask 2; contains the layers for bottom electrodes (BE), to electrodes (TE), switching or oxide layer deposition (OD) and etching (OE) and b) Photographs of a mask used for the Fabricating of the RRAM devices.

The CAD layout of a mask is shown in *Figure* 2.9(a). This mask consists of a bottom and top electrodes as well as oxide design for deposition and etching processes. The photograph

of the mask is shown in *Figure* 2.9(a).

2.3.6 RRAM fabrication flow

The step-wise process flow for fabricating HfO_2 based RRAM devices is shown in *Figure* 2.10 in detail. For all deposition of TE, BE and OD layers, lithography is used to the pattern.

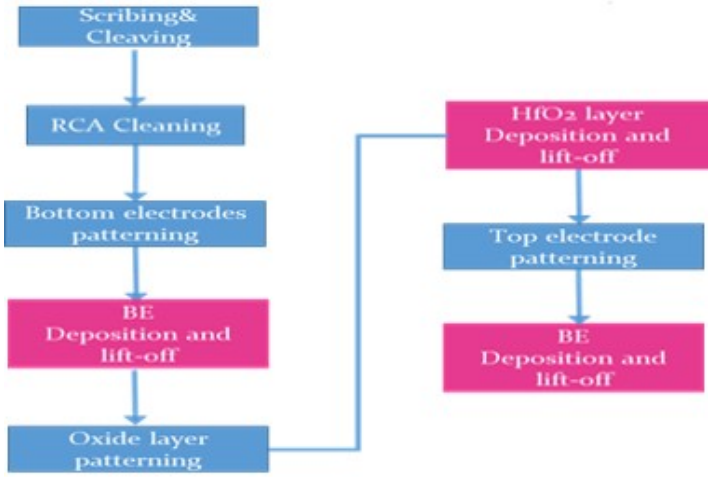

FIGURE 2.10: Process flow of the HfO_2 based RRAM fabrication.

2.4 Irradiation facilities

In employing ion beams for the characterization and modification of the materials, ion-solid interaction plays a significant role. In order, to elucidate the interaction of energetic beams with a material like HfO_2, two different kinds of irradiation have been studied for the devices viz. 1) gamma irradiation and 2) SHI irradiation. Both the facilities are available at IUAC, New Delhi and have been utilized to accomplish the present thesis work.

2.4.1 Gamma irradiation facility

A Cobalt 60 (Co_{60}) source of gamma chamber GC 1200 has been manufactured by the BRIT, Mumbai. The self-shielded source has a capacity of 185 TBq 5000 C_i, dose rate at 9 kGy/hr, about a volume of 1200 cc. The schematic of this process level diagram is shown in *Figure* 2.11(a) and facility setup is shown in *Figure* 2.11(b). The sample for the irradiation is placed inside the chamber at a specified location. The isotope Co_{60}, which is produced from

a bombardment of a neutron with stable Co_{59}, decays into stable $_{60}$Ni by emitting characteristic gamma rays of energies 1.17 MeV and 1.33 MeV. The radio-active reactions are shown below *equation 2.1* and *equation 2.2*.

$$^{60}_{27}\text{Co} \rightarrow^{*}_{28} \text{Ni} + e^{-} + \widetilde{\upsilon_e} + \gamma(1.17MeV) \tag{2.1}$$

$$^{*}_{28}\text{Ni} \rightarrow^{*}_{28} \text{Ni} + \gamma(1.33MeV) \tag{2.2}$$

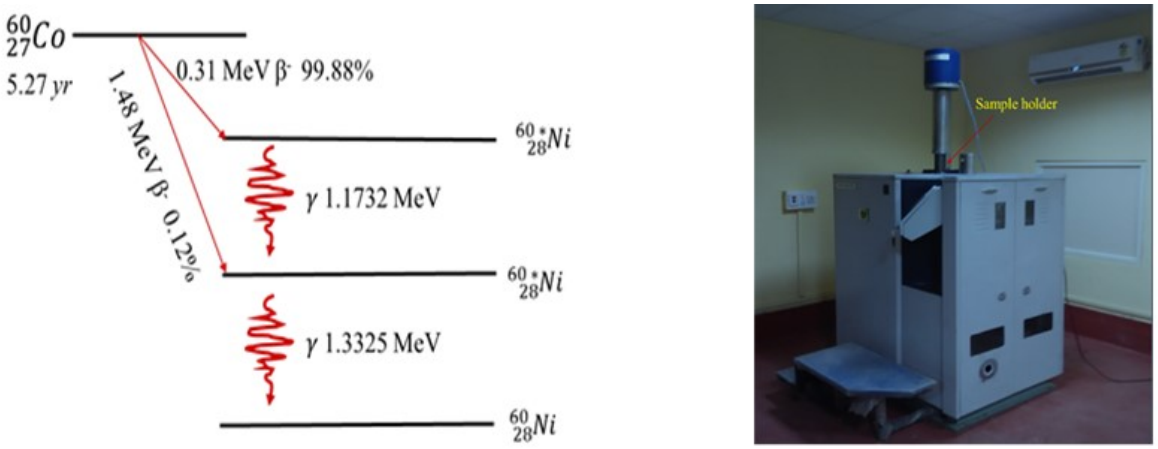

FIGURE 2.11: a) decay mechanism of a gamma source Co_{60} and b) gamma irradiation facility setup at IUAC.

The gamma irradiation effects on the electrical properties of the HfO_2 based devices have been studied at different doses 12 kGy, 24 kGy, and 48 kGy at a constant dose rate of 4.64 kGy/hr.

2.4.2 Swift Heavy Ion Irradiation

For the RF sputtering and e-beam deposition based HfO_2 films of RRAM devices, the SHI experiments have been performed at IUAC, New Delhi by using a tandem type electrostatic accelerator. The schematic diagram is shown in *Figure* 2.12(a) of 15 UD pelletron of tandem Van de Graff accelerator, manufactured by NEC. This kind of pelletron is capable of accelerating ions from a few hundred keV to a few hundred MeV ranges of energies [9-10]. Firstly, stable negatively charged ions are produced from a SNICS ion source. The negative ions with the energy ranging from 50 to 300 keV are generated and pre-accelerated through an injector magnet and the beam enters into an accelerator tube. An insulating SF_6 gas is

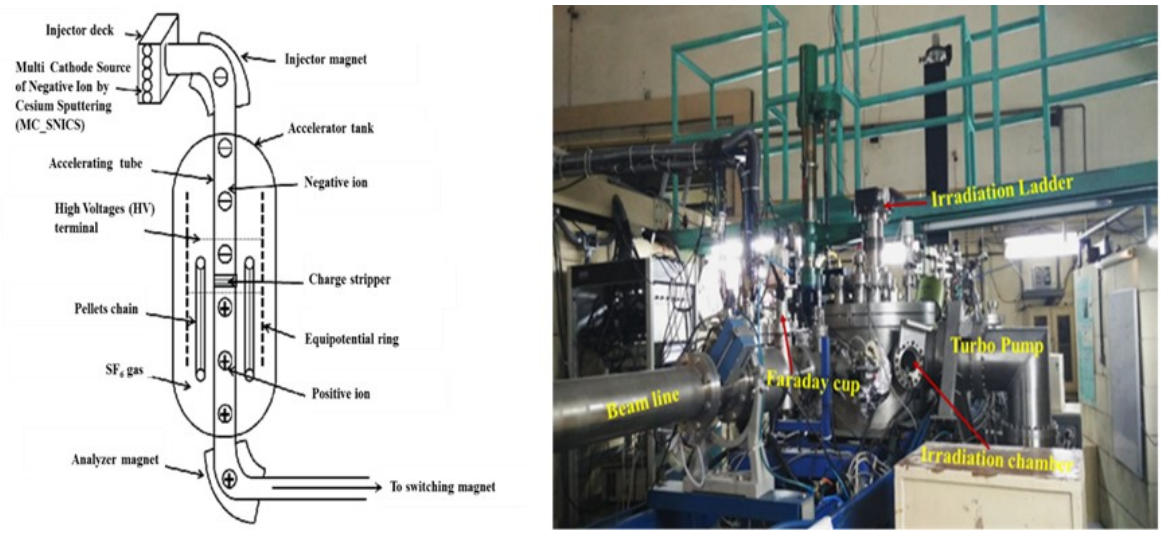

FIGURE 2.12: a) schematic diagram of a pelletron accelerator and b) material science beamline an irradiation chamber at IUAC.

filled in the Accelerating tank at high pressure. The negatively charged ion passes through a stripper foil and gets converted into positively charged ion in the middle of the accelerator, which is the terminal stage where a very high voltage ($\sim$ 15 MV) is attained and the potential gradient is maintained throughout the tube. Further, the positively charged ion is accelerated from the terminal to ground potential. Different charge states of the ions are produced. Depending upon the charge state, ion acquires different energy, as given by *equation 2.3*.

$$E_i(MeV) = E_d + (1+q)V_t \cong (1+q)V_t \tag{2.3}$$

Where E_d is the ion energy produced from the ion source (MC-SNICS) and V_t is the high voltage potential generated at the terminal (in MV). The ion beam current is

measured by FC (FC-L51) as shown in *Figure* 2.12(b). Similarly, the fluence is measured by using the current integrator (integrates the charge collected over time to yield). Hence, the irradiation ion fluence is directly proportional to the irradiation time. The irradiation time is calculated as follows in given *equation 2.4*.

$$time(s) = \frac{fluence(\frac{ions}{cm^2}) * Area(1cm \times 1cm)}{Current(pnA) \times (6.25X10^9)} \tag{2.4}$$

Where t is the time required for irradiating the material. particle nano-ampere (pnA) is calculated by dividing the beam current in nano-amperes with the charge state of the ion.

2.5 Structural, Microstructural and ion beam characterization techniques

There are various characterization and analytical techniques that have been used to study the films. The detailed version of the techniques has been described in the following sections. The Profilometer and RBS are used for estimating the film thickness. FESEM is used to investigate the surface morphology of the thin films deposited by different techniques. XPS and EDS measurements have been performed for the analysis of film stoichiometry. Further, to elucidate the optical parameters of the films, UV-Vis-NIR and PL spectroscopy have been performed. Finally, the electrical transport studies have been conducted by Agilent B1500 A semiconductor device analyzer.

2.5.1 Profilometer

A Profilometer is a basic instrument operated to observe roughness of the surface and the thickness (step heights) of a film. The model of AMBIOS XP 200 Profilometer, having a diameter of 2 μm with a diamond stylus tip, is used for the thickness measurements. The maximum step height it can measure is up to 800 μm with a maximum resolution 1 Åand it gives the 3D profile of the surface and films. It can be done by either using a physical probe (stylus) or by light. Basically, Profilometer has two parts: a sample stage and a detector, one is to hold the sample and other, to determine the points on the sample respectively. The stylus Profilometer is used to detect the surface, probe tip physically moves along the surface of the films to acquire the surface height. A schematic illustration of the Profilometer probe is shown in *Figure* 2.13. The detected optical deflection signal is converted to real-time dimensions in the detector (profile). The technique specifications of the system are given below in *Table* 2.5.

2.5.2 Rutherford Backscattering Spectroscopy

RBS is one of the basic techniques used for the characterization of the elemental composition, film thickness and inter diffusion layers of the films. The schematic diagram is presented in *Figure* 2.14. A target (film) is placed in such a way that it may be bombarded by the incident ion (projectile) with the energy of a few MeV. These ions scatter back at large angles from the film with a certain energy. The process is an elastic collision (non-destructive) between

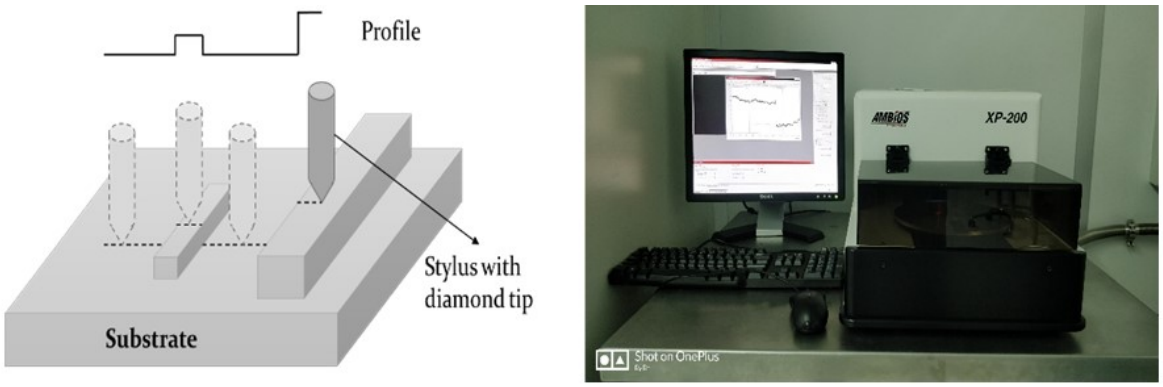

FIGURE 2.13: schematic illustrations of Profilometer scanning of AMBIOS XP100.

TABLE 2.5: The technique specifications of the system.

Model	:	AMBIOS XP 200
Source (stylus Tip)	:	Radius 2.5 μm, Apex angle 60^o, Bevel height 200 μm, Diamond
Stylus Force Range	:	0.03 to 10 mg
Detector	:	Xe filled Count rate or Proportional
Maximum resolution	:	1
Maximum step height	:	800 μm
Scan Length Maximum	:	55 mm
Scan Speed Ranges	:	0.01 to 2.00 mm/sec (scan time > 3 sec)
Sample Stage	:	200 mm diameter with optional vacuum
Stage Translation	:	150 x 178 mm
Stage Rotation	:	Manual operation, 180^o in X-Y plane and tilt for slope correction
Camera Zoom Range	:	40 to 160 X (1 to 4 mm Field Of View)

the projectile and target atoms. It gives a quantitative information and depth profile (several orders of nm) of the heavier mass number elements whereas, very less sensitive to the lighter mass elements. Generally, for RBS measurement, a 2 MeV He^+ ions are used as incident (projectile beam) ions[11]. The kinematic factor of the elastic collisions is given below in *equation 2.5*.

$$k_{RBS} = \frac{E_1}{E_0} = [\frac{\sqrt{(M_2) - (M_1)^2 sin^2\theta} + M_1 cos\theta}{M_2 + M_1}]^2 \tag{2.5}$$

Where M_1 is the mass of the incident (projectile) ion and M_2 is that of the target ions. E_0 is the initial energy of incident ions and E_1 is the energy of backscattered ions and θ is the scattering angle. This kinematic factor provides the mass perception to identify the constituents in the target material. The RBS facilities at IUAC are utilized and the details of

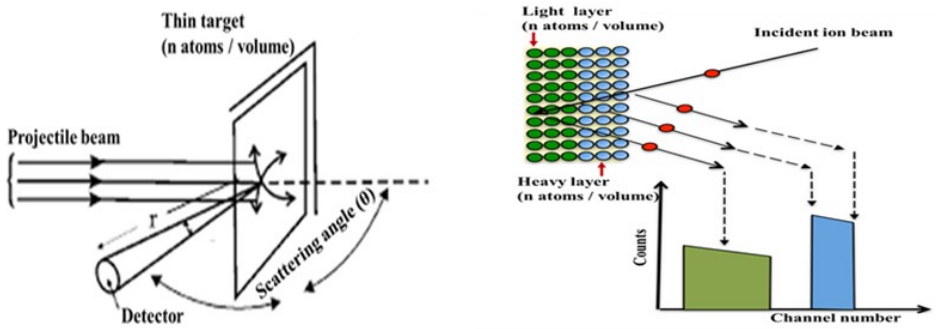

FIGURE 2.14: schematic illustrations of the RBS technique.

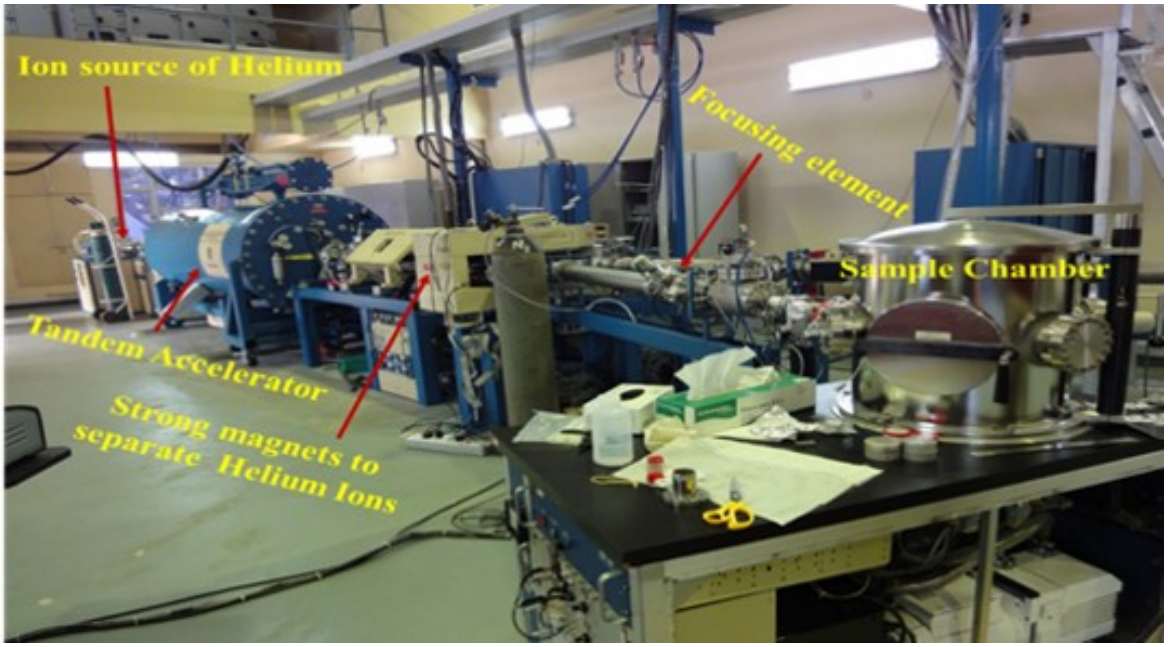

FIGURE 2.15: The experimental setup for the RBS measurement at IUAC.

the RBS experiments are given for the present thesis work. The RBS facility setup presented at IUAC is shown in *Figure* 2.15.

2.5.3 X-Ray Diffraction

XRD is a fundamental, powerful and non-destructive characterization technique that works based on Bragg's law (*Equation 2.6)*. It is used for identifying the crystal structure, texture, crystal orientation, particle/grain size and phase of the material (films or power). It also gives structural parameters such as crystal defects, average crystallite size and strain[12]. The process is governed by the Bragg's Law.

$$2dsin\theta = n\lambda \tag{2.6}$$

where d is interplanar spacing, θ is the diffraction angle and λ is the wavelength of X-rays. XRD is based on the principle of constructive interference of monochromatic X-rays, when incident on film or powder, the atomic spacing of planes with spacing d, and at a Grazing angle θ as shown in *Figure* 2.16. According to Bragg's law *(Equation 2.6)* the wavelength of electromagnetic radiation which relates to the diffraction angle and the lattice spacing in a sample, and produces peaks in the X-ray diffraction pattern.

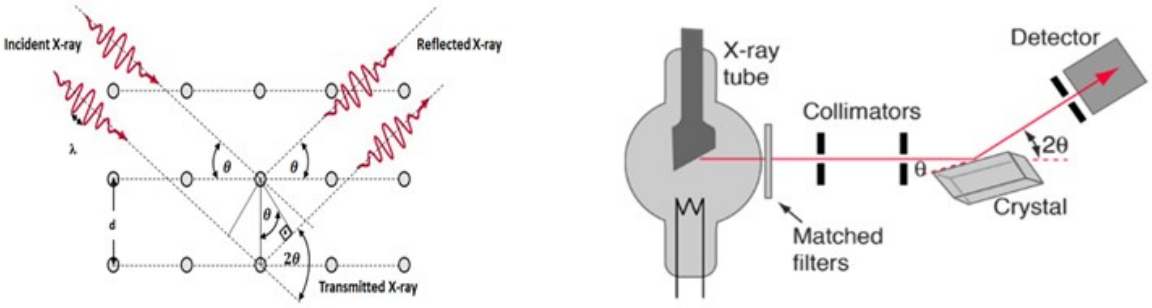

FIGURE 2.16: schematic illustration XRD.

TABLE 2.6: The Technical specifications of the GI-XRD and XRR instrument .

Model	:	Bruker D8 Discover
Source	:	Cu target
Power	:	2 kW
Detector	:	X_e filled Count rate or Proportional detector diffractometer goniometer
Modes of operation	:	Vertical & Horizontal
Accuracy	:	$\pm$ 0.0025
$2\theta^{\,o}$ Measurement range	:	30 to 136^o
Diffractometer radius	:	130 to 230 mm

XRD set up basically consists of three elements: an X-ray tube, a sample holder, and an X-ray detector. X-rays are generated in a cathode ray tube by heating a tungsten filament to produce electrons, accelerating and directed to bombard the target material by applying a DC voltage [13]. It produces K_α and K_β characteristic X-ray spectra. Mostly, Cu, Fe, Mo, Cr are the target materials used. Copper is one of the most common target material among all other targets for single-crystal diffraction, with Cu K_α radiation = 1.5418 Å. These characteristics (K_α) X-rays are filtered by passing through matched filters and produces monochromatic rays. These x-rays will pass through collimators and directed towards the sample (*Figure* 2.16(b)). The diffracted ray produced from this sample is detected by a detector,

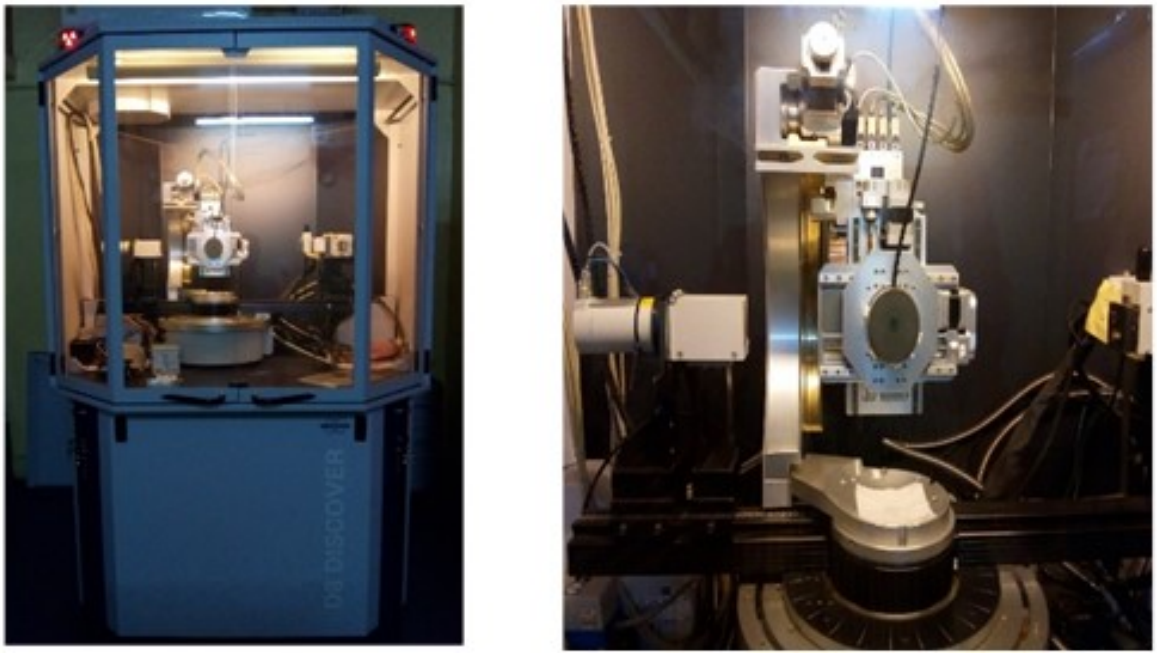

FIGURE 2.17: XRD facilities installed at SoP, UoH.

which gives the XRD pattern. The peaks obtained from the XRD patterns were indexed by using the Joint Committee on JDPDS or PDF-4 software [14].

The incident angle of X-rays should be very small for thin or sub-micron thickness films, so that it suppresses the information of the substrate and gives maximum details of the film and this process is called GI-XRD. This system can be operated in two modes as GI-XRD and XRR. The facilities are shown in *Figure* 2.17 In this present work, the crystal structure of the films was examined in a Bruker D8 Discover GIXRD with a Cu K_α line of 0.15406 nm wavelength and incident angle of 4^o. Similarly, the XRR measurement is performed for the sample to estimate the thickness of the films. The technique specifications of the system are given below in *Table* 2.6.

2.5.4 Field Emission Scanning Electron Microscope

FESEM characterization is one of the versatile techniques used for the studies of surface external morphology (texture), chemical composition, and crystalline structure and orientation of materials. SEM analysis is considered to be "non-destructive", that is, x-rays generated by electron interactions do not lead to volume loss of the sample, so it is possible to analyze the same materials repeatedly. The FE electron gun produces an electron beam of required energy. By applying a high electric field to the metal surface, the electron is emitted from the

filament cathode. The filament is made of a Tungsten wire of diameter about 0.1 mm. Under vacuum, electrons generated by a Field Emission Source are accelerated in a field gradient. The beam passes through Electromagnetic Lenses, focusing on the specimen. As a result of this bombardment, a detector collects and detects the secondary electrons and an image of the sample surface is constructed by comparing the intensity of these secondary electrons to the scanning primary electron beam [15,16].

FIGURE 2.18: (a) schematic illustration of scanning electron microscopy (b) Carl ZEISS, FEG, Ultra 55 FESEM system installed at SoP, UoH.

From a field emission source, electrons are liberated and accelerated in a high electric field gradient. These primary electrons are focused and deflected by electronic lenses within the high vacuum column chamber to produce a narrow scan beam that bombards the object. Images are produced from backscattered electrons with contrast that carry information on the differences in atomic number, whereas secondary electrons give topographic information. The facilities are shown in *Figure* 2.18 In this present work, the surface morphology of the films was examined in a Carl Zeiss, FEG, Ultra 55 FESEM. The technique specifications of the system are given below in *Table* 2.7.

A. Energy Dispersive X-ray Spectroscopy

The EDS is a non-destructive characterization technique used to detect chemical contamination (the type of elements and the percentage of the concentration of each element of the sample) present in the sample. When the high energy electrons are incident on the sample, inner shells are ionized and X-rays are emitted where these inner shells are filled by outer

shell electrons. The energy of emitted characteristic X-rays is a signature of the ionized atom. *Figure* 2.19 shows schematic diagram of the EDS of the characteristic X-ray emission.

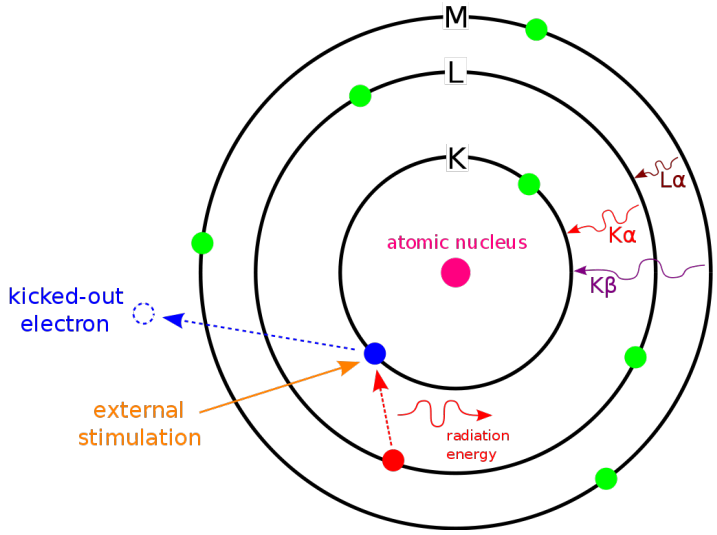

FIGURE 2.19: The schematic diagram of the EDS.

TABLE 2.7: The Technical specification of the FESEM and EDS instrument.

Model	:	Carl Zeiss, FEG, Ultra 55
Resolution	:	3.5 nm at 30 kV
Accelerating Voltage	:	0.2 to 30 kV
Magnification	:	upto 500 kX

In the present thesis, the chemical composition of HfO_2 is determined by using the EDS technique. The spectra are obtained from an in-built EDS setup in the FESEM system of Oxford instruments. The operating voltage of 20 kV is used. INCA software is used for the analysis of the spectra.

2.5.5 X-ray photoelectron spectroscopy

XPS is a surface-sensitive technique that gives the quantitative information about chemical composition and bonding of electronic states within a few nm range depth from the top surface of a sample. When a focused beam of X-rays is directed onto a sample, it measures the kinetic energy of electrons from the top surface of the sample by analyzer and counts (number of electrons by electron detector). A schematic of the XPS is shown in *Figure* 2.20(a). The binding energy of the electrons and the number of electrons provide information about the detected element [15,17]. The main disadvantage of XPS is that it is a destructive method.

FIGURE 2.20: a) schematic of X-Ray Photoelectron Spectroscopy and b) AXIS ULTRA Multi-technique X-ray Photoelectron Spectroscopy installed at IISc, Bangalore.

TABLE 2.8: The Technical specifications of the XPS facility at IISc, Bangalore.

Model	:	Kratos Axis Ultra
Anode HT (kV)	:	(1 - 15, typically 15)
Source (Al Mono) X - rays with energy	:	Al Kα X- rays, E_{photon} 1486.7 eV
Emission current (mA)	:	(1 - 20, typically 15)
Spot Size	:	small spot capabilities (< 15 microns)
Resolution	:	Pass energy 20 or 40 eV

In the present thesis work, XPS of AXIS ULTRA facility, at IISc, Bangalore as shown in *Figure* 2.20(b) is used to identify the peaks of the Hf and O bonding for the RRAM devices. The technical specifications are given in *Table* 2.8. The facility is accessed through INUP.

2.5.6 Ultra Violet-Visible-Near Infrared (UV-Vis-NIR) Spectroscopy

UV-Vis-NIR is one of the basic techniques to study the interaction of light with matter [18]. It covers from 200 to 2600 nm range in the electromagnetic radiation spectrum. Basically, the reflection or absorption of the sample depends upon the transparency of the sample when light (UV region to the NIR region) falls on it.

For the present thesis work, UV-Vis-NIR (model: JASCO V-570) double beam spectrophotometer [18] is used and shown in *Figure* 2.21. The light wavelength ranging from 200 to 2500 nm was used to perform the transmission and absorption measurements on the films (HfO_2) deposited on the Quartz. Pure quartz (air medium) was used as the reference for all the above spectroscopy measurements. The technical specifications are given in *Table* 2.9.

The light source of the deuterium (D_2) lamp is used for UV and a halogen lamp is used for the Vis-NIR spectrum of regions. Based on the range of wavelengths, from the light

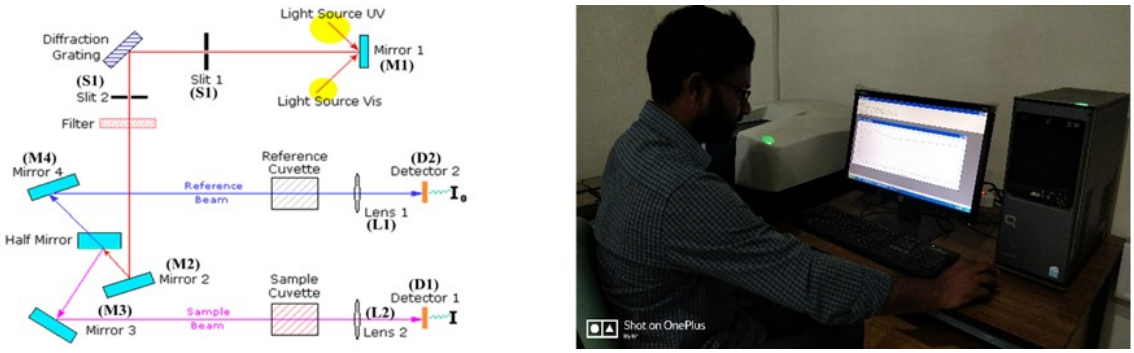

FIGURE 2.21: a) Schematic diagrams and b) facility at SoP, UOH of UV-Vis-NIR spectrophotometer.

TABLE 2.9: The Technical specification of the UV-Vis-NIR instrument.

Model	:	UV - Vis - NIR Spectrometer JASCO V -570
Source	:	Deuterium (UV), Tungsten - Halogen (Vis/NIR)
Detectors	:	Photomultiplier tube for UV- Vis, Lead - Sulphide cell (PbS) for NIR
Wavelength Range	:	200 - 32600 nm
Scan Speed	:	0.3 to 1200 nm/min
Accuracy	:	± 0.15 nm for UV/Vis ± 0.6 nm for NIR
flatness of Base line	:	± 0.001 Å, 4 nm slit
modes of operation	:	Scan, time drive, wavelength programming, concentration
Accuracy of Photometric	:	± 0.003 Åor ± 0.08% T

source, it gets reflected from the mirror (M_1). Then the reflected beam passes through the slit-1(S-1) and strikes the diffraction grating which acts as a monochromator to use the selected - wavelength. The required output light (wavelength) beam is passed through the slit-2 (S-2), then it allows passing through the low/high filter. The beam finally hits the mirror (M_2) before getting split by a half-wave plate.

2.5.7 Photoluminscence

PL is a non-destructive technique and the one of the most used Photo spectroscopy techniques to study the electronic and defect states of the solid thin film, powder and liquid materials. The light from the source is directed on to the sample by using controlled optics as shown in *Figure* 2.22 (a) schematic view and (b) the instrumental set up facility at UoH. When a material is excited with electromagnetic radiation, some of the photons are absorbed

by the material. The absorbed photons excite the inner electrons to the excited states and this process is called photo-excitation. The excited electrons come back to the ground state by losing energy via photons, this process is called photo-luminescence.

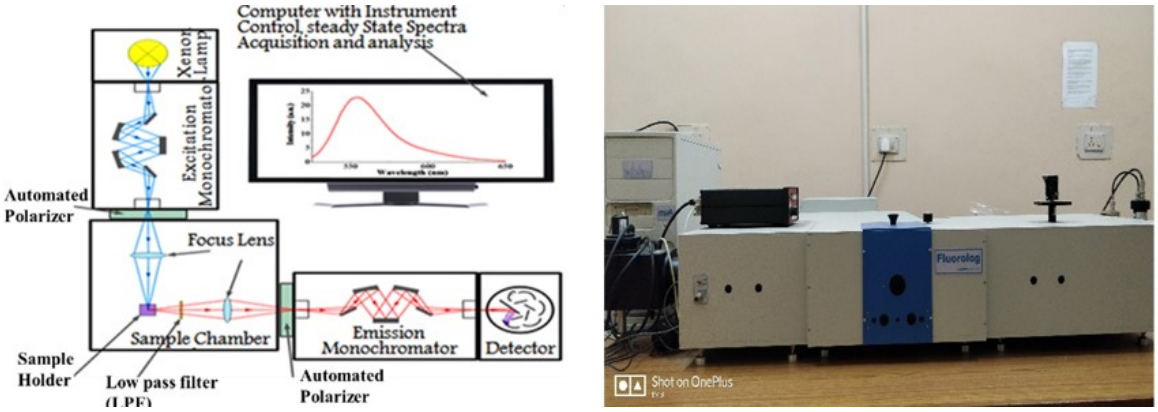

FIGURE 2.22: a) Schematic illustrations and b) facility at SoP, UOH of photo-luminescence.

TABLE 2.10: The technical specifications of the photoluminescence instrument.

Model	:	Flouolog 1427C-Au
source	:	450 W Xenon lamp Ozone resolving type lamp housing
Excitation and emission monochromators	:	Concave, blazed holographic grating, F/2.5, 1300 grooves/mm
Measuring wavelength range	:	220-750 nm and 0 order as standard 220-900 nm with the optional R928 photomultiplier
Spectral band with	:	6 nm
Wavelength	:	1.5 nm
Sensitivity	:	The S/N ratio is 150 or
Wavelength slewing speed	:	about 20,000 nm/min

Continuous lamp (Xenon) is used for the PL measurement in the excitation wavelength range of 220 to 990 nm [19]. The excitation radiation is passed through the monochromator then focused on a sample (incident direction). The emitted photons are collected at an angle of 45 ^{o} with respect to excitation light. The technical specifications are given in *Table* 2.10. One of the main objectives of the present thesis work is to investigate the defects creation/modifications in the HfO_2 material for all the samples.

2.6 Transport properties

The transport properties of the fabricated RRAM devices are measured by using the Agilent B1500 A SDA facility installed at CFN, UoH. The key parameters such as formation, set, reset voltages and similarly, I-V, endurance and retention of these RRAM devices have been measured. The facility is shown in *Figure* 2.23. The computer system or SDA (*Figure* 2.23(a)) along with a stage of the probe station (Model: Signatone-S1160) (*Figure* 2.23(b)) is attached to it [20]. A microscope is attached to a probe station to identify the correct place to land the probes. The probes are Gold coated tungsten with a tip diameter of 20 μm.

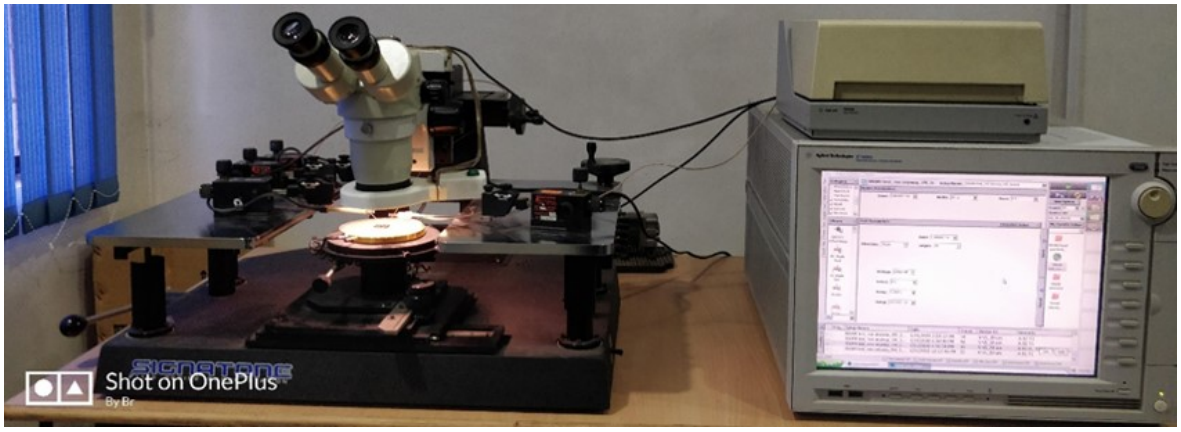

FIGURE 2.23: Photograph of Agilent B1500 semiconductor device analyzer and, attached with a Signatone probe station.

TABLE 2.11: Voltage and sampling measurements parameters.

I-V Sweep		I/V-t Sampling	
Voltage range	Given in respective measurements	Read voltage	100 mV
Voltage step	10 mV	Sampling interval	60 s
Hold time	100 ms	Hold time	10 ms

Basically, the SDA consists of both voltage and current sweeps inbuilt B1511, with an MPSMU. The limits of MPSMU as voltage and current in the range 0 – 100 V and 0 – 100 mA respectively and further the maximum voltage and current resolutions are 0.5 μV and 10 fA, respectively. The Easy expert software of SDA enables the program to run user-defined measurements using SMUs. Voltage sweep is used for I-V and endurance measurements whereas, I/V-t sampling is used for retention measurement. Voltage sweep and sampling measurement parameters are given in *Table* 2.11 .

2.7 Conclusions

Principles of various synthesis, irradiation and characterization techniques used in this work are discussed. The capabilities and limitations of the specific equipment used in this thesis are also discussed. Specific experimental parameters are given in respective chapters.

Bibliography

[1] Selvakumar, N.; Barshilia, Harish C, "Solar Energy Materials and Solar Cells", 98, 1–23 **(2012)**.

[2] L. Zhang, K. Ohuchi, K. Adachi, K. Ishimaru, M. Takayanagi, and A. Nishiyama, Appl. Phys. Lett., vol. 90, no. 19, p. 192103, **(2007)**.

[3] M. Ohring," Materials Science of Thin Films", Academic Press, **(2002)**.

[4] George, J., "Preparation of thin films", Marcel Dekker, Inc., New York, 13–19 **(1992)**.

[5] D. M. Mattox, "Handbook of Physical Vapor Deposition (PVD) Processing", Cambridge University Press, **(2014)**.

[6] Ohring, Milton. Materials Science of Thin Films (2^{nd} ed.). Academic Press. P. 215.

[7] W. Kern, J. Electrochem. Soc., vol. 137, no. 6, p. 1887, **(1990)**.

[8] M. J. Madou, "Fundamentals of Microfabrication and Nanotechnology", CRC Press, **(2011)**.

[9] http://www.iuac.res.in/accel/paras.

[10] http://www.iuac.res.in/accel/pell/index.html.

[11] http://www.iuac.res.in/accel/paras/index.html.

[12] http://prism.mit.edu/xray/oldsite/Bruker

[13] https://www.nano.pitt.edu/sites/default/files/D8

[14] https://acronyms.thefreedictionary.com/JCPDS"

[15] B. David and W. D. Kaplan," Microstructural characterization of materials", 2^{nd} ed. John Wiley & Sons, **(2008)**.

[16] “A Brief History of the Microscopy Society of America”, Microscopy.org.

[17] D. K. Schroder, "Semiconductor Material and Device Characterization", John Wiley Sons, **(2006)**.

[18] O. Stenzel, “The Physics of thin film Optical Spectra: Introduction”, Springer, Germany **(1996)**.

[19] Stephen M. Cohen, “Modular Spectro fluorometer-the Fluorolog-3”.

[20] https://www.keysight.com/en/pd-582565-pn-B1500A/semiconductor-device-analyzer?cc=INlc=eng

Chapter 3

Optimization of HfO_2 thin films for RRAM device fabrication

3.1 Introduction

In IC fabrication, the preparation of the thin films plays a pivotal role [1]. Basically, the thin film is defined based on the layers thickness ranging from few nanometres to micrometres. The films have various applications in the present industry such as optoelectronics, microelectronics, solar panels, and magnetism [2-5]. The materials are chosen depending upon their specific applications. In certain cases, these depend on the surface or the bulk film of the material [1].

The thin film deposition is carried out by various methods such as the PVD methods using solid form material transport and film nucleation [6]. Whereas a solution or a gas form is used for the chemical synthesis method such as CVD [7], ALD [8], sol-gel method [9], dip coating method [10] and spin coating methods [11] come under the chemical synthesis category. Basically, initial stage material is in liquid or gaseous form for chemical synthesis and in solid form in case of the PVD methods. In the PVD system the atomic species travel through a distance from source material target onto the substrate and get deposited due to the applied bias on the target[12]. In general, the famous PVD methods such as RF sputtering [12], e-beam Evaporation [13], and PLD [14,15] are useful for both insulators and metals deposition. similarly, Thermal Evaporation [16], and DC sputtering are better suited for depositing metals[12].

As mentioned above, a few deposition techniques such as, RF/DC magnetron sputtering are employed to optimize and fabricate the thin films. In this, an external power source is

applied to the target, a low-pressure gas in the chamber creates plasma and the ions are made to collide with target material, travers through and get deposited on the substrate. Most of the experiments using the sputtering technique are performed in the inert gas (such as Ar) atmosphere. In the present thesis work, the Ar gas has been used to perform the sputtering technique for HfO_2 based thin films deposition. In RF sputtering technique, when the Ar ion hits the target source material (negatively biased with respect to the substrate) it ejects the atoms from the target. These atomic species travel through a distance in the vacuum chamber and get deposited and then condense on the surface of the substrate. In a continuous process, more and more atoms condense at substrate and form the film. The dielectric materials such as HfO_2 is deposited by many techniques, including RF Magnetron sputtering technique. This simple and more economic method gives better uniformity and good control of the deposition conditions for the films. HfO_2, a high-k dielectric material has immense possibilities and various applications in present IC industries, microelectronics, storage devices, solar devices, solar cells and, optoelectronics [17-20].

In the present chapter,we elaborately discuss about the HfO_2 film deposition conditions and studies such as surface morphology, structure, stoichiometry of the films. The optimization conditions for fabricating the HfO_2 based RRAMs for NVM devices, have also been discussed.

3.2 Experimental details

HfO_2 films were deposited by using RF Magnetron sputtering on Si and quartz substrates. The HfO_2 target of 2-inch diameter, 5 mm thickness and 99.99 % pure (commercially purchased) has been used for the deposition of the films. The standard RCA cleaning process was adopted for cleaning the substrates [21]. Initially, the cleaned samples were loaded in the chamber and the chamber was evacuated to a base pressure of 8 x 10^{-6} mbar. The deposition was performed by introducing some pure Argon (Ar) gas into the chamber. The p-type (1-10 Ω-cm) Si (100) substrates were used to study the structural properties, surface modifications and thickness of the films. Similarly, quartz substrates were used to investigate the optical properties of these films.

To obtain optimum thin film deposition conditions, the substrate to target distance (12 cm) and Ar gas pressure (30 SCCM) are fixed based on previous experiments[22]. The time

of deposition is varied from 15 to 120 minutes. Different characterization techniques have been used to analyse these films. FESEM is used to study the structural and surface morphology of the films while EDS and XPS are used for the elemental composition. The thickness of the film is estimated by using a Profilometer and XRR measurements. Further RBS is employed to confirm the stoichiometry, elemental composition, and film thickness. HfO_2 on quartz substrates were used to investigate the optical properties (transmission spectra) of the films.

RBS measurements were performed using 2 MeV He^{2+} ions at a scattering angle of 165^0. Calibration offset and energy per channel were estimated to be 96 keV and 0.961 keV/ch respectively, using a calibration sample (Au/Glass), to simulate the RBS spectra. These RBS measurements were carried out at IUAC, New Delhi. SIMNRA-7.1 software [23] was used to analyse the RBS data. The in-house Bruker D8 Discover diffractometer equipped with Cu Kα (λ= 1.5405 Å) was used to perform the XRR measurements.

The optical characterization of the films deposited on quartz substrates was carried out by using UV-Vis-NIR spectroscopy. Transmittance measurements were performed in the wavelength range of 190–2000 nm using JASCO V-570 Photo Spectrometer. The optical properties of the films were calculated by using an envelope method [24]. The refractive index of the films is derived from the following *equations*[25].

$$N = 2sT_M - T_m T_M . T_m + S^2 + 12 \tag{3.1}$$

$$n = \sqrt{(N + \sqrt{(N^2) + S^2})} \tag{3.2}$$

where n is the refractive index of the material, S is the substrate refractive index, T_M and T_m are the two adjacent maxima. Thickness of the films is calculated from the transmittance spectra by the following *equation* [25]

$$t = \lambda_1 \lambda_2 2(\lambda_2 n_1 - \lambda_1 n_2) \tag{3.3}$$

where t is the thickness of the film, λ_1, λ_2 are the wavelengths of the two-adjacent consecutive maxima or minima. n_1, n_2 are the refractive indices at adjacent maxima/ minima wavelets. The bandgap of the films was calculated by using Tauc's law [26], which is derived

from the transmittance spectra. The relevant equation is as follows:

$$(\alpha h\nu) = B * (h\nu - E_g)^p \tag{3.4}$$

where,α is the absorbance, which is derived from the transmittance spectra, hν is the photon energy, E_g is the bandgap of the material, B is the parameter of the absorption edge width. The exponent p can be determined by the type of the electronic transition. Here the superscript p value varies from ½ and 2 depending on the type of indirect allowed, and direct allowed transition respectively. HfO_2 is an indirect bandgap material, hence 'n' value is equal to 0.5 [27].

FE-SEM: Carl ZEISS, FEG, ultra-55 was used to scan the surface morphology evolved grains and to measure the film thickness from the cross-sectional image. The deposited HfO_2 films have been studied using 5 kV EHT electron gun at different magnification levels. PL measurements were performed using Fluorolog, Xenon lamp, 450 W, having a resolution of 0.3 nm. PL measurement is very useful to estimate the defects states formed in the films [28]. Each of the films was excited with 300 nm wavelength and the emission was measured in the range of 315 to 700 nm.

3.3 Results and discussions

3.3.1 variation of deposition time

The deposition of the HfO_2 film on Si and quartz substrates has been carried for different intervals. Various characterization techniques have been employed to study the thickness, surface morphology, quality and stoichiometry of these films. Deposition time is varied from 15 to 120 minutes. The thickness of the film is analyzed and estimated by employing various techniques such as profilometer, RBS, XRR, and further study by optical measurement. It is observed that the film thickness is increasing as time increases, as expected (see in *Table* 3.1).

The XRR patterns of the HfO_2 films deposited with different durations are shown in *Figure* 3.1. It is observed that the films deposited at fixed RF power by varying deposition duration are mainly amorphous in nature. From these reflectivity curves, layer parameters such as thickness and density, interface and surface roughness can be determined, regardless of the crystallinity of each layer (single crystal, poly crystalline, and amorphous). At some

TABLE 3.1: The comparison of film thickness measured by XRR and RBS measurements.

	Film thickness	
Deposition time (minutes)	XRR (nm)	RBS (nm)
10	15	-
15	22	10
30	38	35
60	58	57

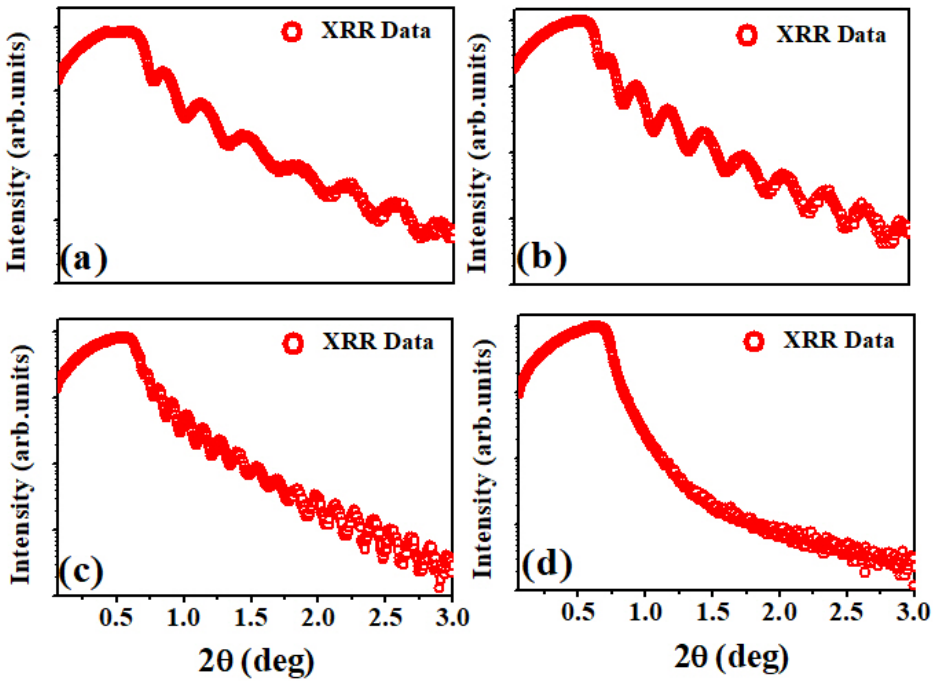

FIGURE 3.1: The XRR spectra of the films of different duration for deposition (a) 15 minutes, (b) 30 minutes, (c) 60 minutes, (d) 120 minutes of HfO_2 on Si substrates.

critical angle, the reflectivity begins to decrease exponentially and it is found to be $\sim 0.6^o$ for these samples with Si as substrate.

The RBS spectra of films obtained with varying the time of deposition are shown in *Figure* 3.2. Calibration offset, energy per channel were estimated to be 96.47 keV and 0.96 keV/ch respectively by using a calibration (Au/Glass) sample. The peak showing at 1800 channel number represents the Hf peak and a small hump at 650 channel number showing 'O' peak. The physical thickness of the film is calculated by dividing it with the nominal density of bulk HfO_2 which is 8.4 atoms/cm^3. The physical thickness of the films for the deposition time 15, 30, 60, and 120 minutes respectively are listed in *Table* 3.1.

EDS is performed for all these films and the stoichiometry of the HfO_2 films is found

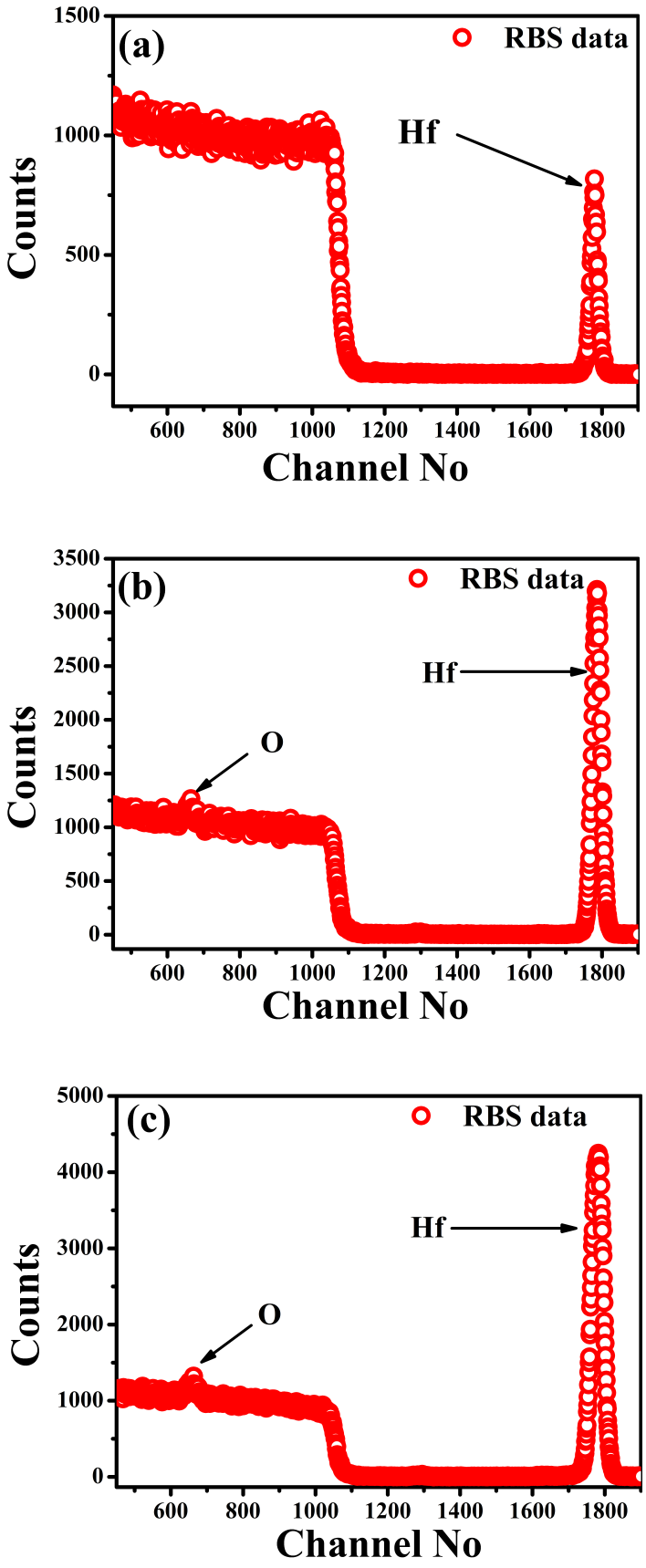

FIGURE 3.2: The RBS spectra (red) and simulation spectra (black) of the films deposited at different times (a) 15 min., b) 30 min., and c) 60 min.

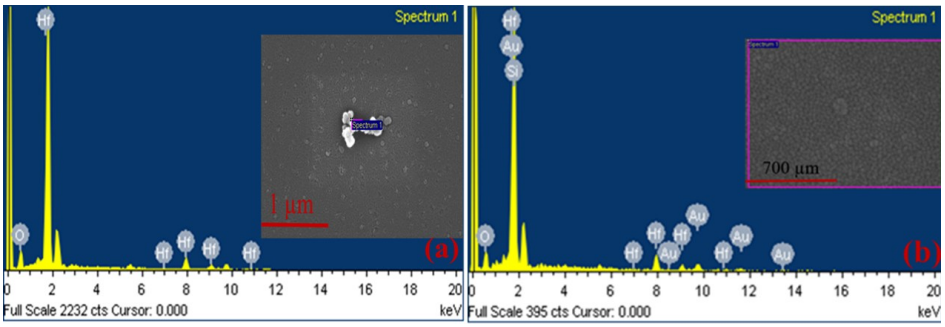

FIGURE 3.3: EDS spectra and FESEM images of a) HfO_2/Si and b) HfO_2/Au/Si sample (Representative).

to be reasonably good if the time of deposition is above 30 minutes. *Figure* 3.3 shows some representative results: a) HfO_2/Si and b) HfO_2/Au/Si of EDS images and corresponding FESEM images. The substrate percentage (such as Au, Si) is subtracted then, weight % is found to be 85% for Hf element, similarly 14 % for the O element and shown in *Table* 3.2.

TABLE 3.2: The weight and atomic % calculation for HfO_2/Si film.

Element	Weight (%)	Atomic (%)
O	14.10	65.14
Hf	85.90	34.86
Total	100	100

The XPS data revealed that the elements present in the films are hafnium and oxygen only. The high resolution core level spectra for the Hf 4f and O 1s of the films deposited at different duration are shown in *Figure* 3.4 . The binding energy of Hf 4f peak is about 16.5- 17 eV. The spectra of the films show the presence of the peaks corresponding to the 4f7/2 and 4f5/2 levels of Hf in HfO_2(spin orbit splitting). The 4f7/2 peak position ($\sim$16.2 eV) is same for these films. The separation between the peaks of 4f7/2 and 4f5/2 is 1.6 eV. It can be interpreted as charge transfer effects promoting the peaks position at higher energy levels [29]. The O/Hf ratio present in the films was extracted using the conventional relative sensitivity factors for the two elements (Hf 4f: 2.221, O 1s: 0.711) and the peak areas. O/Hf ratio is found to be around 1.98 which is closely associated to the stoichiometry of the HfO_2 film.

HfO_2 films deposited on quartz substrates were characterized by UV-Vis-NIR spectroscopy. HfO_2 is a wide bandgap material of about 5.7 eV and almost transparent from near UV to far IR region. The transmission spectra of HfO_2 films deposited with various RF powers is

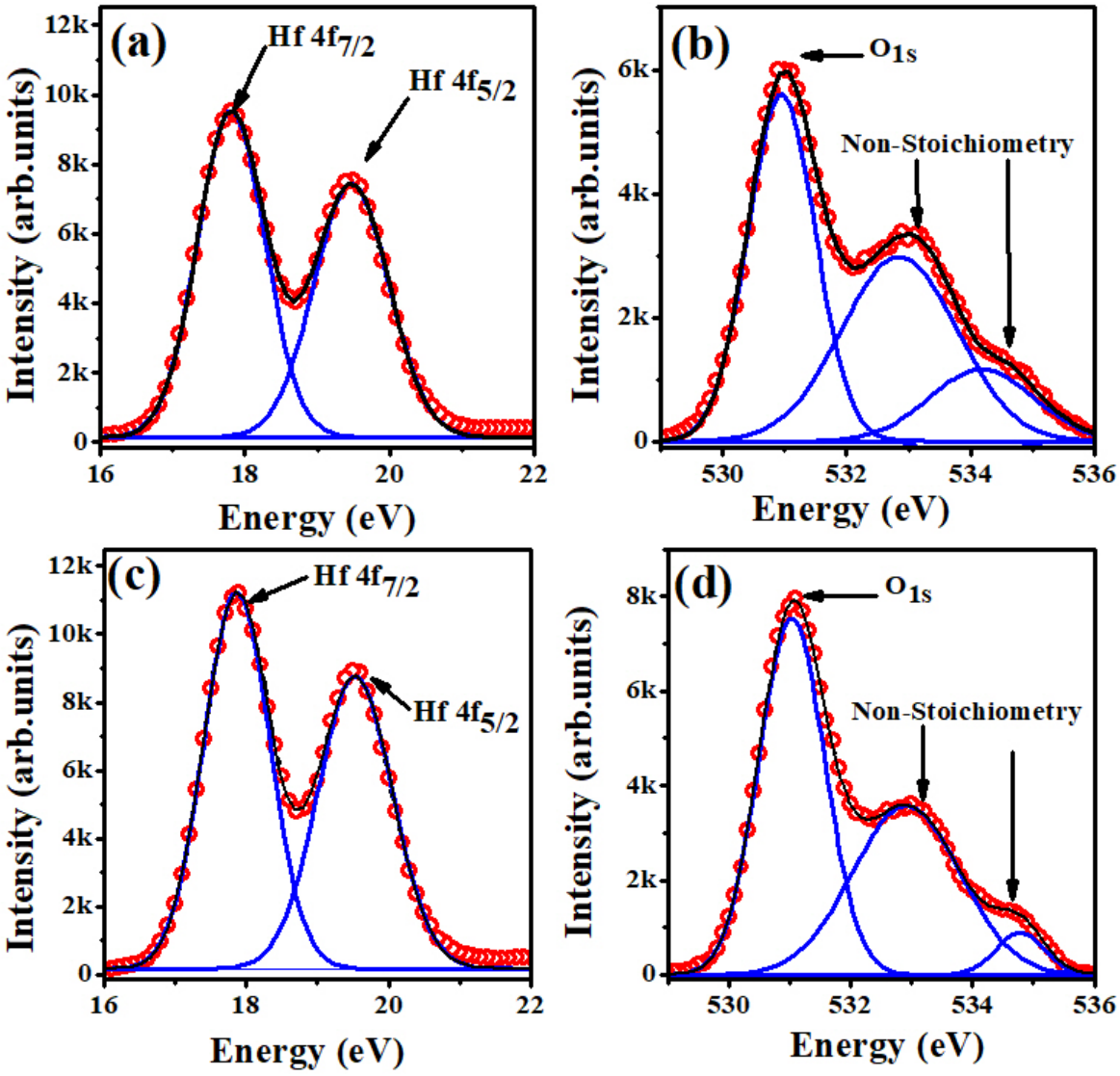

FIGURE 3.4: Core level XPS spectra of the HfO_2 films a), c) Hf 4f, and c), d) O 1s for 50 and 30 nm films respectively.

shown in *Figure* 3.5(a). The preliminary observation is that the transmittance exhibits overall 80 to 90 % of transparency. The bandgap of these thin films is estimated from transmission spectra (*Figure 3.5(b)*). The material HfO_2 falls under the indirect bandgap category, hence 'n' value may be considered as 0.5 [27]. The plots between (α.hν) 0.5 vs (Energy) are shown in *Figure* 3.5(b).

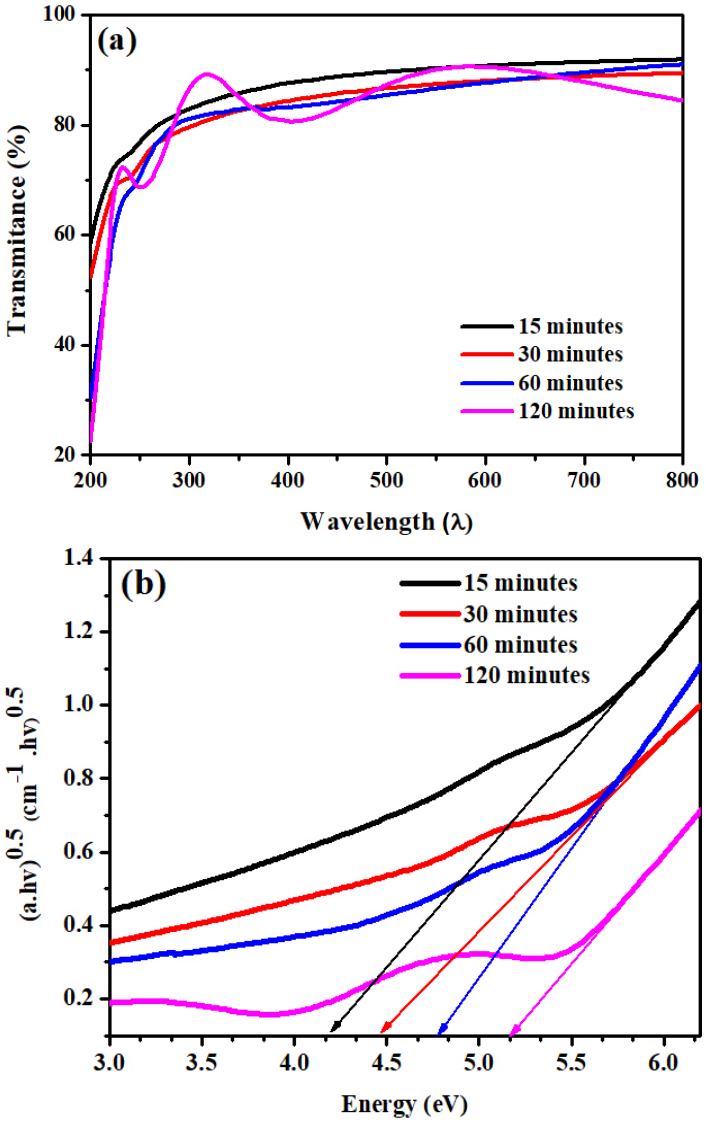

FIGURE 3.5: The optical properties HfO_2 films for different time duration of deposition a) transmission spectra and b)optical bandgap spectra.

Here, the extrapolated linear portion of the curve gives the bandgap value of the HfO_2 film. Hence, the bandgaps of these films are estimated to be 4.2 eV, 4.5 eV, 4.8 eV, and 5.2 eV respectively for 15, 30, 60, and 120 minutes duration of deposition. The variation of the bandgap values with variation of time duration of the deposition is an indication for the film improvement of the quality and growth kinematics with time [30]. The defects creation

and density variation in the films may cause the non-stochiometric films interns' variation in the band gap of the film. Here it is important to know that the nucleation and growth kinetics critically depend on the morphology and other properties of the substrates [6,31]. Hence the quantitative comparisons between films deposited on Si and quartz may not be appropriate. However, this study gives rough estimate of the possible bandgap and other optical properties.

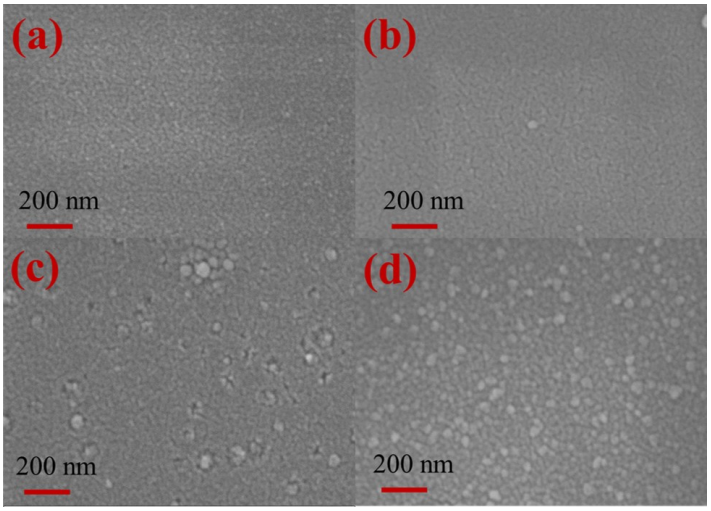

FIGURE 3.6: FESEM images of HfO_2 films deposited at different times: a) 15 min., b) 30 min., c) 60 min., d) 120 min. for Si substrates respectively.

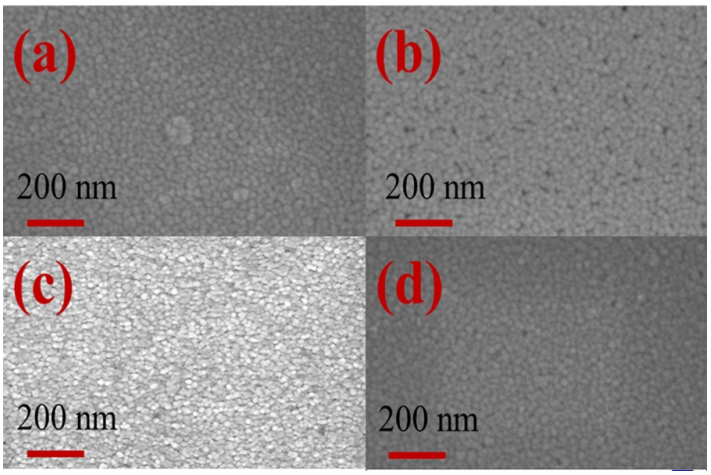

FIGURE 3.7: FESEM images of HfO_2 films deposited at different times: a) 15 min., b) 30 min., c) 60 min., d) 120 min. for Au/Si substrates respectively.

FESEM images for HfO_2 films grown with varying time of deposition are shown in *Figure* 3.6(Si substrate) *Figure* 3.7(Au/Si substrate). FESEM technique is very useful to understand the surface morphology, uniformity, grain size and quality of the film. As time of deposition increases; the surface morphology, the grains and particles agglomeration has been

found to increase. For 120 minutes deposition, the agglomeration of particles is uniformly distributed over the surface. The structure is possible at higher deposition rates and tends to localize surface free energy leading to higher nucleation rates [31]. In this connection, it is worth mentioning earlier reports [32], which are also in support of our present results [33]. As the deposition time increases the formation number of particles and film thickness also increases.

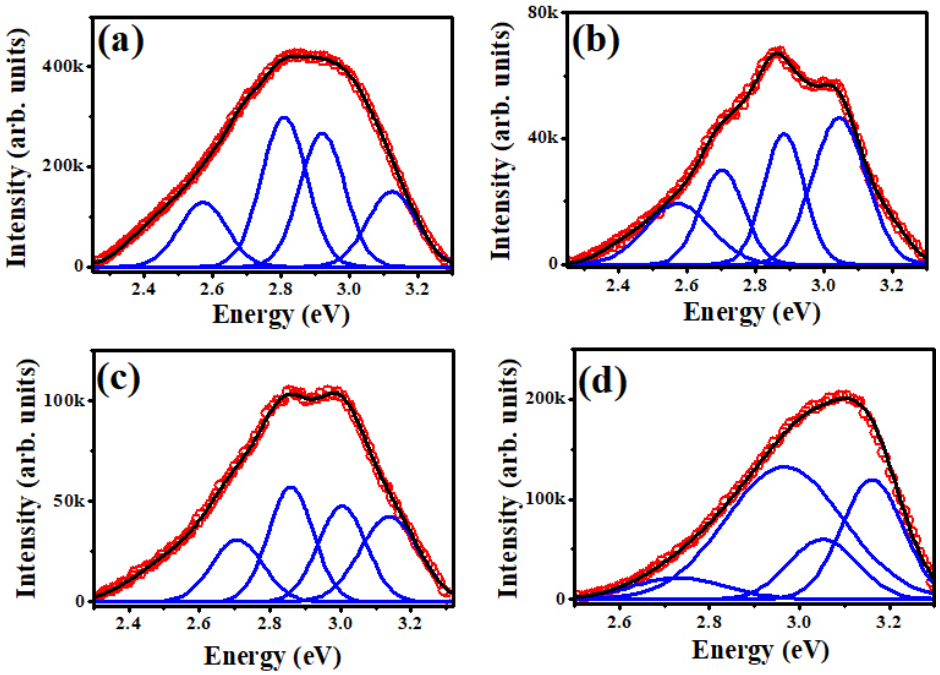

FIGURE 3.8: The Photoluminescence spectra HfO_2 films at different times: a) 15 min., b) 30 min., c) 60 min., d) 120 min. for Au/Si substrate.

The PL spectra of the HfO_2 films deposited at various durations are shown in *Figure* 3.8 The excitation energy was 3.5 eV which is less than the bandgap of the HfO_2 (5.7 eV). Hence the observed emission can be attributed to defect induced mid-bandgap states. A preliminary observation suggests that the intensity of the PL peak increases with duration of the deposition which might be due to increase of film thickness. The PL spectra are relatively broad and the emission is in the range of 2.2 eV to 3.4 eV. The film deposition duration of 15 minutes, 30 minutes and 60 minutes show almost similar kind of spectra except a minor change in intensity. For 120 minutes of duration, emission spectrum shows a shift in peak and positioned at 3.1 eV,indicating possible stress in these films All these spectra are deconvoluted using peak fitting program for peaks at various energy levels are shown in *Table* 3.3. Previous reports suggest that the observed PL is due to shallow and deep level oxygen related defect states or F-centers in HfO_2[34,35]. Hence,the defect peak

positioned at 2.7 eV corresponds to doubly charged oxygen vacancy ($V_O{}^{2+}$) and similarly at 2.9 eV defect peak corresponds to singly charged oxygen vacancy ($V_O{}^{+}$)[34,35].

TABLE 3.3: The details of peak energy for various times of RF sputtering deposition of the thin films.

Device name	Energy of peak position (eV)			
15	2.46	2.71	2.85	2.99
30	2.50	2.68	2.80	2.94
60	2.49	2.71	2.87	3.07
120	2.49	2.71	2.87	3.07

3.3.2 A study of different bottom electrodes for RRAM applications

HfO_2 based thin films of different thicknesses (30 and 50 nm) deposited on different metal surfaces (such as Au, Al, Pt and Au) have also been studied and presented in this section. The RF sputtering power was maintained at 60 W and the Ar gas inlet is set at 30 SCCM. The duration of the deposition was varied and the deposition was performed at room temperature. Film thickness was estimated and is consistent with that of the previous section. The FESEM measurement has been performed to characterize the surface morphological study, grain growth, porosity and micro structures of these deposited films.

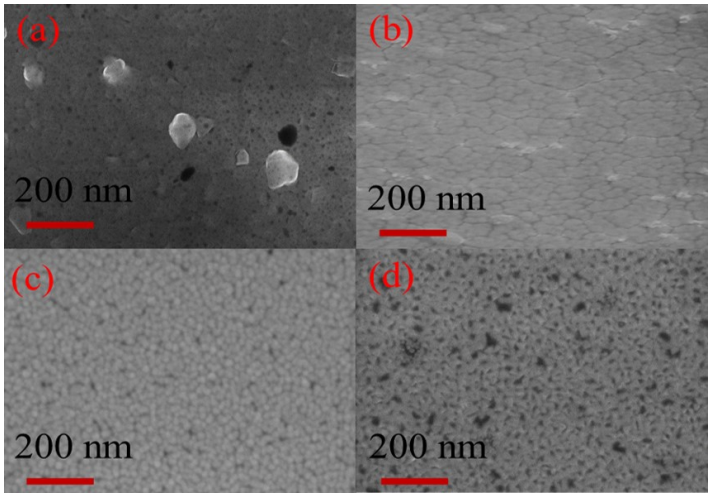

FIGURE 3.9: FESEM images of HfO_2 (50 nm)films deposited on metal substrates a) Al, b) Cu, c) Au and d) Pt substrates respectively.

HfO_2 film deposited on Pt metal seems to be of porous nature in this study. *Figure* 3.9 and *Figure* 3.10 shows the FESEM images of HfO_2 films deposited for 30 minutes and 60 minutes on different metal surfaces. Here, the films deposited on Cu metal substrates are clearly

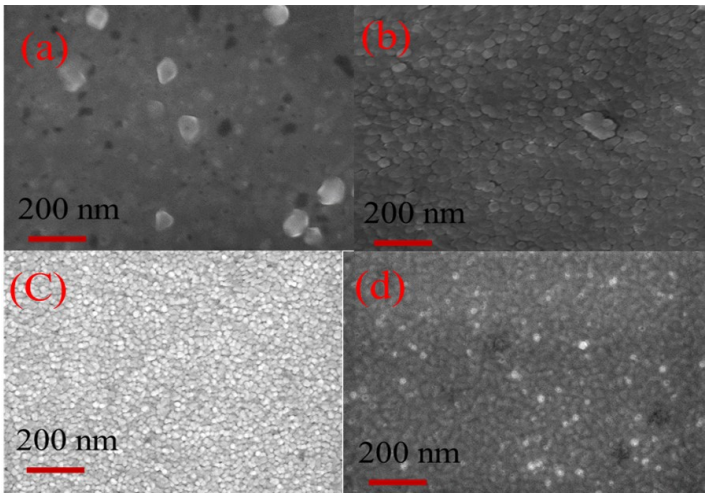

FIGURE 3.10: FESEM images of HfO_2 (30 nm)films deposited on metal substrates a) Al, b) Cu, c) Au and d) Pt substrates respectively.

showing the grain boundaries. Hence, this study provides very useful information on film growth and micro structure dependence on initial substrates. It is observed that as the duration of the deposition time increases the thickness is increased as expected. The porosity of the film's is less with more number of grains of smaller particles. The film uniformity is better and film is continuous as the duration of deposition increases.

The IV characteristics of the different bottom electrode material based MIM structured RRAM devices are shown in *Figure* 3.11. The comparison of parameters of these devices are shown in *Table* 3.4. The resistance ratio is found to be large for the Pt based devices whereas the number of switching cycles are more for the Au as bottom metal electrode. The large Resistance ratio may be expected due to the possibility of forming an interfacial layer between Pt bottom electrode and the insulating or active layer.

TABLE 3.4: A comparison of switching parameters for different bottom metal electrodes.

Bottom electrode	Au	Al	Pt
Set voltage (V)	2.0	2.5	2.0
Reset voltage (V)	-0.45	-1.5	-0.5
Reset current (mA)	10	80	3
Resistance ratio ($R_{Off}/_{On}$)	10^4	5 X 10^4	10^5

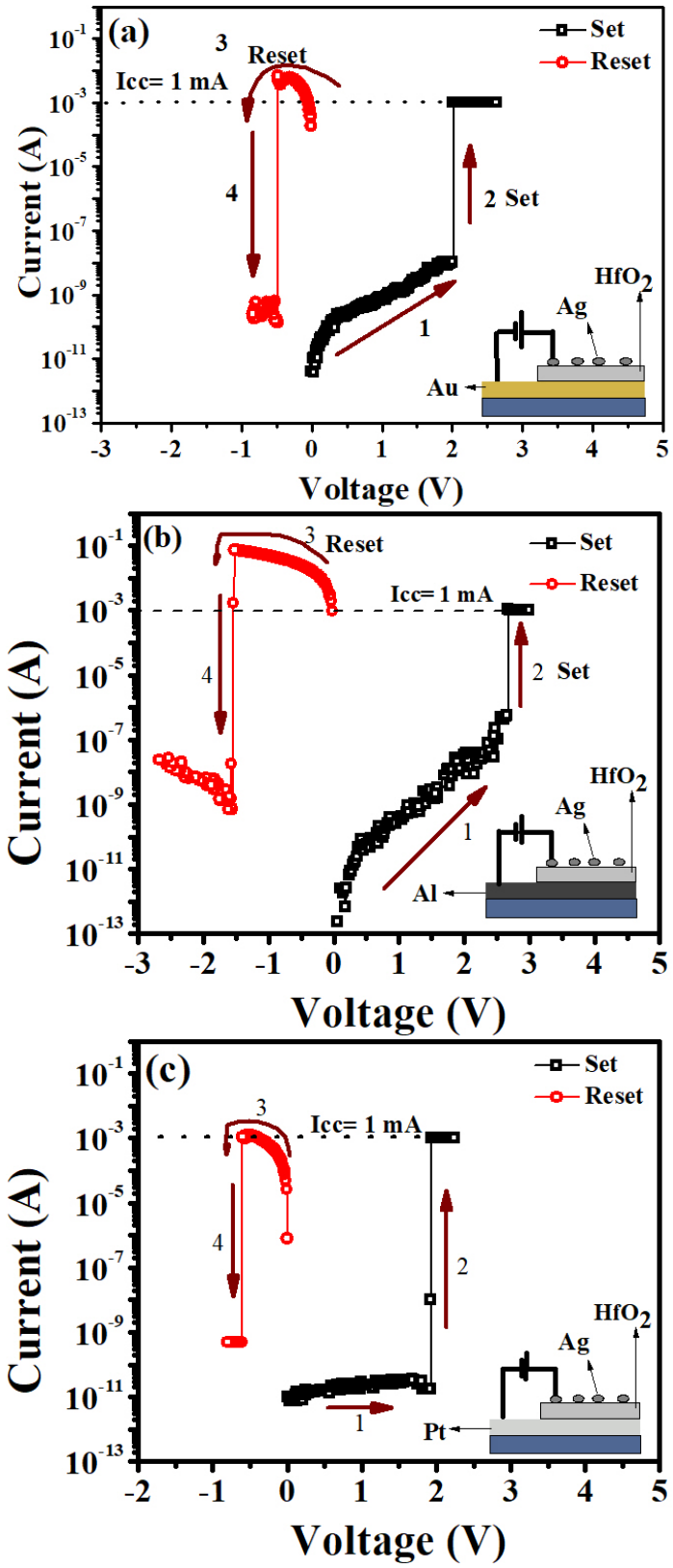

FIGURE 3.11: I-V characteristics of the a) Ag/HfO_2/Au, b) Ag/HfO_2/Al, and c) Ag/HfO_2/Pt MIM RRAM device.

3.3.3 Effects of annealing temperatures on the HfO_2 thin films

The surface morphological changes have been studied for samples subjected to thermal annealing treatment of the HfO_2/Si and HfO_2/Au/Si substrates. These annealing effects on surface and nucleation of the particles in HfO_2 films have been studied from temperatures ranging from 100 ^{o}C to 500 ^{o}C. *Figure* 3.12 shows the FE-SEM images of pristine and annealed HfO_2 films at different temperatures. The films deposited at room temperature and annealed up to 400 ^{o}C, unveil the amorphous nature as observed by XRD patterns. The micro structure and surface morphology of these films are exhibiting uniformity up to 400 ^{o}C. Furthermore, for increasing the annealing temperature the formation of grains like morphology is evident. The possibility of the HfO_2 molecules diffusion and mixing the surroundings there by making grains on surface of the film.

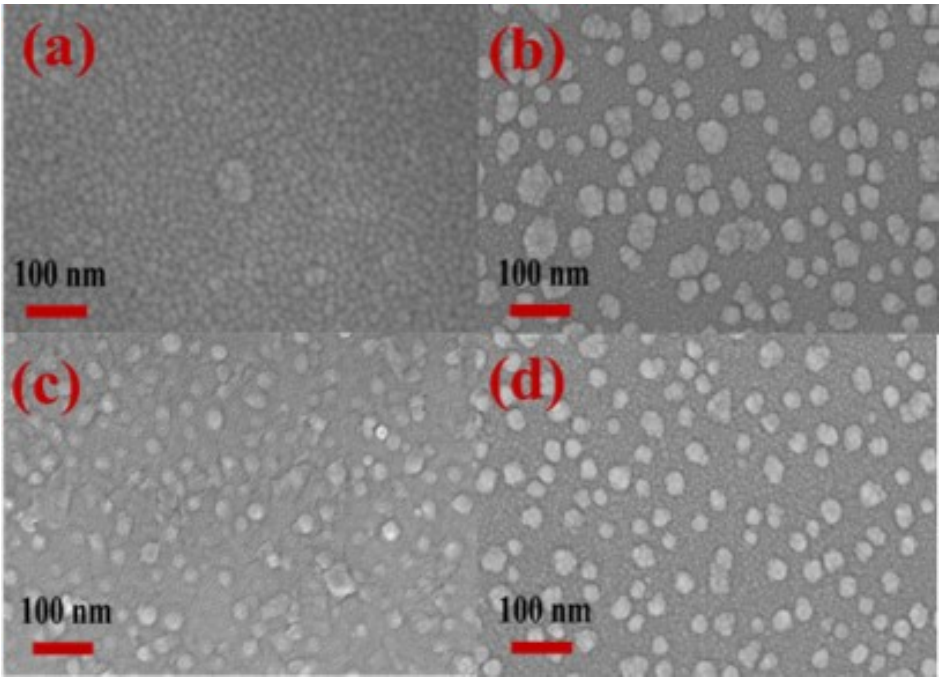

FIGURE 3.12: FESEM images of HfO_2 films deposited and annealed at different temperatures: a) P, b) 200 ^{o}C, c) 400 ^{o}C, and d) 500 ^{o}C.

The *Figure* 3.13 shows the GI-XRD pattern of pristine and the annealed HfO_2 thin films. Amorphous nature has been observed up to a temperature of 400 ^{o}C for these films. Upon increasing to 500 ^{o}C, the surface is found to show grains Growth/formation of grains and transforming to crystalline nature is observed in these samples. The obtained diffraction peaks matches with the standard JCPDS file [PDF No 06-0318] having monoclinic phase of $P_{21/c}$ space group. The observed peaks are found to be at angle of 2θ = 28.5^o, 31.71^o and 34.7^o

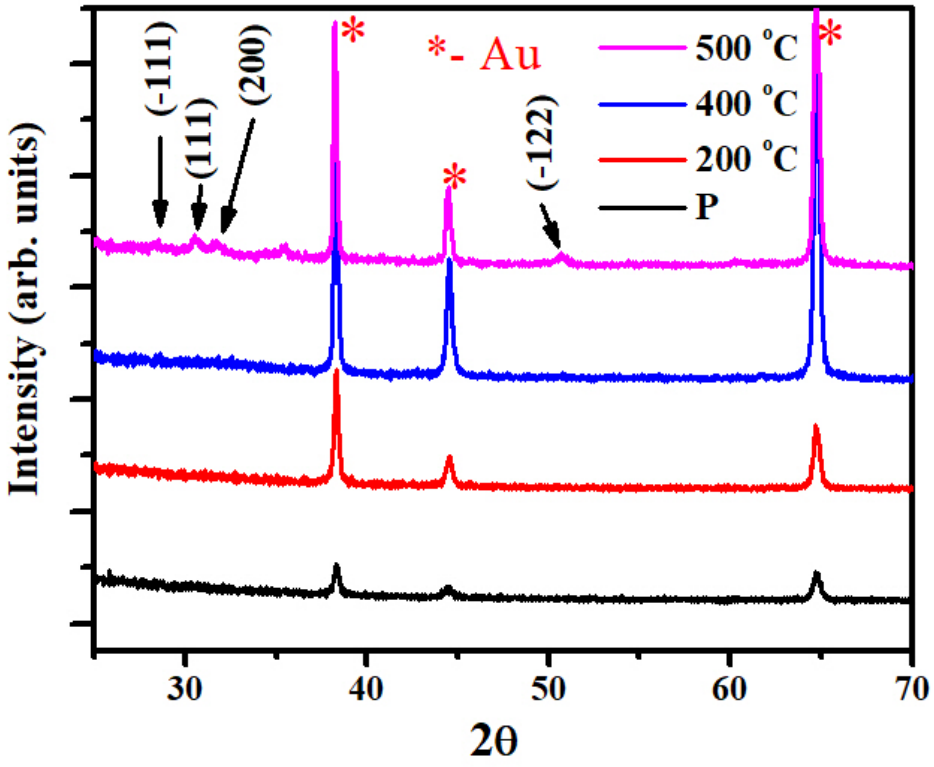

FIGURE 3.13: GI-XRD spectra of pristine and annealed of HfO_2/Au/Si thin films.

corresponding to the diffraction planes (-111), (111) and (200) respectively. At 500 ^oC the (-111) diffraction peak of monoclinic may be inferred as the starting point of phase formation and also in support of the low intensity shown. Although, the phase formation depends on the surface free energy at particular temperatures.

The RF sputtering based HfO_2 film deposition for 30 and 60 minutes are found to be the better optimized films. Furthermore, studies are carried on these parameters to fabricate the HfO_2 based RRAM devices. Annealing of the thin films showed the phase formation and enhancement in the uniformity of the films.

3.4 conclusions

The RF sputtering conditions are studied for growth and formation of microstructures of HfO_2 thin films. HfO_2 thin film growth and micro structures on different metal surfaces are investigated. Depending on the bottom metal surface combination, differences of surface structures were observed. Growth parameters, annealing conditions and metal electrodes

are optimized for fabricating HfO_2 based RRAM devices.These studies have provided useful information for performing the fabrication work presented in next chapters.

Bibliography

[1] J. C. ANDERSON Thin Solid Films, 12, 1-15,**(1972)**

[2] M. Birkholz; K.-E. Ehwald; D. Wolansky; I. Costina; C. Baristyran-Kaynak; M. Fröhlich; H. Beyer; A. Kapp; F. Lisdat Surf. Coat. Technol., 204, 2055–2059 **(2010)**.

[3] van der Kooi, C.J.; Elzenga, J.T.M.; Dijksterhuis, J.; Stavenga, D.G, Journal of the Royal Society Interface., 14, 0933 **(2016)**.

[4] MacLeod, H. Angus, Thin-Film Optical Filters (4th ed.), Taylor Francis, ISBN 978-1-4200-7302-7 **(2010)**.

[5] Sturgeon, W, Trans. Royal Society of Arts, Manufactures, Commerce. London. Cited in Miller, T.J.E 43, 37–52. **(2001)**.

[6] J A Venables, G D T Spiller and M Hanbucken,Nucleation and growth of thin films,Rep. Prog. Phys., Vol 47, pp 399-459, **(1984)**.

[7] Tavares, Janson Swanson, E.J Coulombe, Plasma Processes and Polymers, 5, 759 **(2008)**.

[8] Puurunen, Riikka L, J. Appl. Phys., 97, 121301 **(2005)**.

[9] Klein, L.C. and Garvey, G.J, J. of Non-Crystalline Solids, 38, 45-50 **(1980)**.

[10] Rahaman, M.N, and Boca Raton, Ceramic Processing, CRC Press., 15, 242–244, **(2007)**.

[11] Hanaor, DAH; Triani, Surface and coatings technology, 205, 3658–3664 **(2011)**.

[12] E. Fortunato, P. Barquinha, and R. Martins, Advanced Materials, 24, 2945–2986 **(2012)**.

[13] K. Ishii, Journal of Vacuum Science and Technology A, 7, 256–258 **(1989)**.

[14] He, Zhenping; Kretzschmar, Ilona, Langmuir., 28, 9915–9919 **(2012)**.

[15] I. Adesida, A. Mahajan, E. Andideh, M. Asif Khan, D. T. Olsen, and J. N. Kuznia, Appl. Phys. Lett., 63, 2777 **(1993)**.

[16] Selvakumar, N.; Barshilia, Harish C, Solar Energy Materials and Solar Cells, 98, 1–23 **(2012)**.

[17] Subodh K. Gautam, Abdelhak Chettah, R.G. Singh, Sunil Ojha, Fouran Singh, Nucl. Instr. Meth. Phys. Res. B, 379, 224–229 **(2016)**.

[18] J. Larkin, R. Henley, D. C. Bell, T. Cohen-Karni, J. K. Rosenstein, and M. Wanunu, ACS Nano., 7, 10121 **(2013)**.

[19] E. P. Simonenko, D. V. Sevast'yanov, N. P. Simonenko, V. G. Sevast'yanov and N. T. Kuznetsov, Russ. J. Inorg. Chem., 58, 1669–93 **(2013)**.

[20] M. Lee, N. Zine, A. Baraket, M. Zabala, F. Campabadal, R. Caruso, M. G. Trivella, N. J. Renaulta, and A. Errachid, Sens. Actuator B-Chem., 175, 201-207 **(2012)**.

[21] N. Manikanthababu, N. Arun, M. Dhanunjaya, S. V. S. Nageswara Rao, and A. P. Pathak, "Gamma irradiation-induced effects on the electrical properties of HfO_2-based MOS devices", Radiat. Eff. Defects Solids, vol. 171, no. 1–2, pp. 77–86, **(2016)**.

[22] M. Dhanunjaya, N. Manikanthababu, A. P. Pathak, and S. V. S. Nageswara Rao, "Effect of growth rate on crystallization of HfO_2 thin films deposited by RF magnetron sputtering",AIP Conference Proceedings 1731, 080071 **(2016)**.

[23] M. Mayer, SIMNRA: Simulation of RBS, ERD and NRA Spectra. <http://www.rzg.mpg.de/mam/>.

[24] R Swanepoel, J. Phps. E: Sci. Instrum., 16, **(1983)**.

[25] J. Tauc, R. Grigorovici, and A. Vancu, Phys. Status Solidi, 15, 627-637**(1996)**.

[26] Yi-Lung Cheng and Tian-Cih Bo, Surface and Coatings Technology, 260, 198–204 **(2014)**.

[27] Pankove, J. I. Optical Processes in Semiconductors; Courier Corporation, **(1971)**.

[28] Jie Ni, Qin Zhou, Zhengcao Li, and Zhengjun Zhang, "Oxygen defect induced photoluminescence of HfO_2 thin films", Jie,APPLIED PHYSICS LETTERS 93, 011905 **(2008)**.

[29] N. Manikanthababu, S. Vajandar, N. Arun, A. P. Pathak, K. Asokan, T. Osipowicz, T. Basu, and S. V. S. Nageswara Rao, "Electronic excitation induced defect dynamics in HfO_2 based MOS devices investigated by in-situ electrical measurement", Appl. Phys. Lett. 112, 131601 **(2018)**.

[30] Eunice S. M. Goh, T. P. Chen, C. Q. Sun and Y. C. Liu," Thickness effect on the band gap and optical properties of germanium thin films", Journal of Applied Physics 107, 024305 **(2010)**

[31] M Dhanunjaya, S A Khan, A P Pathak, D K Avasthi and S V S Nageswara Rao, J. Phys. D: Appl. Phys., 50, 505301 **(2017)**.

[32] M. L. Greena) and A. J. Allen, X. Li, J. Wang, and J. Ilavsky, A. Delabie, R. L. Puurunenb, and B. Brijs, "Nucleation of atomic-layer-deposited HfO_2 films, and evolution of their microstructure, studied by grazing incidence small angle x-ray scattering using synchrotron radiation", Appl. Phys. Lett. 88, 032907 **(2006)**

[33] N. Arun, K. V. Kumar, A. P. Pathak, D. K. Avasthi, and S. V. S. Nageswara Rao, “Hafnia-based resistive switching devices for non-volatile memory applications and effects of gamma irradiation on device performance”, Radiat. Eff. Defects Solids, vol. 173, no. 3–4, pp. 239–249, **(2018)**.

[34] T.V. Perevalov, V.Sh. Aliev, V. A. Gritsenko, A. A. Saraev, V.V. Kaichev, Micr. Eng., 109, 21–23 **(2003)**.

[35] D. R. Islamov, V. A. Gritsenko, T. V. Perevalov, ECS Trans., 69, 197-203, **(2005)**.

Chapter 4

Effects of gamma irradiation on the performance of HfO_2 based RRAM devices

4.1 Introduction

As discussed in previous chapters, the RRAM technology has attracted a wide range of applications in current and emerging digital and smart devices. Development and optimization of RRAMs using micro-electronic compatible materials are of great significance in the modern integrated circuit technology. Hence it is interesting to study the new alternate high-k dielectric material, HfO_2, as an insulating medium for RRAMs. Thin HfO_2 film can be sandwiched between two metal electrodes to form simple MIM structures[1,2]. Earlier studies have demonstrated that the RRAMs have certain advantages over conventional NVMs. The key features include the fast switching (ns), high memory density, high retention and endurance. These properties make RRAMs potential candidates to replace the floating gate and other conventional devices [3-5]. Radiation damage and reliability studies attain significance as these memory devices will eventually be used in deep space and other radiation environments like nuclear labs.

In this chapter, we present a study on the effects of gamma irradiation on the switching properties of HfO_2 based RRAM devices. It is well-known that the transistor-based memory devices are highly sensitive to radiation effects. The floating gate in Flash memory needs very accurate operating threshold voltage. Hence the radiation induced electron-hole pairs, carrier traps and broken bonds can severely affect the performance of these floating gate

devices[6,7]. The objective of this chapter is to study the radiation tolerance of HfO_2 based RRAM devices.

In RRAM devices, normally the switching takes place by the formation of conductive filamentary like structures, which is independent of the charge storage capacity in the oxide[6,7]. Hence, it is essential to study the influence of gamma radiation on the switching properties of (HfO_2) based RRAM devices[8-10]. The defects in the oxide [7,11] will affect the performance of the device by means of a change in the resistance value corresponding to HRS and LRS. Gamma irradiation can lead to an increase in the required compliance current during this set process.

This chapter presents a study on the effects of high dose gamma irradiation on the performance of HfO_2 based RRAM devices. Furthermore, the effects of bottom electrode material on the performance of RRAM devices have also been studied[8,13].

4.2 Fabrication and characterization of HfO_2 based RRAM

4.2.1 Sample cleaning and Device fabrication

Boron doped p-type Si (100) [1–10 Ω-cm resistivity] samples were cleaned by ultra-sonication in acetone and deionized water for 10 min. Then these samples were dipped in 10 % HF solution for 2 min to remove the native oxide. A 5 nm thin layer of Cr was deposited by e-beam evaporation at a vacuum level of 1×10^{-6} mbar. This layer gives more adhesiveness to Au and Si. 100 nm thick of Au and Pt as bottom electrodes were deposited by using the thermal evaporation. HfO_2 films of 30 nm and 50 nm of thickness were deposited by using RF sputtering technique through a mask of 2 mm in diameter. 100 nm thick Ag dots of 1 mm diameter were deposited on the surface of HfO_2 dots using a mask to fabricate the required MIM structures as RRAM cells. A schematic showing the structure of these devices is showing in figure 4.1 From these, the film with thickness 30 nm of HfO_2 devices were used to study the effects of the bottom electrode as well as gamma irradiation on their performance. The device structures, their experimental details, and the details of gamma irradiation are listed in *Table* 4.1.

RBS is employed to estimate the thickness and elemental composition of HfO_2 films deposited in the same run but on a Si substrate. 2 MeV He^+ beam has been used to characterize these samples at IUAC, New Delhi. RBS was performed at an annular geometry,

TABLE 4.1: The details of the different metal top electrode RRAM devices.

Sample ID	Device name	flim thickness (nm)	Doses (kGy)
D_1	$Ag/HfO_2/Au/Si$	50	12, 24 and 48
D_4	$Ag/HfO_2/Au/Si$	30	12, 24 and 48
D_5	$Ag/HfO_2/Pt/Si$	30	12, 24 and 48

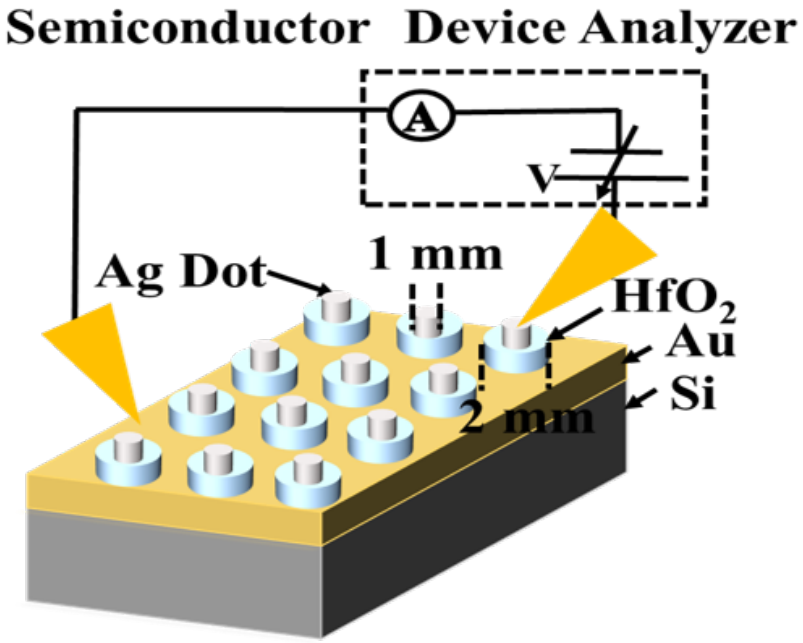

FIGURE 4.1: Electrical connections setup of $Ag/HfO_2/Au$ RRAM device.

with a scattering angle of θ = 166 ^{o}, an incident angle of α = 6 ^{o}, and an exit angle of β = 8 ^{o}. The calibration offset value is 86.102 keV and energy per channel is 0.9724 keV/ch. RBS simulations were performed using SIMNRA 7.02 version software [10]. The thickness of the samples was also estimated by using Ambios XP 200 Profilometer. Bruker D8 Discover X-ray diffraction facility equipped with Cu Kα (λ = 1.5405 Å) radiation was used for performing GI-XRD measurements. FESEM (model: Carl ZEISS, FEG, Ultra 55) was used for surface morphology imaging.

The samples were irradiated by ^{60}Co gamma (1.25 MeV) rays by using the 1200 Gamma chamber available at IUAC. Gamma irradiation was performed with a dose rate of 4.64 kGy/hr on these samples. The samples were irradiated at 24 kGy dose. The electrical measurements such as endurance cycling and retention time test were performed using an Agilent technologies B1500A semiconductor device analyser.

4.2.2 Film characterization

Figure 4.2 shows the RBS spectrum and the corresponding SIMNRA fit of HfO_2/Si sample. The peaks corresponding to Hf and O are clearly observed in the RBS spectrum. The width and area under the curve of these peaks are employed to make initial estimates of the thickness and the composition of these films. Then the SIMNRA simulation is performed by varying the film thickness and Hf and O ratio to fit to the experiment data. From these calculations of Hf and O ratio, it is confirmed that the thickness of films is around 50 nm by assuming the standard density of HfO_2 (9.68 g/cm^2). The thickness observed by RBS is in agreement with that estimated by Profilometer ($\sim$ 55 nm). The films ratios are found to be of oxygen rich (Hf:O :: 1:3.5) by RBS analysis. Generally Hf-rich films are expected as the sputtering rates are high for metals, particularly when the sputtering is performed in inert (Ar) ambiance. However the films seem to be oxygen rich and the excess oxygen may be located in void / interstitial spaces within the oxide / the interface.

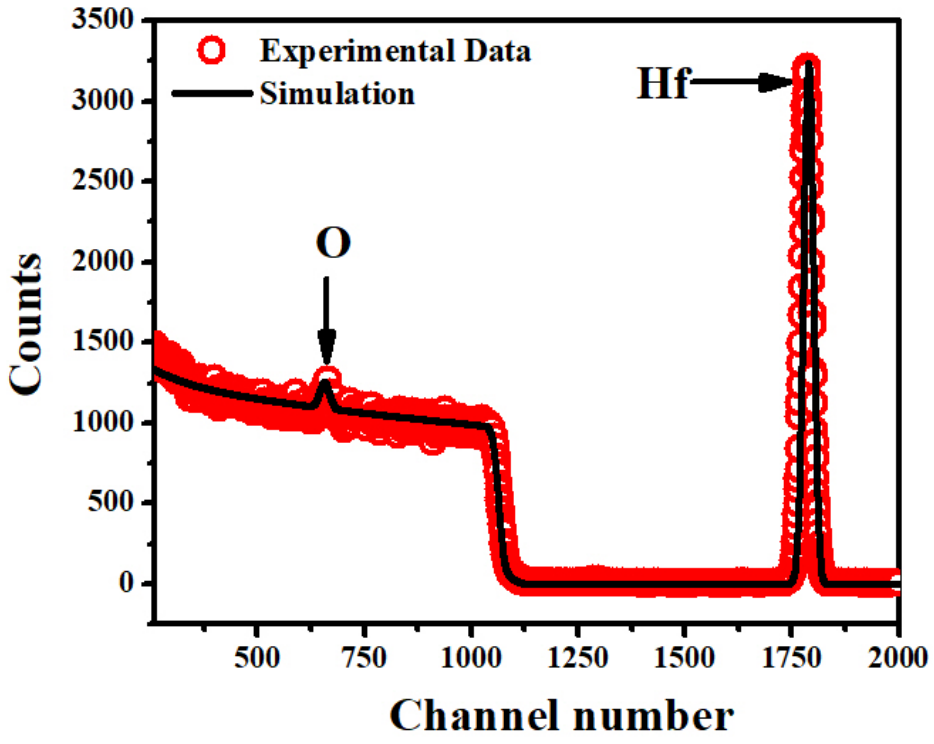

FIGURE 4.2: The RBS spectrum and the corresponding SIMNRA fit.

4.3 results and Discussions

4.3.1 I-V Characteristics of Ag/HfO_2/Au/Si (D_1) RRAM

MIM structures were fabricated using the as grown films in this study. The performance of these RRAM devices is investigated by studying the key parameters such as i) resistance ratio (the discrimination between the two resistive states), ii) retention time test (The durability of the same state) and iii) the endurance cycling (No of switching cycles). These properties are investigated by performing I-V measurements of the RRAM devices using an Agilent B1500A semiconductor device analyser. The basic and critical features of these MIM structures have been elucidated by examining several devices that are fabricated in the same and similar runs over longer times durations.

The Switching characteristics of the device are shown in *Figure* 4.3 (a). The devices are found to be of bi-polar type in nature. The set and reset occur at -1.12 V and the immediate reset $+$ 0.56 V, respectively. A compliance current of 5 mA is used for the set (i.e. from HRS to LRS) operation, termed as I_{CC} is used. This is to protect the device from the permanent breakdown. The HRS and LRS resistance values estimated to be 45 kΩ and 350 Ω respectively for these devices.

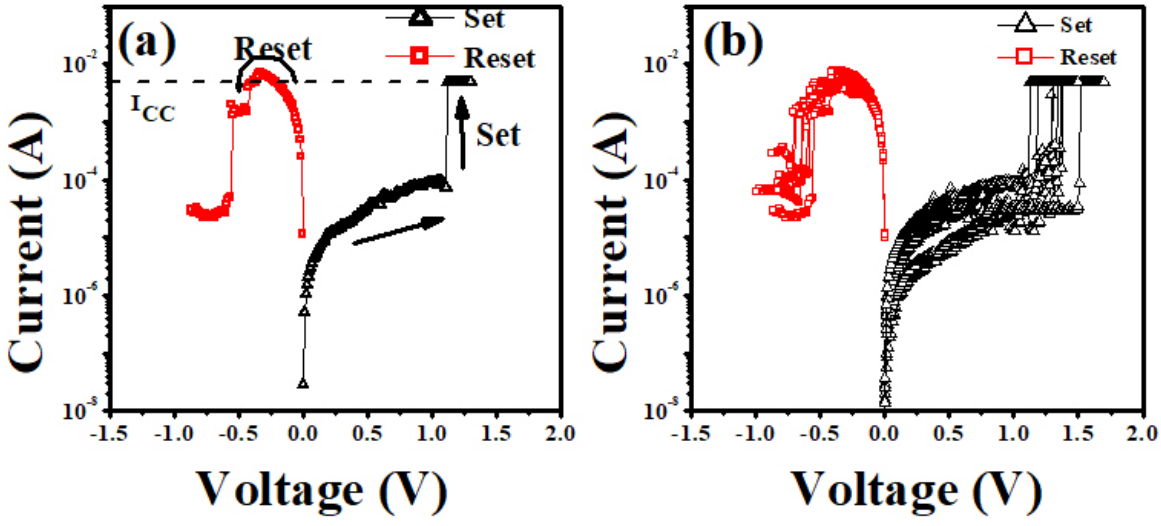

FIGURE 4.3: Switching characteristics of the Ag/HfO_2/Au device structure in (a) bipolar, (b) endurance cycling.

The leakage current across the MIM structures is measured as a function of voltage on electrodes in the range of 0 to 5 V. As expected, the device is initially in the high resistance state. At a certain voltage, the high resistance state is changed to low a resistance state

resulting in a sharp increase in the current (occurrence of soft breakdown) may be due to the formation of filament like structure that act as conducting paths between top and bottom electrodes [14-17]). This voltage is termed as Set voltage. A reverse voltage (0 to -5 V) is applied to get back its initial high resistance state and at this point it is termed as the Reset voltage.

The endurance cycling of $D_1(Ag/HfO_2/Au)$ device is shown in *Figure* 4.3 (b). The measurement is carried out for 50 cycles of set and reset voltages. In these RRAM devices, we have observed that the switching cycles are consistent during the endurance test when the reset voltages are in the range of 0.65 - 0.85 V and the set voltages are in the ranges of 1.0 – 1.5 V. The resistive switching in this device is mainly attributed to the formation of conductive filaments in the dielectric layer [14-17]. The distributive range of the set voltage values is expected to be due to the uncertainty and randomness of filamentary formation paths. The occurrence of the filaments need not follow the same path for all cycles (in all measurements). The double logarithm of the current and voltages characteristics of these devices are shown in *Figure* 4.4. Ohmic behaviour is observed in LR and at lower voltage region for the HR state and non-Ohmic nature at higher voltage regions.

BY performing a linear fitting, the slopes are estimated to be 0.96 and 1.05 for the LR and lower voltage of HR states respectively. The non-Ohmic region has a slope of 1.56 for higher voltages of HR state. Corresponding calculated dielectric constants are listed in *Table* 4.2. Further, at higher voltage regions, to calculate dielectric constants, the conduction mechanism models such as SC and PF (*Figure* 4.5) are employed.

TABLE 4.2: Slopes of curves in *Figure* 4.5 and their corresponding calculated dielectric constants of $Ag/HfO_2/Au$.

	Slope	
	SC	PF
slope	4.02	1.32
Dielectric constant	2.61	98

To realise the conduction mechanisms for the devices, the set (HRS) curves are fitted with SC (Ln (I) Vs $V^{0.5}$) and PF (Ln (I/V) Vs $V^{0.5}$) models. The below equations (4.1) and (4.2) are used to calculate the dielectric constants of the devices.

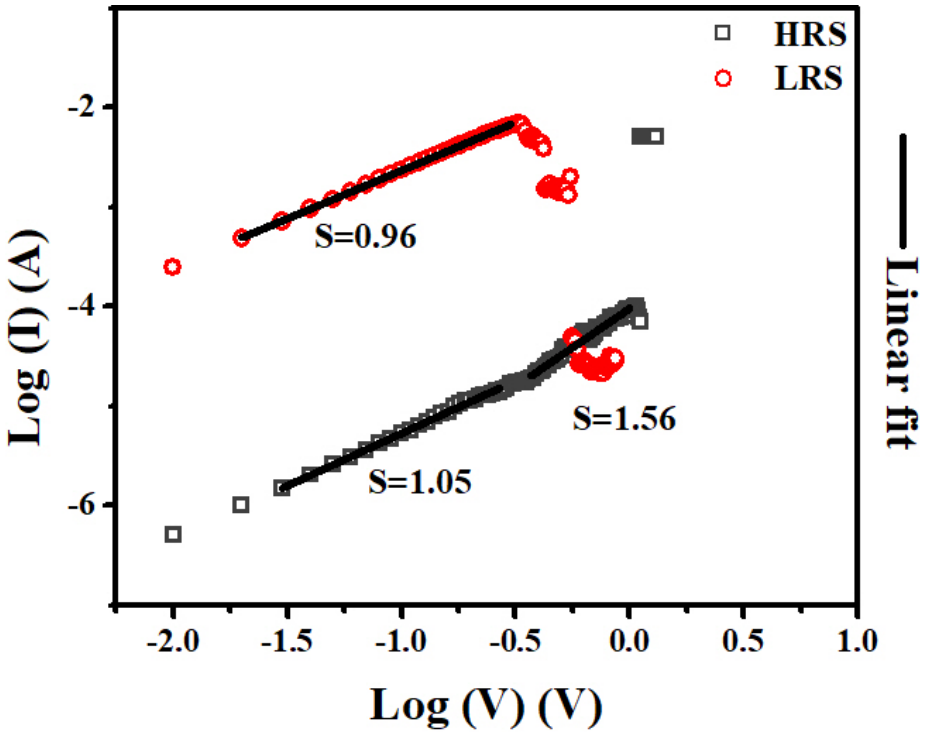

FIGURE 4.4: Log I vs Log V graphs of Bipolar switching characteristics of $Ag/HfO_2/Au$ device.

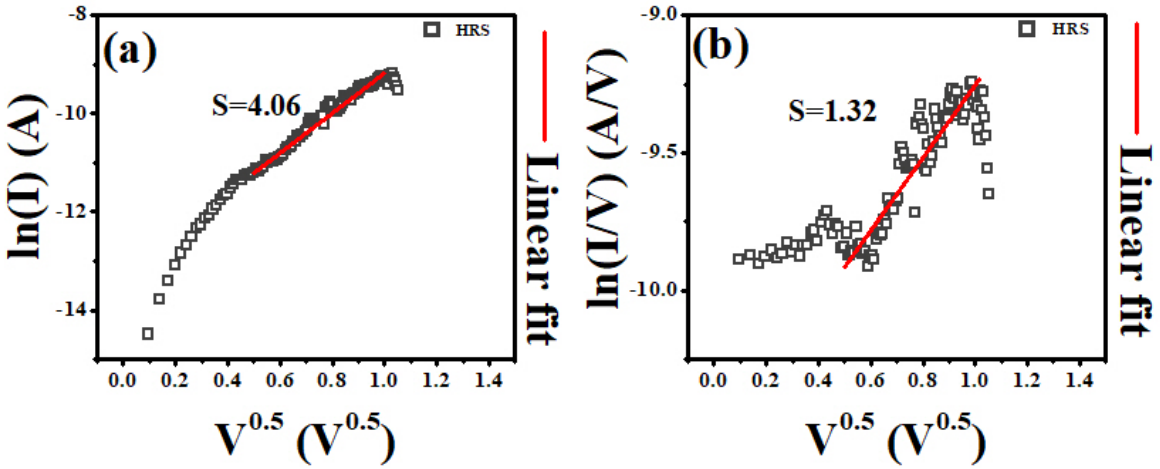

FIGURE 4.5: The switching characteristics fitted to (a) Schottky emission model and (b) Pool-Frenkel model for the bipolar switching of the $Ag/HfO_2/Au$ structure.

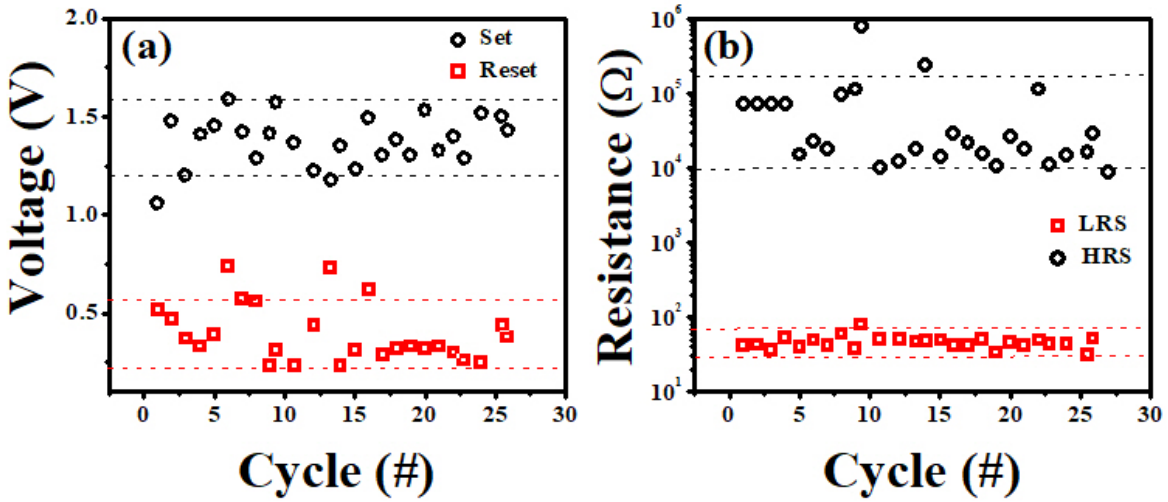

FIGURE 4.6: The stability characteristics of the $Ag/HfO_2/Au$ based devices on (a) set and reset voltages (b) resistance values in the LR and HR states.

$$\varepsilon_{SC} = \frac{q^3}{(KTS)^2 4\pi\varepsilon_0} \tag{4.1}$$

$$\varepsilon_{PF} = \frac{q^3}{(KTS')^2 4\pi\varepsilon_0} \tag{4.2}$$

Where, q is electronic charge (1.60 x10^{-19}) Coulombs, k is Boltzmann constant (1.38 x 10^{-23} J/K), T is temperature (K), ε_0 is permittivity of free space (F/m), d is thickness of the film, and S, S' are slopes of the curves. Similarly, the ε_{SC} and ε_{PL} is relative permittivity of Schottky, Pool-Frenkel conduction respectively.

The above, *Figure* 4.6 (a) reveals the variation in set, reset voltages and, (b) resistance values for LRS, HRS over various switching cycles. It is observed that the range of distribution in set and reset voltages vary similarly, in HRS for the device.

4.3.2 Effects of gamma irradiation on the switching properties of RRAM devices

A set of fabricated devices were subjected to gamma irradiation at a high doses of 12 kGy and 24 kGy, and 48 kGy at a constant dose rate of $\sim$ 4.64 kGy/hr at room temperature. I-V characterization was performed after exposing the devices to gamma radiation.

Gamma radiation generates Compton scattered electrons and the electron-hole (e-h) pairs in dielectric materials which can further create or mobilize the defects in materials.

The number of energetic electrons and secondary e-h pairs are known to be directly proportional to the energy deposited in material by gamma irradiation [7,18]. It is evident from the RRAM devices that the creation of defects effectively gives cumulative effects on device performance. The observed wide variation in set voltage clearly indicates the randomness in the selection filament paths that take the device from HRS to LRS and vice-versa. The randomness in the filament formation process has significantly increased due to gamma irradiation. This is evident by the observed increase in the ranges of set and reset voltage distributions. Oxygen vacancies (O^{2-}) are known to be charged in different states. Hence the motion of oxygen vacancies under electric fields can significantly influence the formation of conducting filaments in oxide. Similarly, the electro migration of interstitial metal ions (like Hf) and the metal ions from electrodes in disordered medium can also influence the filament formation process. Gamma irradiation is expected to produce more oxygen vacancies which can cause the observed increase in the randomness of filaments formation.

This can result in an undesirable broad range in the distribution of set and reset voltages. This is an important feature that needs special attention in oxide based MIM devices. However, the controlled production of vacancies at precise depth / location (like by ion irradiation) has an advantage in reducing the forming voltage [6]. At the same time, the random production of vacancies as a result of radiation damage has adverse effects. Hence it is important to understand these effects to improve the reliability as well as the switching properties of these new class of memory devices. The observed decrease in HRS can be attributed to the trapped charges and vacancies induced inside the dielectric thin films by gamma irradiation. Therefore, we can predict that the oxygen vacancy related defects are dominant and play a major role in the switching mechanism which can be inferred from the retention test that the resistance state is un-stable and not consistent with the irradiated device. Further the gamma irradiation can cause annealing effects in the dielectric material [19] which may lead to phase transformations in HfO_2 [20]. The performance of these devices is observed to be adversely affected by the gamma irradiation. The observed difference in set and reset voltages is very significant. However, the reset voltages did not exhibit much variation when the devices are subjected to 24 kGy.

At the same time a significant variation is observed in case of the set voltage curves. From this, we can predict that the gamma irradiation affects the switching characteristics of the device and this uncertainty of state value will undoubtedly corrupt the data stored

in it. Hence it is very important to perform more detailed studies in this direction to study and improve the radiation tolerance levels of these devices. It is interesting to note that the fluctuations in the retention of HRS state in gamma irradiated samples are much less when compared to that of the pristine samples. The set voltages variation for the endurance cycling is ranged from 0.5 to 2.0 V for 24 kGy dose. A detailed comparison for switching characteristics performance of pristine, 12 kGy and 24 kGy gamma irradiated RRAM devices are given in *Table* 4.3.

TABLE 4.3: The Switching characteristics for pre and post gamma irradiated $Ag/HfO_2/Au$ (D_1) devices.

2*Switching parameters	pre-irradiation	post-irradiation		
	As deposited	12 kGy	24 kGy	48 kGy
Set voltage (V)	1.0 to 1.5	1.0 to 1.8	0.5 to 2.0	Sho
Reset voltage (V)	-1.0 to -1.5	-0.65 to 1.0	-0.5 to -1.25	r
R_{on} resistance ()	30	50 to 100	10 to 100	t
R_{off} resistance ()	100 k to 10 M	1 M	2 M	e
resistance Ratio ($R_{off}/_{on}$)	3 X 10^3	10^4	2 X 10^2	d

In this study of the gamma irradiation on the RRAMs, we observe that 24 kGy dose has significant influence and leads to deteriorating effects on the device performance. The Resistance ratio value of these devices is also low and hence it is difficult to discriminate the HR and LR states of the device.

All these devices are measured for a time of 10^4 s by applying a read pulse of 0.1 V at equal intervals of 60 s. The probing voltage is chosen to be low so that it will not change the state of the device. This is meant for estimating the resistance state of the device by measuring current for an applied voltage. Each resistance (LR and HR) state is measured independently and the data is shown in *Figure* 4.7. The retention time data shown in fig for these devices is consistent with those reported in literature [21]. These measurements clearly confirm the formation of good quality, reliable and reproducible RRAM devices prior to irradiation. These devices were then subjected to Gamma irradiation to explore the effects of defects on their performance and to examine their reliability.

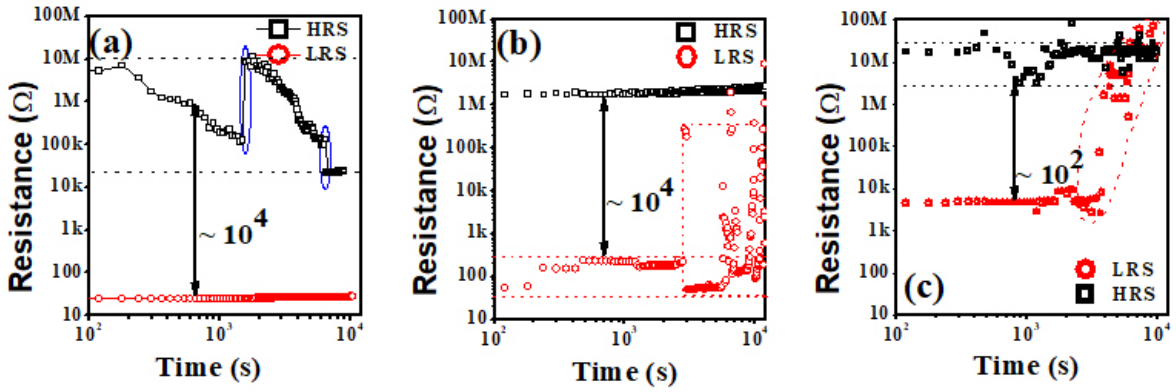

FIGURE 4.7: LRS and HRS resistance states of retention test for a) before, b) after 12 kGy, and c) 24 kGy gamma irradiation doses of D_1 devices.

4.4 Effects of bottom electrode and gamma irradiation on the switching properties of RRAM devices

4.4.1 I-V Characteristics of pristine devices

As mentioned earlier, 30 nm films were deposited to fabricate two sets of devices, namely 1) Ag/HfO_2(30 nm)/Au/Si (D_4) and 2) Ag/HfO_2(30 nm)/Pt/Si (D_5) which were fabricated to study the influence of electrode material (Au or Pt) on the switching parameters and radiation response of HfO_2 based RRAM devices. The endurance cycling and the retention time measurements have been performed and compared. *Figure* 4.8 shows the set and reset cycle of un-irradiated (0 kGy) (a) D_4 and (b) D_5 devices respectively.

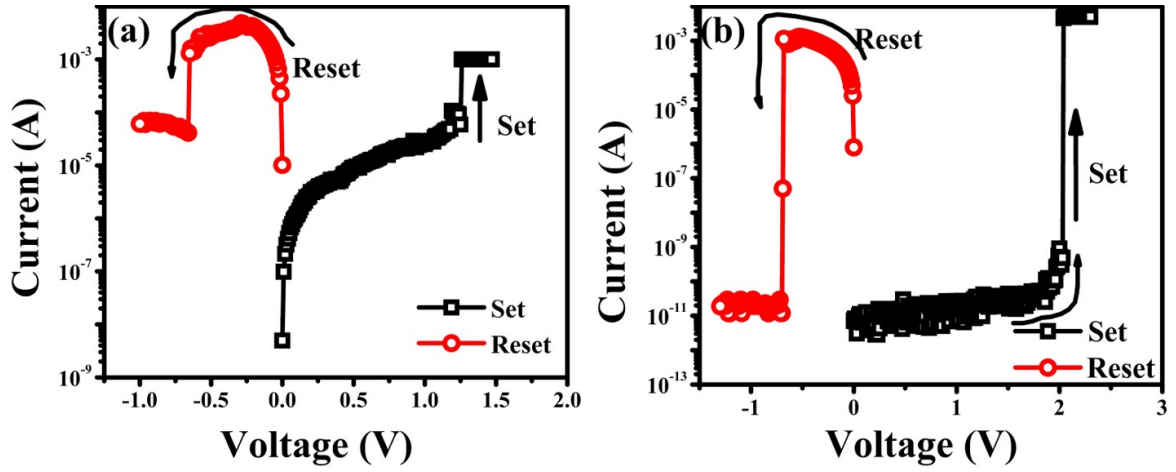

FIGURE 4.8: I-V curves of Set and Reset for both (a) D_4 (b) D_5 devices.

The switching mechanisms can be understood by invoking the concept of filaments formation and conduction in HfO_2 matrix. The filament formation may be led by the migration

of charged oxygen vacancies, to form conductive paths between top and bottom electrodes through the insulating HfO_2 layer [14,22]. For D_4 device the distribution of set and reset voltages range from 1.25 to 1.5 V and from -0.5 to -0.75 respectively. Similarly, for D_5 device set voltages are in the range of 2.0 to 2.25 and reset voltages are in the range of - 0.75 to -1.5 V.

It is observed that in case of Pt as bottom electrode devices, the switching takes place at higher voltages. The HfO_2 thin layer grown on Pt is expected to offer higher electrical resistance due to possible oxidation at the interface (formation of Pt-O bonds) [16,23-24]. Whereas in the case of Au, the oxidation at interface is not expected. If the switching mechanism is dominated by migration of Ag ions from the top electrode then both devices would have behaved in similar manner. We have employed different metal electrodes to study the significance of metal ion migration from top electrode to active medium in HfO_2 based devices. The study indicates that the effect of metal ion migration from the top electrode is not very significant in determining the switching properties of these devices. Rather the bottom electrode and possible oxidation at insulator /metal interface are likely to play critical roles in this respect. It is important to note that the effects of oxidation at top electrode are expected to be the same for both sets of devices.

The similar behaviour is observed in the retention time tests as well. The results of the retention time tests of Pristine RRAM devices D_4 and D_5 are shown in *Figure* 4.9 respectively. The resistance ratio (R_{Off}/R_{On}) of devices with Pt as bottom electrode is observed to be six orders of magnitude greater than that of the device with Au as bottom electrode.

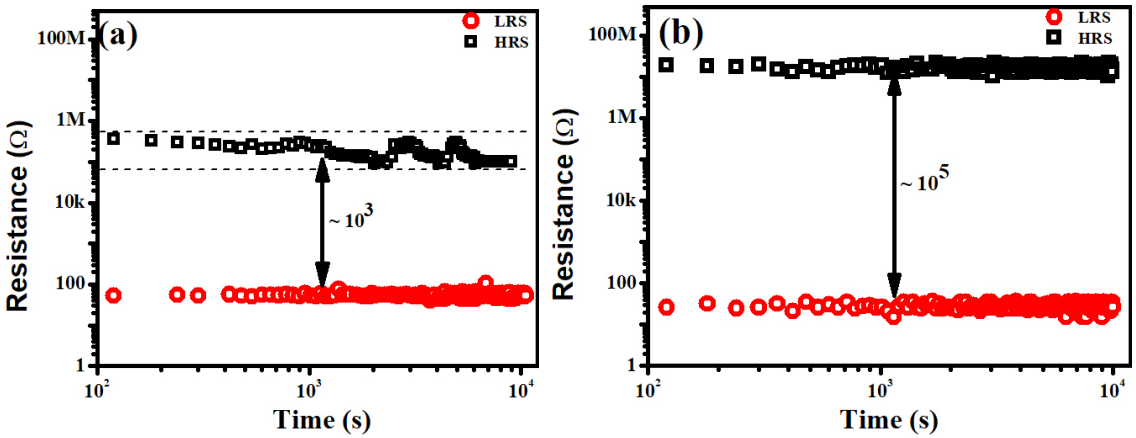

FIGURE 4.9: Retention time of both (a) D_4, and (b) D_5 devices.

From the retention test, Resistance ratio of the Pt based device is two orders higher than

that of the Au based device. It is clearly envisaged that the set and reset states can easily be differentiated and the difference is more pronounced in case of Pt based devices. Hence these studies clearly indicate that the influence of the bottom electrode has a critical role on the switching properties of RRAM devices.

4.4.2 Effects of gamma irradiation on stability of RRAMs for data retention

Some of these RRAM devices from each set were irradiated by gamma rays. In the same manner as earlier studies, different doses (namely 12, 24 and 48 kGy) were used for irradiation. For all these devices, switching parameters such as endurance and retention time tests were performed before and after irradiation. The switching performance parameters of D_4 are given in *Table* 4.4 pre and post gamma irradiation. We have observed an increase in HRS resistance and non-uniform switching behaviour after a dose of 12 kGy. The possible irradiation induced annealing effects at lower doses may reduce the trap states within the bandgap of oxide material and can lead to the observed reduction in the leakage currents [8,25].

The reduction in the leakage currents and the consequent increase in the HRS values may indicate the improvement of device performance due to low dose gamma irradiation. However, the higher doses lead to the deterioration of the device performance. Distortion and non-stability of the switching behaviour and retention time are observed at an increased dose level that is twice the initial one (i.e 24 kGy). The devices are totally shorted at a dose of 48 kGy and no switching behaviour is observed at all in these devices. This implies that the large number of vacancies produced in the oxide formed permanent conducting filaments between the metal electrodes. It is important to note and/or to improve this limit before employing these devices in radiation environments. In *Figure* 4.10 and *Figure* 4.11, the cumulative probability distributions of R_{LRS} and R_{HRS} of D_4 devices for pre and post irradiation. The 24 kGy dose has created more damage and destroyed the switching nature of the devices. The stability of the HRS is greatly affected and only $\sim$ 40 % of resistance values of HRS are observed in the data of retention tests. The gamma irradiation creates many traps and oxygen vacancies, thereby increasing the number and randomness of filaments leading to the observed instability and even the permanent damage (short) at higher doses. The R_{HRS} decrease can be attributed to the increase in the oxygen vacancies [26-28].

The present study is focused on the influence of the electrode material on the switching performance and the radiation response of these devices. Gamma irradiation induced annealing effects are observed at lower dose in this study. Hence,the study is extended to the devices D_5.

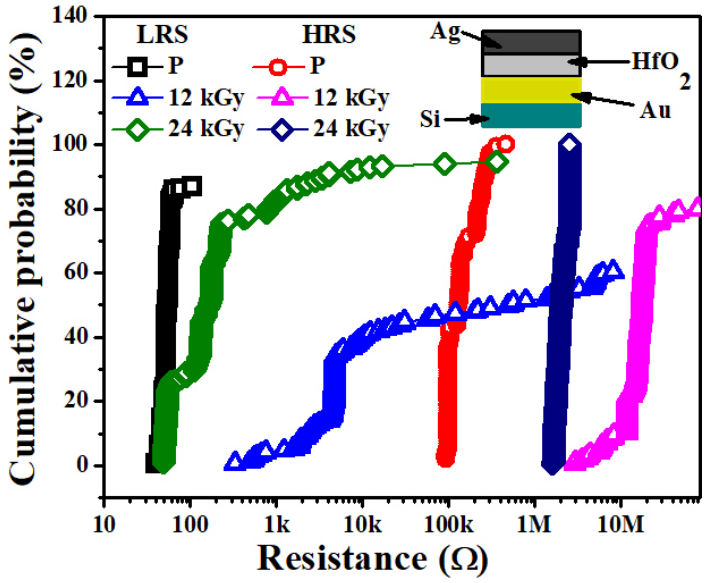

FIGURE 4.10: CDF of LRS and HRS resistance of D_4 devices.

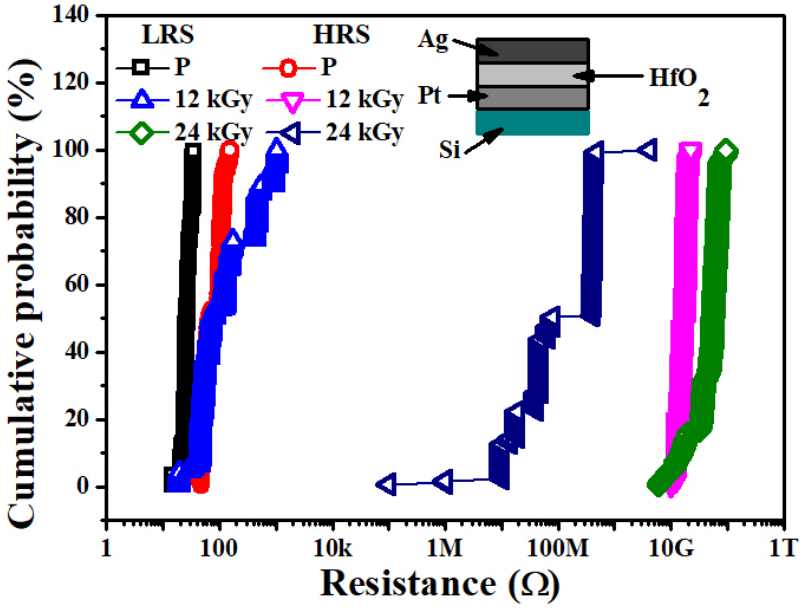

FIGURE 4.11: CDF of LRS and HRS resistance of D_5 devices.

The switching performance parameters of these D_5 are given in *Table* 4.5 for pre and post gamma irradiation. As discussed above, for 12 kGy dose the devices show annealing effects, thereby leading to an increase in R_{RHS} and set voltages as well. The switching parameters of

both sets of devices (D_4 and D_5) are almost same after gamma irradiation although their initial values are different, indicating that the Pt based devices are more susceptible to gamma irradiation. The randomness and fluctuations or non-uniform switching in RRAM devices after gamma irradiation are seen in irradiated devices. The randomness in switching may be attributed to the production of higher density of charged oxygen vacancies which are mobile under the influence of electric field. The conduction paths or filaments formation is affected and altered. Hence, it is important to understand and elucidate gamma irradiation effects on RRAM devices.

TABLE 4.4: The Switching characteristics for pre and post gamma irradiated $Ag/HfO_2/Au$ (D_4) devices.

Switching parameters	pre-irradiation	post-irradiation		
	As deposited	12 kGy	24 kGy	48 kGy
Set voltage (V)	1.25 to 1.5	1.0 to 3.0	1.0 to 3.5	Sho
Reset voltage (V)	-0.5 to -0.75	-0.5 to -2.0	-0.5 to 2.0	r
R_{on} resistance (Ω)	50	10 k	2 k	t
R_{off} resistance (Ω)	500 k	10 M	2 M	e
resistance Ratio ($R_{off}/_{on}$)	1 X 10^4	10^3	10^3	d

TABLE 4.5: The Switching characteristics for pre and post gamma irradiated $Ag/HfO_2/Pt$ (D_5) devices.

Switching parameters	pre-irradiation	post-irradiation		
	As deposited	12 kGy	24 kGy	48 kGy
Set voltage (V)	1.8 to 2.2	1.0 to 2.2	1.0 to 3.0	Sho
Reset voltage (V)	-0.75 to -1.5	-1.0 to - 3.0	-0.5 to 2.0	r
R_{on} resistance (Ω)	40	100 to 10k	100 to 50 k	t
R_{off} resistance (Ω)	100 G	1 to 100 M	1 M to 1 G	e
resistance Ratio ($R_{off}/_{on}$)	25 X 10^9	10^4	10^4	d

The effects of gamma irradiation at a higher dose (of 24 kGy) on the device parameters are compared and analysed. The devices almost lost their significance after 24 kGy irradiation and are completely shorted at 48 kGy. It is noticed that there is a decrease in R_{HRS} for Pt based devices after gamma irradiation. Earlier studies in literature also showed similar analyses in TiO_2 and WO_x based devices [29,30].

Similar effects have been observed in the case of the HfO_2 films as well. In *Figure* 4.12, the resistance degradation of RRAM devices after 24 kGy dose in HRS at 0.5 V is shown for

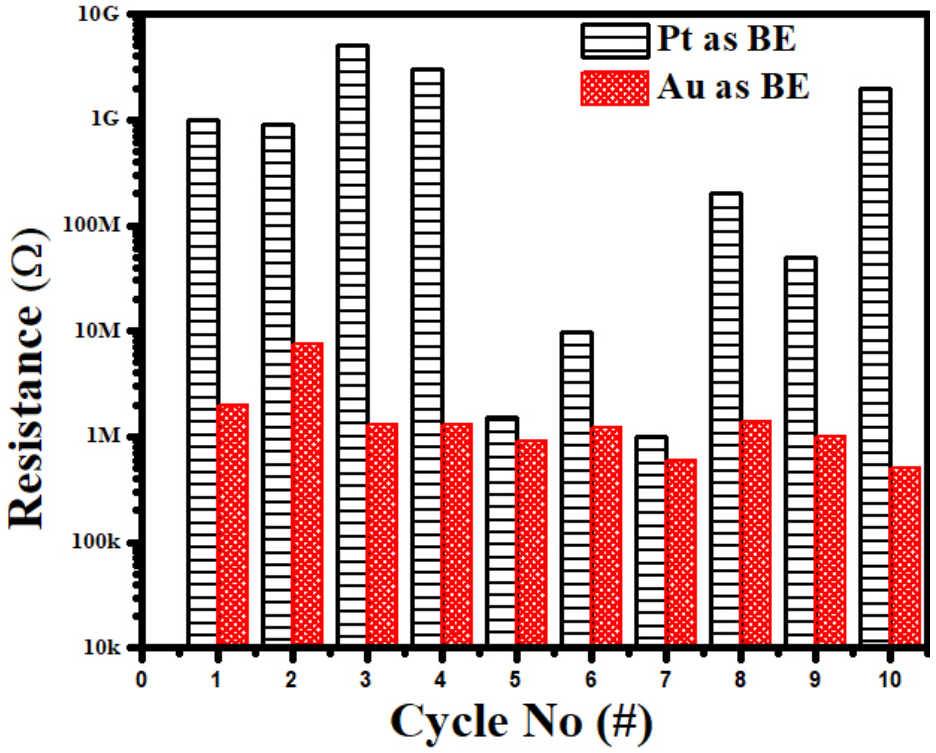

FIGURE 4.12: The resistance degradation of RRAM devices after 24 kGy dose at 0.5 V

both the devices. Here, it is found that the Resistance in HR state decreases after few cycles and thereby increases the randomness and fluctuations, which resulted in non-uniform switching nature in Pt based devices[30]. It is not so well known that due to the gamma irradiation Hf-O bonds break inside the material, thereby creating oxygen interstitials and oxygen vacancies [31]. For even higher dose of 48 kGy radiation, devices totally fail in their performance characteristics. All the devices are found to be in shorted condition. The trapped charges cause higher leakage current and may lead to the failure of the devices.

Gamma radiation generates the electron-hole pairs in materials. The number of these pairs are directly proportional to the energy deposited in material by gamma irradiation [6,7,30]. Electrons leave the insulator due to higher mobility than the holes leading to less resistance with higher radiation dose. The fraction of holes is captured in trapping sites thus forming positive radiation induced charge in the insulator. Thus decrease in HRS can be attributed to the radiation induced trap charges inside the dielectric thin film. This effectively reduces the memory window which indicates cumulative device degradation after gamma irradiation. However, the 24 kGy irradiated samples failed to show the pronounced resistive switching and did not obey the SCLC mechanism. This may be due to the high

radiation dose exposure resulting in a considerable amount of lattice defects that cause the rupture of bonds. It has been reported that such defects may introduce oxygen vacancies, interstitial and substitutional defects within the crystal lattice creating a barrier in current filament formation for resistive switching mechanisms[31].

4.5 conclusions

HfO_2 films have been deposited by RF sputtering technique. The following device structure were tested for switching performance $Au/HfO_2/Au$ (D_1), $Au/HfO_2/Au$ (D_4) and $Au/HfO_2/Pt$ (D_5). All the RRAM devices exhibited resistive switching behavior. The set voltage, reset voltages variation, endurance cycling and retention time differences have been observed for the bottom as Pt with Au. The effects of gamma irradiation on the performance of all these devices have been studied in detail. A low dose treatment has improved the device performance and the devices are damaged when subjected to higher doses [13].

Bibliography

[1] 33. R. Waser, R. Dittmann, C. Staikov, K. Szot, "Redox-based resistive switching memories nanoionic mechanisms, prospects, and challenges", Adv. Mater. 21, 2632–2663 **(2009)**. h ttps://doi.org/10.1002/adma.200900375

[2] 6. M. Lanza, "A review on resistive switching in high-k dielectrics: a nanoscale point of view using conductive atomic force microscope", Materials (Basel) 7(3), 2155–2182 **(2014)**. http s://doi.org/10.3390/ma7032155

[3] Yao shuai, Shengqiang zhou, Danilo bürger, Manfred helm, and Heidemarie Schmidt J. Appl. Phys. **(2011)**, 109, 124117.

[4] R. zazpe, P. Stoliar, F. Golmar, R. Llopis, F. Casanova, and L. E. Hueso., Appl. Phy. Lett. **(2013)**, 103, 073114.

[5] Umesh chand, Kuan-chang huang, Chun-yang huang, and Tseung-yuen tseng, IEEE Tran. Elec. Devices., **(2015)**, 62, 11.

[6] N. Arun, K. V. Kumar, A. P. Pathak, D. K. Avasthi, and S. V. S. Nageswara Rao, "Hafnia-based resistive switching devices for non-volatile memory applications and effects of gamma irradiation on device performance", Radiat. Eff. Defects Solids, vol. 173, no. 3–4, pp. 239–249, **(2018)**, doi: 10.1080/10420150.2018.1425863.

[7] N. Manikanthababu, N. Arun, M. Dhanunjaya, S.V.S. Nageswara Rao and A. P. Pathak , Rad. Eff. and Def. in Sol., **(2016)**, 171, 77-86.

[8] N. Manikanthababu, N. Arun, M. Dhanunjaya, V. Saikiran, S. V. S. Nageswara Rao, and A. P. Pathak, "Synthesis, characterization and radiation damage studies of high-k dielectric (HfO_2) films for MOS device applications", Radiat. Eff. Defects Solids, vol. 170, no. 3, pp. 207–217, **(2015)**.

[9] M.N. Saleh, D.K. Venkatachalam, R.G. Elliman., Current App. Phy., **(2014)**, 14, 88-92.

[10] Katrina A. Morgan, Ruomeng Huang, Kenneth Potter, Chris Shaw, William Redman-White, and C. H. De Groot, IEEE Tran. Elec. Device., **(2014)**, 61, 6.

[11] P.C. Mcintyrea, ECS Trans., **(2007)**, 11, 235-249.

[12] (SRIM) M. Mayer, SIMNRA: Simulation of RBS, ERD and NRA Spectra. <http://www.rzg.mpg.de/mam/>.

[13] N. Arun, K. Vinod Kumar, A. Mangababu, S. V. S. Nageswara Rao, and A. P. Pathak, "Influence of the bottom metal electrode and gamma irradiation effects on the performance of HfO_2-based RRAM devices", Radiat. Eff. Defects Solids, vol. 174, no. 1–2, pp. 66–75, **(2019)**, doi: 10.1080/10420150.2019.1579213.

[14] Deng Ning, Pang Hua, and Wu Wei, Chin. Phys. B, **(2014)**, 23, 10, 107306.

[15] F. Palumbo, E. Miranda, G. Ghibaudo, and V. Jousseaume, IEEE electron device letters, **(2012)**, 33, 7.

[16] Jiehun Kang and In-Sung Park. IEEE transactions on electron devices, **(2016)**, 63, 6.

[17] Gilbert Sassine, Selina la barbera, and Nabil najjari, Jour. Vac. Sci. Technol., **(2016)** 34.

[18] Holt, Joshua; Cady, Nathaniel, Yang-Scharlotta, Jean, IEEE, IIRW Final Report **(2015)**, 978-1-4673-8.

[19] Kirti Agashe , Nisha Sarwade , Sangeeta Joshi , Madhavi Thakurdesai , Smita Surwase , Pravin Tirmali , Kandasami Asokan Nuclear Instruments and Methods in Physics Research Section B: Beam Interactions with Materials and Atoms, **(2017)**, 403, 38-44.

[20] M. Dhanunjaya, D. K. Avasthi, A. P. Pathak, S. A. Khan, and S. V. S. Nageswara Rao, "Grain fragmentation and phase transformations in hafnium oxide induced by swift heavy ion irradiation", Appl. Phys. A Mater. Sci. Process., vol. 124, no. 9, p. 0, **(2018)**, doi: 10.1007/s00339-018-2000-z.

[21] L. D. V. Sangani and M. G. Krishna, "Oxygen Affinity of Metal Electrodes as Control Parameter in Tuning the Performance of Cu_xO-Based Resistive Random Access Memory Devices", Phys. Status Solidi Appl. Mater. Sci., vol. 1900392, pp. 1–7, **(2019)**, doi: 10.1002/pssa.201900392.

[22] S. Privitera, G. Bersuker, S. Lombardo, C. Bongiorno, and D. C. Gilmer, "Conductive filament structure in HfO_2 resistive switching memory devices", Solid. State. Electron., vol. 111, pp. 161–165, **(2015)**.

[23] J. H. Yoon et al., "Pt/Ta_2O_5/HfO_{2-x}/Ti Resistive Switching Memory Competing with Multilevel NAND Flash", Adv. Mater., vol. 27, no. 25, pp. 3811–3816, **(2015)**.

[24] Y. C. Yang, F. Pan, Q. Liu, M. Liu, and F. Zeng, "Fully room temperature fabricated nonvolatile resistive memory for ultrafast and high density memory application", Nano Lett., vol. 9, no. 4, p. 1636, **(2009)**.

[25] H. García et al., "Electrical Characterization of Defects Created by γ-Radiation in HfO_2-Based MIS Structures for RRAM Applications", J. Electron. Mater., vol. 47, no. 9, pp. 5013–5018, **(2018)**.

[26] J. Ni, Q. Zhou, Z. Li, and Z. Zhang, "Oxygen defect induced photoluminescence of HfO_2 thin films", Appl. Phys. Lett., vol. 93, no. 1, pp. 2–4, **(2008)**.

[27] T. V. Perevalov, V. S. Aliev, V. A. Gritsenko, A. A. Saraev, and V. V. Kaichev, "Electronic structure of oxygen vacancies in hafnium oxide", Microelectron. Eng., vol. 109, pp. 21–23, **(2013)**.

[28] Y. S. Lin et al., "Resistive switching mechanisms relating to oxygen vacancies migration in both interfaces in Ti / HfO_x / Pt memory devices," J. Appl. Phys., vol. 113, p. 64510, **(2013)**.

[29] A. Chen, "A review of emerging non-volatile memory (NVM) technologies and applications", Solid. State. Electron., vol. 125, pp. 25–38, **(2016)**.

[30] W. Duan, J. Wang, and X. Zhong, "The effect of γ-rays irradiation on the electrical properties of WO_x film-based memory cells," Epl, vol. 119, no. 2, pp. 2–6, **(2017)**.

[31] J. T. Ryan, P. M. Lenahan, A. Y. Kang, J. F. Conley, G. Bersuker, and P. Lysaght, "Identification of the atomic scale defects involved in radiation damage in HfO_2 based MOS devices," IEEE Trans. Nucl. Sci., vol. 52, no. 6, pp. 2272–2275, **(2005)**.

Chapter 5

Effects of Swift Heavy Ion (SHI) irradiation on performance of RRAM devices

5.1 Introduction

As mentioned in previous chapters, RRAMs devices have been identified as potential building blocks for future non-volatile memory and reconfigurable hardware devices [1,2]. RRAMs have attracted significant attention because of their high density memory architecture [3,4], low power consumption [5], faster switching[5] and longer retention time when compared to conventional NVM devices [6,7]. These emerging devices are expected to replace the currently used floating gate devices, in near future [8-10]. Applications of RRAMs are not only limited to data storage devices but also to processing elements such as logic gates [11]. "In-memory computation" is envisaged with the advent of RRAM based digital logic circuits. Based on the very nature of the switching mechanisms involved, RRAMs also find applications in neuromorphic systems [12,13]. Hence it may become indispensable, in future, to deploy RRAMs in space and nuclear electronics which operate in radiation harsh environments. In this connection, it is, thus, important to study the effects of ion irradiation, radiation damage and reliability of these devices.

However, such studies are very limited in literature[14-16].SHI irradiation is a versatile technique to engineer material properties as well as to simulate the radiation damage in laboratory. Radiation damage produced in space over longer periods can be realized in shorter intervals by selecting appropriate species and energy. Further, the damage due to

fission fragments in Nuclear reactors and radiation from solar flares / supernova can be estimated directly by SHI irradiation studies. Previous reports suggested that in general, the RRAMs are more tolerant to radiation when compared to floating gate devices [17]. However the effects of radiation damage critically depend on the nature of materials, their phases and interfaces that constitute the device[14].

As discussed earlier, RS behavior has been reported in many transition metal oxides including HfO_2 [4,18,19], ZrO_2, Cu_xO [20], TiO_2 [21], TaO_x, WO_x [22]. HfO_2 seems to be the most promising material for future microelectronic compatible RRAMs [5,23], in view of its success as a gate dielectric in MOS devices [24,25]. Radiation damage studies indicate that both electron and hole traps coexist in HfO_2, whereas only electron traps exist in SiO_2 [23,26]. It is shown that the SHI irradiation can improve the performance of an HfO_2 based MOS device below a critical fluence (track overlap fluence) and the device is deteriorated above this fluence [25]. Further, the effects of SHI irradiation critically depend on the initial phase of the material, size and shapes of the grains [27-29]. Monoclinic phase is introduced when amorphous HfO_2 is subjected to SHI irradiation. However, irradiation on an initially monoclinic phase HfO_2 resulted in the evolution of tetragonal phase [29]. Gamma irradiation studies presented in the previous chapter indicated that a low dose treatment (below 12 kGy) can improve the performance of HfO_2 based RRAMs. The devices are totally damaged when subjected to a higher dose (48 kGy) [30]. The distribution in SET and RESET voltages is found to increase at higher doses [19,30]. A recent report on the effects of 1.1 GeV Au irradiation on the performance of RMBE grown monoclinic-HfO_x based RRAMs (TiN/m-HfO_{2-x}/Pt/Au/c-Al_2O_3) emphasizes the importance of such studies in this domain [8]. There are, however, no studies on the effects of swift Ag ion irradiation on the switching performance of amorphous HfO_2-based RRAM devices.

This chapter deals with the RRAM devices with thin RF sputtered amorphous HfO_2 layer as switching medium [31]. Patterned Au/HfO_2/Au based RRAM structures have been fabricated by using various thin film deposition and photolithographic techniques. The influence of 120 MeV Ag irradiation on the structural properties of HfO_2 and consequent effects on the switching properties of corresponding RRAM devices has been investigated. Here it is important to note that the initial phase, shape and size distribution of grains, interfaces and the electronic energy loss play critical role in determining the effects of SHI irradiation [29][45-46]. Further the effects of film thickness and the device area on the performance of

RRAM devices and their radiation response have also been studied.

5.2 Experimental details

HfO_2 thin films, of 50 and 30 nm thickness, were produced by RF Magnetron sputter deposition from a target of 2-inch diameter and 3 mm thickness in the Ar atmosphere (30 SCCM). The 100 nm thickness Au top and bottom electrodes were prepared by e-beam evaporation using a 6-kW power supply for the electron gun at a constant deposition rate of 1.0 Å/s. A thin layer of 10 nm Cr was deposited by thermal evaporation on Si prior to the deposition of bottom electrode (Au) for good adhesion. The base pressure for the RF magnetron sputtering and evaporation processes were 4.2 x 10^{-6} and 1 x 10^{-6} mbar, respectively. HfO_2-based RRAM devices were fabricated on Si substrates (p-type with $\rho \sim$ 1-10 Ω-cm). The standard RCA processes were employed for cleaning Si substrates [19,32]. The devices were fabricated using standard in-house photo lithography techniques in class 1000 cleanroom. A photoresist of i-line positive tone and an ultraviolet (UV) mask aligner (MJB4 of Suss Microtech) were used for photoresist exposure. Bottom electrode (BE), active layer (HfO_2) and top electrode (TE) were deposited through different masks as needed. Process flow of lithography, deposition and lift-off has been performed at each stage, as explained in chapter2. *Figure* 5.1 shows the different stages of lithography for fabricating crossbar structure of RRAM devices employed in this work

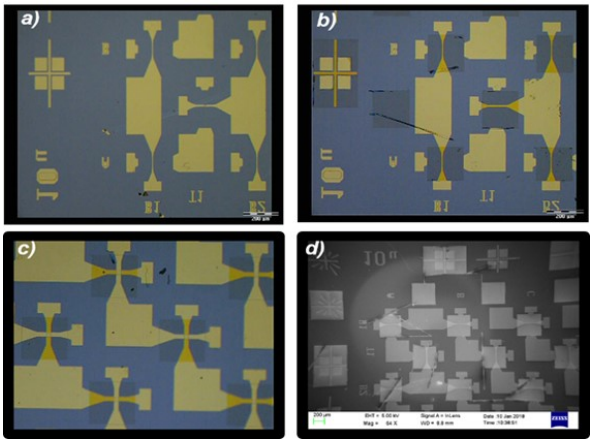

FIGURE 5.1: Images showing the device structures at different processing steps, a step-1: bottom electrodes of width 10 µm, b step-2: HfO_2 film deposited on the bottom electrode through a square mask, c step-3: top electrode showing the cell structure and probing pads and d an FESEM image showing the cross bar structure of devices.

Four sets of devices (labelled as R_1-R_4) with active area of 10 µm x 10 µm and 20 µm x 20 µm and thickness of 50 nm and 30 nm were fabricated and the details are given in *Table* 5.1. Further, the SHI irradiation using the 15 MV Pelletron accelerator at the IUAC, New Delhi has been performed on R_3 and R_4 devices to investigate the effects on the performance of these RRAM devices. For this purpose, a 120 MeV Ag ion beam with a relatively low beam current of 0.5 particle-nA (pnA) was maintained throughout the experiment. The ion fluence was varied in the range of 5 x 10^{10} to 5 x 10^{12} ions/cm^2, as ion beam annealing effects are expected in this fluence range [25].

TABLE 5.1: The details of the RRAM devices.

Device name	flim thickness (nm)	Area (µm ^{2})
R_1	50	10 ×10
R_2	50	20 ×20
R_3	30	10 ×10
R_4	30	20 ×20

The film thickness was estimated by using a stylus Profilometer. PL measurements were performed on pristine and irradiated R_3-series samples in the neighborhood of TE contact region. An excitation wavelength of 355 nm (3.5 eV which is below the bandgap of HfO_2) was employed to study defect dynamics. Current-Voltage (I-V) measurements, endurance cycles and retention tests were carried out by using an Agilent technologies B1500 A semiconductor device analyzer. Appropriate current compliance circuits are used to realize LRS and HRS without damaging the devices. DC sweeps of positive voltage were applied on the top electrode with respect to the bottom metal (grounded) electrode. The continuous cycling pulses were applied to study the RS behavior and the endurance of these devices. The current compliance is limited to 1 mA and 18–35 mA to avoid possible hard breakdown of the device during the set and reset processes, respectively [22,33,34].

5.3 Results and Discussions

5.3.1 Characteristics of pristine devices

I-V characteristics of devices R_1 and R_2 (representative curves) shown in *Figure* 5.2 exhibit unipolar resistive switching behavior. Different regions in these characteristics are labeled

with numbers to show the paths of set (1, 2) and reset (3) operations. The set and reset voltages are found to be 2.16 V and 0.5 V respectively for the R_1 device. Similarly, set and reset voltages are 2.92 V and 0.49 V respectively for the R_2 device. A similar forming-free and unipolar RS phenomenon was earlier reported for HfO_2 based RRAM devices [20,35,36] and was attributed to the formation and rupture of columnar conducting paths, known as filaments, in oxide thin film [6,37-39]. However, bipolar switching and coexistence of bipolar and unipolar switching were also widely reported in HfO_2-based RRAM devices It is worth noting that the electrode materials, nature of the interfaces and the phase of HfO_2 are critical in determining the switching behavior of RRAMs[8,36,40-44]

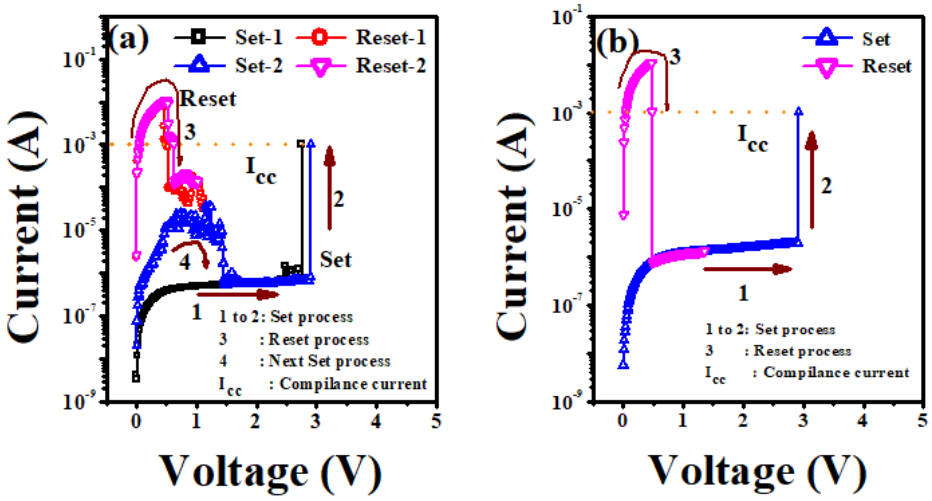

FIGURE 5.2: I-V Characteristics showing the RS behavior of a) R_1 and b) R_2 RRAM devices.

The present result is consistent with the previous reports, where unipolar switching was reported in HfO_2 when top electrode is Au [35, 45–48]. Forming free and unipolar switching behavior are advantageous for practical devices. It is known in literature that conductive filaments due to vacancies dominate over metal-ion-based filaments in HfO_2 [40–43]. This is particularly true when the electrodes are chemically inert, as in the present case. It is also observed that the contribution of V_O^{2+} type vacancies is significant for the formation of conducting filaments in HfO_2 when compared to that of other types of defects [40–43]. When a positive voltage is applied on the top electrode, O^{2-} ions are expected to migrate towards the top electrode, facilitating the formation of V_O^{2+} type conducting filaments [49]. However, neither the O^{2-} nor the V_O^{2+} bind to the Au metal electrodes when voltage is removed [50, 51].

Indeed, the binding of V_O^{2+} with Au is observed to be weaker when compared to other

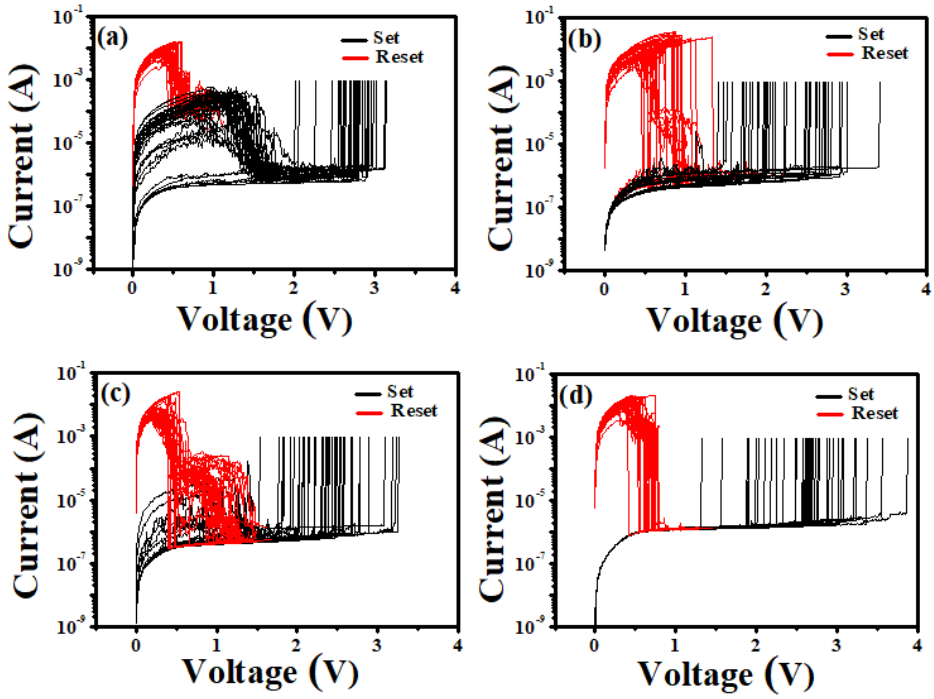

FIGURE 5.3: The endurance cycling of a) R_1, b) R_2, c) R_3 and d) R_4 RRAM devices.

metals [50, 51]. In addition, the possibility of out-diffusion of O^{2-} into atmosphere through the Au electrode under positive bias stress has also been reported [50–52]. The interface models that explain various types of mechanisms leading to unipolar and bipolar switching [34, 36] are not directly applicable in this study, as both the electrodes (top and bottom) are made of a chemically inert metal, Au. The combination of these two factors (out-diffusion and weak binding of V_O^{2+} to Au) and the fact that there is no interface that can act as a reservoir to store O^{2-} ions to enable the reset process when polarity is reversed causes unipolar switching. Hence, unipolar switching showed better performance when compared to the bipolar switching in these Au/HfO_2/Au-based RRAM devices. Therefore, the reset process can mainly be attributed to the Joule heating effects and corresponding phase changes in HfO_2. This is consistent with the fact that higher compliance currents were required for the reset process and large dispersion observed in voltages and the comparison is shown in *Figure* 5.3 and *Figure* 5.4. Several other competing processes such as the movement of vacancies in the direction of electrodes or from filaments to the resistive oxide layer or recombination with oxygen interstitials may also occur during the reset process. The reset process and the stability of the devices may further be improved by introducing an inter-layer between the top electrode and the oxide with high oxygen affinity materials like Al [20] or Hf [53].

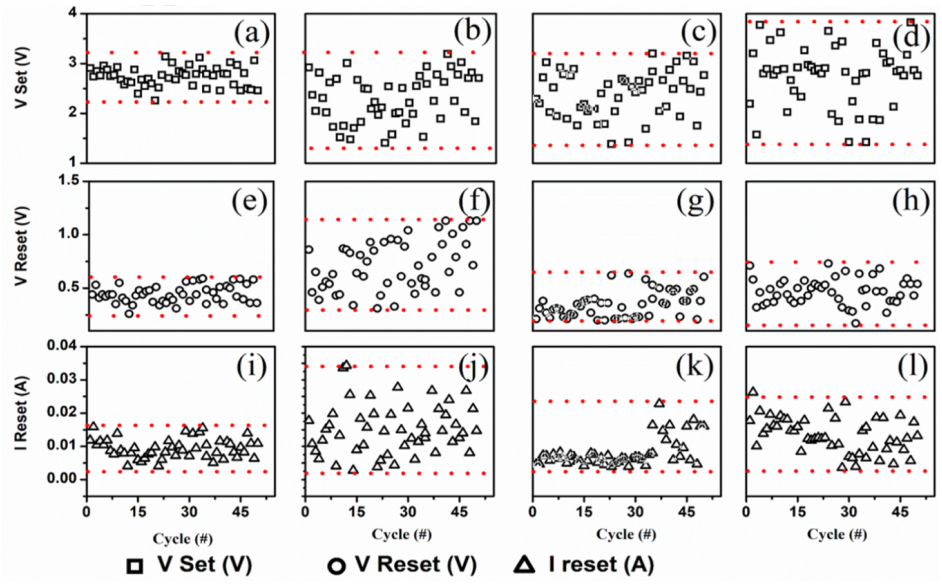

FIGURE 5.4: The comparison of set, reset voltages (V) and reset current (I)values,R_1: a,e,i, R_2: b,f,j, R_3:c,g,k, and R_4: d,h,l respectively of RRAM devices over first 50 cycle.

It is observed that the device R_1 did not reach complete reset (see *Figure* 5.2 (a)), indicating that some filaments still exist within the oxide. As a result, there is a steep increase in the current during the second set cycle (4) and an additional reset process before the actual set (5) operation. This indicates the possibility of multi-level switching in HfO_2-based RRAM devices [18, 53, 54]. The possible out-diffusion of O^{2-} ions during the set process [50–52] may deplete the concentration of oxygen in the vicinity of the top electrode. The possible gradient in oxygen concentration may further lead to the slow reset process and to introduce the observed intermediate state. This kind of gradual reset process was earlier demonstrated in RRAMs with "HfO_x/HfO_2" bilayer as switching medium [44]. These processes can be controlled by carefully selecting appropriate interfaces, voltage windows and compliance currents as needed. The endurance cycles indicated that there is a finite spread in the set and reset voltages of these devices (R_1–R_4).

The observed non-uniform switching behavior is possible due to the randomness in the formation of filamentary conduction channels and their areal density [55, 56]. Hence the size, shape and areal distribution of filaments can significantly influence this kind of switching behavior. The spread in the set and reset voltages is found to be less for devices with smaller active area (like R_1 over R_3) as expected [57]. Here, it is important to note that there are intermediate states in the reset cycles [18, 54], particularly for devices with smaller active area. Less number and thinner filaments are expected in devices with smaller active areas

[36], The progressive drop in the current may correspond to the reduction in the conductivity of the filaments [57, 58].

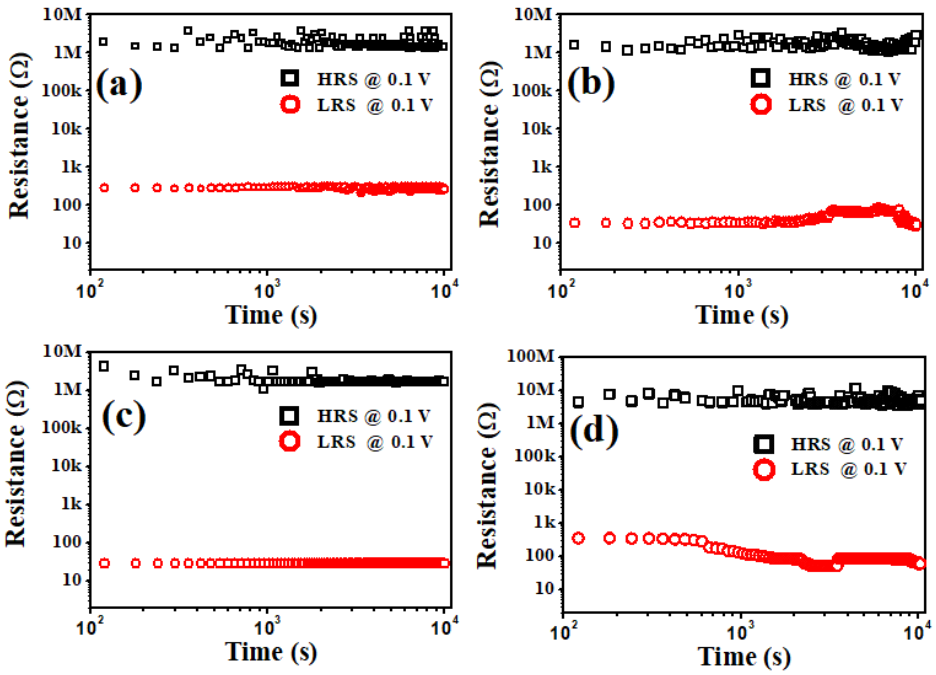

FIGURE 5.5: The retention time (over an interval of 10^4 sec) a) R_1, b) R_2, c) R_3 and d) R_4 of RRAM devices.

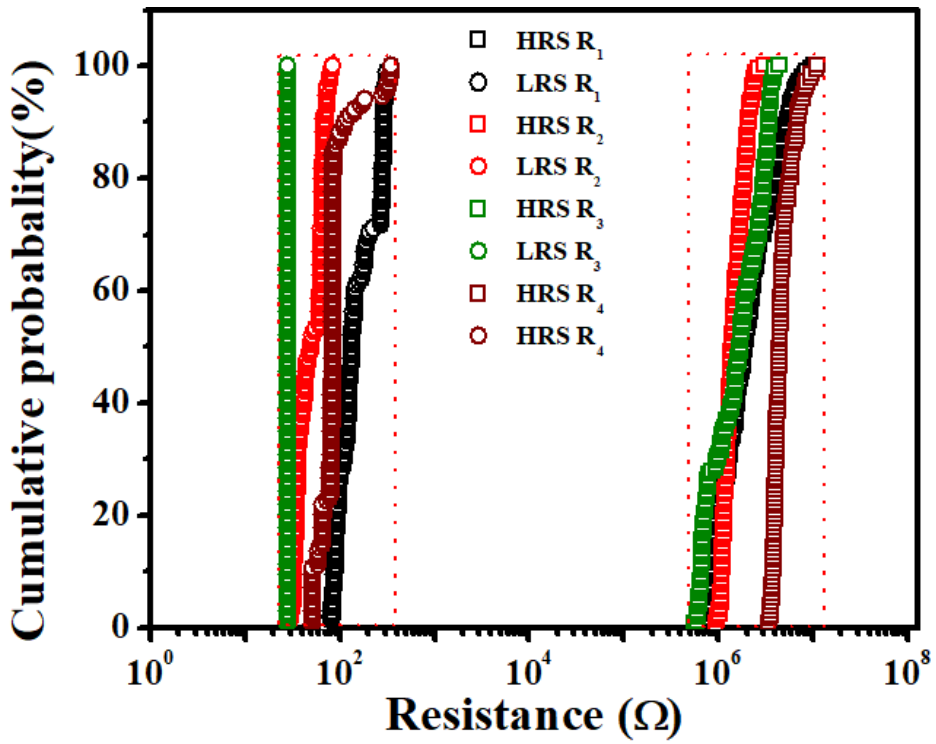

FIGURE 5.6: The cumulative distribution of HRS and LRS at 0.1 V bias of R_1 to R_4 RRAM devices.

The distribution of the set voltage (V_{Set}), reset voltages (V_{Reset}) and the reset current (I_{Reset}) for all four RRAM devices have also been studied in detail. The range of I_{Reset} is found to be lesser for R_1 and R_3 when compared to that of R_2 and R_4 devices. The average I_{Reset} is estimated to be 18 mA for R_1 and 35 mA for R_2. The number of filaments formed and their shapes depend on the active area of the device. The value of I_{Reset} depends on the previous set value which can influence the size and number density of the filaments. The number of filaments that are to be ruptured for achieving the reset is larger in the devices with larger active area [17]. Moreover, the current density is also lower in these devices, which is consistent with the literature [6]. The resistance values and cumulative distribution function (CDF) of the RRAM devices (R_1 to R_4) measured for each state are presented in *Figure* 5.5 and *Figure* 5.6. A positive bias voltage of 0.1 V is applied in intervals of 60 s and the current is measured to perform the retention test of these devices. These measurements were performed for each state individually (i.e., LRS or HRS) for all these devices. The resistance ratio between HRS to LRS (R_{Off} /R_{On}) is estimated to be 10^4 for R_1 and R_3 and 10^5 for R_2 and R_4 devices. This demonstrates the large stability between the LRS and HRS level of these RRAM devices fabricated in this study. In fact, the state of the devices can be clearly differentiated based on their resistance (i.e., as HRS or LRS).

5.3.2 Effects of SHI irradiation on the performance of RRAM devices

In SHI irradiation, energetic ions interact with a material and lose their energy via electronic energy loss (S_e) which dominates at high ion energies (>0.5MeV/μ) and nuclear energy loss (S_n) which dominates at low energies («0.5MeV/μ) [31]. The current interest in this field is to elucidate the effects of S_e on the structural modifications of materials and consequent effects on the performance of corresponding devices. The critical value of S_e for forming ion tracks (or damaged regions) in HfO_2 is estimated to be about 20 keV/nm [29]. 120 MeV Ag ion beam employed such that the S_e (∼24.86 keV/nm in HfO_2) not only dominates S_n (∼13.67 keV/nm) but also remains uniform throughout the film. It is important to point out that the penetration depth of the Ag ions (range = ∼ 8.49 μm) is much greater than the thickness of films. As a consequence, Ag ions will come to rest only in the substrate. The electronic energy deposition can result in deep defects and trap centers and other defects. RRAM devices (R_3 and R_4 series) were subjected to different irradiation fluence (5 x 10^{10}, 1 x 10^{11}, 5 x10^{11} and 5 x 10^{12} ions/cm^2) to study the effects on their performance. It was earlier

reported that the ion induced annealing effects dominate for this fluence range in the case of HfO_2 based MOSCAPs [15,25,32]. Here, RRAM devices are subjected to similar irradiation conditions to investigate the consequent effects on their switching parameters. *Figure* 5.7 shows representative I-V curves of pristine and irradiated (R_3 series) samples indicating significant shift in the set and reset voltages as a function of fluence.

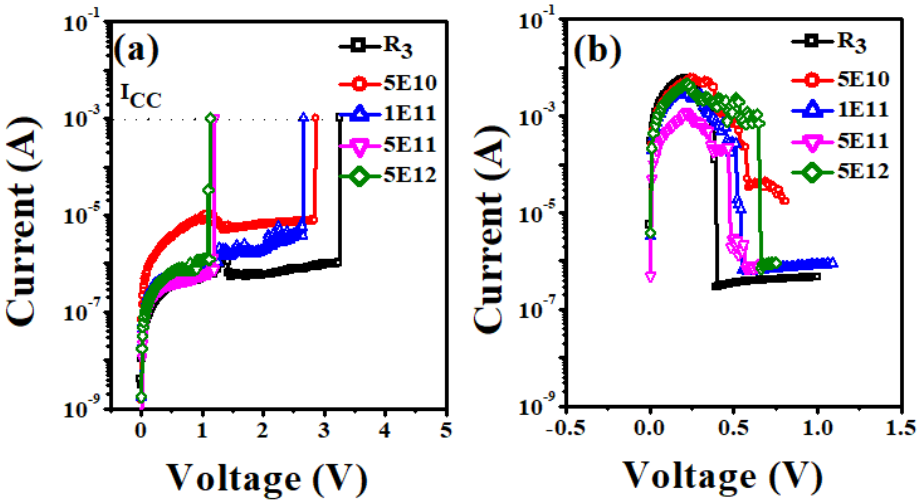

FIGURE 5.7: I-V Characteristics showing the RS behavior of R_3 series (pristine and irradiated at different fluence) devices: a) Set curves and b) Reset curves.

The mean values of switching voltages and the corresponding distributions are shown as function of fluence in *Figure* 5.8.

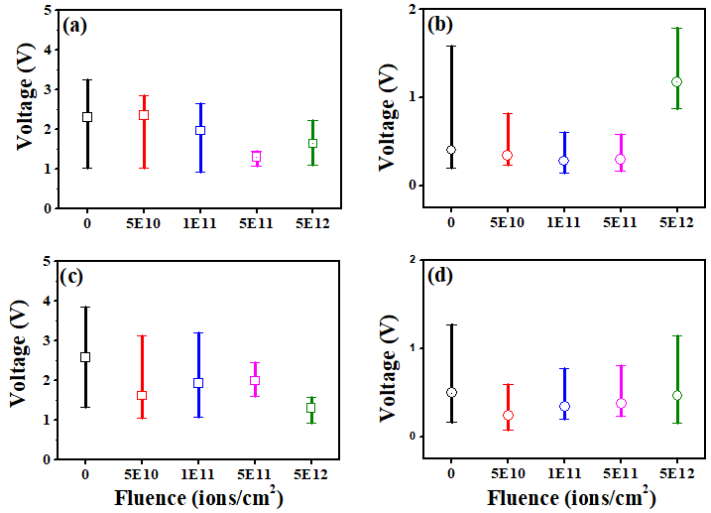

FIGURE 5.8: The distribution of set and reset voltages of pristine and irradiated of R_3 (a, b) and R_4 (c, d) devices (Symbol represents the mean value of switching voltage and the bars represent corresponding minimum and maximum values).

Unlike MOSCAPs, RRAM exhibited an increase in the leakage current in HRS at lower

fluence which may be due to the difference in initial conditions. HfO_2 films are deposited on the surfaces of Au in case of RRAMs and on the surface of SiO_2 in case MOSCAPs. Correspondingly, the average values of V_{Set} and the V_{Reset} decrease with increase in fluence below the critical fluence,though the variation in the V_{Reset} is not significant. Most important observation is that the ranges of V_{Set} and V_{Reset} distributions decreased up to a fluence of 5 x 10^{11} ions/cm^2 (see *Figure* 5.8), This is more evident in *Figure* 5.9 where the endurance curves of pristine and low fluence (5 x 10^{11} ions/cm^2) irradiations are shown.

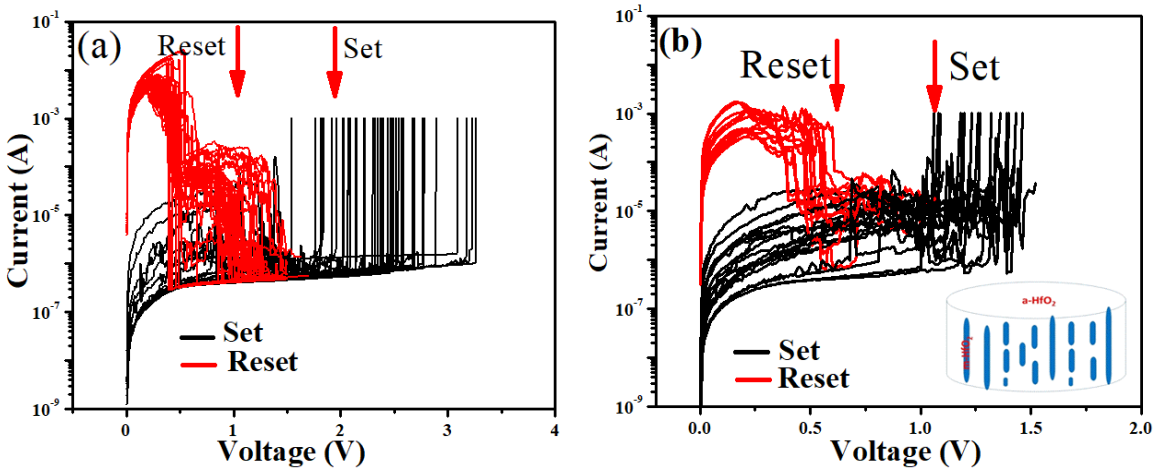

FIGURE 5.9: Endurance curves of a) pristine device and b) the devices irradiated to a fluence of 5 x 10^{11} ions/cm^2.

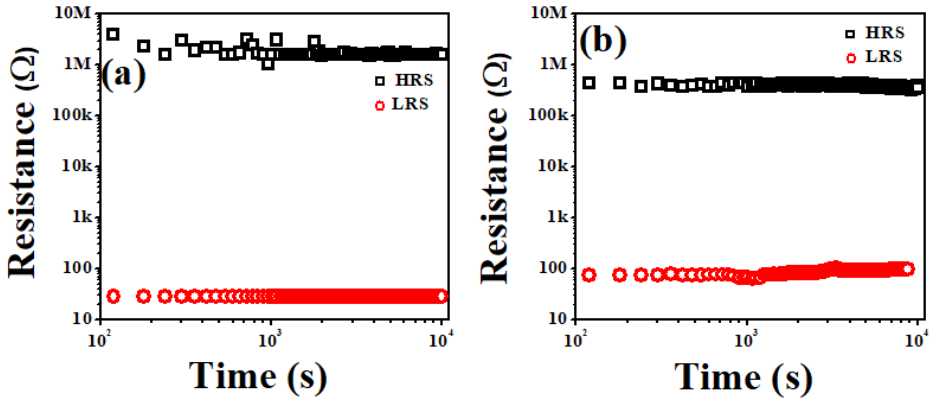

FIGURE 5.10: The retention time (over an interval of 10^4 s) test data of a) R_3—Pristine sample and b) R_3—Irradiated sample (critical fluence of 5 x 10^{11} ions/cm^2.

Similarly, the data of the retention test is shown *Figure* 5.10 for the pristine and irradiated (at critical fluence of 5 x 10^{11} ions/cm^2) devices (of R_3). It is observed that the resistance is little lower in HRS in irradiated devices (*Figure* 5.10(b)) as compared to that of the pristine

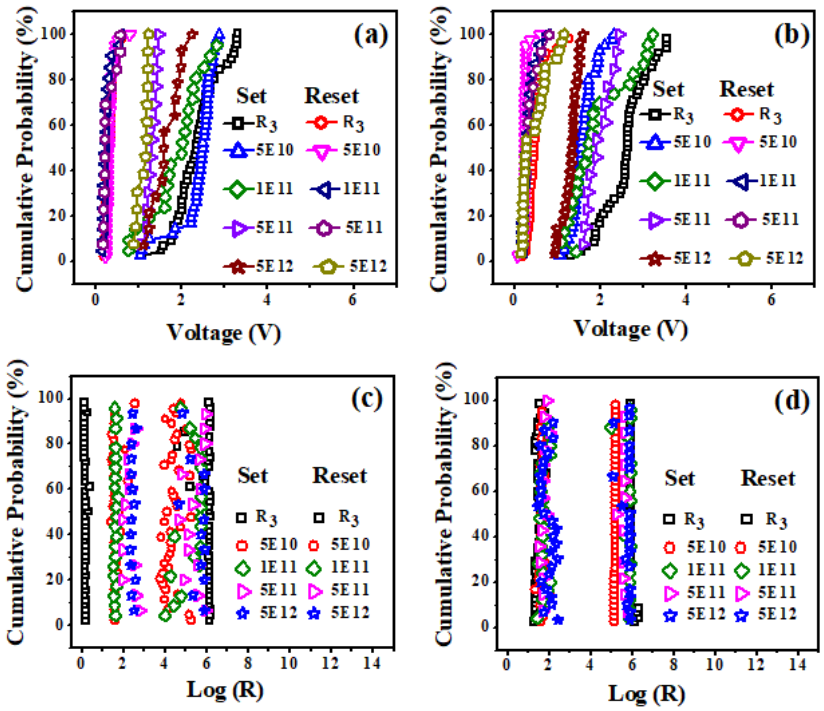

FIGURE 5.11: The distribution of set and reset voltages of pristine and irradiated devices. Cumulative probability of set and reset voltages of (a) R_3 series and (b) R_4 series. Cumulative probability of LRS and HRS states of (c) R_3 series and (d) R_4 series.

devices (*Figure* 5.10(a) and *Figure* 5.6). Similarly, the resistance is little higher in LRS. However, there is no significant change in the retention time at critical dose as compared to that of the pristine device. CDF of switching voltages and resistances (Log(R)) are presented in *Figure* 5.11 for both R_3 and R_4 series devices. This analysis clearly depicts the effects of SHI irradiation on the RS behavior of RRAMs. The slopes of set/reset curves indicate a possible reduction of spread in the set and reset voltages as a function of fluence.

As stated earlier, SHI irradiation can create amorphous or crystalline tracks or columnar defects in various materials [49]. We have recently shown that the SHI irradiation can induce an amorphous to monoclinic transformation in HfO_2 nanoparticles embedded in amorphous HfO_2 thin films, above a critical fluence (5 x 10^{11} ions/cm^2: track overlap fluence) [29]. Hence, the formation of isolated and incomplete m-HfO_2 tracks/clusters below this fluence is also possible in the present case. The track diameters are expected to be around 10 nm [25] and the number of tracks will be of the order of fluence (i.e., 5 x 10^{11} ions/cm^2). It is also important to note that the diameters of conducting filaments are also in the same range (3–10 nm) in HfO_2 [36]. It would, thus, appear that the result of the SHI process is to create a composite wherein isolated m-HfO_2 columnar tracks are embedded

in the pristine a-HfO_2 matrix (as depicted as a cartoon in the inset of *Figure* 5.9(b)). It is proposed that these tracks are acting as nucleation centers for filament formation under bias stress. Hence the formation of filaments in irradiated devices will not be as random as that would be in unirradiated films. This is not only reducing the switching voltages but also reducing the spread in switching voltages. The dispersion in SET voltages is reduced significantly in devices that are subjected to low fluence (*Figure* 5.8). The sample irradiated with a fluence of 5 x 10^{11} ions/cm^2 shows a clear gap between SET and RESET voltages (See *Figure* 5.9). Then the device gets damaged at higher doses (above track overlap fluence) leading to random switching. The overlap in the range of set and reset voltages (see *Figure* 5.7 and *Figure* 5.8) beyond a critical fluence (5 x 10^{11} ions/cm^2) is perhaps due to the production of high density of defects and/or possible ion beam mixing effects across electrode and oxide interfaces (Au/HfO_2). Nucleation centers are no longer isolated above the track overlap fluence. This is consistent with the hypothesis that the isolated tracks in irradiated samples act as nucleation centers for the formation of conducting filaments during the set process. It is worthwhile mentioning that SHI irradiation is an efficient method to realize the isolated nucleation centers in the switching medium. This study also suggests a scope for examining nano-wire embedded oxide layers as efficient switching media for RRAM devices.

Hence the study suggests that the SHI irradiation can play a vital role in lowering the set and reset voltages and voltage ranges. Hence, a low fluence treatment of RRAM devices with SHI irradiation not only reduces the set and reset voltages but also reduces the distribution in switching voltages. However, the devices are damaged above this fluence. This is also evident from *Figure* 5.12 and *Figure* 5.13 which shows the number of endurance cycle vs set and reset voltages of pristine and irradiated samples.

The devices subjected to higher fluence got switched only for about 20 times out of 50 continuous set and reset cycles though the devices did not fail completely. These devices will switch again if another endurance cycle is started. However, on an average, they will switch for about 20 times out of 50 continuous cycles. This is consistent qualitatively with our earlier studies on HfO_2-based MOS devices [19, 30]. Thus, as interpreted before, beyond a critical fluence there is an overlap of ion tracks over the same device area resulting in complex damage. To identify the possible reasons for difference in behavior of pristine and SHI samples, FESEM and PL experiments were carried out on HfO_2 films that are deposited and irradiated in the same runs.

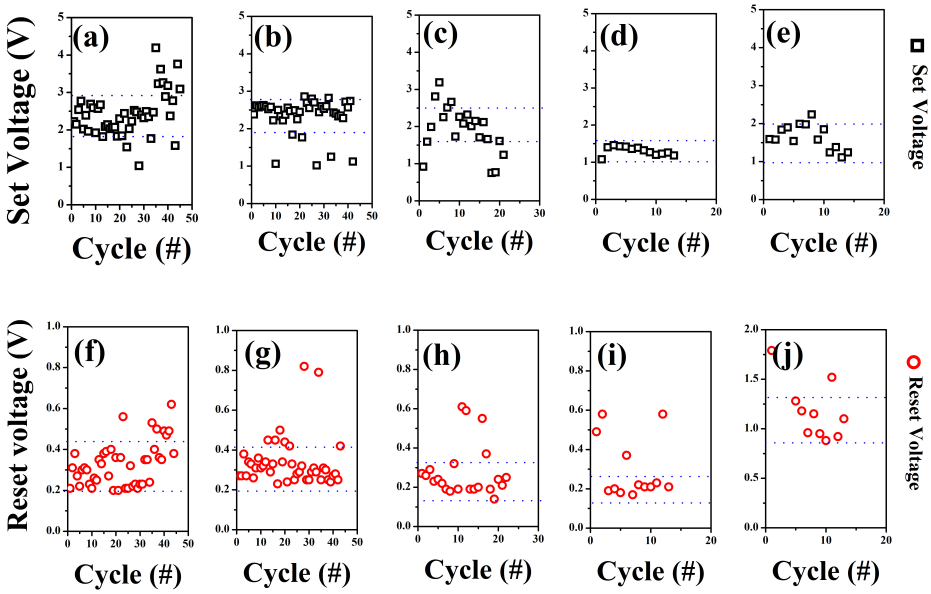

FIGURE 5.12: The set voltage a)R_3,b) 5E10, c) 1E11, d) 5E11, e) 5E12 ions/cm^2 and reset voltage f)R_3,g) 5E10, h) 1E11, i) 5E11, j) 5E12 ions/cm^2 comparison over first 50 cycle of 10 µm x 10 µm RRAM devices.

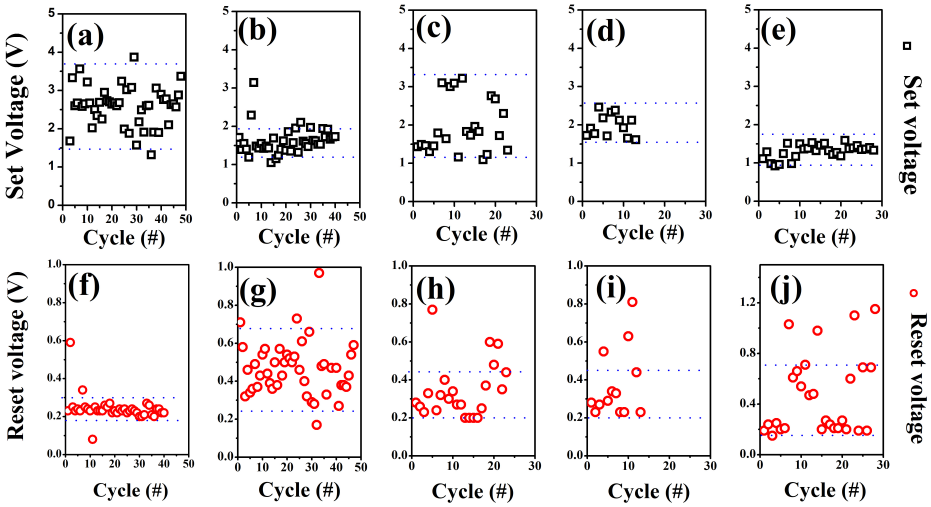

FIGURE 5.13: The set voltage a)R_3,b) 5E10, c) 1E11, d) 5E11, e) 5E12 ions/cm^2 and reset voltage f)R_3,g) 5E10, h) 1E11, i) 5E11, j) 5E12 ions/cm^2 comparison over first 50 cycle of 20 µm x 20 µm RRAM devices.

The PL measurements were performed for the R_3 sample before and after SHI irradiation. The excitation energy is chosen to be 3.5 eV, which is less than the bandgap of HfO_2. PL spectra and the deconvoluted peaks for the samples shown in *Figure* 5.14 correspond to various types of defects in the pristine and irradiated samples [29, 59]. The fitting is performed using a peak fit program for identifying the oxygen related vacancies in the HfO_2. Before irradiation, the peak positions are at 2.7 eV, 2.9 eV and 3.0 eV for R_3 sample. The intensity of these peaks decreases at low fluence and increases at higher fluences. The peak position

at 2.7 eV can be attributed to the doubly charged positive oxygen vacancy (V_O^{2+}) while the peak at 2.9 eV is associated with singly charged positive oxygen defect (V_O^{2+}) state [37]. The existence of these vacancy type defects in the RF sputtered a-HfO_2 films is responsible for the observed forming free switching with lower set voltages. A recent calculation [60] predicted a significant decrease in the energy barriers for creation and migration of vacancy type defects in m-HfO_2 under bias stress due to the injection of excess electrons into the oxide. Further, we noted minor changes in the peak positions of PL spectra as a function of irradiation fluence. The changes are significant for high fluence (beyond the critical fluence).

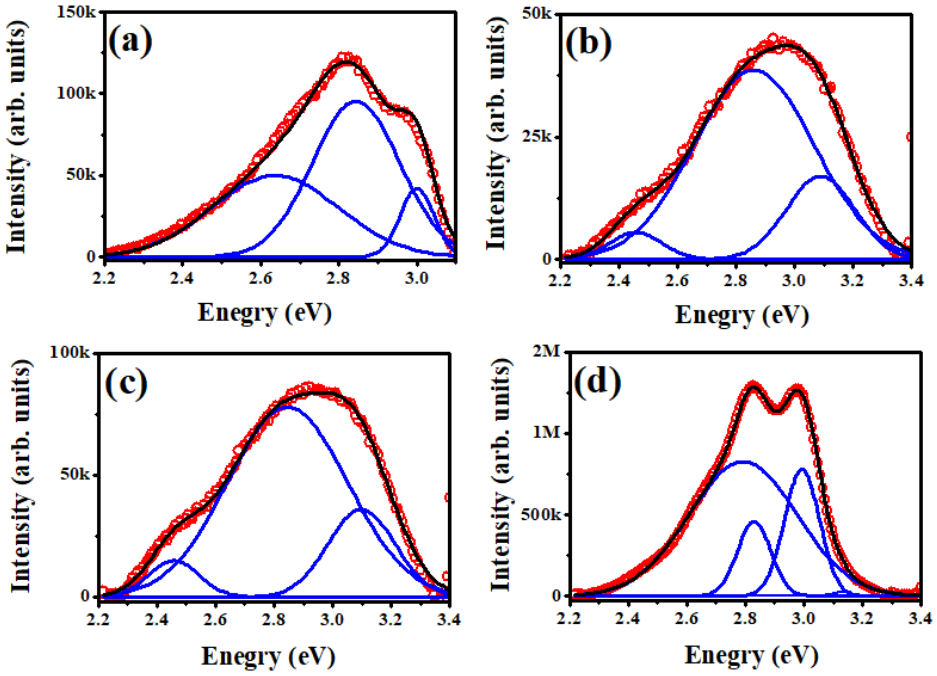

FIGURE 5.14: The PL spectra of the device R_3 a) Pristine b) 5E10 c) 5E11 and d) 5E12 ions/cm^2 (solid lines indicate fitting and de-convoluted peaks).

Basically, only two types of defects are populated in this case, indicating the possible re-configuration of defects as a result of SHI irradiation. The oxygen-related defects in HfO_2 films were earlier reported and most of those studies are consistent with our previous and present work [33]. In a recent study [8], it was shown that the performance of "TiN/monoclinic-HfO_{2-x}/Pt/Au" RRAMs is affected only at higher fluence (> 10^{12} ions/cm^2) when irradiated with 1.1 GeV Au ions (S_2 = 50.3 keV/nm in HfO_2). Most of the devices did not experience event upset and retained the stored data even at higher fluences. However, in the present study, the active layer is an amorphous film deposited on the surface of Au by RF sputtering. The observed effects are significant even though the Se is less (24.86 keV/nm in HfO_2) in the present study when compared to the earlier report [25]. It is, therefore, evident

that SHI can be used to tune the performance parameters of such devices. Significantly, the present study also demonstrates the presence of a critical ion fluence beyond which there is deterioration in set and reset parameters, indicating the range of radiation hardness of the devices. This information is expected to be useful for applications in nuclear and space electronics.

5.4 Conclusions

HfO_2 based RRAM devices were fabricated to study the effects of SHI irradiation on their performance. These devices are found to be of forming free type with uni-polar switching behavior. They have exhibited good endurance cycles with high resistance ratio ((R_{Off}/R_{On}) >10^5) and retention time. It is shown that the SHI irradiation can improve or deteriorate the performance of these devices based on the fluence. The spread in switching voltages is reduced with increase in fluence, indicating that the switching windows can be narrowed by selecting a proper combination of ion species, energy and fluence for irradiation. The set voltage is found to decrease with increase in fluence whereas the change in reset voltage is not significant. The overlap of set and reset voltages and the reduction of endurance above a critical fluence highlights the significance of radiation damage in these devices.

At lower fluences,possible creation of isolated nucleation centers, at lower fluences, for the formation of filaments during the set process is envisaged as a reason for the observed improvement in the dispersion in set voltages. Introduction of such isolated nucleation centers by other methods (like nano-wire embedded oxides etc.) in switching medium can be examined in future. These results provide useful information to tailor as well as to study the reliability of these devices in radiation harsh environment.

Bibliography

[1] M.A. Zidan, J.P. Strachan, W.D. Lu, "The future of electronics based on memristive systems", Nat. Electron. 1(1), 22–29 **(2018)**. https://doi.org/10.1038/s41928-017-0006-8

[2] D.B. Strukov, G.S. Snider, D.R. Stewart, R.S. Williams, "The missing memristor found", Nature 453(7191), 80–83 **(2008)**. https://doi.org/10.1038/nature06932

[3] D. Ielmini, "Resistive switching memories based on metal oxides: Mechanisms, reliability and scaling", Semicond. Sci.Technol. 31(6), 1–25, **(2016)**. https://doi.org/10.1088/0268-1242/31/6/063002

[4] F. Palumbo, "Formation and characterization of filamentary current paths in HfO_2-based resistive switching structures", IEEE Electron. Dev. Lett. 33(7), 1057–1059 **(2012)**. https://d oi.org/10.1109/LED.2012.2194689

[5] A. Sawa, "Resistive switching in Rapid advances in information technology rely on high-speed", Mater. Today 11(6), 28–36 **(2008)**. https://doi.org/10.1016/S1369-7021(08)70119-6

[6] M. Lanza, "A review on resistive switching in high-k dielectrics: a nanoscale point of view using conductive atomic force microscope", Materials (Basel) 7(3), 2155–2182 **(2014)**. http s://doi.org/10.3390/ma7032155

[7] A. Chen, "Solid-state electronics: a review of emerging nonvolatile memory (NVM) technologies and applications", Solid State Electron. 125, 25–38 **(2016)**. https://doi.org/10.1016/j. sse.2016.07.006

[8] S. Petzold, S.U. Sharath, J. Lemke, E. Hildebrandt, C. Trautmann, L. Alff, "Heavy Ion radiation effects on hafnium oxide-based resistive random access memory", IEEE Trans. Nucl. Sci. 66(7), 1715–1718 **(2019)**. https://doi.org/10.1109/ TNS.2019.2908637

[9] M. Alayan, M. Bagatin, S. Gerardin, A. Paccagnella, L. Larcher, E. Vianello, E. Nowak, B. De Salvo, L. Perniola, "Experimental and simulation studies of the effects of heavy ion irradiation on HfO_2-based RRAM cells", IEEE Trans. Nucl. Sci. 64(8), 2038–2045 **(2017)**. https://doi.org/10.1109/ TNS.2017.2721980

[10] Y. Chen, "ReRAM: history, status, and future", IEEE Trans. Electron. Dev. 67(4), 1420 **(2020)**

[11] S. Kvatinsky, K. Talisveyberg, D. Fliter, A. Kolodny, U.C. Weiser, E.G. Friedman, "Models of memristors for SPICE simulations", 27^{th} Conv. Electr. Electron. Eng. Isr. (IEEE, 2012) pp. 1–5 **(2012)**. https://doi.org/10.1109/EEEI.2012. 6377081

[12] X. Hong, D.J. Loy, P.A. Dananjaya, F. Tan, C. Ng, W. Lew, "Oxide based RRAM materials for neuromorphic computing", J. Mater. Sci. 53(12), 8720–8746 **(2018)**. https://doi.org/10. 1007/s10853-018-2134-6

[13] R. Islam, H. Li, P. Chen, W. Wan, H. Chen, B. Gao, H. Wu, S. Yu, K. Saraswat, H. Philip Wong, "Device and materials requirements for neuromorphic computing", J. Phys. D 52(11), 1–24 **(2019)**. https://doi.org/10.1088/1361-6463/aaf784

[14] D.S. Korolev, A.N. Mikhaylov, A.I. Belov, V.A. Sergeev, I.N. Antonov, A.P. Kasatkin, O.N. Gorshkov, D.I. Tetelbaum, "Influence of ion irradiation on the resistive switching parameters of SiO_x-based thin-film structures", J. Phys. Conf. Ser. 643(1), 1–5 **(2015)**. https://doi.org/10.1088/1742-6596/ 643/1/012094

[15] B. Butcher, X. He, M. Huang, Y. Wang, Qi. Liu, H. Lv, M. Liu, W. Wang, "Proton-based total-dose irradiation effects on Cu/HfO_2:Cu/Pt ReRAM devices", Nanotechnology 21(47), 1–5 **(2010)**. https://doi.org/10.1088/0957-4484/21/47/475206

[16] D.M. Fleetwood, P.S. Winokur, J.R. Schwank, "Using laboratory X-Ray and cobalt-60 irradiations to predict CMOS device response in strategic and space environments", IEEE Trans. Electron. Dev. 35(6), 1497–1505 **(1998)**

[17] U.S. Joshi, "Ion irradiation: a tool to understand oxide RRAM mechanism", Rad. Eff. Def. Sol. 166(8–9), 724–733 **(2011)**. h ttps://doi.org/10.1080/10420150.2011.583246

[18] X. Lian, E. Miranda, S. Long, L. Perniola, M. Liu, J. Sun~e´, "Three state resistive switching in HfO_2-based RRAM", Solid. State. Electron. 98, 38–44 **(2014)**. https://doi.org/10.1016/j. sse.2014.04.016

[19] N. Arun, K.V. Kumar, A.P. Pathak, D.K. Avasthi, S.V.S. Nageswara Rao, "Hafnia-based resistive switching devices for nonvolatile memory applications and effects of gamma irradiation on device performance", Rad. Eff. Def. Sol. 173(3–4), 239–249 **(2018)**. https://doi.org/10.1080/10420150.2018. 1425863

[20] L.D.V. Sangani, C.R. Kumar, M.G. Krishna, "Interfacial electrode-driven enhancement of the switching parameters of a copper oxide-based resistive random-access memory device", J. Electron. Mater. 45(1), 322–328 **(2016)**. https://doi. org/10.1007/s11664-015-4074-0

[21] L.D.V. Sangani, K.V. Sri, M.A. Mohiddon, M.G. Krishna,"Low temperature Au induced crystallization of titanium dioxide thin films for resistive switching applications", RSC Adv. 5(83), 67493–67499 **(2015)**. https://doi.org/10.1039/c5 ra09022a

[22] W. Duan, J. Wang, X. Zhong, "The effect of rays irradiation on the electrical properties of WO_x film-based memory cells", Lett. J. Explor. Front. Phys. 119, 27003-P1-27003-P4 **(2017)**. https://doi.org/10.1209/0295-5075/119/27003

[23] N. Manikanthababu, N. Arun, M. Dhanunjaya, V. Saikiran, S.V.S. Nageswara Rao, A.P. Pathak, "Synthesis, characterization and radiation damage studies of high-k dielectric (HfO_2) films for MOS device applications", Rad. Eff. Def. Sol. 170(3), 207–217 **(2015)**. https://doi.org/10.1080/10420150.2014. 980259

[24] N. Arun, J. Prabana, K.V. Kumar, A.P. Pathak, S.V.S. Nageswara, "Fabrication of HfO_2 based MOS and RRAM devices: a study of thermal annealing effects on these devices", AIP. Proc. 030216, 4–7 **(2019)**. https://doi.org/10.1063/1. 5113055

[25] N. Manikanthababu, S. Vajandar, N. Arun, A.P. Pathak, K. Asokan, T. Osipowicz, T. Basu, S.V.S. Nageswara Rao, "Electronic excitation induced defect dynamics in HfO_2 based MOS devices investigated by in-situ electrical measurements", Appl. Phys. Lett. 112(131601), 1–5 **(2018)**. https://doi.org/10. 1063/1.5012269

[26] M.R. Shaneyfelt, D.M. Fleetwood, J.R. Schwank, K.L. Hugh, "Charge yield for cobalt-60 And 10-Kev X-ray irradiations Of MOS devices", IEEE Trans. Electron. Dev. 38(6), 1187–1194 **(1991)**

[27] A. Benyagoub, "Mechanism of the monoclinic-to-tetragonal phase transition induced in zirconia and hafnia by swift heavy ions", Phys. Rev. B 72(9), 21–24 **(2005)**. https://doi.org/10. 1103/PhysRevB.72.094114

[28] M. Dhanunjaya, D.K. Avasthi, A.P. Pathak, S.A. Khan, S.V.S. Nageswara Rao, "Grain fragmentation and phase transformations in hafnium oxide induced by swift heavy ion irradiation", Appl. Phys. A 124(587), 1–10 **(2018)**. https://doi.org/10.1007/s00339-018-2000-z

[29] M. Dhanunjaya, S.A. Khan, A.P. Pathak, D.K. Avasthi, S.V.S. Nageswara Rao, "Ion induced crystallization and grain growth of hafnium oxide nano-particles in thin-films deposited by radio frequency magnetron sputtering", J. Phys. D 50, 1–8 **(2017)**. https://doi.org/10.1088/1361-6463/aa9723

[30] N. Arun, K. Vinod Kumar, A. Mangababu, S.V.S. Nageswara Rao, A.P. Pathak, "Influence of the bottom metal electrode and gamma irradiation effects on the performance of HfO_2-based RRAM devices", Rad. Eff. Def. Sol. 174(1–2), 66–75 **(2019)**. https://doi.org/10.1080/10420150.2019.1579213

[31] F. El Kamel, Z. Ben Cheikh, M.A. Soussou, A. Moadhen, K. Khirouni, "Structural, optical and dielectric characterization of Au/HfO_2/(Pt, TiN) capacitors", Thin Solid Films 645, 282–289 **(2018)**. https://doi.org/10.1016/j.tsf.2017.10.061

[32] N. Manikanthababu, N. Arun, M. Dhanunjaya, S.V.S. Nageswara Rao, A.P. Pathak, "Gamma irradiation-induced effects on the electrical properties of HfO_2 based MOS devices", Rad. Eff. Def. Sol. 171(1–2), 77–86 (**(2016)**. https://doi.org/10.1080/10420150.2015.1135152

[33] R. Waser, R. Dittmann, C. Staikov, K. Szot, "Redox-based resistive switching memories nanoionic mechanisms, prospects, and challenges", Adv. Mater. 21, 2632–2663 **(2009)**. h ttps://doi.org/10.1002/adma.200900375

[34] P.C. Akshara, N. Basu, J. Lahiri, G. Rajaram, M.G. Krishna, "Resistive switching behaviour of amorphous silicon carbide thin films fabricated by a single composite magnetron sputter deposition method", Bull. Mater. Sci. 43(123), 1–8 **(2020)**. h ttps://doi.org/10.1007/s12034-020-02093-8

[35] J.Y. Son, D.Y. Kim, H. Kim, W.J. Maeng, Y.S. Shin, Y.H. "Shine, A HfO_2 thin film resistive switch based on conducting atomic force microscopy", Electrochem Solid-State Lett 14(8), 311–313 **(2011)**. https://doi.org/10.1149/1.3574526

[36] H. Akinaga, H. Shima, "Resistive random access memory (ReRAM) based on metal oxides", Proc. IEEE 98(12), 2237–2251 **(2010)**. https://doi.org/10.1109/JPROC.2010.207083

[37] G. Sassine, L. Barbera, N. Najjari, D. Lyon, E.C. De Lyon,"Interfacial versus filamentary resistive switching in TiO_2 and HfO_2 devices", J. Vac. Sci. Technol. B 34(1), 012202-1-012202–6 **(2016)**. https://doi.org/10.1116/1. 4940129

[38] K.H. Xue, B. Traore, P. Blaise, L.R. Fonseca, E. Vianello, G. Molas, B. De Salvo, G. Ghibaudo, B. Magyari-Kope, Y. Nishi, "A combined ab initio and experimental study on the nature of conductive filaments in $Pt/HfO_2/Pt$ resistive random access memory", IEEE Trans. Electron. Dev. 61(5), 1394–1402 **(2014)**. https://doi.org/10.1109/TED.2014.2312943

[39] U. Celano, Y. Yin Chen, D.J. Wouters, G. Groeseneken, M. Jurczak, W. Vandervorst, "Filament observation in metal-oxide resistive switching devices", Appl. Phys. Lett. 102(12), 2011–2014 **(2013)**. https://doi.org/10.1063/1.4798525

[40] K.L. Lin, T.H. Hou, J. Shieh, J.H. Lin, C.T. Chou, Y.J. Lee, "Electrode dependence of filament formation in HfO_2 resistive switching memory", J. Appl. Phys. 109, 084104 **(2011)**. http s://doi.org/10.1063/1.3567915

[41] J.H. Stathis, "Reliability limits for the gate insulator in CMOS technology", IBM J. Res. Dev. 46(2/3), 265–286 **(2002)**

[42] M.A. Alam, B.E. Weir, P.J. Silverman, "A study of soft and hard breakdown—part II: principles of area, thickness, and voltage scaling", IEEE Trans. Electrin. Dev. 49(2), 232–238 (**(2002)**

[43] F. Nardi, C. Cagli, D. Ielmini, S. Spiga, "Reset current reduction and set-reset instabilities in unipolar NiO RRAM", International Memory Workshop **(2011)**, pp. 160–163

[44] T. Tan, Du. Yihang, Ai. Cao, Y. Sun, H. Zhang, G. Zha, "Resistive switching of the HfO_x/HfO_2 bilayer heterostructure and its transmission characteristics as a synapse", RSC Adv. 8, 41884–41891 **(2018)**. https://doi.org/10.1039/c8ra06230g

[45] H.Y. Lee, Y.S. Chen, P.S. Chen, T.Y. Wu, F. Chen, C.C. Wang, P.J. Tzeng, M.-J. Tsai, C. Lien, "Low-power and nanosecond switching in robust hafnium oxide resistive memory with a thin Ti cap", IEEE Trans. Electron. Dev. 31(1), 44–46 **(2010)**. https://doi.org/10.1109/LED.2009.2034670

[46] S. Lee, W.-G. Kim, S.-W. Rhee, K. Yong, "Resistance switching behaviors of hafnium oxide films grown by MOCVD for nonvolatile memory applications", J. Electrochem. Soc. 155(2), 92–96 **(2008)**. https://doi.org/10.1149/ 1.2814153

[47] Heng Yuan Lee, Pang Shiu Chen, Tai Yuan Wu, Ching Chiun Wang, Pei Jer Tzeng, Cha Hsin Lin, Frederick, Chen, MingJinn Tsai, and Chenhsin Lien,"Electrical evidence of unstable anodic interface in $Ru/HfO_x/TiN$ unipolar resistive memory" Appl. Phys. Lett. 92, 142911 **(2008)**. https://doi. org/10.1063/1.2908928

[48] M.Y. Chan, T. Zhang, V. Ho, P.S. Lee, "Resistive switching effects of HfO_2 high-k dielectric. Microelectron", Eng. 85, 2420–2424 **(2008)**. https://doi.org/10.1016/j.mee.2008.09. 021

[49] T. Nagata, M. Haemori, Y. Yamashita, H. Yoshikawa, Y. Iwashita, K. Kobayashi, "Oxygen migration at $Pt/HfO_2/Pt$ interface under bias operation", Appl. Phys. Lett. 97, 082902-1-082902–3 **(2010)**. https://doi.org/10.1063/1. 3483756

[50] K.M. Neyman, C. Inntam, A.V. Matveev, V.A. Nasluzov, N. Ro¨sch, "Single d-metal atoms on Fs and Fs defects of MgO(001): a theoretical study across the periodic table", J. Am. Chem. Soc. 127, 11652–11660 **(2005)**. https://doi.org/ 10.1021/ja052437i

[51] X.-Q. Gong, A. Selloni, O. Dulub, P. Jacobson, U. Diebold," Small Au and Pt clusters at the anatase $TiO_2(101)$ surface: behavior at terraces, steps, and surface oxygen vacancies", J. Am. Chem. Soc. 130, 370–381 **(2008)**. https://doi.org/10. 1021/ja0773148

[52] P. Gonon, M. Mougenot, C. Valle´e, C. Jorel, V. Jousseaume, H. Grampeix, F. El Kamel, "Resistance switching in HfO_2 metal-insulator-metal devices", J. Appl. Phys. 107, 074507 (2010). https://doi.org/10.1063/1.3357283

[53] R. Nakajima, A. Azuma, H. Yoshida, T. Shimizu, T. Ito, S. Shingubara, "Hf layer thickness dependence of resistive switching characteristics of Ti/Hf/HfO_2/Au resistive random access memory device", Jpn. J. Appl. Phys. 57(61), 066 **(2018)**. https://doi.org/10.7567/JJAP.57.06HD06

[54] D.S. Jeong, H. Schroeder, U. Breuer, R. Waser, "Characteristic electroforming behavior in Pt/TiO_2/Pt resistive switching cells depending on atmosphere", J. Appl. Phys. 104(12), 123716 **(2008)**. https://doi.org/10.1063/1.3043879

[55] X. Zhang, "Resistive switching characteristics of Ni/HfO_2/Pt ReRAM", J. Semicond. 33(5), 2011–2013 **(2012)**. https://doi. org/10.1088/1674-4926/33/5/054011

[56] A. Chen, "Area and thickness scaling of forming voltage of resistive switching memories", IEEE Electron Device Lett. 35(1), 57–59 **(2014)**. https://doi.org/10.1109/LED.2013. 2288262

[57] Y. Li, S. Long, Y. Liu, C. Hu, J. Teng, Q. Liu, H. Lv, J. Sun~e´, M. Liu, "Conductance quantization in resistive random access memory", Nanoscale Res Lett 10(1), 420 **(2015)**. https://doi. org/10.1186/s11671-015-1118-6

[58] G. Niu, P. Calka, M.A. der Maur, F. Santoni, S. Guha, M. Fraschke, P. Hamoumou, B. Gautier, E. Perez, C. Walczyk, C. Wenger, "Geometric conductive filament confinement by nanotips for resistive switching of HfO_2-RRAM devices with high performance", Sci. Rep. 6(1), 1–9 **(2016)**. https://doi.org/ 10.1038/srep25757

[59] M. Kong, B. Li, C. Guo, P. Zeng, M. Wei, W. He, "The optical absorption and photoluminescence characteristics of evaporated and IAD HfO_2 thin films", Coatings 9, 307 **(2019)**. h ttps://doi.org/10.3390/coatings9050307

[60] J.W. Strand, J. Cottom, L. Larcher, A.L. Shluger, "Effect of electric field on defect generation and migration in HfO_2", Phys. Rev. B 102, 014106 **(2020)**. https://doi.org/10.1103/Ph ysRevB.102.014106

Chapter 6

Non-stoichiometric HfO_x thin films and effects of Swift Heavy Ion irradiation on the performance of corresponding RRAM devices

6.1 Introduction

As discussed in previous chapters, RRAMs have attracted much attention due to their high storage density, low power and switching voltages. It is found that the switching process is mainly due to the formation of the conducting filaments taking place in the insulator film. These filaments formation can occur either from metallic ions or oxygen vacancies in the films presented. The resistive switching behavior and memory effect for many of the metal oxide (WO_x, ZnO_x, ZrO_2, TaO_x, CuO_x) based RRAM devices have been demonstrated [1-3]. The set and reset voltages are directly related to the formation and rupture of the conductive filaments in the insulating layer [4,5]. To investigate filamentary like conductive paths made of the oxygen vacancies or metallic ions in the non-stoichiometric HfO_x film-based devices, we have prepared and studied the switching characteristics of HfO_x based RRAM devices. It is observed that the range of distribution and variability in the set and reset voltages may be attributed to the randomness in the formation of the filamentary conductive paths in the dielectric layer. This adversely affects the switching characteristics of these RRAM devices. Therefore, it is worth mentioning that the film deposition conditions and stoichiometry also

play pivotal roles in the operation of the corresponding RRAM devices [6]. In this connection, non- stoichiometric HfO_x films were prepared by e-beam evaporation method. Two different methods namely, 1) thermal annealing and 2) SHI irradiation were employed to investigate the switching characteristics of the corresponding RRAM devices. As mentioned above, oxygen vacancies play an important role with metal electrodes interfaces in resistive switching. Many researchers have already reported the role of the interfacial layer formed with the top metal electrode for different switching layer materials[7]. The thin interfacial layer of metal-oxide contact can act like an oxygen reservoir and contributes to better and enhanced switching parameters[8-10].

The active metal electrodes (like Ag, Cu) favor resistive switching by dissolution of the metal ions into the insulating layer, thereby forming the filaments from the other end of the metal in metal-insulator-metal structures. Such devices are termed as CBRRAMs. In this connection, it is also important to elucidate more information of the metal electrodes, the role of interfacial layer formation and resulting switching characteristics for the RRAM devices. Different metals such as Au, Al and Cr were used as top electrodes for fabrication of the RRAM devices. As mentioned earlier, the RRAM device switching characteristics like set operation, reset operation, endurance cycling and retention time tests were performed to elucidate the effects of thermal annealing, SHI irradiation and metal electrodes in detail.

6.2 Experimental details

Electron beam evaporation method [11] is employed for the deposition of the non-stoichiometric HfO_x thin films. These films have been used for fabricating crossbar structures like RRAM devices. Si (p-type with $\rho \sim$ 1-10 Ω-cm) were used as a substrate for making these crossbar structures of the patterned RRAM devices. Primarily, Si substrates were cleaned by standard RCA process [12]. To fabricate a crossbar structure, a standard in-house photo lithography in class 1000 cleanroom) technique was employed. A photo-resist of i-line positive tone and an UV mask aligner (MJB4 of Suss Microtech) were used for photoresist exposure. BE, active layer (HfO_x) and TE were deposited through different masks at each stage as per the requirement. Process flow of lithography, deposition and liftoff have been performed at each stage as explained in the previous chapter.

A newly purchased e-beam evaporation system is installed and optimized for preparing thin films. This system is employed to deposit HfO_x films in this study. First, the chamber was evacuated to 1 x 10^{-6} mbar and a 6 kW power supply was used to power-up the electron gun. Deposition was performed at a constant rate of $\sim$ 1.0 Å/s. The granular powder with purity of 99.99 % is used for making the pellet. These pellets were used for the evaporation and to get high quality HfO_x thin films for fabricating the RRAM devices. A vacuum chamber with 2.0 x 10^{-5} mbar was used during deposition of the films. The optimization of thin films was performed by varying the deposition time. Furthermore, films with different thickness have been fabricated and characterized. Among them, the devices made up of a film thickness of 30 nm with an effective active device area of 10 µm x 10 µm have been chosen to perform various studies.

A set of samples fabricated in the same run, were treated with different annealing temperatures to elucidate the performance of RRAM devices. Then, the effects of the SHI on the switching performances have been investigated. Finally, interfacial induced switching characteristics by different top metal electrodes have been studied in detail. The annealing is performed using a tubular furnace in the N_2 atmosphere at University of Hyderabad. SHI irradiation was performed using a 15 MV Pelletron accelerator at the IUAC, New Delhi. 120 MeV Ag ion beam with a relatively low beam current of 0.5 pnA was maintained throughout the experiment. The ion fluence was varied in the range of 5 x 10^{10} to 5 x 10^{12} ions/cm^2 as ion beam annealing effects are expected in this fluence range [13]. The bottom and top metal electrode contacts were deposited by using thermal evaporation technique while maintaining a vacuum of 1.0 x 10^{-5} mbar, throughout the deposition process.

The film thickness was estimated by using a stylus profilometer. The FESEM (model: Carl ZEISS, FEG, Ultra 55) equipped with EDS attachment is used for estimating the concentration of various elements present in the thin films. XRR and GI-XRD with Cu Kα (λ = 1.5405 Å) of Cu Kα line are employed to elucidate the films surface roughness, film thickness and crystal structure of the films respectively. Further, XPS measurement is performed to investigate the elemental composition and stoichiometry of the thin film (HfO_x/Si). UV-Vis-NIR spectroscopy measurement were carried out to estimate the band gap and transmission percentage of the thin films (HfO_x/Quartz). PL measurements were performed on pristine, annealed and irradiated samples in the neighborhood of TE contact region. An excitation

wavelength of 375 nm (below the bandgap of HfO_2) was employed to study the defect dynamics. I-V measurements, endurance cycles and retention tests were carried out by using an Agilent technologies B1500 semiconductor device analyzer.

6.3 Characterization of the HfO_x thin films

6.3.1 Structural studies of HfO_x on Si substrates

The HfO_x thin films were deposited by e-beam evaporation on Si substrates. For these thin films, physical properties such as thickness, surface morphology, surface roughness and quality of the film have been studied in detail. The optimization and preparation of these films were carried out by varying the deposition time from 15 to 120 minutes. The film thickness is measured by various techniques such as profilometer and cross sectional FE-SEM. The XRR technique is used to estimate, correlate and confirm/check thickness with profilometer and cross- sectional SEM. The details of these techniques have been explained in the experimental section (*chapter 2*).

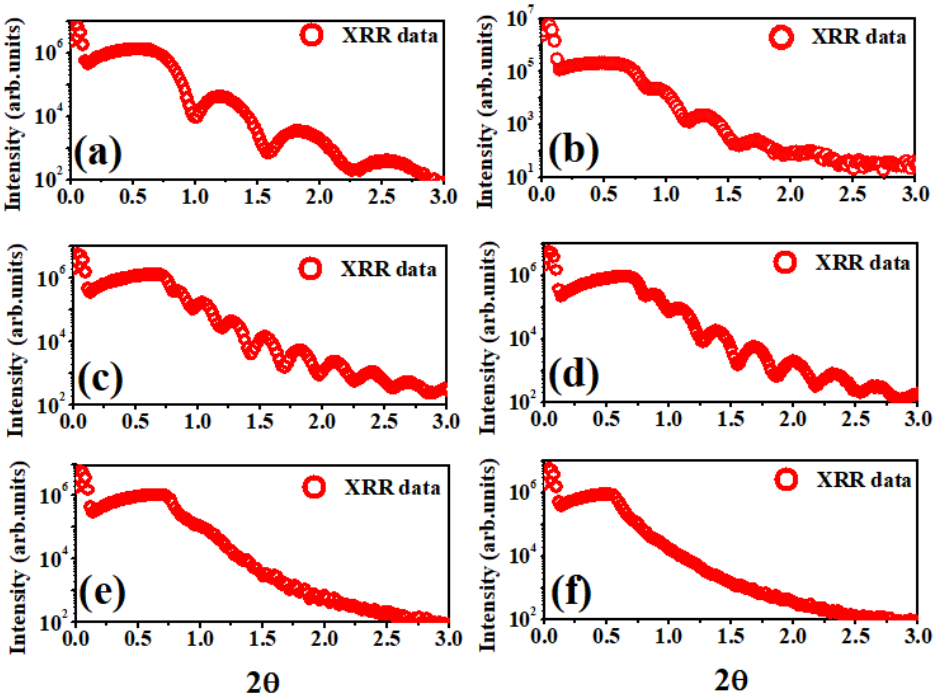

FIGURE 6.1: The XRR spectra of the films of different duration for deposition (a) 10 minutes, (b) 15 minutes, (c) 30 minutes, (d) 60 minutes, (e) 120 minutes and (f) 180 minutes of HfO_x on Si substrates.

The XRR patterns of HfO_x/Si samples are shown in *Figure* 6.1. The layer parameters such as film thickness and density, interface of layers and surface roughness can be determined

from these reflectivity curves, regardless of the crystallinity of each layer (single crystal, poly crystalline, and amorphous). At a critical angle, the reflectivity begins to decay exponentially and it is found to be $\sim 0.2^{0}$ for these samples. The film thickness is calculated as discussed in earlier sections (chapter 2) using interference fringes and the estimated values are tabulated (*Table* 6.1).

The estimated, measured and approximated values of HfO_x film thickness are shown in the *Table* 6.1. As expected, the film thickness is dependent on the duration of evaporation and increases as the duration of the evaporation time increases. Higher deposition rates may not ensure the proper density, grain size, shape and stoichiometry of the films.

TABLE 6.1: The film thickness measured by XRR measurement.

	Film thickness
Deposition time (minutes)	XRR (nm)
10	15
15	22
30	38
60	58
120	113
180	205

The stoichiometry is examined by employing XPS measurements and the films are found to be of non-stiochiometric HfO_x. The high resolution core level spectra for the Hf 4f and O 1s of the film are shown in *Figure* 6.2. The spectra of the film show the presence of Hf corresponding to the 4f 7/2 (17.59 peak/eV), 4f 5/2 (19.22 peak/eV) and a Hf metal rich (16.08 peak/eV) levels of Hf in HfO_x (spin orbit splitting). The separation between the peaks of 4f 7/2 and 4f 5/2 is 1.63 eV. It can be interpreted as charge transfer effects promoting the shift of peak position towards higher energy levels. XPS reveals that the films deposited by e-beam evaporation, are Hf metal rich (16.08 peak/eV) in nature and contain of non-lattice oxygen (O-O bond at 529.22 and 532.46 peak/eV). Comparing the areas under O 1s and Hf 4f peaks, the stoichiometry composition ratio of O and Hf elements at the surface layer of the HfO_x are 60.37/39.63 (%) for 30 nm.

HfO_x films were deposited on quartz substrates to characterize their optical properties by UV-Vis-NIR(transmission) spectroscopy. Pure stoichiometry film of HfO_2 is a wide bandgap material 5.7 eV and is almost transparent from near UV to far IR region. *Figure* 6.3 shows the optical transmittance spectra 0f HfO_x/Quartz films for different thickness. The

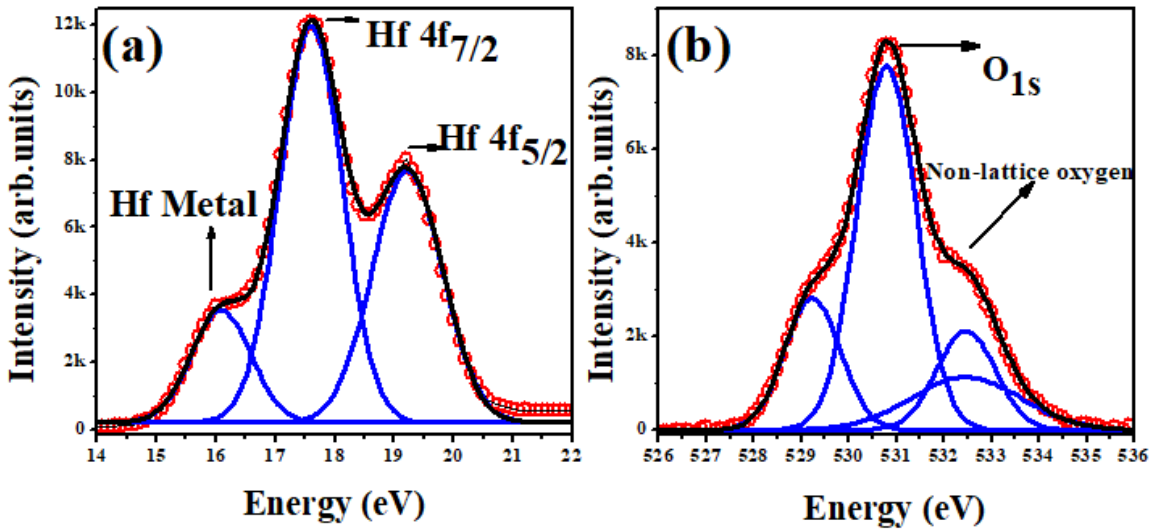

FIGURE 6.2: The XPS core level spectra of Hf and O elements for HfO_x/Si thin film.

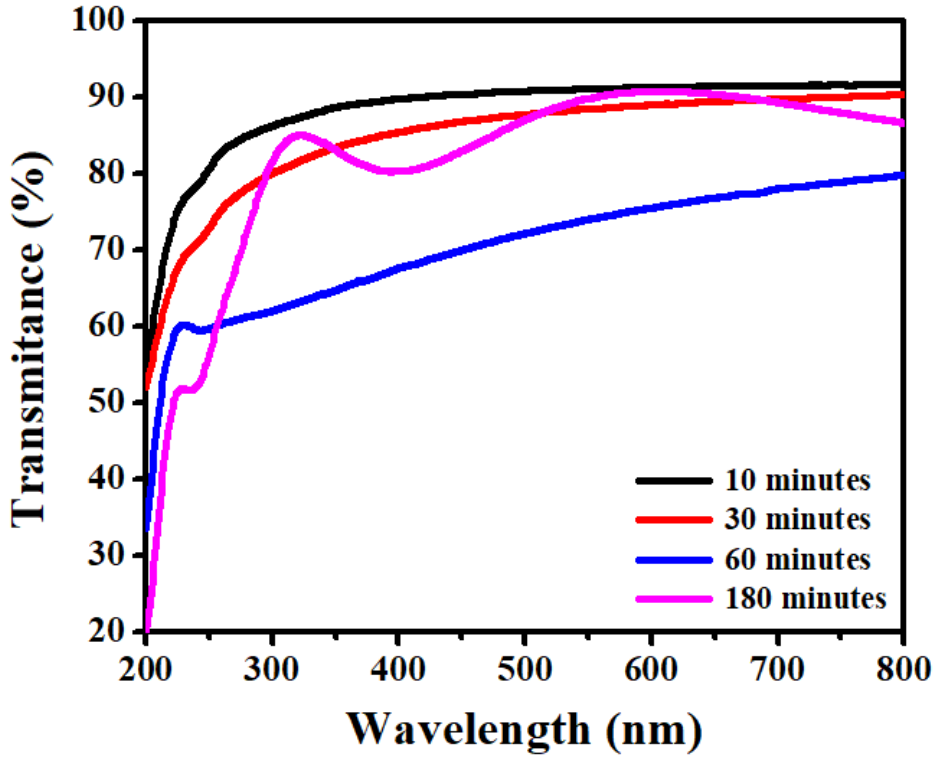

FIGURE 6.3: The optical transmittance spectra of HfO_x/Quartz films for different thickness.

preliminary observation is that the transmittance exhibits overall 80 to 90 % of transparency for these films.

The PL measurements were performed for these thin films deposited on Au/Si substrates. The corresponding analysis is used to explain the defect mechanisms or the role of the defect's formation in the dielectric switching layer for the performance of RRAM devices

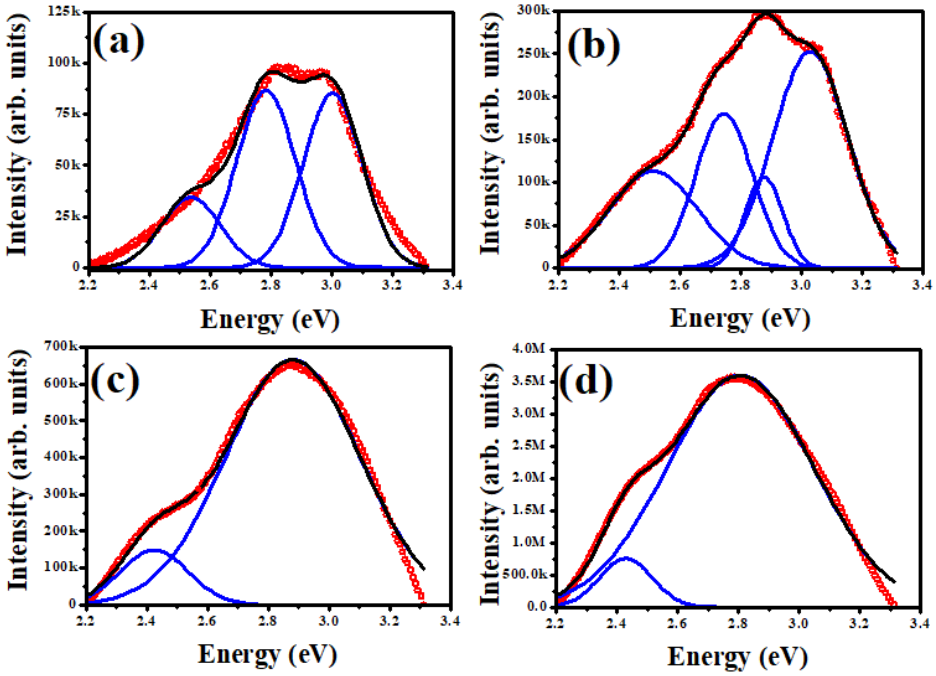

FIGURE 6.4: The Photoluminescence spectra of HfO_x films evaporated on Au/Si substrates for different thickness, a) 10 minutes, b) 30 minutes, c) 60 minutes, and d) 180 minutes.

before and after SHI irradiation. An excitation wavelength of 355 nm (3.5 eV which is below the bandgap of HfO_2) was employed to study the defect dynamics. PL spectra along with the de-convoluted peaks for the samples are shown in *Figure* 6.4. The fitting (red color) is performed by using a peak fit program for identifying the oxygen related vacancies in the HfO_x films. Mainly, the peak positions are found at 2.6 eV, 2.8 eV, 2.9 eV, 3.0 eV and 3.1 eV (blue in color). The different peak positions are interpreted to be the origin of oxygen vacancies in the dielectric layer.

The position and broadening of these PL peaks are found to change with film thickness,the defect peak position at 2.7 eV might be related to the positively double charged oxygen vacancy V_0^{2+} and similarly at 2.9 eV defect peak can be associated with positively single charged oxygen defect V_0^{+} state.The oxygen related defects in HfO_2 film are earlier reported and most of those studies are consistent with our previous and present results [14]. Here it is important to note that the V_0^{2+} defects play a major in the formation of filaments during resistive switching. Existing of these defects is responsible for the observed formation free resistive switching phenomenon in this study

6.3.2 Surface imaging and cros sectional analysis of the HfO_x on Au/Si substrates

FESEM images of HfO_x films deposited on Au/Si substrate are shown in *Figure* 6.5. We notice a good uniformity and smooth surface for films deposited at shorter intervals. Furthermore, as the time of deposition increases, (thicker films) the increase in size of grains and particles cluster formation among them has been observed.

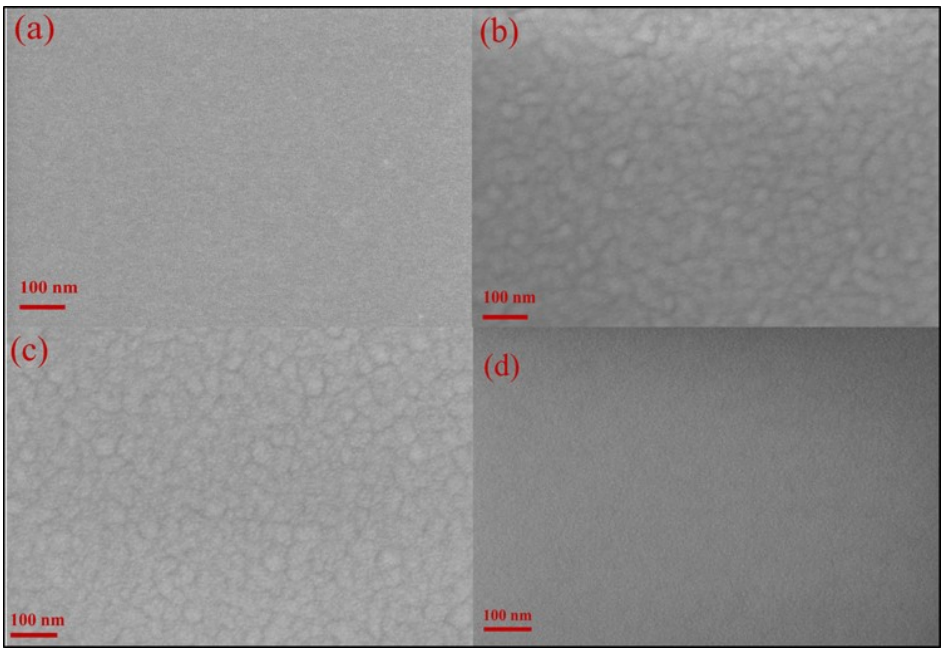

FIGURE 6.5: FESEM images of HfO_x films evaporated on Au/Si substrate for different thickness, a) 10 minutes, b) 30 minutes, c) 60 minutes, and d) 180 minutes.

In addition, a cross-sectional view of FESEM has been employed to investigate and further confirm the thickness of these films. All these images are of HfO_x films deposited on Au/Si substrates and the same have been shown in *Figure* 6.6. The HfO_x film interface formation is observed to be purely dependent on the surface morphology and roughness of the previous layer. as expected, the film thickness increased with increase in the time of deposition. To cross check and verify the film thickness a cross-sectional SEM and profilometer measurements are conducted. The calculated and estimated values are tabulated in *Table* 6.2. These values are consistent with each other, within the experiments.

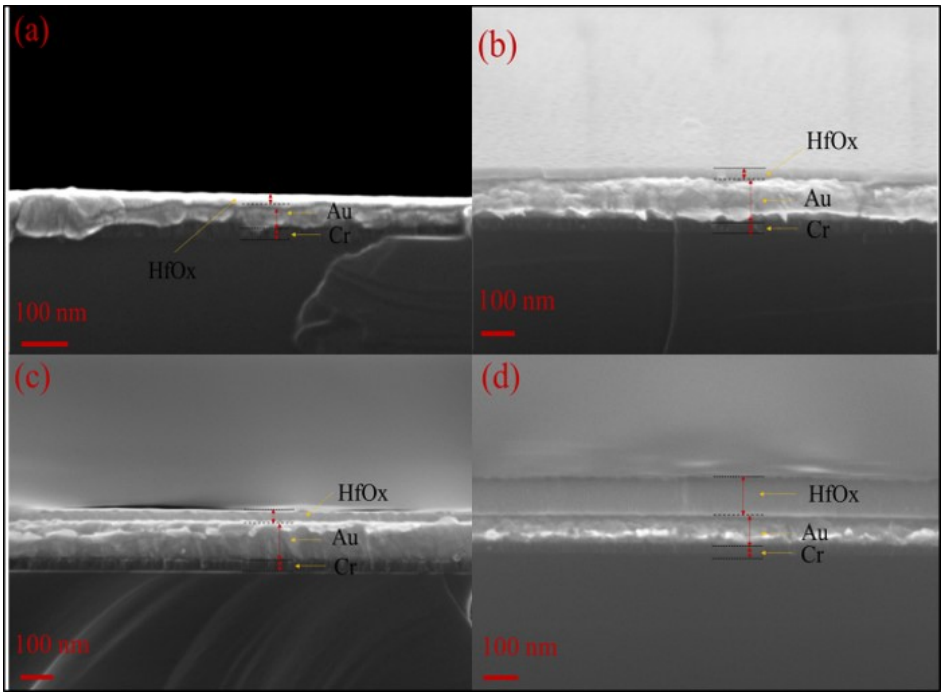

FIGURE 6.6: FESEM Cross-sectional view images of HfO_x films evaporated on Au/Si substrate for different thickness, a) 10 minutes, b) 30 minutes, c) 60 minutes, and d) 180 minutes.

TABLE 6.2: The comparison of HfO_x film thickness deposited on Au/Si substrates.

	Film thickness	
evaporation time (minutes)	profilometer (nm)	Cross-sectional FESEM (nm)
10	$\sim$ 12	15
15	$\sim$ 18	-
30	$\sim$ 25	35
60	$\sim$ 65	57
120	$\sim$ 105	-
180	$\sim$ 198	182

6.4 Effects of thermal annealing on the performance of RRAM devices

6.4.1 Device characterization

The detailed labeling of these devices are given in *Table* 6.3 and all these devices have been fabricated by lithography technique. A cross bar like structure of 10 μm $\times$10μm active area is used for the device fabrication. The pristine (R_5) and annealed (300 and 500 ^{o}C) HfO_x (30 nm) devices were investigated.

TABLE 6.3: The Temperature variation details of the devices

Aneealing temperature (^{o}C)	Device name
Pristine (0)	R_5
300	R_5-(i)
300	R_5-(ii)

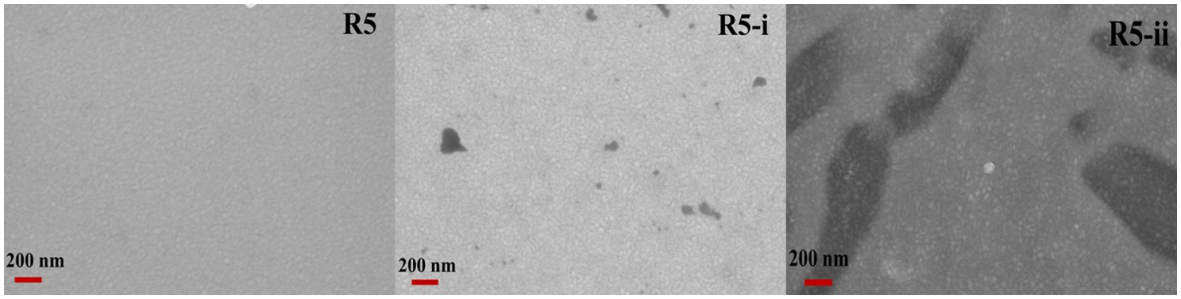

FIGURE 6.7: The FESEM images for pre and post thermal annealing temperatures.

To elucidate the morphological and structural changes on the films, pre and post annealing samples were characterized by FESEM technique (Note the images are taken before top electrode deposition). The top surface view of the HfO_x films for pristine and annealed samples are shown in *Figure* 6.7. It is noticed that a small amount of cluster formations start at 300 ^{o}C and further increase in the growth of these particles clusters takes place at an annealing temperature of 500 ^{o}C.

The GI-XRD patterns of the pre and post annealed RRAM devices are shown in *Figure* 6.8. The crystal structure and phase transformations of the thin films are revealed by the XRD measurements. Hence, here it may be mentioned that the present devices have not undergone any phase transformations. Moreover, all these films are found to be amorphous in nature both pre and post annealing. It is expected that the crystalline nature or phase transformation depends on the initial stage and thickness of the thin film. The peaks obtained in the GI-XRD patterns are purely from the electrode material (Au) and one peak from the substrate (Si) material. Stoichiometric films actually show monoclinic phase at these temperatures and such transformation was observed in RF sputtered HfO_2 films studied in previous chapters. A marked difference is that the crystalline phase is not observed in case of the present HfO_x films deposited by e-beam evaporation technique even after thermal annealing at 500 ^{o}C.

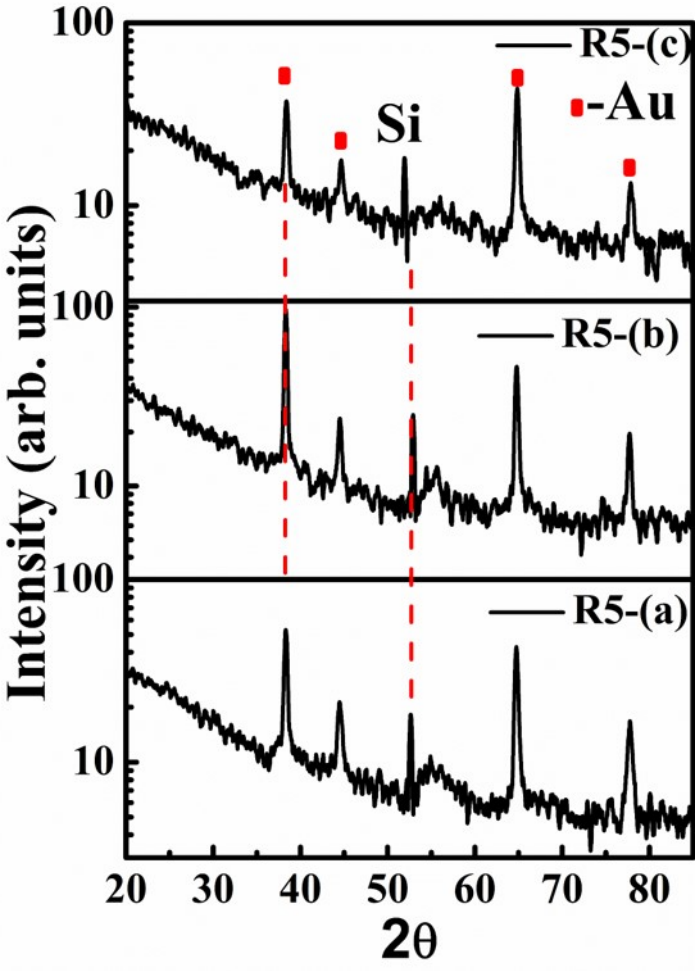

FIGURE 6.8: The GI-XRD pattern of a) R_5, b) R_5-(i) and R_5-(ii) pre and post thermal annealing of the RRAM devices.

6.4.2 I V or switching characteristics of the devices

The DC switching characteristics of the R_5 series (pre and post annealing) devices are shown in *Figure* 6.9. The obtained set voltages are 1.0, 1.5 V and 2.6 for R5, R_5-(i) and R_5-(ii) devices respectively. Similarly, the reset voltages are 0.5 V, 0.5 V and 0.7 V for the devices R_5, R_5-(i) and R_5-(ii) respectively.

In all the cases, the current compliance is kept constant at 1 mA in set process to avoid the permanent breakdown of the thin dielectric layer. From the first set of curves of each device, different slopes are observed in set and reset curves. The effects of annealing may be attributed to the remnant filaments in the switching layer. The formation of these filaments may be attributed to the conduction and slope variations in the set curves of the RRAM devices. Further, not much of difference is found in reset voltages as compared to the set voltages but the reset currents are found to increase as 2.0 mA, 1.2 mA and 10.0 mA for the

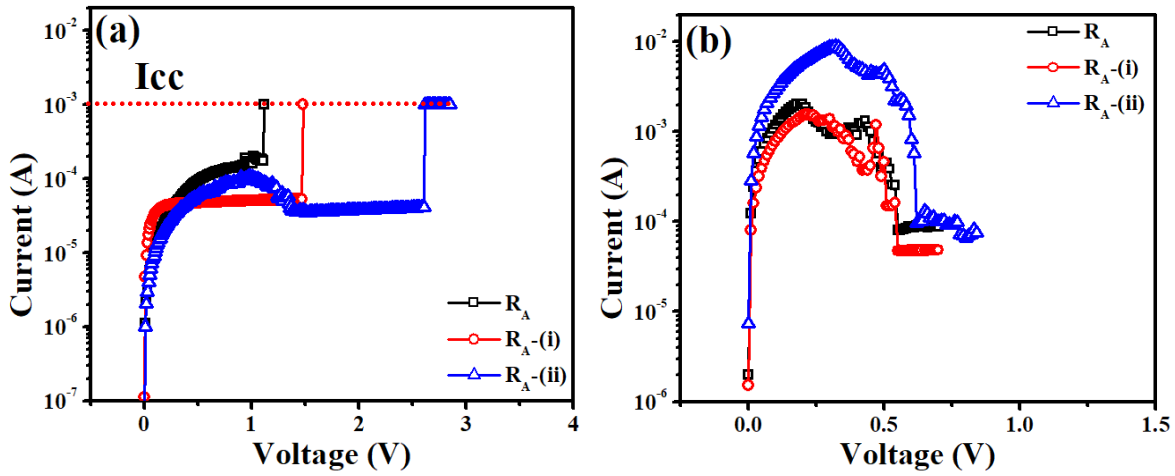

FIGURE 6.9: I-V Characteristics showing the RS behavior of R_5 series (pristine and annealed) devices a) Set curves and b) Reset curves.

R_5, R_5-(i) and R_5-(ii) devices respectively.

The annealed devices are found to be switching at higher voltage (set and reset operations) levels when compared to the pristine devices. Here, it is evident from the reset current that it also depends on the previous set curve to get reset (or switch back to HRS of the RRAM device). In earlier reports, it was suggested that the effects of annealing will improve the stoichiometry and also reduce the defects in the film. Due to thermally induced inter diffusion of oxygen ions and vacancy defects[15]. This is consistent with the existing reports and similar effects have been observed in the present study[16]. Furthermore, the endurance cycling has been performed for these devices and the data is shown in *Figure* 6.10. The effects of annealing are evident from the improvements seen on the performance of endurance cycling, of resistance of the RRAM devices. Then it is also found that the curves are more precisely controlled by following the same conductive filamentary paths for the set operation in a similar manner that occurred in the pristine devices. The unipolar resistive switching behaviour observed in crossbar structures originates from the formation/rupture of a few nanometer-sized filament like percolation paths [17,18]. The processes are discussed in previous chapters.

These percolation paths are trap-assisted tunneling trajectories through the defects, which are generated or recombined according to suitable probabilities depending on the local electric fields and defect structures. This is one of the models to explain the conduction mechanism in the switching layer. Some of the reports suggest that the progressive formation/rupture of the filaments by the conductance quantization under voltage sweeping

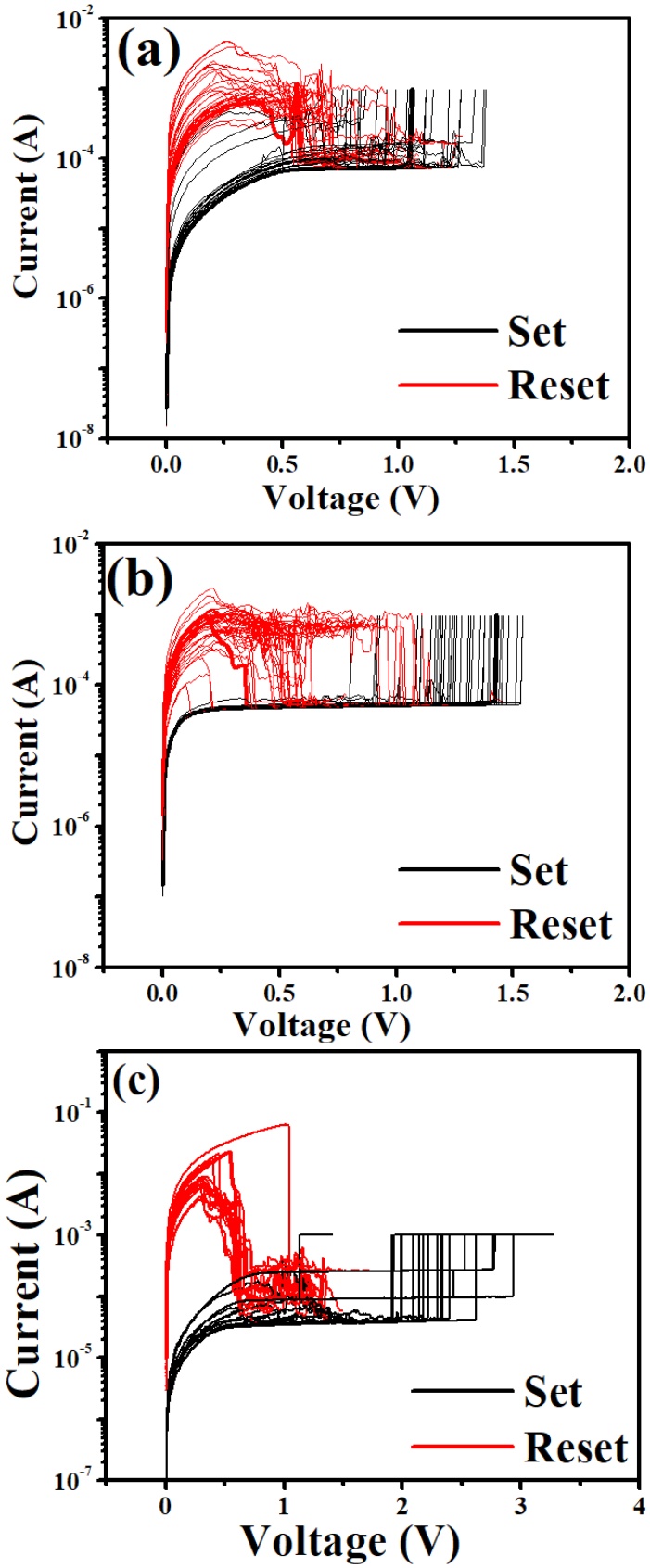

FIGURE 6.10: The endurance cycling a) R_5, b) R_5-(i) and R_5-(ii) of the RRAM devices (black represents set curves and red for reset curves.

mode[19-21]. The electrochemical reaction results in the formation of CF (set operation) and joule-heating-assisted oxidation followed by the diffusion of metal ions or oxygen vacancies (V_o) under the concentration gradient and the applied electric field for the reset operation[4,22,23]. In our study also, devices exhibit the similar kind of behavior for pre-annealed devices. Interestingly, the variation is found to be reduced for the post annealed devices. Hence, the R_5-(ii) devices perform good endurance cycling but the variation in set voltages is expected to depend on the length and thickness of the filamentary paths for each set operation.

The sample annealed at 500 ^oC (R_5-(ii) device) showed prominent behavior in resistive switching performance. It may be concluded that the annealing temperature results in increase in grain boundaries (GB), which act as current leak paths for switching RRAM devices[24]. The aggregation of oxygen vacancies with different charge (V_O^+,V_O^{2+}) states may be interpreted as the formation of conducting filaments for set operation and similarly distribution (depart) of them as reset operation in deciding the switching characteristics of RRAM devices[25]. To understand the conduction mechanism, a schematic view of the R_5-(ii) device is shown in *Figure* 6.11 (a), where (b) and (c) are the set and reset operation respectively. The oxygen ion moves/drifts towards electrodes or scatters in the film during set operation by the external applied electric field. These positively charged oxygen vacancies make way for filamentary paths for the conduction during the set operation. In contrast, the filaments can rupture/break back by filling the vacancies by oxygen ions during the reset operation. Hence, it can be understood that the scatter and refill of the oxygen ion is responsible for the resistive switching [9].

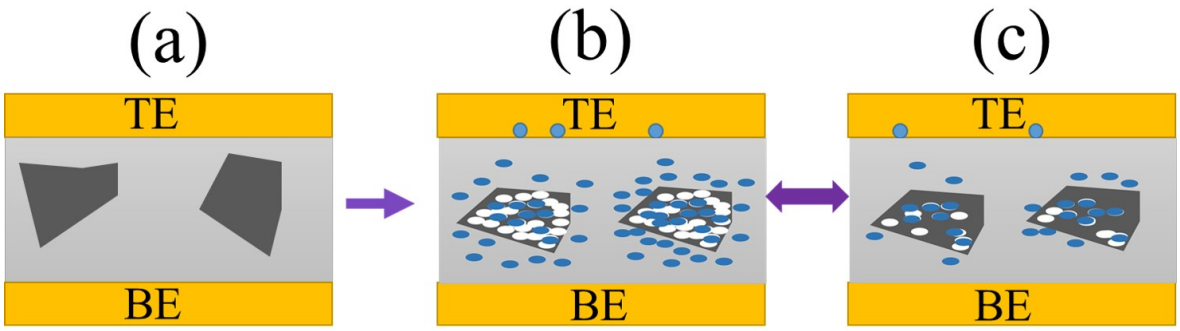

FIGURE 6.11: The schematic view of conduction mechanism for R_5-(ii) RRAM device (the blue circles represent the oxygen ions and the white circles represent the oxygen vacancies).

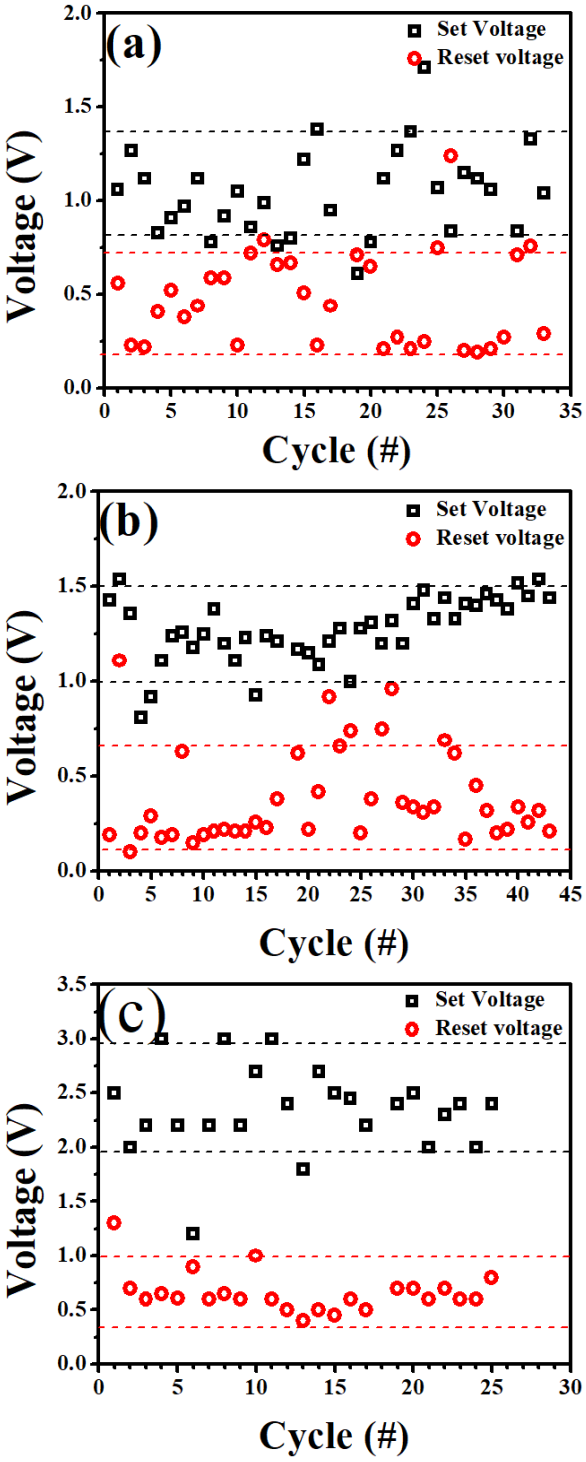

FIGURE 6.12: The set and reset voltages variation as the endurance cycles for a) R_5, b) R_5-(i) and c) R_5-(ii) of these RRAM devices.

Furthermore, the discrimination between the two stable states (on as set and off as reset) is clearly distinguished but it has higher set and reset voltages. As mentioned above, the reset currents are also little higher than remaining RRAM devices. Hence as expected, the

annealing effects improve the stoichiometry of the film and enhance the performance of devices[16]. The effects of the annealing are evident and also clearly indicate the improvement and uniformity of set and reset voltages for R_5-(i) and R_5-(ii) RRAM devices. By extracting/plotting the distribution of the set and reset voltages versus numbers endurance cycles are shown in *Figure* 6.12. The overlap between SET and RESET bands has decreased with increasing voltage

To analyze the performance of these devices, comparison is performed by defining a band of voltages for set and reset operations,$\Delta|Vset|$ and $\Delta|Vreset|$, over a number of endurance cycles. The $\Delta|Vset|$ is 1.03 V, 1.37 V and 2.33 V for R_5, R_5-(i) and R_5-(ii), respectively while the $\Delta|Vreset|$ values are 0.43 V, 0.38 V and 0.66 V for the same devices. The switching parameter of set and reset voltages, range of distribution for these devices is illustrated by plotting the cumulative distribution probability as shown in *Figure* 6.13.

In continuation of the above discussion and to investigate and analyze the conduction mechanism of charge transport for these devices, double log I-V plots are shown in *Figure* 6.14. From slopes, of linear fitting curves, of the devices in the LR and HR states, the LR states are nearly equal to one which indicates that the devices are Ohmic (slope $\sim$ 1) in nature. This Ohmic behavior in the LR state supports the filament formation in resistive switching. It is evident that the high voltage region (> 0.5 V) of the HR state shows non-Ohmic behavior for these devices. Significantly, the slope is lower for R_5-(i) in comparison to R_5-(ii) and for R_5 device it is close to Ohmic conduction in higher voltage region.

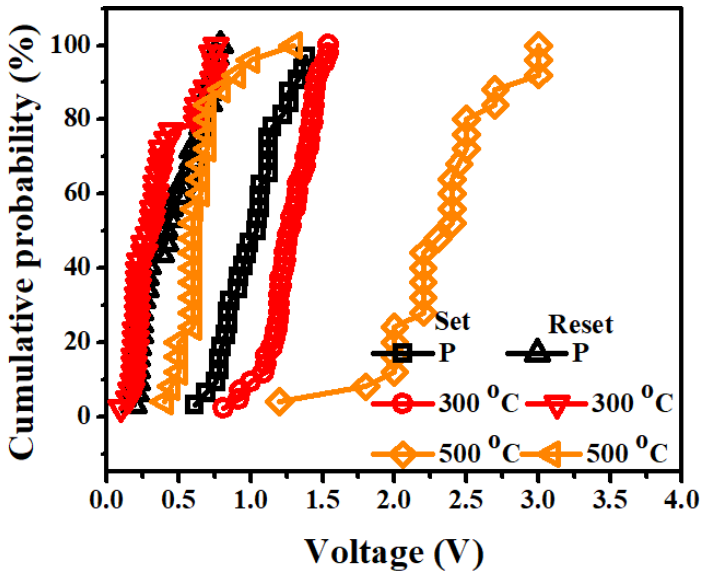

FIGURE 6.13: Cumulative probability of V_{set} and V_{reset} voltages of the devices R_5, R_5-(i) and R_5-(ii).

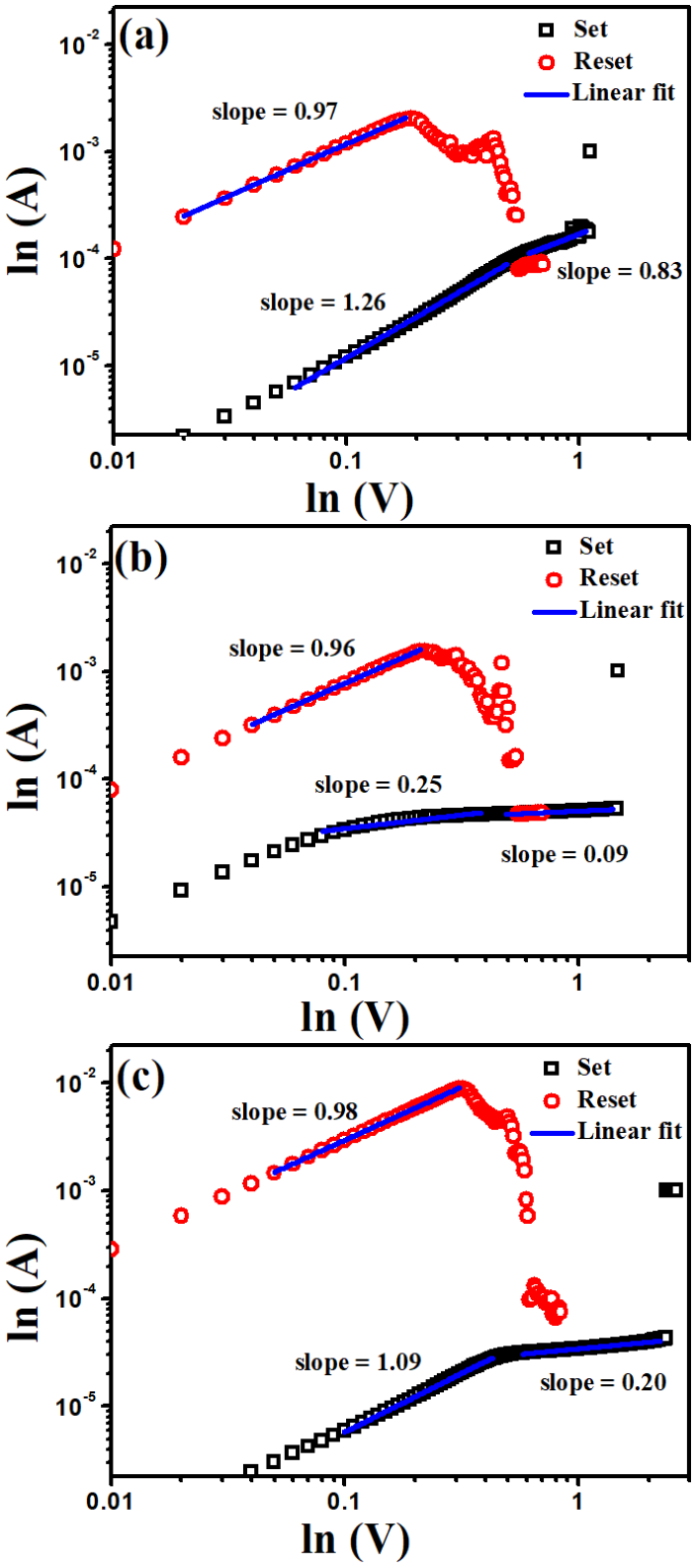

FIGURE 6.14: (a), (b) and (c) the double log I-V plots, linear fittings for the devices R_5, R_5-(i) and R_5-(ii) respectively.

Retention time measurements for LRS and HRS resistances (R_{LRS} and R_{HRS})were performed for all the RRAM devices and the data is shown in *Figure* 6.15. These measurements

were performed for a duration of $> 10^4$ s and the voltage pulsed input of amplitude 100 mV, width of 100 µs. It is observed that all the RRAM devices are showing good retention time. The R_5-(ii) device has retained its state for longer times but for times $> 10^3$s, a small dip of variation in R_{HRS} is noticed. R_{LRS} is very stable throughout the measurement for all the devices. The resistance ratio (R_{HRS}/R_{LRS}) is 40 and 50 for R_5 and R_5-(i) devices respectively. Similarly, the resistance ratio of the R_5-(ii) device 125, which is almost 3 times higher than the other devices. From this, it is evident that the annealing process improves the resistance ratio of the RRAM devices. It is noteworthy to mention here that same effects were observed (*Figure* 6.12) for the device (R_5-(ii)), getting higher switching voltages (set and reset) and less variation in the switching voltages as the endurance cycling number progresses. It is also consistent and coinciding with the above discussion that the annealing improves the switching performances of the HfO_x based RRAM devices.

To investigate the role of the oxygen vacancies for the RRAM device for pre and post thermal annealing effects, the PL measurements are employed. The PL peaks are de-convoluted using a peak fit program to identify the defects in these films. Mainly, the major peaks at energy of 2.4, 2.7, 2.8, 2.9 eV and 3.1 eV are considered to fit the curve. The PL spectra are shown in *Figure* 6.16 (a-c). It is known from the earlier reports that the PL originates in HfO_x from deep level defects due to oxygen vacancies and interstitial states [9,19]. These O vacancies are electron traps below the conduction band edge (E_c). It was reported that the PL peaks corresponds to the different types of poly O vacancies and F- centers in HfO_2 [26]. The intensity of PL emission from HfO_x films is found to be decreased initially and then increased for 500 ^{o}C. However changes in the intensity are not considered here for any quantitative estimates in view of possible sample to sample variation. The detailed shifts of energy in peak position of the RRAM device are listed in *Table* 6.4.

TABLE 6.4: The details of peak energy for pre and post thermal annealing of the RRAM devices.

Device name	Energy of peak position (eV)				
R_5	2.46	2.71	2.85	2.99	3.13
R_5- (i)	2.50	2.68	2.80	2.94	-
R_5- (ii)	2.49	2.71	2.87	3.07	3.18

Here, we observe a small but very consistent blue shift together with an increase in intensity upon annealing temperature, which suggests that the electronic excitations induced

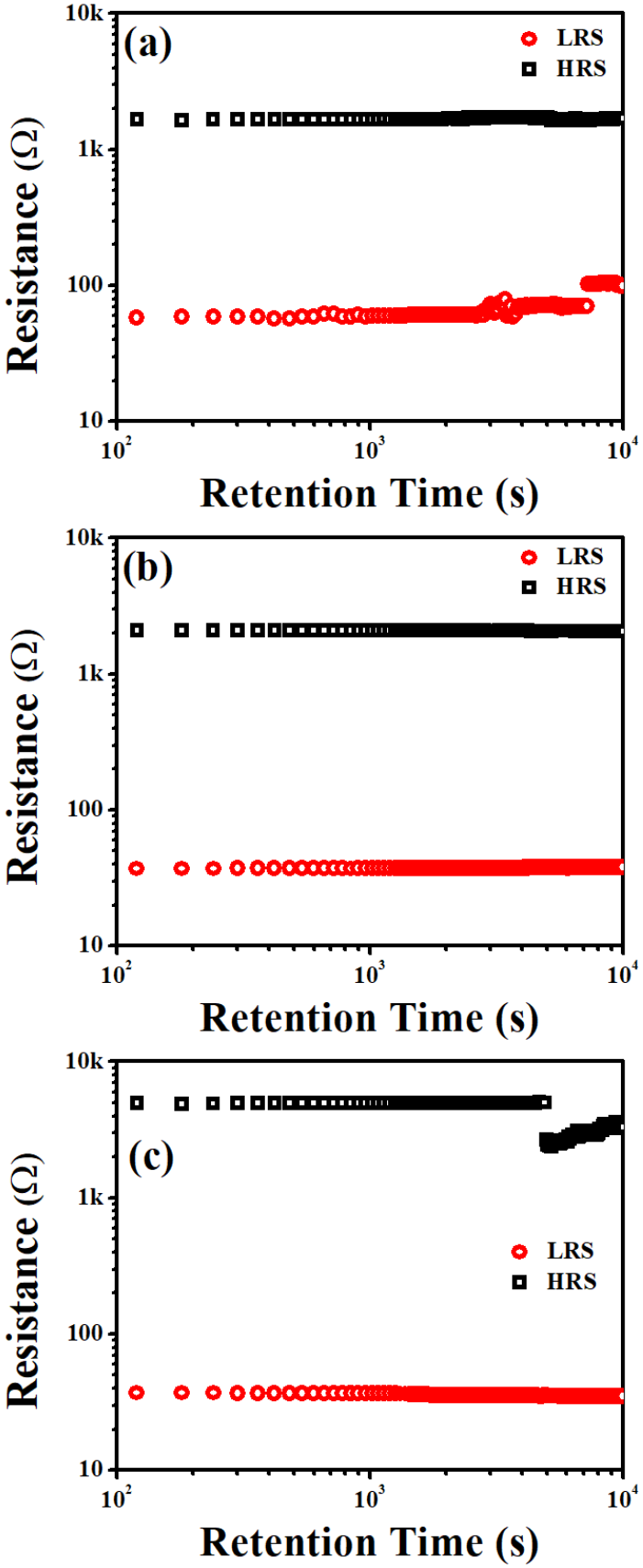

FIGURE 6.15: Retention curves of device (a) R_5, (b) R_5-(i) and (c) R_5-(ii).

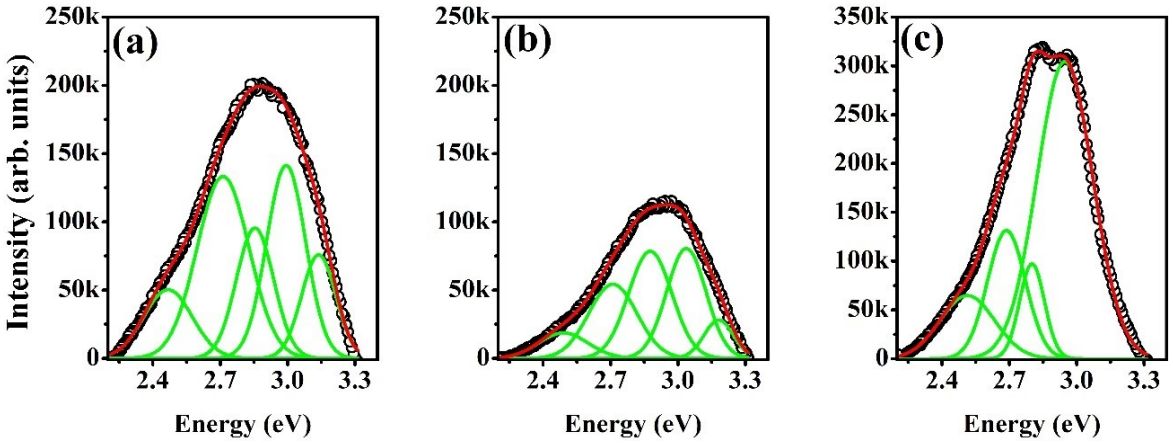

FIGURE 6.16: The Photoluminescence spectra of RRAM devices a) Pristine (R_5), b) 300 ^{o}C (R_5-(i)), c) 500 ^{o}C (R_5-(ii)).

by thermal treatment caused annealing of defects. This is further supported by the direct observation of the improved performance of RRAMs devices annealed at 500 ^{o}C.

6.5 Effects of the SHI on switching performance of the RRAM devices

6.5.1 Characterization of the RRAM devices

To elucidate the microstructure and surface morphology of the films (prior to top electrode deposition) that existed pre and post SHI, FESEM measurements were performed. *Figure* 6.17 shows the FESEM images of the RRAM devices of pre and post ion irradiation. It is observed that the surface morphology changes with increase in the fluence. It is observed that the particles are getting defragmented and get uniformly distributed over the surface and their size decreases as fluence increases. It can be interpreted as the ion induced grain fragmentation in the HfO_x films and is consistent with our earlier reports[14,13]. There are few research reports in the literature on ion-induced grain fragmentation in fluoride and HfO_2 thin films. As we know SHI undergoes electronic energy loss within the films when these pass through it. This ion-induced electronic energy loss within the film plays an important role in the observed grain fragmentation and morphological changes. Actually, SHI irradiation leads to a property, called ion-induced smoothing of surfaces.

The PL measurements were performed for the RRAM device before and after SHI irradiation. The excitation energy was chosen to be 3.5 eV, which is less than the band-gap of

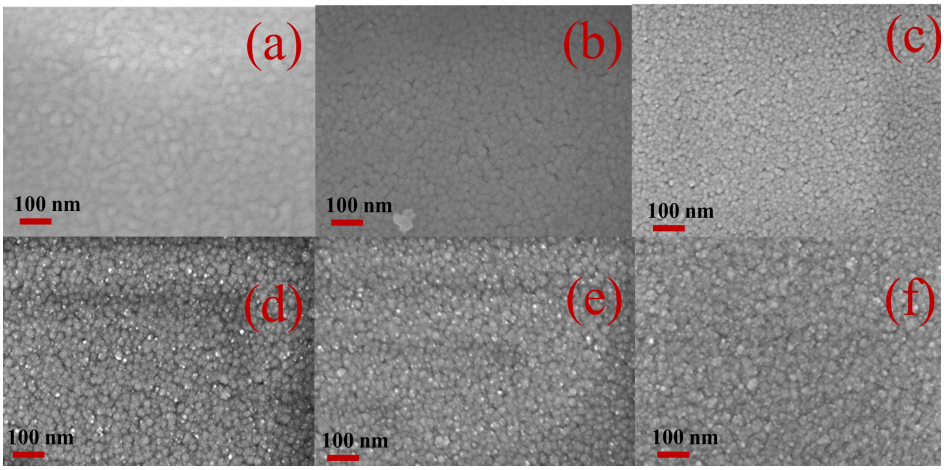

FIGURE 6.17: FESEM images of the (HfO_x/Au/Si) RRAM devices (a) Pristine, (b) 5E10, (c) 1E11, (d) 5E11, (e) 1E12, and (f) 5E12 ions/cm^2.

HfO_2 [12,25]. PL spectra and the deconvoluted peaks for the samples are shown in *Figure* 6.18.

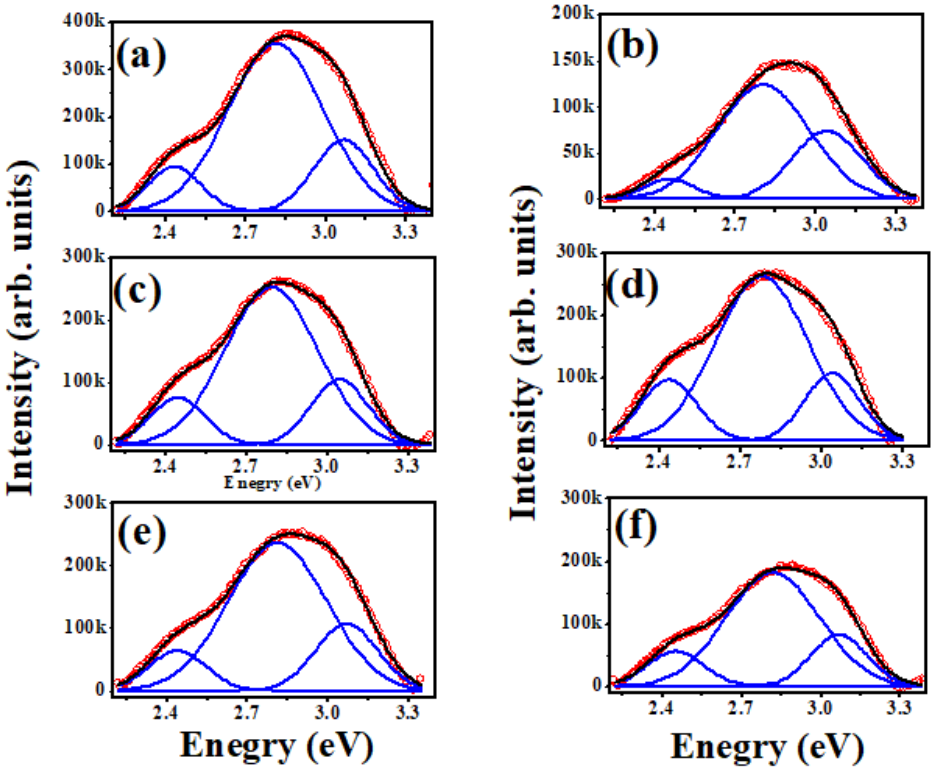

FIGURE 6.18: The PL spectra of the RRAM devices (a) Pristine, (b) 5E10, (c) 1E11, (d) 5E11, (e) 1E12, and (f) 5E12 ions/cm^2 (solid lines indicate fitting and de-convoluted peaks).

The fitting is performed by using a peak fit program for identifying the oxygen related vacancies in the thin films. Before irradiation, the peak positions are at 2.4 eV, 2.9 eV and 3.0 eV for Pristine devices. The intensities of these peaks are found to decrease as fluence

increases. The changes in the intensity can be interpreted as the changes in the density of oxygen related vacancy type defects in the dielectric. The defect peak position at 2.9 eV might be related to the positive singly charged oxygen vacancy. The oxygen related defects in HfO_x films were earlier reported and most of those studies are consistent with our previous and present work[14].

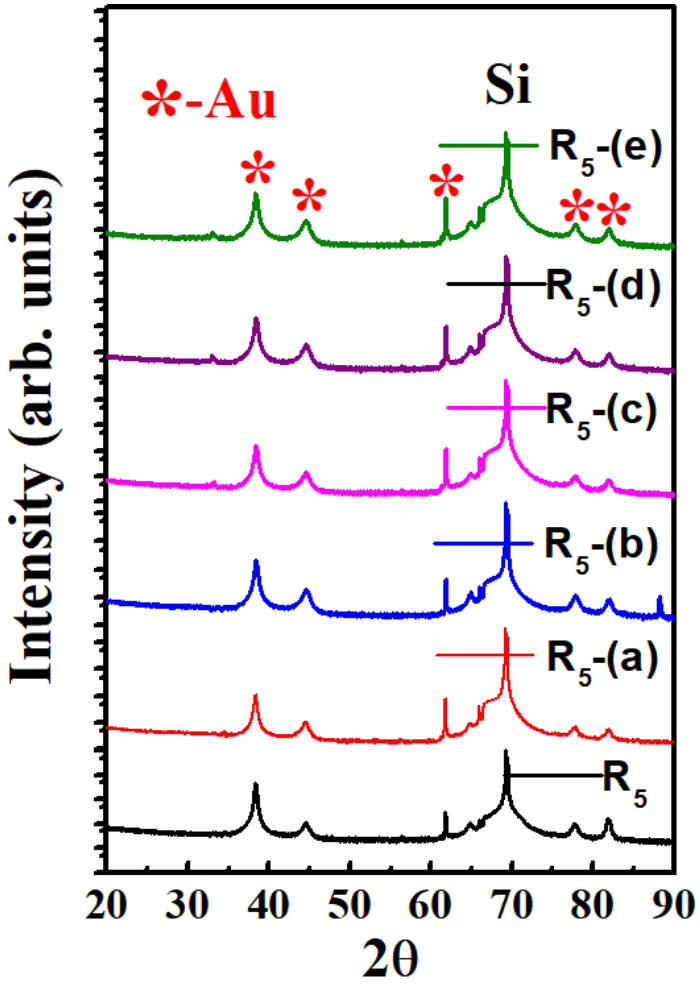

FIGURE 6.19: GI-XRD spectrum of the RRAM devices (a) Pristine, (b) 5E10, (c) 1E11, (d) 5E11, (e) 1E12, and (f) 5E12 ions/cm^2.

To study further, the effects of energetic ions on the crystal structure of these films, XRD measurements were performed. From the FESEM images it is observed that the particle or grain size of the HfO_x thin films decrease as the fluence increases (5E10 to 5E12 ions/cm^2). It is expected that the defragmentation of the HfO_x is favoring for surface smoothing as fluence increases. More interestingly, all these films revealed the amorphous nature from GI-XRD analysis and the GI-XRD patterns are shown in *Figure* 6.19. Only, the background Au and Si substrates peaks were obtained. Again, the introduction of monoclinic phase was observed

when RF sputtered HfO_2 was subjected to SHI irradiation however such a crystalline phase is not observed, within the experimental limits, in case of the e-beam evaporated HfO_x films.

6.5.2 The effects on switching performance of the RRAM devices

The sample specifications of the available RRAM devices with respect to SHI irradiation have been given below in *Table* 6.5.

TABLE 6.5: Details of the RRAM devices for SHI irradiation.

Ion Energy (MeV)	Average stopping power		Irradiation Fluence	Device Name
	Electronic	Nuclear		
	(S_e)(keV/μ)	(S_n)(keV/μ)	(ions/cm^2)	
Ag,120	2.48 X 10 ^{4}	1.36 X 10 ^{2}	Pristine	R_5
"	"		5E10	R_5-(a)
			1E11	R_5-(b)
"	"		5E11	R_5-(c)
			1E12	R_5-(d)
"	"		5E12	R_5-(e)

The I-V Switching curves of the crossbar (Au/HfO_x (30 nm)/Au/Si) structure with an active area of 10 μm $\times$10μm RRAM device are shown in *Figure* 6.20. The set and reset voltages are 0.98 V and 0.59 V respectively for the pristine (R_5 device. Possible reasons for the observed uni-polar switching behaviour are discussed in previous chapters.

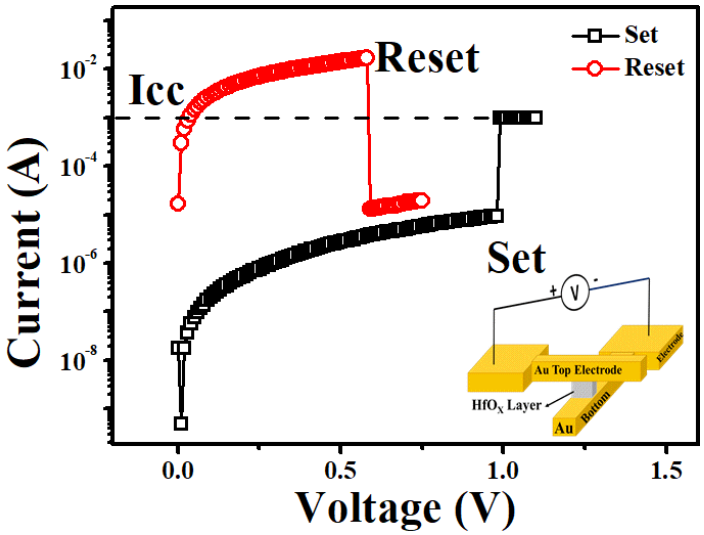

FIGURE 6.20: I-V Characteristics showing the RS behavior of pristine RRAM device.

Here, the set and reset curves of the pristine and irradiated RRAM devices have been shown in *Figure* 6.21 (a) and (b) respectively. The set and reset voltages have been found to increase as fluence increases for the RRAM devices. It may be expected that the redistribution of oxygen vacancies is responsible for the formation of filamentary like conductive path in the insulating material. The formation and rupture of these filaments in the RRAM devices lead to the switching between two stable resistive states.

The transition from HRS to LRS by formation of conductive filaments is Set operation while breaking/rupture of them leads back to HRS from LRS resulting in reset operation are clearly observed. The *Figure* 6.22 (a) and (b) show the average values of V_{Set} and V_{Reset} distribution as a function of fluence. Most importantly, the ranges of V_{Set} and V_{Reset} distributions increasing up to a fluence of 5 x 10^{11} ions/cm^2, possibly due to ion induced annealing effects [13,27-29]. It is worthwhile mentioning that SHI can play a vital role in determining the structural, optical and electrical properties of the thin films. However, beyond a critical fluence (5 x 10^{11} ions/cm^2) perhaps filling of oxygen vacancy by ion irradiations result in the high resistance and set voltages. Here it is important to note the contrast that the switching voltages increase in case of SHI irradiated HfO_x based device whereas the switching voltages decreased in case of the SHI irradiated HfO_2 devices studied in the previous chapter. This is an important difference and is consistent with the explanation given in terms of pre-existing defects and their role in the formation of conducting filaments.

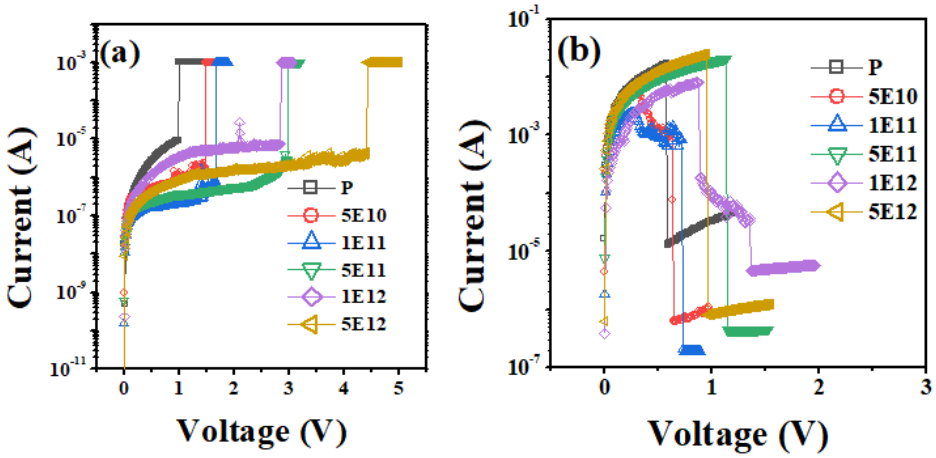

FIGURE 6.21: I-V Characteristics showing the RS behavior of RRAM device (pristine and irradiated at different fluence) devices: a) Set curves and b) Reset curves.

The randomness/fluctuations of the set and reset voltages may be expected from uncertainty of the generation of oxygen vacancies or metallic ions filamentary paths for the

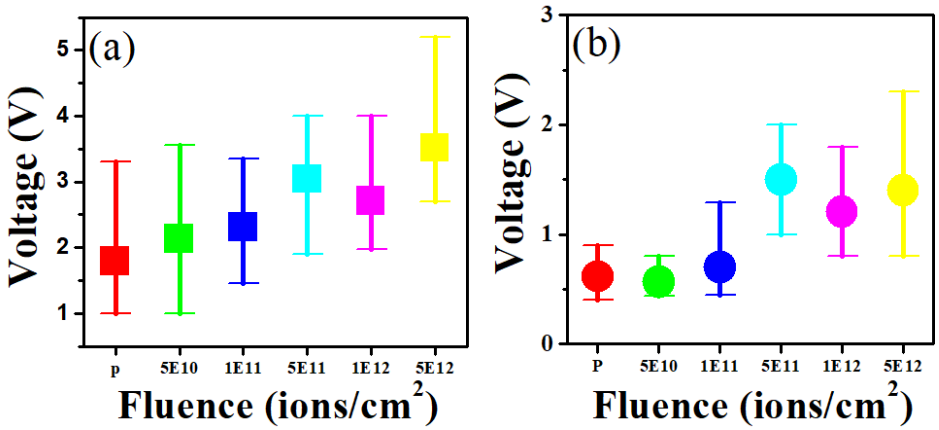

FIGURE 6.22: The distribution of set voltages of pristine and irradiated of (a) set and (b) reset devices (Symbol represents the mean value of switching voltage and the bars represent corresponding minimum and maximum values).

conduction in the switching layer [9,19]. The ion irradiation also plays a significant role in tuning the switching parameters of the RRAM devices [13,30]. While passing through the film, the ion interacts with it and anneal or create the defects along its path. Sometimes these defects can improve or deteriorate the performance of the devices [13,23,30]. It is observed that, post ion irradiation, the mean set voltages increase (see in *Figure* 6.22 (a)) whereas the reset voltages are found to decrease up to certain fluence and then start increasing.

This can be attributed to the possible annealing of defects by electronic excitations caused during SHI irradiation. This effect may lead to an improvement of the device performance. A similar kind of behavior was observed for MOS devices in our previous work [30,31] and the RRAM work in the previous chapter [32]. As expected, and explained in our earlier chapters, after the initial uniform ion irradiation reaches a critical fluence, it is an overlap of the ion tracks on the same device. Therefore, the next ion that is incident after this critical fluence, will not find a fresh spot and hence will fall on an already irradiated area. Multiple hits by ions at the same points are considered to be responsible for the creation of excess defects. SHI irradiation can cause annealing or creation of defects and affect the interfaces as a function of fluence. The creation of more defects may lead to poor switching performance of the devices. It is noticed that the overlapping of set and reset voltages increase as fluence increases as shown in *Figure* 6.23. More interestingly, it is observed the that increase in mean set voltages signifies the ion-induced annealing effects at all ion fluences.

To further understand the percentage of variation and to estimate the variation of the set and rest voltages of these devices, a statistical analysis of the cumulative distribution

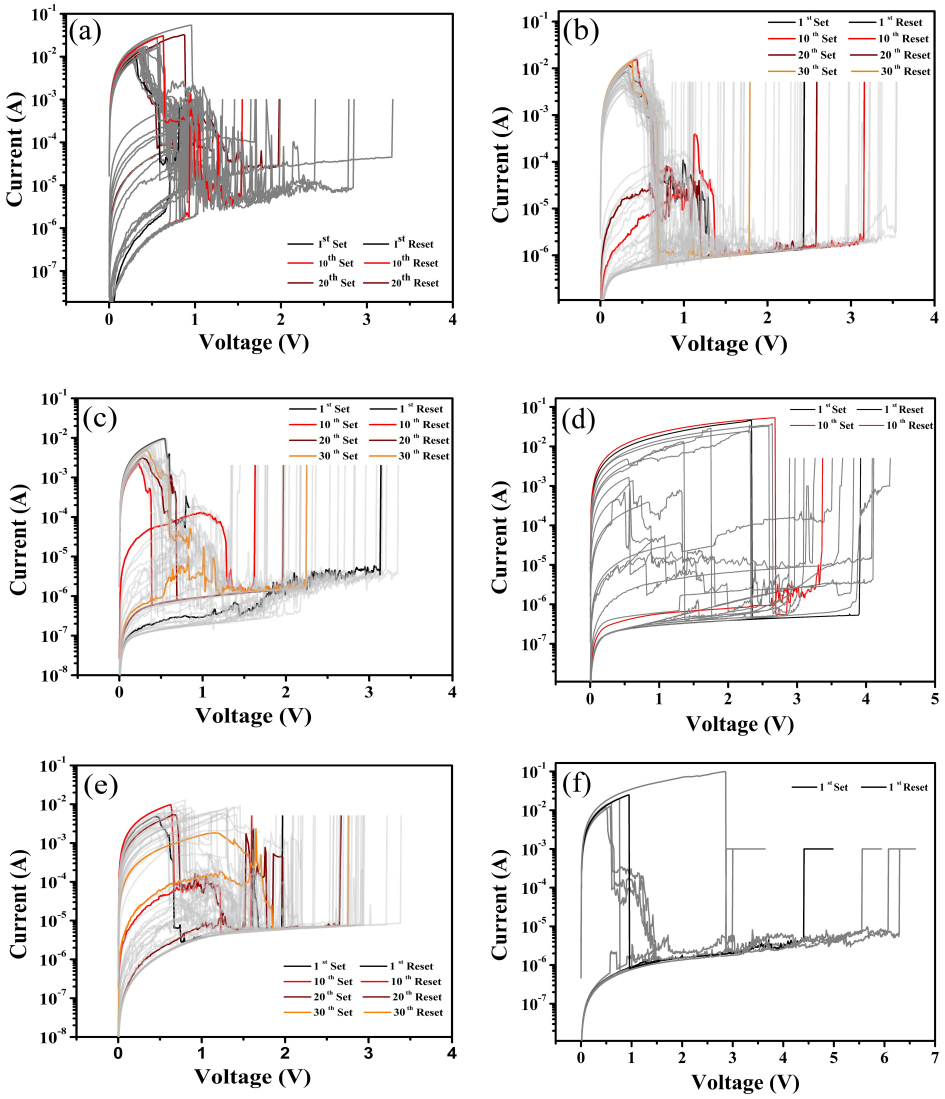

FIGURE 6.23: The endurance cycling pre and post irradiation of the RRAM devices (a) R_5 (pristine), (b) 5E10, (c) 1E11 and (d) 1E12 ions/cm^2.

probability has been carried out and shown in *Figure* 6.24. It is noticed that the occurrence of the reset voltages is more stable and less prone to distribution at lower fluences than the set voltages. Similarly, to elucidate the influence of SHI on the reset current of the RRAM devices, the CDF is shown in *Figure* 6.25. Here, it is found that it follows a similar trend as that of the reset voltages, i.e. a decrease in reset current up to a critical fluence and further increase with fluence (see in *Figure* 6.23 (d-f)). Hence, it may be inferred that the lower fluence shows the effects of annealing on the RRAM devices. It is as expected that the formation of filamentary conductive paths takes place at higher set voltages. It is contrary in the case of reset voltages and currents to that of set voltages. Hence, the power dissipation is calculated to analyze overall performance of the RRAM devices. Here, the average values

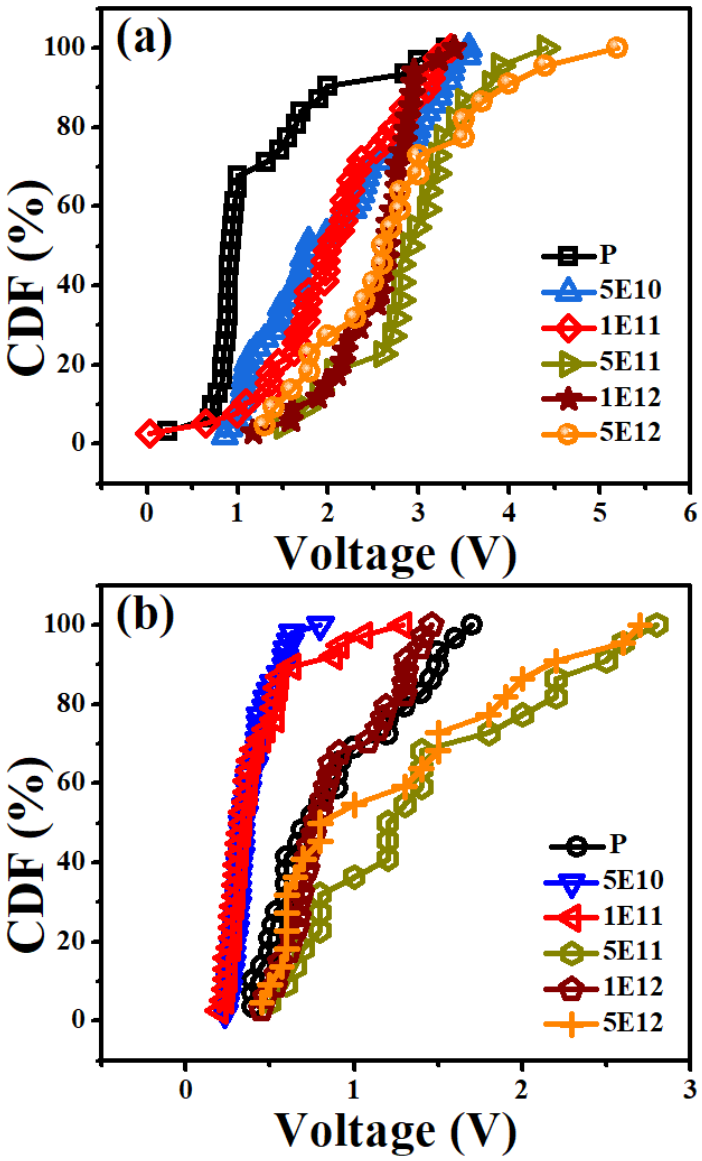

FIGURE 6.24: The Cumulative distribution probability of pristine and irradiated devices. (a) set voltages and (b) reset voltages.

of set and reset voltages and rest currents are given in *Table* 6.6.

TABLE 6.6: The details of switching parameters of the HfO_x based RRAM devices (pre and Post SHI irradiation).

Parameters	Fluence (ions/cm^2)					
	0 (Pristine)	5E10	1E11	5E11	1E12	5E12
Set voltages (V)	1.24	2.05	2.06	2.8	2.53	4.2
Reset voltages (V)	0.88	0.38	0.4	1.2	0.8	0.8
Reset current (mA)	11	10	4.4	28	6.5	25

As per the above discussion, the observed resistive switching is due to the filamentary formation/rupture (either oxygen vacancies or metallic ions) for set and reset operations.

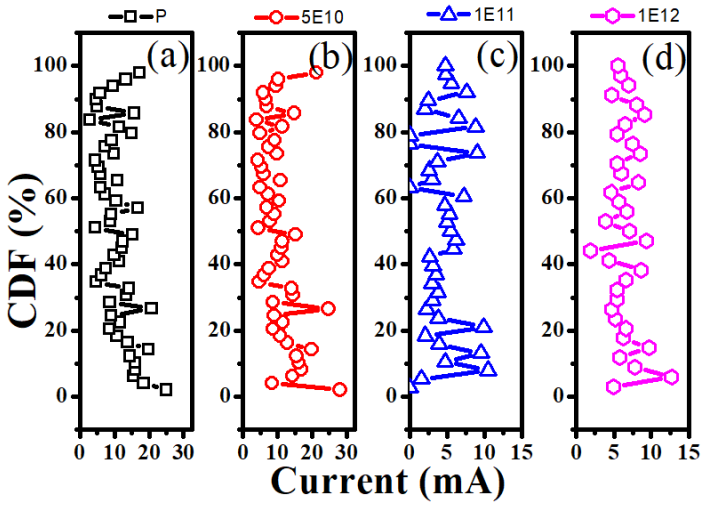

FIGURE 6.25: The CDF of the reset current of pre and post SHI irradiation (a) R_5 (pristine), (b) 5E10, (c) 1E11 and (d) 1E12 ions/cm^2 for the RRAM devices.

To study and understand the conduction mechanism for filamentary paths in the RRAM devices, a linear fitting of the curves logI-logV plots is shown in *Figure* 6.26. The Ohmic nature is observed in LR state for all these devices (pre and post SHI irradiation), which further confirms the filamentary type conduction. Then, the HR state is found to be non-Ohmic.

Retention measurements were carried out to investigate the stability of the data stored at the LRS and HRS for all the RRAM devices. *Figure* 6.27 shows the retention curves of the RRAM devices (pre and Post SHI irradiation). A continuous voltage pulse with an interval of 60 s of a 0.1 V is applied for more than10^4 s to inspect the stability of the state for the devices. The pristine device is found to be unstable at LR state. Whereas, the retention time curves have shown better stability for the post SHI irradiation, except for a sudden jump observed for the fluence of 1E11. Hence, it is noteworthy that the low dose SHI can improve the device stability and may be used in storage memory devices for retaining the data for long years without any distortion.

It is important to note that these results are in contrast with the results presented the in previous chapter. The switching voltages (currents) decreased with increase in RF sputtered HfO_2 based RRAMs whereas the switching voltages/currents increases with in case of e-beam based deposited HfO_x based RRAMs devices. RF sputtered films are of good stoichiometry whereas the e-beam deposited films are of sub-stiochiometric. The interdifussion of "O" vacancy is expected to be quite different in the sub-stiochiometric films, SHI/thermal annealing has improved the stiochiometry of the e-beam deposited films. however it is

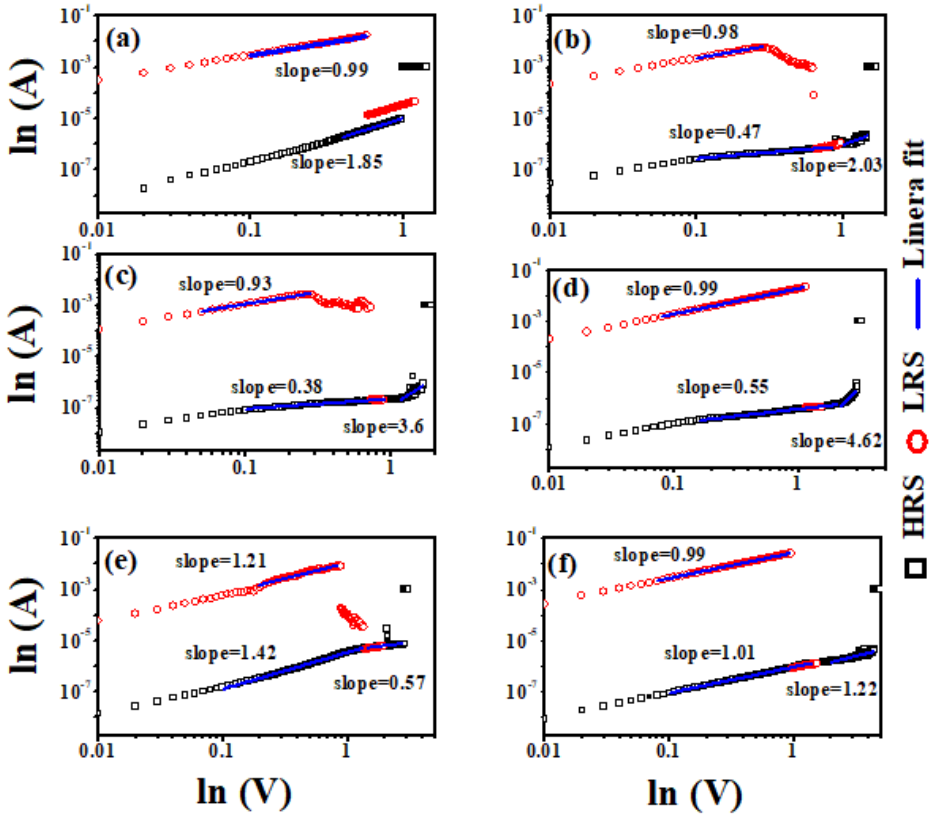

FIGURE 6.26: The double log I-V plots, linear fittings (a) R_5 (pristine), (b) 5E10, (c) 1E11, (d) 5E11, (e) 1E12 and (f) 5E12 ions/cm^2 of the RRAM devices.

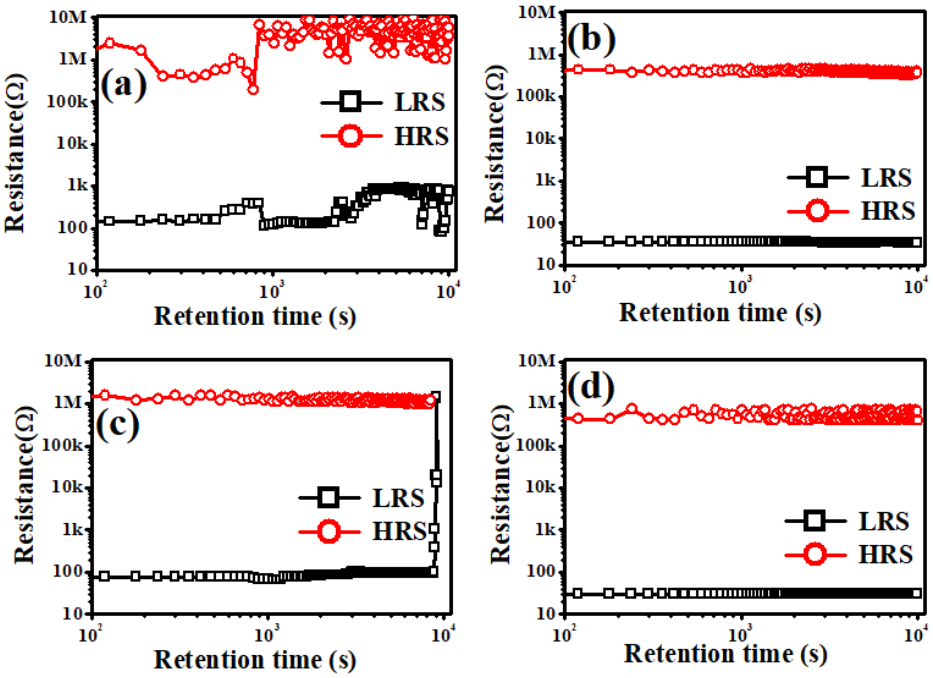

FIGURE 6.27: The retention time measurements (a) Pristine, (b) 5E10, (c) 1E11 and (d) 1E12 ions/cm^{2}of the RRAM devices.

very important to note that the main observation is the overlap between set and reset bands which increase with increase in ion fluence. It is demonstrated that the low fluence SHI can improve the device performance in both (RF & e-beam) cases.

6.6 A study: a role of Interfacial Layer (IL) on the switching characteristics of RRAM devices

Three sets of RRAM devices with different top electrodes are studied and presented. The detailed structure of devices is given in the *Table* 6.7.

TABLE 6.7: The details of the different metal top electrode RRAM devices)

Top electrode	Device structure	Device name
Au	$Au/HfO_2/Au/Si$	R_5
Cr	$Cr/HfO_2/Au/Si$	R_6
Al	$Al/HfO_2/Au/Si$	R_7

The schematic of these stacks is shown in *Figure* 6.28. For the sake of clarity, hereafter the devices will be called as R_5, R_6 and R_7 as Au, Cr and Al as TE RRAM devices respectively.

Figure 6.29,displays I-V characteristics, set and reset voltages (representative curves) for the first cycle of each (R_5, R_6 and R_7) of these RRAM devices. We find higher voltages for set and reset operation for the R_7 (Al as TE) devices than that of other devices. The possibility of interfacial layer formation between switching layer and top electrode contact can be expected for the for the Al and Cr metal electrodes[33]. It is well known that Al is easily oxidizable in nature. So it is expected that a thin interfacial layer growth that may lead to the observed increase in overall switching layer thickness. Further it may be interpreted that the thin layer act as an oxygen reservoir and can play an important role in the resistive switching process.

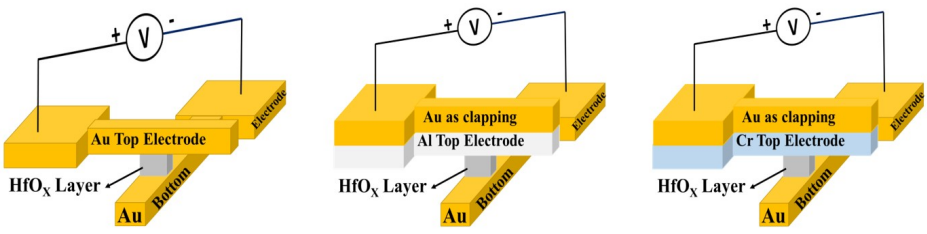

FIGURE 6.28: The schematic sketch of different top electrode RRAM devices.

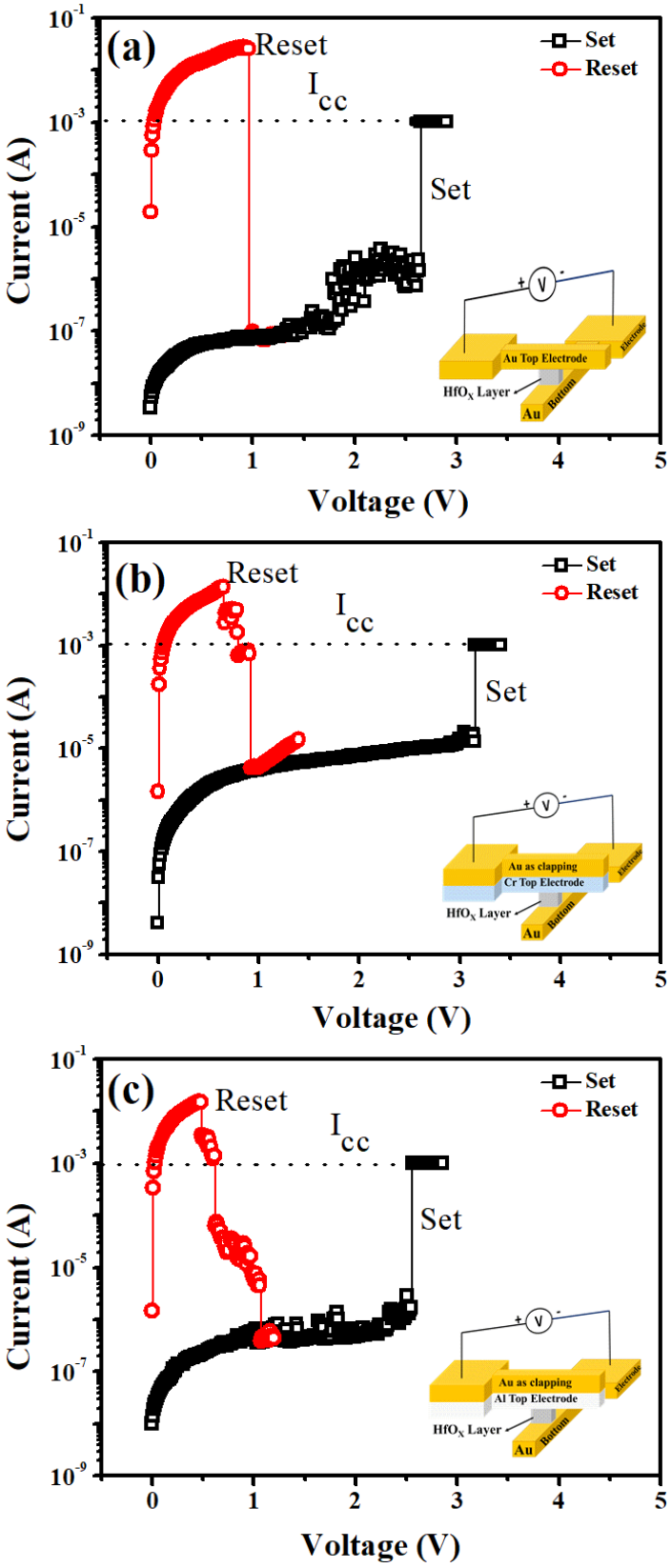

FIGURE 6.29: The set and reset voltage curves of a) R_5, b) R_6 and c) R_7 RRAM devices.

The endurance cycling of the RRAM devices is shown in *Figure* 6.30 (a-c).

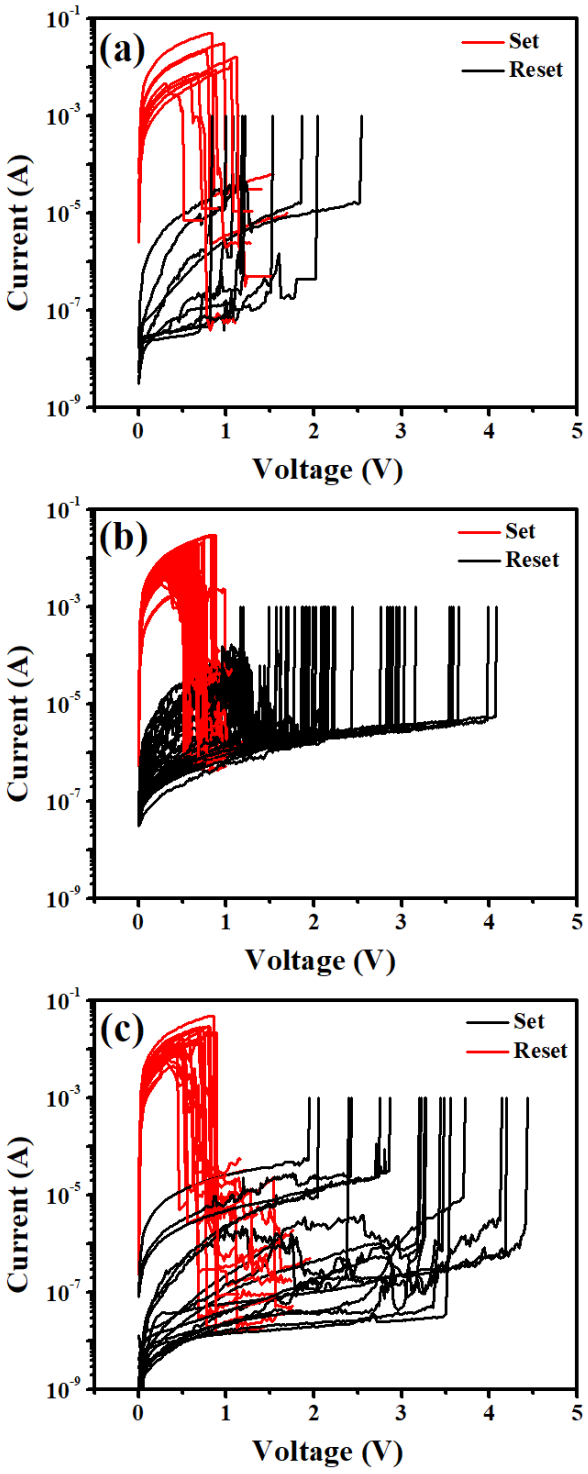

FIGURE 6.30: The endurance cycling of a) R_5, b) R_6 and c) R_7 RRAM devices.

Here, the R_6 (Cr as top electrode) device is found to show good resistive switching behavior. It is exhibiting a greater number of successful switching cycles (endurance cycling)

than the other devices conducted over a 50 cycle of each set and reset operation. As explained earlier, the thin interfacial layer is crucial for the good switching behaviour and it is evident that CrO_x is performing better than the AlO_x.

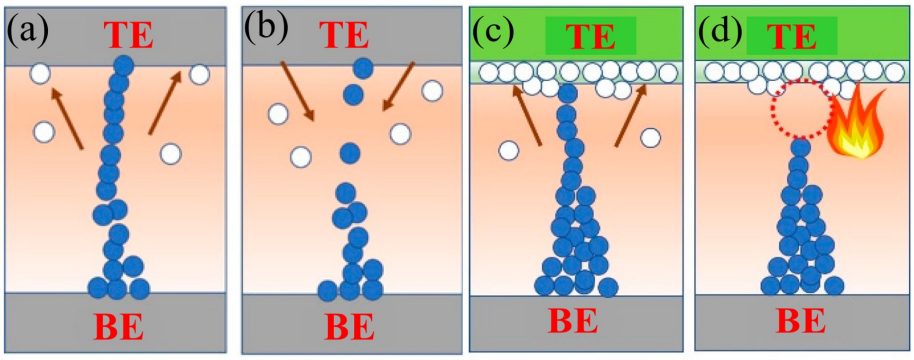

FIGURE 6.31: The schematic view (a) set, (b) reset and (c) Set, (d) reset operation with and with interfacial layer formation for the RRAM device respectively (the blue circles present the oxygen vacancies and the white circles present the oxygen ions).

The *Figure* 6.31 shows the pictorial view of the device with and without thin interfacial layer formation. The noble or inert metals like (Au) are less susceptible to form oxide and to form an interfacial layer. Here *Figure* 6.31(a) and (b) show the set and reset operation for R_5 device (Au as top electrode) respectively. The oxygen vacancies or metallic ions favor the formation of filamentary conductive paths in the dielectric layer for resistive switching. Whereas the oxidizable metal can form the interfacial layer, it can act as an oxygen ion reservoir (see *Figure* 6.31 (c) and (d)). Similarly, (c) and (d) show set and reset operations for the oxidizable metal -electrode based RRAM devices, respectively.

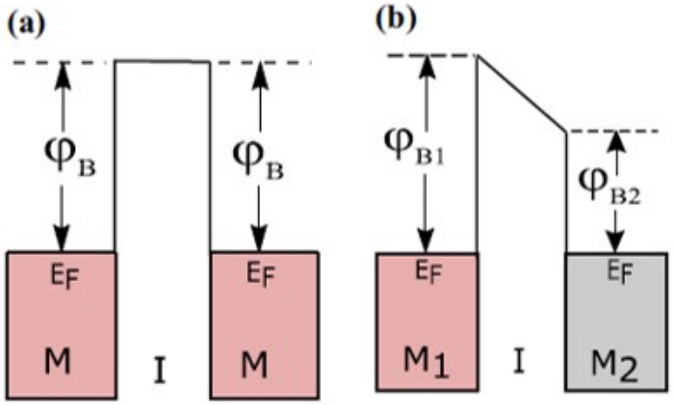

FIGURE 6.32: A pictorial view of the a) symmetric and b) asymmetric metal electrodes energy band diagram.

In other words, it can be understood that the work function of the metal contact with dielectric layer also influences the switching performance of the RRAM device. *Figure* 6.32 shows the pictorial view of (a) symmetric (R_5 device) and (b) asymmetric (R_6 and R_7 devices) metal electrodes work function. Asymmetrical metal electrode has the probability of reducing the potential barrier and the internal tunneling effects are expected in RRAM devices. The symmetric metal electrode is found to show switching at higher set and reset voltages. In contrast, the asymmetric metal combination gives good endurance and it is evident that the interfacial layer enhances the switching behavior of RRAM devices.

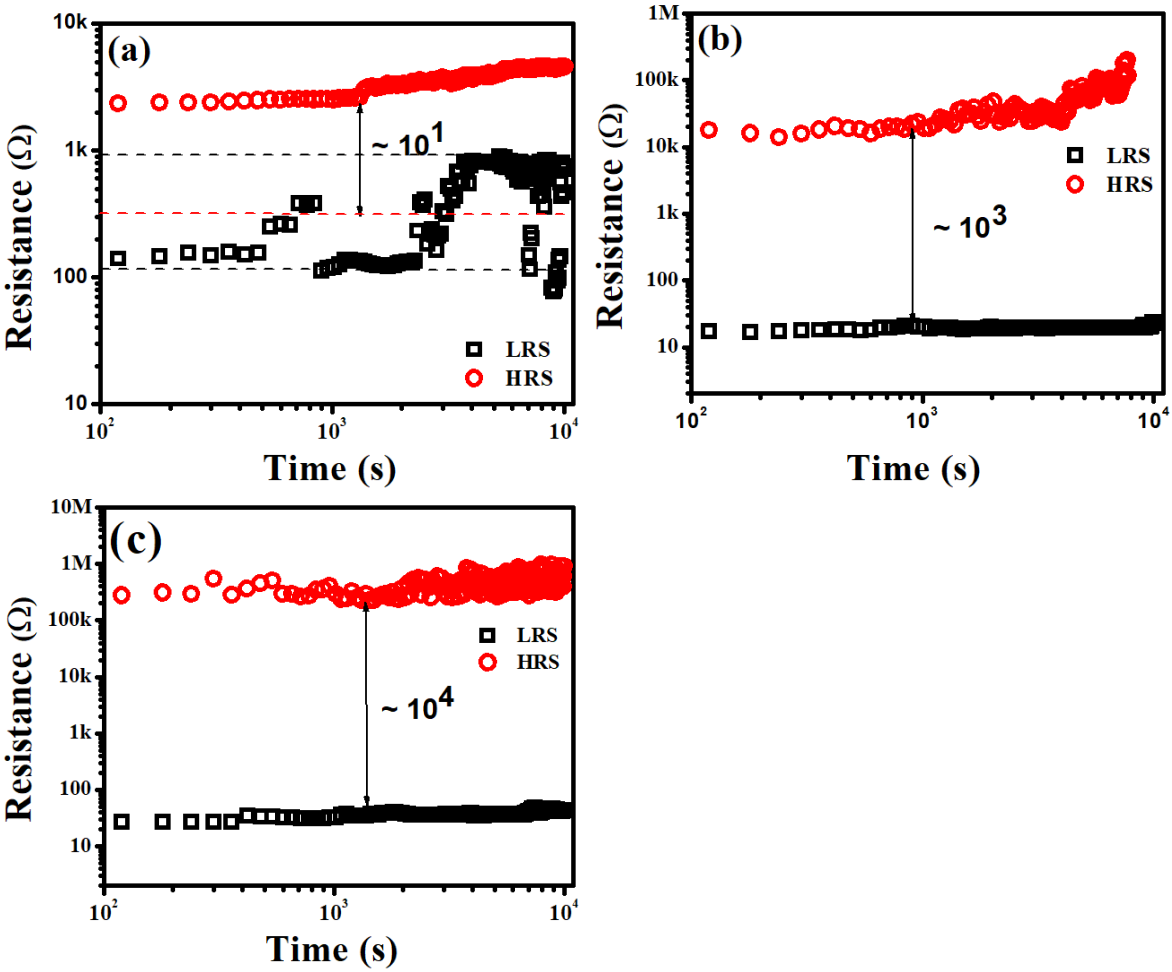

FIGURE 6.33: The retention time (over an interval of 10^4 sec) of a) R_5, b) R_6 and c) R_7 RRAM devices.

It is noticed that R_7 these devices have a greater number of fluctuations/variations in endurance cycling. Furthermore, the R_7 device has higher set voltage and reset current than the R_5 and R_6 devices. To investigate the stability of the data read or write operations for these devices, the retention time tests were performed. The data of the retention time tests

of these devices are shown in *Figure* 6.33 (a-c). It is found to indicate an increase of the HRS with increase of time for the R_6 devices. Significantly, R_7 showed the stable resistance ratio (R_{off}/R_{on}) about an order $\sim 10^4$, which is almost 3 and 1 order greater than R_5 and R_7 devices respectively. The LRS values are found to be 0.1$\pm$0.9 kΩ, 0.02 $\pm$0.01 and 0.02$\pm$0.02 kΩ are for R_5, R_6 and R_7 devices respectively. From LRS, it is indicating that the R_5 has lower stability.

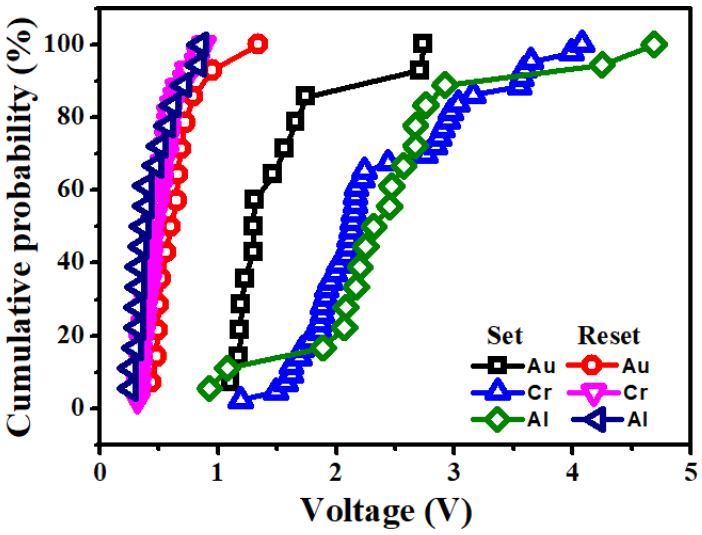

FIGURE 6.34: The cumulative distribution of set and reset voltages of R_5, R_6 and R_7 RRAM devices.

As explained above, the oxygen ions drift towards the anode thereby leaving positively charged oxygen vacancies in the film for LR state. It is observed that the R_5 device has large variation for the LR state (see in Figure *Figure* 6.33 (a)). The uncertainty of oxygen vacancies assisted filamentary conductive paths is more for R_5 device. In other words, the non-reactive or inert metal (Au) electrode will have less probability of interfacial layer above HfO_x to the top electrode resulting in a higher LR state (R_{off}). To analyze the effects of electrode material on the switching voltages, the cumulative probability function of these devices is shown in *Figure* 6.34. The average set voltage (V_{Set}), reset voltage (V_{Reset}) and reset current (I_{Reset}) are quantified for these devices. It is noticed that the average values of V_{Set} are 1.5, 2.4 and 2.5 V for R_5, R_6 and R_7 respectively. Similarly, the V_{Reset} values are 0.6, 0.5, and 0.45 V for the same devices. Furthermore, I_{Reset} are found to be 4, 10, and 12.2 mA for R_5, R_6 and R_7 respectively. It is noticed that the set & reset current are increasing whereas the reset voltage is decreasing among these RRAM devices (R_5, R_6 and R_7).

To investigate the conduction mechanism, linear fitting of curves has been performed for

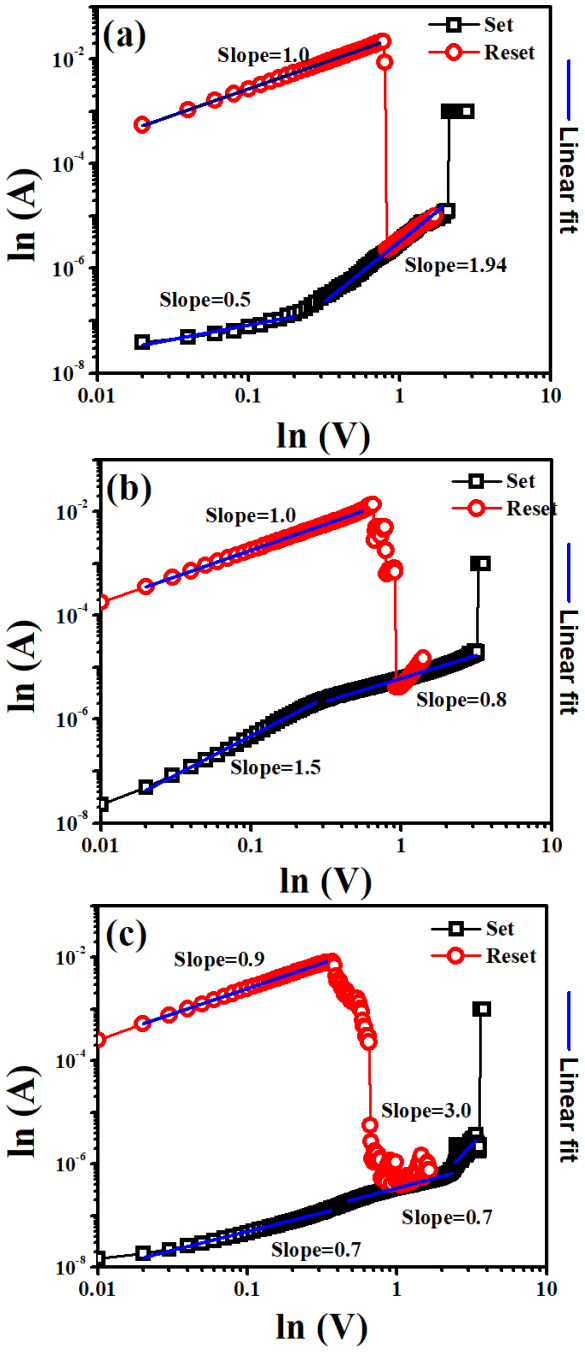

FIGURE 6.35: a), b) and c) the double-log I–V plots, linear fittings for the devices R_5, R_6 and R_7 respectively.

these devices. The linear fitted curves of logI–logV plots are shown in *Figure* 6.35 (a-c). The LR state showed the Ohmic behavior for all the RRAM devices. Here, HR state is found to be non-Ohmic in nature for the entire region of the set curves of the devices. Interestingly, R_6 device is showing Ohmic nature even at high voltage regions. This investigation verifies the role of the top electrode and the interfacial layers of the RRAM devices. Improvement in switching properties have been seen for R_6 device. Hence, the study indicates that the work

function of the top electrode also has a significant effect on the performance of the RRAM devices (Al = 4.06–4.26, Cr = 4.5 and Au = 5.10–5.47). In the present study, Cr has proven to be the most prominent and suitable metal top electrode for resistive switching among the considered metal electrodes.

6.7 Conclusions

HfO_x based crossbar structure RRAM devices have been fabricated successfully. Effects of thermal annealing and SHI irradiation on the switching performance of RRAM devices have been studied in detail. It is noticed that the annealing at 500 ^oC improves the endurance cycling and resistance ratio of the RRAM devices. The R_5-(ii) exhibited better switching characteristics and the set and reset operation of the filamentary conduction mechanism is explained based on the percolation model. It is also noticed that the stability of RRAM devices has been improved upon annealing. Further, the effects of SHI irradiation on the performance of RRAM devices are investigated and presented. 120 MeV Ag^{7+} ions with various fluence are used to elucidate the switching characteristics of these RRAM devices. It is observed that the SHI also plays an important role in tuning the set and reset voltages. Significantly, SHI irradiation improved the RRAM device characteristics below a critical fluence.

Finally, the role of the top electrode and consequent formation of interfacial layer on the resistive switching behavior is also presented. It is observed that the formation of an interfacial layer has a great impact on the performance of RRAM devices. The optimum work function metal electrode (Cr) shows good switching behavior, resistance ratio and retention time test. Electron beam evaporated sub-stiochiometric HfO_x based RRAM devices have been fabricated. These devices have exhibited superior switching perfomance. Further it is shown that the performance of the devices can be improved/tuned by subjecting them to thermal annealing & SHI irradiation. The effects of various metal electrodes are also studied.

Bibliography

[1] M. Kong, B. Li, C. Guo, P. Zeng, M. Wei, and W. He, "The optical absorption and photoluminescence characteristics of evaporated and IAD HfO_2 thin films," Coatings, vol. 9, no. 5, **(2019)**, doi: 10.3390/coatings9050307.

[2] L. D. V. Sangani and M. G. Krishna, "Oxygen Affinity of Metal Electrodes as Control Parameter in Tuning the Performance of Cu_xO-Based Resistive Random Access Memory Devices," Phys. Status Solidi Appl. Mater. Sci., vol. 1900392, pp. 1–7, **(2019)**, doi: 10.1002/pssa.201900392.

[3] D. S. Jeong et al., "Emerging memories: Resistive switching mechanisms and current status," Reports Prog. Phys., vol. 75, no. 7, **(2012)**, doi: 10.1088/0034-4885/75/7/076502.

[4] Q. Liu et al., "Controllable growth of nanoscale conductive filaments in solid-electrolyte-based ReRAM by using a metal nanocrystal covered bottom electrode," ACS Nano, vol. 4, no. 10, pp. 6162–6168, **(2010)**, doi: 10.1021/nn1017582.

[5] T. Nagata, M. Haemori, Y. Yamashita, H. Yoshikawa, K. Kobayashi, and T. Chikyow, "Observation of filament formation process of $Cu/HfO_2/Pt$ ReRAM structure by hard x-ray photoelectron spectroscopy under bias operation," J. Mater. Res., vol. 27, no. 6, pp. 869–878, **(2012)**, doi: 10.1557/jmr.2011.448.

[6] T. V. Perevalov, D. V. Gulyaev, V. S. Aliev, K. S. Zhuravlev, V. A. Gritsenko, and A. P. Yelisseyev, "The origin of 2.7 eV blue luminescence band in zirconium oxide," J. Appl. Phys., vol. 116, no. 24, pp. 2–6, **(2014)**, doi: 10.1063/1.4905105.

[7] L. D. V. Sangani, C. R. Kumar, and M. G. Krishna, "Interfacial Electrode-Driven Enhancement of the Switching Parameters of a Copper Oxide-Based Resistive Random-Access Memory Device," J. Electron. Mater., vol. 45, no. 1, pp. 322–328, 2016, doi: 10.1007/s11664-015-4074-0.

[8] M. Lanza, "A review on resistive switching in high-k dielectrics: A nanoscale point of view using conductive atomic force microscope," Materials (Basel)., vol. 7, no. 3, pp. 2155–2182, **(2014)**, doi: 10.3390/ma7032155.

[9] S. U. Sharath et al., "Thickness independent reduced forming voltage in oxygen engineered HfO_2 based resistive switching memories," Appl. Phys. Lett., vol. 105, no. 7, **(2014)**, doi: 10.1063/1.4893605.

[10] Q. Zhou and J. Zhai, "Resistive switching characteristics of $Pt/TaO_x/HfN_x$ structure and its performance improvement," AIP Adv., vol. 3, no. 3, **(2013)**, doi: 10.1063/1.4794687.

[11] D. M. Mattox, Handbook of Physical Vapor Deposition (PVD) Processing: Film Formation, Adhesion, Surface Preparation and Contamination Control (Noyes Publications, Westwood, N.J, **(1998)**, 945 pp

[12] N. Manikanthababu, N. Arun, M. Dhanunjaya, V. Saikiran, S. V. S. Nageswara Rao, and A. P. Pathak, "Synthesis, characterization and radiation damage studies of high-k dielectric (HfO_2) films for MOS device applications," Radiat. Eff. Defects Solids, vol. 170, no. 3, pp. 207–217, **(2015)**.

[13] N. Manikanthababu et al., "Electronic excitation induced defect dynamics in HfO_2 based MOS devices investigated by in-situ electrical measurements," Appl. Phys. Lett., vol. 112, no. 13, **(2018)**, doi: 10.1063/1.5012269.

[14] M. Dhanunjaya, D. K. Avasthi, A. P. Pathak, S. A. Khan, and S. V. S. Nageswara Rao, "Grain fragmentation and phase transformations in hafnium oxide induced by swift heavy ion irradiation," Appl. Phys. A Mater. Sci. Process., vol. 124, no. 9, **(2018)**, doi: 10.1007/s00339-018-2000-z.

[15] M. Modreanu, S. Monaghan, I. M. Povey, K. Cherkaoui, P. K. Hurley, and M. Androulidaki, "Investigation of bulk defects in amorphous and crystalline HfO_2 thin films," Microelectron. Eng., vol. 88, no. 7, pp. 1499–1502, **(2011)**, doi: 10.1016/j.mee.2011.03.107.

[16] N. Arun, J. Prabana, K. V. Kumar, A. P. Pathak, and S. V. S. Nageswara, "Fabrication of HfO_2 based MOS and RRAM devices: A study of Thermal Annealing Effects on these Devices," vol. 030216, no. July, pp. 4–7, **(2019)**, doi: 10.1063/1.5113055.

[17] S. Long et al., "A Model for the Set Statistics of RRAM Inspired in the Percolation Model of Oxide Breakdown," vol. 34, no. 8, pp. 999–1001, **(2013)**.

[18] S. Long et al., "Compact Analytical Models for the SET and RESET Switching Statistics of RRAM Inspired in the Cell- Based Percolation Model of Gate Dielectric Breakdown," pp. 1–8, **(2013)**.

[19] S. U. Sharath et al., "Control of Switching Modes and Conductance Quantization in Oxygen Engineered HfO_x based Memristive Devices," vol. 1700432, pp. 1–13, **(2017)**, doi: 10.1002/adfm.201700432.

[20] Y. Li et al., "Conductance Quantization in Resistive Random Access Memory," Nanoscale Research Letters, vol. 10, no. 1. Nanoscale Research Letters, **(2015)**, doi: 10.1186/s11671-015-1118-6.

[21] M. M. Mallol, M. B. Gonzalez, and F. Campabadal, "Impact of the HfO_2/Al_2O_3 stacking order on unipolar RRAM devices," Microelectron. Eng., vol. 178, pp. 168–172, **(2017)**, doi: 10.1016/j.mee.2017.05.024.

[22] M. Saadi et al., "On the mechanisms of cation injection in conducting bridge memories: The case of HfO_2 in contact with noble metal anodes (Au, Cu, Ag)," J. Appl. Phys., vol. 119, no. 11, **(2016)**, doi: 10.1063/1.4943776.

[23] B. K. You et al., "Reliable Memristive Switching Memory Devices Enabled by Densely Packed Silver Nanocone Arrays as Electric-Field Concentrators," **(2016)**, doi: 10.1021/acsnano.6b04578 .

[24] "Effect of crystallization on the reliability of unipolar resistive-switching in HfO_2-based dielectrics," Curr. Appl. Phys., vol. 14, pp. 88–92, **(2014)**.

[25] L. G. Wang et al., "Excellent resistive switching properties of atomic layer-deposited Al_2O_3 /HfO_2/Al_2O_3trilayer structures for non-volatile memory applications," Nanoscale Res. Lett., vol. 10, no. 1, **(2015)**, doi: 10.1186/s11671-015-0846-y.

[26] J. Ni, Q. Zhou, Z. Li, and Z. Zhang, "Oxygen defect induced photoluminescence of HfO_2 thin films," Appl. Phys. Lett., vol. 93, no. 1, pp. 2–4, **(2008)**, doi: 10.1063/1.2952288.

[27] K. A. Morgan, R. Huang, K. Potter, C. Shaw, W. Redman-White, and C. H. De Groot, "Total dose hardness of TiN/HfO_x/TiN resistive random access memory," IEEE Trans. Nucl. Sci., vol. 61, no. 6, pp. 2991–2996, **(2014)**, doi: 10.1109/TNS.2014.2365058.

[28] N. Manikanthababu et al., "Effects of ion irradiation on the structural and electrical properties of HfO_2 /SiON/Si p-metal oxide semiconductor capacitors," Thin Solid Films, vol. 682, no. March, pp. 156–162, **(2019)**, doi: 10.1016/j.tsf.2019.03.009.

[29] X. He and R. E. Geer, "Heavy ion radiation effects on TiN/HfO_2/W resistive random access memory," IEEE Aerosp. Conf. Proc., **(2013)**, doi: 10.1109/AERO.2013.6497401.

[30] N. Manikanthababu, M. Dhanunjaya, S. V. S. Nageswara Rao, and A. P. Pathak, "SHI induced effects on the electrical and optical properties of HfO_2 thin films deposited by RF sputtering," Nucl. Instruments Methods Phys. Res. Sect. B Beam Interact. with Mater. Atoms, vol. 379, pp. 230–234, **(2016)**, doi: 10.1016/j.nimb.2016.01.042.

[31] N. Manikanthababu, N. Arun, M. Dhanunjaya, S. V. S. Nageswara Rao, and A. P. Pathak, "Gamma irradiation-induced effects on the electrical properties of HfO_2-based MOS devices," Radiat. Eff. Defects Solids, vol. 171, no. 1–2, pp. 77–86, **(2016)**, doi: 10.1080/10420150.2015.1135152.

[32] N. Arun, L.D. Varma Sangani, K. Vinod Kumar, A. Mangababu, M. Ghanashyam Krishna, A. P. Pathak, and S.V.S. Nageswara Rao, "Effects of swift heavy ion irradiation on the performance of HfO_2 thin films based resistive random access memory devices",Journal of Materials Science: Materials in Electronics, **(2021)**

[33] Y. T. Li, S. B. Long, Q. Liu, H. B. Lü, S. Liu, and M. Liu, "An overview of resistive random access memory devices," Chinese Sci. Bull., vol. 56, no. 28–29, pp. 3072–3078, **(2011)**, doi: 10.1007/s11434-011-4671-0.

Chapter 7

Conclusions and future scope

7.1 conclusions

HfO_2 thin films have been optimized by RF sputtering followed by annealing using a tubular furnace in N_2 environment. Thermal annealing induced a phase transition from amorphous to monoclinic at above 500 ^oC temperature. MIM like crossbar structures of the HfO_2 based RRAM devices have been fabricated to investigate their switching properties. Influence of the bottom electrode and the effects of gamma irradiation on the performance of these devices have been studied and reported. Two different active areas of 10 μm x 10 μm and 20 μm x 20 μm lithography-based RRAMs have been fabricated by using RF sputtering technique. Effects of SHI on the electrical properties of these RRAM devices are investigated. More interestingly, it is found to be lowering the set voltages at higher fluence ranges. Non-stoichiometric HfO_2 thin films have been optimized and fabricated by using e-beam evaporation technique. Effects of Thermal annealing and SHI irradiation on switching properties of the RRAM devices have been elucidated. We find significant annealing effects at lower fluences by SHI of non-stoichiometric HfO_x based RRAM devices. Effects of the top metal electrode on the performance of these RRAM devices have also been investigated. It is important to study the effects of metal electrodes and the interface of metal-insulator in the switching mechanism of these RRAM devices.

The main observation is that a low dose gamma / SHI irradiation improves the switching properties of HfO_2 and HfO_x based RRAM devices. However the device performance is deteriorated when the fluence is above a critical value. This critical fluence is close to the track-overlap fluence in case of SHI irradiation. The work presented in this thesis provides

useful information to tailor the switching performance of the emerging microelectronic compatible RRAM devices. The study also shines light on the possible radiation damage and reliability issues of this technologically important class of devices. The study may be extended to further understand the basic mechanisms that are governing the radiation damage and to stretch the tolerance limits of these devices in future.

7.2 Future scope:

Fabrication of low power RRAM devices with potential for use in embedded systems is of current interest. The present study can be extended to develop appropriate electrode/active layer combinations for performance enhancement of sub-stoichiometric, hydrogenated and defect engineered oxide based RRAM devices on hard and flexible substrates. H-implantation and/or thin-film deposition in hydrogen atmosphere may be performed for synthesizing hydrogenated metal oxide films. It is also important to study and improve the switching speeds of these devices. The effects of vacancy defects may be elucidated if in-situ Raman, in-situ PL and switching speed measurements are performed by fabricating transparent RRAMs.

There is a current interest in producing defect assisted conducting channels in dielectrics to reduce / tuned the formation, set and reset voltages. Hence, controlled amounts of defects may be created by ion irradiation at precise locations and depth regions to tailor the switching properties of RRAMS. It is also critical to study the effects of crystalline phases in HfO_2 on the performance of the corresponding RRAM devices. An attempt may also be made to control the switching properties by optimizing the metal/dielectric barrier, stoichiometry and defect profiles in the active medium to obtain low power, high speed and high density RRAM devices. Fabrication of "Schottky contact based unidirectional RRAM" devices for developing non-volatile memory arrays and logic circuits is another challenge. RRAMs also find applications in gas and bio-sensors. "Design, modeling and development of RRAM based simple digital logic circuits" is another important aspect in this area. The ultimate objectives are to realize in-memory computation and applications in neuromorphic systems, apart from replacing the present volatile RAM and the floating gate based NVMs by RRAMs in computers and smart devices around us. These are only few open ends among many in this critical area of research. The technology finds numerous applications in the emerging

area of the Internet of things. The study may be extended to further understand the basic mechanisms that are governing the radiation damage and to stretch the tolerance limits of these devices in future.

Effects of Gamma and Swift Heavy Ion irradiation on the performance of HfO2 based Resistive Random Access Memory (RRAM) Devices

by Nimmala Arun

Effects of Gamma and Swift Heavy Ion irradiation on the performance of HfO2 based Resistive Random Access Memory (RRAM) Devices

ORIGINALITY REPORT

29%	7%	27%	3%
SIMILARITY INDEX	INTERNET SOURCES	PUBLICATIONS	STUDENT PAPERS

PRIMARY SOURCES

1	N. Arun, L. D. Varma Sangani, K. Vinod Kumar, A. Mangababu, M. Ghanashyam Krishna, A. P. Pathak, S. V. S. Nageswara Rao. "Effects of swift heavy ion irradiation on the performance of HfO2-based resistive random access memory devices", Journal of Materials Science: Materials in Electronics, 2021 Publication	13%
2	N. Arun, K. Vinod Kumar, A. P. Pathak, D. K. Avasthi, S. V. S. Nageswara Rao. "Hafnia-based resistive switching devices for non-volatile memory applications and effects of gamma irradiation on device performance", Radiation Effects and Defects in Solids, 2018 Publication	4%
3	N. Arun, K. Vinod Kumar, A. Mangababu, S. V. S. Nageswara Rao, A. P. Pathak. " Influence of the bottom metal electrode and gamma irradiation effects on the performance of HfO -	3%

Student's Paper.
S. V. S. Nageswara Rao
Prof. S.V.S. NAGESWARA RAO
School of Physics
University of Hyderabad
Hyderabad-500 046, INDIA.
10/02/2021.

Student's Paper.
S. V. S. Nageswara Rao
Prof. S.V.S. NAGESWARA RAO
School of Physics
University of Hyderabad
Hyderabad-500 046, INDIA.
10/02/2021.

Student's Paper.
S. V. S. Nageswara Rao
Prof. S.V.S. NAGESWARA RAO
School of Physics
University of Hyderabad
Hyderabad-500 046, INDIA.
10/02/2021.

based RRAM devices ", Radiation Effects and Defects in Solids, 2019
Publication

4	Kirti Agashe, Nisha Sarwade, Sangeeta Joshi, Madhavi Thakurdesai, Smita Surwase, Pravin Tirmali, Kandasami Asokan. "Effect of gamma irradiation on resistive switching of Al/TiO 2 /n + Si ReRAM", Nuclear Instruments and Methods in Physics Research Section B: Beam Interactions with Materials and Atoms, 2017 Publication	<1%
5	iopscience.iop.org Internet Source	<1%
6	aip.scitation.org Internet Source	<1%
7	M. Dhanunjaya, D. K. Avasthi, A. P. Pathak, S. A. Khan, S. V. S. Nageswara Rao. "Grain fragmentation and phase transformations in hafnium oxide induced by swift heavy ion irradiation", Applied Physics A, 2018 Publication	<1%
8	Submitted to University of Hyderabad, Hyderabad Student Paper	<1%
9	P. Kondaiah, Habibuddin Shaik, G. Mohan Rao. "Studies on RF magnetron sputtered HfO2 thin films for microelectronic applications", Electronic	<1%

Electrodes as Control Parameter in Tuning the Performance of Cu O-Based Resistive Random Access Memory Devices ", physica status solidi (a), 2019
Publication

19	"Polymer Insulation Applied for HVDC Transmission", Springer Science and Business Media LLC, 2021 Publication	<1%
20	digitalcommons.njit.edu Internet Source	<1%
21	Submitted to North West University Student Paper	<1%
22	wiki.itap.purdue.edu Internet Source	<1%
23	N. Manikanthababu, N. Arun, M. Dhanunjaya, V. Saikiran, S.V.S. Nageswara Rao, A.P. Pathak. " Synthesis, characterization and radiation damage studies of high-k dielectric (HfO) films for MOS device applications ", Radiation Effects and Defects in Solids, 2014 Publication	<1%
24	N. Arun, J. Prabana, K. Vinod Kumar, A. P. Pathak, S. V. S. Nageswara Rao. "Fabrication of HfO2 based MOS and RRAM devices: A study of thermal annealing effects on these	<1%

Student's Paper
S.V.S. Nageswara Rao

Prof. S.V.S. NAGESWARA RAO
School of Physics
University of Hyderabad
Hyderabad-500 046, INDIA.

	Internet Source	<1%
81	Jain, I.P.. "Ion beam induced surface and interface engineering", Surface Science Reports, 201103 Publication	<1%
82	doi.org Internet Source	<1%
83	Chulho Jung. "RESISTIVE SWITCHING AND THRESHOLD CURRENT OF Cr-DOPED SrTiO3 THIN FILMS DEPOSITED BY PULSED LASER DEPOSITION", Integrated Ferroelectrics, 4/2007 Publication	<1%
84	Kolla Lakshmi Ganapathi, Navakanta Bhat, Sangeneni Mohan. " Influence of O flow rate on HfO gate dielectrics for back-gated graphene transistors ", Semiconductor Science and Technology, 2014 Publication	<1%
85	Submitted to Indian Institute of Technology, Bombay Student Paper	<1%
86	Submitted to Indian Institute of Technology Guwahati Student Paper	<1%

87	www.frtofamerica.com Internet Source	<1%
88	etheses.whiterose.ac.uk Internet Source	<1%

Exclude quotes	On	Exclude matches	< 14 words
Exclude bibliography	On		

UNIVERSITY OF HYDERABAD
SCHOOL OF PHYSICS
Centre for Advanced Studies in Electronics Science and Technology (CASET)

Dr. S.V.S.Nageswara Rao
Professor

Date: 10-02-2021
Hyderabad

This is to certify that the thesis titled "**Effects of Gamma and Swift Heavy Ion irradiation on the performance of HfO_2 based Resistive Random Access Memory (RRAM) Devices**" being submitted by Mr. **Nimmala Arun** (Reg.no., **14PHPE03**), has been screened by the Turnitin software at Indira Gandhi memorial library (IGML), University of Hyderabad. This software shows 29% similarity index out of which 21% is from the candidate's own publications (where he is the first author) and is directly related to this thesis.

From the detailed similarity index report, it is observed that the remaining **8%** is within the accepted limits. Hence the thesis may be considered for submission.

S.V.S. Nageswara Rao

Prof. S V S Nageswara Rao
(Supervisor) 11/02/2021.

Prof. S.V.S. NAGESWARA RAO
School of Physics
University of Hyderabad
Hyderabad-500 046, INDIA.

School of Physics, University of Hyderabad, Hyderabad – 500 046, India
Phone: +91 40 23134329; Fax: +91 40 2301022;
e-mail: svnsp@uohyd.ac.in, nageshphysics@gmail.com